Interplay of Topology, Localization, and Non-Hermiticity in Low-dimensional Systems realized through Electrical Circuits

A
Thesis Submitted
in Partial Fulfillment of the Requirements
for the Degree of
DOCTOR OF PHILOSOPHY
By

DIPENDU HALDER
Registration Number: 206121102

Under the Supervision of Dr. SAURABH BASU

Department of Physics
Indian Institute of Technology Guwahati
February, 2025

Declaration

This is to certify that the thesis entitled "**Interplay of Topology, Localization, and Non-Hermiticity in Low-dimensional Systems realized through Electrical Circuits**", submitted by me to the *Indian Institute of Technology Guwahati*, for the award of the degree of Doctor of Philosophy, is a bonafide work carried out by me under the supervision of Dr. Saurabh Basu. The content of this thesis, in full or in parts, has not been submitted to any other university or institute for the award of any degree or diploma. I also wish to state that, to the best of my knowledge and understanding, nothing in this thesis amounts to plagiarism.

Signed:

Dipendu Halder
Registration Number: 206121102
Department of Physics,
Indian Institute of Technology Guwahati, Guwahati-781039, Assam, India.

Date:

Disclaimer

The bibliography included in this thesis is, by no means, complete, but it contains the ones that we have consulted extensively. We apologize for inadvertently omitting some research papers, review articles, and other scientific documents relevant to the focus of this thesis, which could have been cited. For illustrative purposes, some of the figures in this thesis are taken from other sources and properly cited.

Certificate

This is to certify that the thesis entitled "**Interplay of Topology, Localization, and Non-Hermiticity in Low-dimensional Systems realized through Electrical Circuits**", submitted by Mr. Dipendu Halder (206121102), a research scholar in the *Department of Physics*, *Indian Institute of Technology Guwahati*, for the award of the degree of Doctor of Philosophy, is a record of an original research work carried out by him under my supervision and guidance. The thesis has fulfilled all requirements as per the regulations of the institute, and in my opinion, has reached the standard needed for submission. The results embodied in this thesis have not been submitted to any other University or Institute for the award of any degree or diploma.

Signed:

Supervisor: Dr. Saurabh Basu
Professor, Department of Physics,
Indian Institute of Technology Guwahati, Guwahati-781039, Assam, India.

Date:

Dedicated to my beloved
parents and sister
&
to the cherished memory of
late Satya Sir.

Acknowledgements

First and foremost, I convey my deepest gratitude to my supervisor, Prof. Saurabh Basu, for his constant guidance, encouragement, and profound insight throughout my doctoral journey. His patience, clarity of thought, and unwavering support have been instrumental in shaping both my research and my scientific outlook. I sincerely appreciate the time and care he devoted to mentoring me, and I consider myself extremely fortunate to have worked under his supervision.

I am also thankful to the chairman of my doctoral committee, Dr. Pankaj Kumar Mishra, and to the committee members, Prof. Debaprasad Maity and Dr. Kanhaiya Pandey, for their careful evaluation of my progress each year and for their constructive remarks and valuable suggestions. I extend my appreciation to all the faculty members of the Physics department for their cordial and supportive attitude whenever assistance was required.

My sincere thanks go to our collaborators, Prof. Ronny Thomale, Prof. Bilal Tanatar, Dr. Sudin Ganguly, Ms. Srijata Lahiri, Mr. Koustav Roy, and Mr. Koustav Gogoi, for their expertise, insightful discussions, and enthusiasm, all of which greatly enriched this work and broadened my perspective. I am especially indebted to Dr. Sudin Ganguly and Srijata for the numerous discussions and brainstorming sessions that played a crucial role in shaping my research and deepening my understanding of the subject. I also appreciate the use of AI-based language tools (e.g., chatGPT)for grammar checking, summarization, paraphrasing, and improving text clarity. I gratefully acknowledge my group members, seniors and juniors alike, Dr. Kuntal Bhattacharyya, Dr. Shilpi Roy, Dr. Sayan Mondal, Dr. Mijanur Islam, Srijata, Koustav, Shreya, Gourab, and Ayan, for their cooperation and support, with special thanks to Shreya, Gourab, and Kuntal da for their constant encouragement.

I also wish to thank my close friends, particularly Ankita, Soumen, Chinmoy, Gorachand, Ankan, Sourav, Sanjib, Nayan, Debeshwar, Pranjal, Supriyo, Arnab, Subhajit, Swargiary, Samten, Sanu, and Kuntal, who have been companions since my graduation. My heartfelt thanks to my seniors, especially Rony da, Mrinal da, Golam da, and Dipankar da, for their guidance and warmth. In particular, I am grateful to Ankita for her emotional support and motivation during difficult times; her empathy and readiness to help have been a constant source of strength.

Beyond academics, I would like to acknowledge the large cricket community, both the departmental team and the Bengal Tigers, Raj da, Debu da, Suchit da, Soumya, Vishal, Shailesh, Pradeep, Debu 2.0, Bhagwat, Shoaib, and Subhankar. The countless matches

in PPL, CL, ISPL, and many informal games, along with the friendships formed, made my PhD journey memorable and joyful. Similarly, I thank the football group, Surojit da, Sahabub da, Arghya da, Nihar, Subrata da, Niloy, Chinmoy da, Roson da, Sourav da, Swarup da, Subhasis, and Hubba, for the many matches in PFL and other tournaments that provided much-needed balance and camaraderie.

Above all, I owe my deepest and most heartfelt gratitude to my family, especially my parents and my sister. Their unwavering encouragement, sacrifices, and unconditional love have been the foundation of my journey. To my dear sister, I am profoundly thankful for always standing beside me with constant support and affection.

Sincerely
Dipendu Halder

Acronyms

1D One-Dimensional

2D Two-Dimensional

AA Aubry-André

AL Anderson Localization

BBC Bulk-Boundary Correspondence

BHZ Bernevig-Hughes-Zhang

BZ Brillouin Zone

CS Chiral Symmetry

DL Delocalization-Localization

EP Exceptional Point

Eq. Equation

Fig. Figure

GBZ Generalized Brillouin zone

H.c. Hermitian Conjugate

HOTP Higher-Order Topological Phase

HST Hybrid Skin Topological

IP Impedance Profile

IPMF In-Plane Magnetic Field

IPR Inverse Participation Ratio

LDOS Local Density of States

mIPR Maximum Inverse Participation Ratio

NH Non-Hermitian

nPT Non-Parity-Time-Symmetric

OBC Open Boundary Condition

PBC Periodic Boundary Condition

PHS Particle-Hole Symmetry

PT Parity-Time

QHE Quantum Hall Effect

QP Quasi-Periodic

QSH Quantum Spin Hall

RMS Root-Mean-Square

SOSE Second-Order Skin Effect

sPT Parity-Time-Symmetric

SSH Su-Schrieffer-Heeger

TB Tight-Binding

TI Topological Insulator

TRS Time-Reversal Symmetry

VP Voltage Profile

Contents

Abstract

In recent decades, the study of topology in shaping material properties has become a central theme in modern-day condensed matter physics. Additionally, the non-Hermitian (NH) systems reveal a wealth of intriguing phenomena, including the non-Hermitian skin effect, non-Bloch band theory, exceptional points, and the concept of the generalized Brillouin zone. Among various experimental platforms, topolectrical circuits have emerged as a particularly versatile and easy-to-fabricate analogue for condensed matter systems.

The first chapter provides a detailed account of the introduction, whereas the second chapter discusses the methodologies and the working principles of the topolectrical circuits. The third chapter of the thesis investigates the NH Su-Schrieffer-Heeger model, considering a $\mathcal{PT}$-symmetric model with onsite gain and loss, as well as the other without $\mathcal{PT}$ symmetry (non-reciprocal hopping). We uncover a range of topological and localization phenomena, including the condition for exceptional points, the breakdown of bulk-boundary correspondence, the presence or absence of skin effect, and the construction of the generalized Brillouin zone. In the fourth chapter, we study a longer-range one-dimensional model with intra- and inter-orbital hoppings, featuring two NH variants tied to $\mathcal{PT}$ symmetry, and show that the skin effect is direction-dependent. Interestingly, our findings reveal the absence of skin effect in the non-reciprocal model, which we explain using pseudo-Hermiticity and non-Bloch band theory. In the fifth chapter, we investigate a disordered NH Aubry-André model and show an interplay between Anderson localization and the skin effect. The voltage profile of the circuit exhibits confinement at the interface, analogous to the skin effect, while the phenomenon of Anderson localization in the circuit can be perceived via a predicted localization behavior near the excitation node. The sixth chapter involves exploring the (2D) NH Bernevig-Hughes-Zhang model, demonstrating that a spin-dependent NH balanced gain/loss potential induces competition between first- and higher-order topological phases. Using projected spin spectra and the spin Chern number, we elucidate the revival of the first-order topological phase. The seventh chapter involves investigating the second-order skin effect, specifically the hybrid-skin topological effect in a brick-wall lattice, a variant of the honeycomb lattice, where we observe dynamically stable corner skin modes. To provide a sound experimental platform for the results obtained in each chapter, we propose electrical circuits composed of standard components that capture all the key features arising from the interplay between topology and non-hermiticity. We conclude the eighth chapter by summarizing the important results on NH topological and localization properties of the TB models and their corresponding TECs obtained in our thesis.

List of Publications

1. Dipendu Halder, Sudin Ganguly, & Saurabh Basu, *Properties of the non-Hermitian SSH model: role of PT symmetry*, **J. Phys.: Condens. Matter**, Dec 2022, **35**, 105901; DOI: 10.1088/1361-648X/acadc5.

2. Dipendu Halder, Ronny Thomale & Saurabh Basu, *Circuit realization of a two-orbital non-Hermitian tight-binding chain*, **Phys. Rev. B**, March 2024, **109**, 115407; DOI: 10.1103/PhysRevB.109.115407.

3. Dipendu Halder & Saurabh Basu, *Parsing skin effect in a non-Hermitian spinless BHZ-like model*, **J. Phys.: Condens. Matter**, May 2024, **36**, 335301; DOI: 10.1088/1361-648X/ad4940.

4. Dipendu Halder, Srijata Lahiri & Saurabh Basu, *Competing topological phases in a non-Hermitian time-reversal symmetry broken Bernevig-Hughes-Zhang model*, **Phys. Rev. B**, Sept 2024, **110**, 115132; DOI: 10.1103/PhysRevB.110.115132.

5. Dipendu Halder & Saurabh Basu, *Controlled probing of localization effects in the non-Hermitian Aubry-André model via topolectrical circuits*, **Phys. Rev. B**, June 2025, **111**, 235447; DOI: 10.1103/7t7k-qg49.

6. Koustav Roy, Dipendu Halder, Koustabh Gogoi, Bilal Tanatar & Saurabh Basu, *Floquet Non-Bloch formalism for a Non-Hermitian ladder: from theoretical framework to topolectrical circuits*, **Phys. Rev. Research**, December 2025, **7**, 043331; DOI: 10.1103/s3b6-wz16.

7. Dipendu Halder, Srijata Lahiri & Saurabh Basu, *Second-order Skin Effect in a Brick-Wall Lattice*, **arxiv (cond-mat.mes-hall)**, March 2026; arXiv:2603.24843.

Conferences Attended

1. Presented poster in the Conference on Condensed Matter Physics at Physical Research Laboratory, India, in 2023.
2. Presented poster in the Research and Industrial Conclave at IIT Guwahati, India, in 2023.
3. Presented poster in the annual conference on Quantum Condensed Matter at National Institute of Science Education and Research, India, in 2023.
4. Presented poster in the annual conference on Quantum Condensed Matter at IIT Guwahati, India, in 2024.
5. Delivered oral presentation in the APS Global Physics Summit 2025 in California, USA, in 2025. Awarded with APS Global Physics Summit DCMP Graduate Student Travel Awards.
6. Presented poster in the Advanced School and Conference on Quantum Matter at Trieste, Italy, in 2025.
7. Delivered for oral presentation in the APS Global Physics Summit 2026 in Denver, USA, in 2026.

List of Figures

List of Tables

Chapter 1

Introduction

Since the development of the band theory of electronic properties through quantum mechanics in the 1920s, condensed matter physics has been primarily driven by the search for materials with varied physical and transport characteristics. One of the most significant achievements in understanding material properties has been the systematic classification of quantum phases based on spontaneous symmetry breaking. In this framework, each ordered phase is characterized by an order parameter associated with a symmetry-breaking, so that a phase transition is indicated by a change (sudden or gradual) in its value. The specific pattern of symmetry breaking uniquely determines this order parameter. Such a formalism is provided by the effective field theory known as the Landau–Ginzburg theory [6]. This approach relies solely on general features, including the symmetry properties and dimensionality of the order parameter. It therefore offers a universal, unified description of a wide range of quantum states of matter. Once a state of matter is achieved, that is, the system gets into a stable phase (energy is minimized), it is going to be there forever. For example, the loss of conducting properties (onset of an insulating phase) is marked by the vanishing of electronic conduction over finite distances in a crystal.

This symmetry-based viewpoint on phase transition was soon supplemented by an experimental breakthrough in 1980, when Von Klitzing, Dorda, and Pepper [7] observed an unexpected transport phenomenon in a two-dimensional (2D) electron gas formed at a semiconductor heterojunction under a strong magnetic field. In this system, the longitudinal conductance was found to vanish, while the Hall conductance developed a sequence of precisely quantized plateaus at values $\nu e^2/h$ ($\nu = 1, 2, 3, \ldots$; e : charge of electron, h :

Plank's constant), which later became known as 'Integer Quantum Hall Effect'. Although the applied magnetic field explicitly breaks time-reversal symmetry in a quantum Hall system, the emergence of these quantized phases is not accompanied by spontaneous symmetry breaking. Arguably, no conventional order parameter exists to distinguish between the different quantum Hall phases. The essential physics instead lies in the spatial arrangement of the electronic states: electrons in the bulk are localized, whereas those near the boundary remain delocalized and form robust edge-conducting channels. This bulk–edge dichotomy is the defining characteristic of a *topological phase* of matter and marked a fundamental shift in the understanding of quantum phases.

1.1 Topology in Condensed Matter Physics

Although the quantum Hall effect (QHE) is widely regarded as the starting point of topological condensed matter physics, the accompanying theoretical advances were equally crucial in shaping the field. A landmark contribution came in 1982, when D. J. Thouless, M. Kohmoto, M. P. Nightingale, and M. Den Nijs demonstrated that the Hall conductance is insensitive to microscopic details of the system [8]. Instead, it is governed by a global topological property of the filled Bloch bands. In their formulation, the integer ν appearing in the quantized Hall conductance ($\nu e^2/h$) was identified with a mathematical object known as the Chern number, thereby elevating it to the status of a *topological invariant*. From a geometrical standpoint, this Chern number corresponds to the quantized flux of an effective gauge field defined over a compact manifold, such as the toroidal Brillouin zone (BZ). This insight makes it clear that the quantization observed in the QHE has a fundamentally topological origin rather than a dynamical one. The natural question that follows is how topology explicitly enters the physical description of such systems, or which precise mathematical framework can be used to identify, classify, and characterize such topological phenomena? To address this, it is instructive first to recall how topological ideas arise in geometry.

To organize and compare geometric objects, mathematicians introduced the notion of topological invariance, which allows shapes to be grouped into broad equivalence classes. A familiar example is the classification of 2D surfaces by the *number of holes* they possess, known as the *genus*. From this perspective, the surface of a perfect sphere is topologically equivalent to that of an ellipsoid, since one can be smoothly deformed into the other without introducing or removing any holes. The intuitive notion of genus can be formulated rigorously in mathematics through an integral over the local curvature of a surface, which defines the topological invariant [9] (ν for the case of QHE). Analogously, physics admits topologically quantized observables that can be written as invariant integrals over momentum space [8]. Such quantities remain unchanged under smooth deformations of system parameters. Their values can change only during a *topological*

phase transition. For example, a coffee cup and a donut are considered topologically equivalent, as both contain exactly one *hole*. In quantum mechanical systems, for example, consider a general many-particle Hamiltonian whose ground state is separated from the excited states by a finite energy gap. In this context, a smooth deformation corresponds to a continuous change of the Hamiltonian (say, via tuning some external agent, such as an electric field) that preserves the bulk energy gap. With this definition, the topological implications become meaningful for quantum-mechanical systems. Under this framework, two gapped quantum states belonging to different topological classes cannot be continuously connected without closing the gap. Any transformation between them necessarily involves a quantum phase transition, at which the system becomes gapless. Through such admissible deformations, seemingly different quantum phases can be grouped into the same topological equivalence class, culminating in the development of topological band theory and topological insulators (TIs), semimetals, and superconductors [10–13].

In the QHE, the Hall conductance is robust and determined by a global topological invariant; thus, the QHE is considered the *birth of topological physics* within the broad purview of condensed-matter systems. Importantly, the specific form and nature of the topological invariants are not universal but depend on the symmetry class to which a given system belongs. For Hermitian TIs, this dependence is systematically captured by the so-called *ten-fold way* classification [14]. This scheme categorizes systems according to the presence or absence of three fundamental symmetries: (i) time-reversal symmetry (TRS), which reverses the direction of time and checks whether the Hamiltonian remains invariant; (ii) particle-hole symmetry (PHS), which interchanges particles and holes; and (iii) chiral symmetry (CS), which arises as a combination of the former two. A complete classification of TIs and superconductors is provided by exactly ten distinct symmetry classes, determined by the interplay of fundamental symmetries and spatial dimensionality. This central result was first systematically established by A. Altland and M. Zirnbauer [15], also known as 'AZ symmetry class'. To see why only ten classes arise, consider first TRS, represented by an anti-unitary operator $\mathcal{T}$. A Hamiltonian may (i) lack TRS altogether, denoted by $\mathcal{T} = 0$; (ii) be invariant under time reversal with $\mathcal{T}^2 = +1$ (described as $\mathcal{T} = +1$); or (iii) be invariant under time reversal with $\mathcal{T}^2 = -1$ (described as $\mathcal{T} = -1$). An entirely analogous trichotomy applies to PHS (also known as charge-conjugation symmetry), $\mathcal{C}$, for which the Hamiltonian may satisfy $\mathcal{C} = 0$, $\mathcal{C} = +1$, or $\mathcal{C} = -1$. Taken together, these possibilities suggest $3 \times 3 = 9$ distinct ways in which a Hamiltonian H can transform under TRS and PHS. However, CS is defined as the product $\Gamma = \mathcal{T}\,.\,\mathcal{C}$. For all combinations except the case $\mathcal{T} = \mathcal{C} = 0$, the value of Γ is uniquely fixed. When both TRS and PHS are absent, however, CS may either be absent ($\Gamma = 0$) or present ($\Gamma = 1$). Accounting for this extra distinction leads to a total of $(3 \times 3 - 1) + 2 = 10$ inequivalent symmetry classes. Let us quickly illustrate the role of symmetry in topology in a lower dimension by considering a simple one-dimensional

(1D) toy model. A canonical example is the Su–Schrieffer–Heeger (SSH) model [16], introduced in 1979 by Wu-Pei Su, John R. Schrieffer, and Alan J. Heeger to describe the physics of a long polyacetylene chain with Carbon atoms attached to Hydrogen atoms. A corresponding tight-binding (TB) model is defined on a lattice whose unit cell contains two sublattices, connected by alternating intra-cell (e.g., $C = C$ double bond) and inter-cell ($C - C$ single bond) hopping amplitudes that are generally unequal. Owing to this structure, the SSH model respects all three fundamental symmetries, TRS, PHS, and CS, and consequently falls into the BDI symmetry class [17]. In a regime where intra-cell hopping is weaker than inter-cell hopping, the system enters a topological phase. Under open boundary condition (OBC), this phase is characterized by the emergence of two zero-energy edge states. The corresponding topology is quantified by a winding number, which is a topological invariant for the BDI class in one dimension and takes the values 1 or 0 for the topologically non-trivial and trivial phases, respectively. We shall return to this discussion more elaborately again in Chapter 3. For the moment, however, we shift our focus back to the post-QHE developments.

Following the discovery of the integer QHE, a natural question emerged: could there exist a quantum analogue of the Hall effect in magnetic materials, such as a ferromagnet? Indeed, ferromagnetic materials exhibit an *anomalous* Hall effect, in which the transverse voltage is much larger than that observed in non-magnetic conductors [18]. Researchers then asked whether a phase with quantized Hall conductance could arise in the complete absence of an external magnetic field and in a non-magnetic material. A decisive answer was provided in 1988 by F. D. M. Haldane, who introduced the first concrete theoretical model exhibiting quantized Hall conductance without any net orbital magnetic field [19]. This now-celebrated construction, known as the *Haldane model*, is a TB model on a honeycomb lattice featuring real nearest-neighbor hopping amplitudes and complex next-nearest-neighbor hopping terms. The latter breaks TRS while maintaining zero net magnetic flux through the unit cell. This work demonstrated that a non-trivial topological phase with a non-zero Chern number, supporting a quantized Hall response, can be generated purely through lattice-scale quantum effects, precluding the presence of Landau levels [7]. Although the Haldane model established the theoretical feasibility of a quantum anomalous Hall state, identifying a realistic route to realizing this phase in actual materials remained an open challenge for nearly two decades. Progress came indirectly, through developments in closely related, yet distinct phenomena; namely, the spin Hall effect and its quantized counterpart, the quantum spin Hall (QSH) effect. In the spin Hall effect [20, 21], an applied electric field generates a transverse flow of spin angular momentum, resulting in a finite spin current perpendicular to the field direction. In contrast, the net charge current in that direction remains zero. Unlike the conventional charge Hall effect, this phenomenon respects TRS and can therefore occur in materials even in the absence of an external magnetic field. Thus, the QSH effect can be viewed as a superposition of two quantum anomalous Hall states, one

for spin-up and one for spin-down electrons, with opposite chirality. As a consequence, the transverse charge Hall conductance cancels out, whereas a non-vanishing quantized spin Hall conductance survives. In this regard, C. L. Kane and E. J. Mele extended the idea underlying the Haldane model to a honeycomb lattice composed of spin-$\frac{1}{2}$ electrons in 2005 [22]. Importantly, TRS remains intact in this setting. As a result, these helical edge states are protected against non-magnetic impurities and disorder, since elastic back scattering between the two counter-propagating channels is forbidden by symmetry. Despite this elegant theoretical proposal, the intrinsic spin–orbit coupling in graphene is found to be extremely weak, rendering the experimental realization of the QSH effect in graphene impractical. Motivated by this limitation, in 2006, B. A. Bernevig, T. L. Hughes, and S. C. Zhang proposed an alternative and experimentally viable platform for realizing the QSH effect: a CdTe/HgTe/CdTe sandwiched quantum well structure [23]. The band structure of HgTe is inverted, while CdTe has a conventional band structure. If the thickness of the HgTe layer is tuned, then a band inversion occurs within the quantum well, resulting in a topological phase transition. Konig et al. confirmed this prediction experimentally 1 year later [24]. The theoretical model for this experiment will be discussed in more detail in Chapter 6.

1.2 Non-Hermitian Systems and their Properties

While parallel advances were being made on both theoretical and experimental fronts in topological condensed matter, a different direction within quantum mechanics was also developing rapidly, one that would become increasingly important for practical systems: non-Hermitian (NH) quantum mechanics [25]. Hermiticity is a foundational principle of quantum mechanics [26], as it ensures that physical observables are represented by Hermitian ($H = H^\dagger$) operators. This requirement guarantees both the conservation of probability and the reality of the corresponding eigenvalues. However, it was recognized early in the development of quantum theory that many realistic systems are inherently non-conservative, exchanging energy or particles with their environment. In such non-ideal systems, processes involving gain and loss naturally violate probability conservation, thereby breaking hermiticity. Describing these systems, therefore, necessitates the use of NH Hamiltonians. It should be emphasized, however, that this non-conservation is only local: although individual subsystems may exhibit gain or loss, the total energy of the complete setup, including the environment, remains conserved. In this sense, the fundamental principle of energy conservation is never violated. A simple example is a light bulb in an electrical circuit: it converts electrical energy into radiation and heat, which appears as a loss from the viewpoint of the circuit alone, even though the total energy of the larger system is conserved. The development of a theoretical framework for NH systems is especially important for experimental studies, where dissipation and

loss are almost unavoidable. Motivated by these insights, NH systems have since been explored extensively, revealing a rich set of physical phenomena with direct implications for modern topological physics [1, 25, 27–40].

In 1998, C. M. Bender and collaborators showed that not necessarily NH systems had to possess complex eigenspectra [41, 42]. Instead, real eigenvalues can emerge when the Hamiltonian satisfies parity-time ($\mathcal{PT}$) symmetry, which can be viewed as an exclusive variant of the pseudo-hermiticity [43] (shall be discussed later). However, a system possessing $\mathcal{PT}$ symmetry can also have two distinct phases: (i) $\mathcal{PT}$-unbroken phase, characterized by a real spectrum, and (ii) $\mathcal{PT}$-broken phase, where complex eigenvalues emerge. The transition between these two phases occurs at special critical points in parameter space, known as exceptional points (EPs) [44], which play a central role in the physics of NH systems. At an EP, not only do the eigenvalues merge, but the corresponding eigenvectors also coalesce, rendering the Hamiltonian non-diagonalizable. Also, the left eigenvector (eigenvector of $H^\dagger$) and the right eigenvector (eigenvector of H) of an NH Hamiltonian differ from each other, as the eigenvectors no longer form an orthonormal set due to the non-hermiticity. Instead, they form a biorthonormal set of eigenvectors and satisfy the biorthonormal condition given by,

$$H^\dagger \left|\Psi_n^{\mathrm{LE}}\right\rangle = E_n^* \left|\Psi_n^{\mathrm{LE}}\right\rangle; \quad H \left|\Psi_m^{\mathrm{RE}}\right\rangle = E_m \left|\Psi_m^{\mathrm{RE}}\right\rangle; \quad \left\langle\Psi_n^{\mathrm{LE}}|\Psi_m^{\mathrm{RE}}\right\rangle = \delta_{nm}, \tag{1.1}$$

where Ψ_n^{LE} and Ψ_m^{RE} are the left and right eigenvectors corresponding to the eigenvalues E_n^* and E_m respectively. Another interesting phenomenon, which arises due to the interplay between non-hermiticity and topology, is the non-Hermitian skin effect [45]. It refers to a phenomenon in which the eigenstates of a lattice with OBC become spatially localized, in sharp contrast to the extended Bloch-wave eigenstates characteristic of Hermitian systems, posing a question on the bulk-boundary correspondence (BBC) of an NH system. Additionally, since for a general NH Hamiltonian, the relation $H^* = H^T$ is not satisfied, the ten-fold way symmetry classification is also modified. As a consequence, each of the three conventional symmetries, TRS, PHS, and CS, can yield different constraints depending on whether the corresponding operator acts on H^* or on H^T. In addition, the sub-lattice symmetry, defined through $\Gamma H \Gamma^{-1} = -H$ with $\Gamma^2 = 1$, is no longer equivalent to CS in the NH setting. Therefore, instead of three symmetry types, one must now consider six distinct symmetry operations: TRS, TRS†, PHS, PHS†, CS, and sub-lattice symmetry. Taking this generalized symmetry structure into account significantly extends the original AZ classification to a much richer 38-*fold classification* [35]. These non-trivial features of NH Hamiltonians have revealed a broad spectrum of new NH topological and localization phenomena. In the following, we discuss the essential properties of NH systems and outline their relevance in greater detail.

1.3 Symmetry Considerations; $\mathcal{PT}$ Symmetry

We begin by discussing a key property of NH Hamiltonians, which forms the basis of a substantial portion of this thesis. In conventional quantum mechanics, hermiticity of the Hamiltonian operator, expressed as $H^\dagger = H$, is imposed to ensure the reality of the energy eigenvalues. In contrast, this stringent mathematical requirement can be relaxed to the more physically motivated condition of spacetime reflection invariance, namely $\mathcal{PT}$ symmetry, defined by

$$[H, \mathcal{PT}] = 0. \tag{1.2}$$

The $\mathcal{PT}$ operator swaps the signs of the spacetime coordinates,

$$\mathcal{PT} : (x, y, z, t) \to (-x, -y, -z, -t).$$

Since $\mathcal{PT}$ invariance constitutes a weaker constraint on hermiticity, the ramifications of $\mathcal{PT}$ symmetry have emerged as a fertile ground for both theoretical and experimental research. By now, the field has grown extensively, with a large number of published articles, numerous review papers [31, 42], books [32], and doctoral theses. These studies encompass a wide range of experimental works that are directly or indirectly connected to $\mathcal{PT}$ symmetry, spanning optical setup [46–51], laser and photonic systems [52–56], atomic systems [57], phononics [58, 59], acoustics [60–62], metamaterials [63–65], and mechanical systems [66–68].

A primary technique to create a $s\mathcal{PT}$ Hamiltonian is to begin with a Hermitian Hamiltonian, which is $s\mathcal{PT}$ in nature, and then to perform an $s\mathcal{PT}$ *deformation* of this Hamiltonian [41]. The resulting Hamiltonian, obtained by complex analytic continuation of the original Hermitian Hamiltonian, remains $s\mathcal{PT}$ but is no longer Hermitian. To illustrate the construction of a $s\mathcal{PT}$ Hamiltonian we perform a simple $\mathcal{PT}$ deformation of the quantum harmonic-oscillator Hamiltonian

$$H = \frac{1}{2}p^2 + \frac{1}{2}x^2. \tag{1.3}$$

The above Hamiltonian is Hermitian, that is, $H^\dagger = H$, and the corresponding eigenvalues, E_n, are all real and positive,

$$E_n = n + \frac{1}{2} \quad (n = 0,\ 1,\ 2,\ ...). \tag{1.4}$$

The parity operator, $\mathcal{P}$, is a linear Hermitian operator that performs space reflection, so $\mathcal{P}^2 = I$ (I is the unity operator) and $\mathcal{P}^{-1} = \mathcal{P}$. Consequently, under the parity operation, both the position operator, x, and the momentum operator, p, change sign,

$$\mathcal{P}x\mathcal{P}^{-1} = -x, \qquad \mathcal{P}p\mathcal{P}^{-1} = -p, \tag{1.5}$$

while the time-reversal operator leaves x-invariant, but changes the sign of p,

$$\mathcal{T}x\mathcal{T}^{-1} = x, \qquad \mathcal{T}p\mathcal{T}^{-1} = -p, \tag{1.6}$$

where $\mathcal{T}^2 = I$ and $\mathcal{T}^{-1} = \mathcal{T}$. However, unlike $\mathcal{P}$, $\mathcal{T}$ is anti-linear because it changes the sign of the complex number i,

$$\mathcal{T}i\mathcal{T}^{-1} = -i. \tag{1.7}$$

The operations of $\mathcal{P}$ and $\mathcal{T}$ are independent and thus $\mathcal{P}$ and $\mathcal{T}$ commute $[\mathcal{P}, \mathcal{T}] = 0$. According to the definitions above, we see that the Hamiltonian in Eq. (1.3) satisfies Eq. (1.2), and thus this Hamiltonian is $s\mathcal{PT}$ as well as Hermitian. Now we introduce non-hermiticity in Eq. (1.3) by including ix, which is NH in nature but possesses $\mathcal{PT}$ symmetry. Therefore, we specifically use ix operator to perform a $s\mathcal{PT}$ deformation of H,

$$H = \frac{1}{2}p^2 + \frac{1}{2}x^2 + \varepsilon ix, \tag{1.8}$$

where ε is a real parameter. Now H is $s\mathcal{PT}$, and hence H commutes with the $\mathcal{PT}$ operator. A quick calculation verifies an interesting result, namely the eigenvalues of H in Eq. (1.8) are all real,

$$E_n = n + \frac{1}{2}(1 + \varepsilon^2) \quad (n = 0,\, 1,\, 2,\, ...). \tag{1.9}$$

Even though the eigenvalues of H are real, the associated eigenfunctions $\psi_n(x)$ are generally complex. Nevertheless, $\psi_n(x)$ decays exponentially as $x \to \pm\infty$. A key feature of these states is that they are all $s\mathcal{PT}$. Specifically, up to an overall phase factor, $\psi_n(x)$ remains unchanged under the simultaneous replacement $i \to -i$ (complex conjugation) and $x \to -x$. In addition, the deformed eigenfunctions retain their mutual orthogonality,

$$\int_{-\infty}^{\infty} dx\, \psi_m(x)\psi_n(x) = 0 \quad (m \neq n),$$

for all real ε. The Hermitian Hamiltonian obtained at $\varepsilon = 0$ therefore represents only a particular member of this family and is *not* fundamentally distinct from $\varepsilon \neq 0$. This illustrates that, while hermiticity guarantees a real spectrum, it is not a necessary condition for one.

1.3.1 $\mathcal{PT}$-broken and unbroken Phases

The example above might lead one to conclude that the eigenvalues of any $s\mathcal{PT}$ Hamiltonian are all real. Unfortunately, this conjecture is not valid either. Let us prove this through a simple example. Let ψ be an eigenstate of H with eigenvalue E, and H is $s\mathcal{PT}$, that is, $[H, \mathcal{PT}] = 0$. Now, a theorem from linear algebra states that if two operators A and B commute, then they are simultaneously diagonalizable; that is, an

eigenstate of A is also an eigenstate of B [69]. Similarly, if H and $\mathcal{PT}$ commute, then they are simultaneously diagonalizable; that is, an eigenstate of H is also an eigenstate of $\mathcal{PT}$,

$$\mathcal{PT}\psi = \lambda\psi, \tag{1.10}$$

with λ being an eigenvalue of $\mathcal{PT}$ operator corresponding to the eigenvector, ψ. Since, $\mathcal{P}^2 = \mathcal{T}^2 = I$ and $[\mathcal{P}, \mathcal{T}] = 0$ it follows that $(\mathcal{PT})^2 = I$. Subsequently, if we multiply the above equation on the left by $\mathcal{PT}$, we obtain,

$$\mathcal{PT}^2\psi = \mathcal{PT}\lambda\psi \quad \Rightarrow \quad I\psi = \mathcal{P}\lambda^*\mathcal{T}\psi \quad \Rightarrow \quad \psi = \lambda^*\lambda\psi. \tag{1.11}$$

This verifies that $|\lambda| = 1$, and hence, the eigenvalues of the $\mathcal{PT}$ operator trace a unit circle in the complex plane. Finally, we multiply the time-independent Schrödinger's equation by the $\mathcal{PT}$ operator on the left and divide the resulting equation by λ (as $\lambda \neq 0$), and conclude that $E = E^*$. While this argument is accurate, the conclusion is not generally correct. The flaw in the preceding argument lies in a misstatement of the elementary Theorem: *it implicitly assumes that both operators A and B are linear.* As a result, it is not generally valid to conclude that an eigenstate of H must also be an eigenstate of $\mathcal{PT}$. Although $\mathcal{PT}$ commutes with H, it is not a linear operator; rather, $\mathcal{PT}$ is anti-linear due to the complex conjugation carried out by $\mathcal{T}$. However, if an eigenstate of an $s\mathcal{PT}$ Hamiltonian is simultaneously an eigenstate of $\mathcal{PT}$, then the associated energy eigenvalue is necessarily real. Accordingly, when a $s\mathcal{PT}$ Hamiltonian ($[H, \mathcal{PT}] = 0$) possesses an entirely real spectrum, it is said to be in the $\mathcal{PT}$-unbroken phase, whereas the appearance of complex eigenvalues signals that the Hamiltonian corresponds to a $\mathcal{PT}$-broken phase.

1.3.2 Pseudo-hermiticity and $\mathcal{PT}$ Symmetry

At this stage, one might be tempted to conclude that $\mathcal{PT}$ symmetry alone guarantees a real spectrum even for an NH Hamiltonian. However, the situation is more subtle. As we shall see, hermiticity by itself is not a sufficient condition for obtaining real eigenvalues, and, likewise, the presence of $\mathcal{PT}$ symmetry is not by itself necessary to ensure spectral reality. In 2001, Ali Mostafazadeh showed that apart from the $\mathcal{PT}$ symmetry, another condition for an NH Hamiltonian to exhibit real eigenvalues is the pseudo-hermiticity [43]. Let us discuss this in detail. An NH Hamiltonian H is said to be η-pseudo-Hermitian, if there exists an operator η, such that H satisfies the following condition,

$$H^\dagger = \eta\, H\, \eta^{-1}. \tag{1.12}$$

Note that choosing $\eta = 1$ reduces the above equation to the condition of the Hermiticity of the Hamiltonian. The pseudo-Hermitian Theorem states that,

Theorem: Let H have a discrete spectrum and a complete biorthonormal system of eigenvectors $\{|\psi_n\rangle, |\phi_n\rangle\}$. Then H is pseudo-Hermitian if and only if one of the following conditions holds,

1. H has a real spectrum;
2. The complex eigenvalues come in complex conjugate pairs, and the multiplicity of complex conjugate eigenvalues is the same.

A direct implication of this Theorem is the following Corollary,

> *Corollary*: Every NH (or $s\mathcal{PT}$) Hamiltonian with a real spectrum and a complete set of biorthonormal eigenvectors is pseudo-Hermitian. Note that, in general, an NH Hamiltonian may not admit a complete biorthonormal system of eigenvectors.

1.4 Exceptional Points

In this section, we are going to explore the existence of EPs [44] of an NH Hamiltonian. At these points, the Hamiltonian becomes ill-defined, and a certain number of linearly independent eigenvectors coalesce, rendering it non-diagonalizable. This is different from the Hermitian degeneracies, where the eigenvectors become orthogonal at a Dirac point [10]. Although EPs had been understood at a theoretical level for several decades, their controlled experimental realization has become possible only in recent years. This development has triggered intense interest, and EPs are now encountered across a wide range of physical platforms, including acoustic [70, 71], optical [72], photonic [73–78], mechanical [79], and electronic [80–85] systems. Beyond these settings, EPs have also been explored in atomic and molecular physics [86], superconductivity [87–89], and studies of quantum phase transitions [90]. Additionally, their presence gives rise to a number of remarkable phenomena, such as unidirectional invisibility [91, 92], double refraction [49], laser mode selectivity [76, 93], non-reciprocal energy transfer [94], and unconventional quantum dynamics of exciton–polaritons [95, 96].

EPs generically occur in eigenvalue problems that depend on a particular parameter of the Hamiltonian(s). To find them, one must vary such a parameter. Let us take an example,

$$\begin{aligned} H(\lambda) &= H_0 + \lambda V \\ &= \begin{pmatrix} \omega_1 & 0 \\ 0 & \omega_2 \end{pmatrix} + \lambda \begin{pmatrix} \epsilon_1 & \delta_1 \\ \delta_2 & \epsilon_2 \end{pmatrix} \end{aligned}$$

where ω_k and ϵ_k determine the energies E_k, $k = 1, 2$. The expression for the eigenvalues of the system is given by,

$$E_{1,2}(\lambda) = \frac{1}{2}\Big(\omega_1 + \omega_2 + \lambda(\epsilon_1 + \epsilon_2) \pm \sqrt{(\epsilon_1 - \epsilon_2)^2 + 4\delta_1\delta_2}\sqrt{(\lambda - \lambda_1)(\lambda - \lambda_2)}\Big).$$

Now the eigenvalues and eigenvectors of the above matrix coalesce at the following values of λ,

$$\lambda_1 = \frac{-i(\omega_1 - \omega_2)}{i(\epsilon_1 - \epsilon_2) + 2\sqrt{\delta_1\delta_2}}.$$
$$\lambda_2 = \frac{-i(\omega_1 - \omega_2)}{i(\epsilon_1 - \epsilon_2) - 2\sqrt{\delta_1\delta_2}}.$$

At these values of λ, E_k will take the following form,

$$E(\lambda_{1,2}) = \frac{\epsilon_1\omega_2 - \epsilon_2\omega_1 \mp i\sqrt{\delta_1\delta_2(\omega_1 + \omega_2)}}{\epsilon_1 - \epsilon_2 \mp 2i\sqrt{\delta_1\delta_2}},$$

that is, the eigenvalues are the same for each λ_1 and λ_2. Similarly, at those values of λ, the right eigenvectors are given by,

$$|\phi_1\rangle = \begin{pmatrix} \frac{+i\delta_1}{\sqrt{\delta_1\delta_2}} \\ 1 \end{pmatrix} \qquad \text{for} \quad \lambda = \lambda_1$$

and

$$|\phi_2\rangle = \begin{pmatrix} \frac{-i\delta_1}{\sqrt{\delta_1\delta_2}} \\ 1 \end{pmatrix} \qquad \text{for} \quad \lambda = \lambda_2.$$

The corresponding left eigenvectors are given by,

$$\left\langle\tilde{\phi_1}\right| = \begin{pmatrix} \frac{+i\delta_2}{\sqrt{\delta_1\delta_2}} & 1 \end{pmatrix} \qquad \text{for} \quad \lambda = \lambda_1$$

and

$$\left\langle\tilde{\phi_2}\right| = \begin{pmatrix} \frac{-i\delta_2}{\sqrt{\delta_1\delta_2}} & 1 \end{pmatrix} \qquad \text{for} \quad \lambda = \lambda_2.$$

Note that the eigenvectors also coalesce at λ_1 and λ_2. Consequently, the eigenvectors do not span the full Hilbert space, and the system becomes defective at $\lambda = \lambda_1$ and $\lambda = \lambda_2$, suggesting them as the EPs of the system. The right and left eigenvectors are also orthogonal to each other at the EPs, that is, the scalar product $\left\langle\tilde{\phi_k}\middle|\phi_k\right\rangle$ for $k = 1, 2$ vanishes, which is referred to as *self-orthogonality* and in turn, a special case of biorthonormal condition (Eq. (1.1)). From a mathematical standpoint, EP can be described as the situation in which the algebraic multiplicity of an eigenvalue exceeds its geometric multiplicity, leading to an incomplete set of eigenfunctions and a defective Hamiltonian [44]. In general, when an m-dimensional Hamiltonian becomes non-diagonalizable at an EP with energy ε_0, it can be transformed into a Jordan block of order m. In this situation,

the system retains m degenerate eigenvalues, while a single linearly independent eigenvector exists, signaling the presence of an m-th order EP [97]. More broadly, an $m \times m$ matrix representing an m-dimensional Hamiltonian may host an EP of arbitrary order $n \leq m$. In such cases, the Hamiltonian can be cast into a block-diagonal form, where one block consists of an $n \times n$ Jordan block, and the remaining block is a $(m-n) \times (m-n)$ diagonal matrix. A quantitative measure of the self-orthogonality of eigenfunctions is provided by phase rigidity. The phase rigidity r_α is defined as [30],

$$r_\alpha = \frac{\langle \tilde{\phi_\alpha} | \phi_\alpha \rangle}{\langle \phi_\alpha | \phi_\alpha \rangle}, \tag{1.13}$$

where $\tilde{\phi_\alpha}$ and ϕ_α denote the biorthonormal left and right eigenvectors associated with the state α. As the system approaches an EP, the left and right eigenvectors progressively align with each other, leading to the vanishing of the phase rigidity ($r_\alpha \to 0$). By contrast, in a Hermitian system, the phase rigidity is $r_\alpha = 1$. It is also worth noting that NH systems can also host exceptional contours. These structures consist entirely of EPs, with the phase rigidity vanishing over a continuous curve rather than at an isolated point [98]. To realize exceptional contour in a system, the following criteria are stated below,

$$\text{Re } \det[H(\delta)] = 0.$$
$$\text{Im } \det[H(\delta)] = 0.$$

Such exceptional contours are known to preserve quantized topological charges [99].

1.5 Non-Hermitian Skin Effect (NHSE)

By now, it is evident that NH descriptions not only provide an appropriate framework for open systems but also give rise to new physics, unconventional phenomena, and novel applications. A key principle in the study of topological phases is the BBC, which asserts that the bulk topological invariants manifest as symmetry-protected boundary states; that is, the behavior of the edge of a system can be predicted from its bulk. The boundary insensitivity of bulk quantities is essential because it allows us to choose a convenient boundary condition. In particular, the periodic boundary condition (PBC) leads to a band-theory picture in momentum space. However, the BBC of topological systems was set up for a debate once NH systems were introduced. In particular, a mere change of boundary conditions from periodic to open was sufficient to drive all the bulk states from being extended to exponentially localized [45, 100]. These results are highly counterintuitive when viewed from the perspective of Hermitian topological systems. The underlying mechanism was termed the *non-Hermitian skin effect* [1, 38, 45, 101, 102], a phenomenon induced by non-hermiticity in which the eigenstates of a lattice with

OBC become spatially localized, in stark contrast to the extended Bloch-wave nature of eigenstates in Hermitian systems. NHSE has been realized in various experimental setups, including topolectrical [4, 103–109], photonic lattices [110–115], optical ring-resonators [116, 117], phononic and acoustic systems [118–124], and mechanical [125–128] systems.

The origin of this concept can be traced back to the pioneering works of Hatano and Nelson [129, 130] in the late 1990s, where a 1D disordered system with non-reciprocal nearest-neighbor hopping was studied. They demonstrated that such non-reciprocity-induced non-hermiticity can suppress Anderson localization, resulting instead in a mobility region that supports unidirectional transport. Although their primary focus was on vortex depinning and localization rather than topology, the physics they uncovered was very similar to NHSE. Let us first describe the Hatano-Nelson model [129]:

$$\hat{H}_{\mathrm{HN}} = \sum_i \left[(t+g) c_{i+1}^\dagger c_i + (t-g) c_i^\dagger c_{i+1} \right], \tag{1.14}$$

where i is the site index, and $c_i^\dagger$ and c_i are the fermionic creation and annihilation operators, respectively. $t \in \mathbb{R}$ and $g \in \mathbb{R}$ represent the hopping and the non-reciprocity introduced within the hopping terms, respectively. In matrix representation, the Hamiltonian becomes,

$$H_{\mathrm{HN}} := \begin{pmatrix} 0 & t-g & 0 & \cdots \\ t+g & 0 & t-g & \cdots \\ 0 & t+g & 0 & \cdots \\ \vdots & \vdots & \vdots & \ddots \end{pmatrix}.$$

Under the PBC, that is, for $[H_{\mathrm{HN}}]_{1,N} = t \pm g = [H_{\mathrm{HN}}]_{N,1}$, the complex energy spectrum is obtained via the relation,

$$E_k = (t+g)e^{ik} + (t-g)e^{-ik},$$

where $k = 2\pi j/L$ with $j = 0, 1, \cdots, L-1$ and L denoting the total number of lattice sites. Fig. 1.1(a) illustrates a pictorial representation of the Hatano-Nelson model for the OBC and PBC configurations, respectively. When $tg \neq 0$, the resulting PBC spectra trace out an ellipse in the complex energy plane, as shown via the blue curve in Fig. 1.1(b). In contrast, the eigenspectra under the OBC are a straight line along the real (x) axis, denoted in red. The explanation for the reality of the OBC eigenspectra is as follows. By employing an imaginary gauge transformation, the OBC Hamiltonian can be mapped

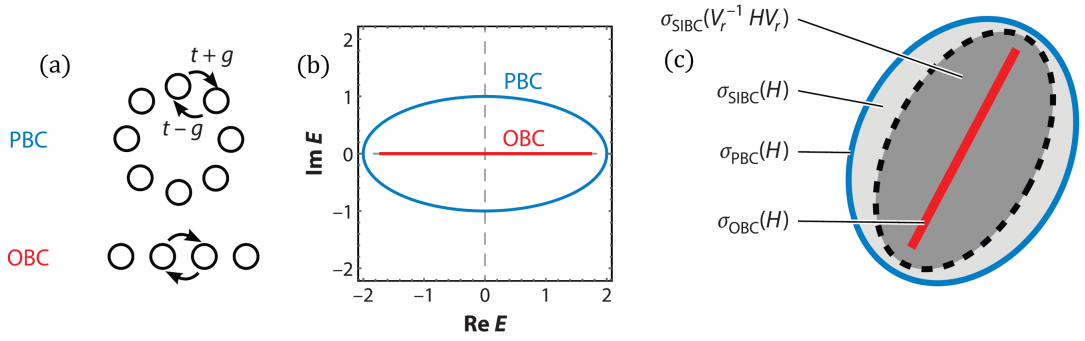

FIGURE 1.1: (a) PBC and OBC configuration for the Hatano-Nelson model. (b) Energy eigenvalues are plotted for the PBC (in blue) and OBC (in red) in the complex plane with $t = 1$ and $g = 0.5$. (c) Schematic diagram of the PBC, SIBC, and OBC spectra in the presence of NHSE. The area with the dotted boundary designates the SIBC spectrum under an imaginary gauge transformation V_r, given via Eq. (1.16). The figures are adopted from Ref. [1].

onto an equivalent Hermitian Hamiltonian without asymmetry,

$$H_{\mathrm{HN}}^{(\mathrm{sim})} := V_r^{-1} H_{\mathrm{HN}} V_r = \begin{pmatrix} 0 & \sqrt{t^2-g^2} & \cdots \\ \sqrt{t^2-g^2} & 0 & \cdots \\ \vdots & \vdots & \ddots \end{pmatrix}, \tag{1.15}$$

where $V_r[i, j] = r^i \delta ij$ with $r = \sqrt{(t+g)/(t-g)}$. Note that the imaginary gauge transformation introduced in Eq. (1.15), when applied to the creation and annihilation operators, leads to

$$V_r^{-1} c_i^\dagger V_r = r^i c_i^\dagger \quad \text{and} \quad V_r^{-1} c_i V_r = r^{-i} c_i. \tag{1.16}$$

This transformation effectively shifts the Bloch momentum from k to $k - i \log r$. Since it is a similarity transformation, it preserves the eigenspectra of the Hamiltonian. Consequently, the OBC spectrum of the Hatano–Nelson model coincides with that of the Hermitian matrix $H_{\mathrm{HN}}^{(\mathrm{sim})}$. Fig. 1.1(b) depicts the OBC spectra (red curve), which lie along a line on the real axis of the complex plane, in sharp contrast to the PBC spectra (blue curve), which form an ellipse within the same plane. The separate plots indicate the breakdown of the BBC. Consequently, the OBC eigenstates are obtained from those of $H_{\mathrm{HN}}^{(\mathrm{sim})}$ (Eq. (1.15)) through the similarity transformation V_r and are exponentially localized at any of the boundaries, depending upon the sign of g. The discussion above provides a qualitative understanding of the NHSE and the associated breakdown of the BBC, specifically for the clean Hatano–Nelson model. We now move beyond this intuitive picture and formulate a more general description based on a topological perspective.

1.5.1 Topological Origin of NHSE

Since all Bloch wavefunctions that are extended under PBC in Hermitian systems become localized under OBC in the Hatano–Nelson model [129], given by Eq. (1.14), this behavior appears to signal the absence of topology for the case of NHSE. However, N. Okuma *et al.* demonstrated that the NHSE can also have a topological origin [131]. The condition for the occurrence of the NHSE in a general system can be formulated as follows,

Theorem: The OBC bulk spectrum cannot possess a non-trivial winding number. As a direct consequence, if the PBC spectral curve carries a non-trivial winding number, the corresponding OBC bulk spectral curve must differ from the PBC one. Equivalently, NHSE necessarily emerges in such a situation.

Let us examine the mathematical reasoning underlying this Theorem in more detail. Because no simple analytical expression exists for the OBC spectrum, a direct comparison between the OBC and PBC spectra is generally not feasible. For this reason, the proof for this theorem proceeds in two steps: 1. a comparison between the PBC spectrum and that under a *semi-infinite* boundary condition (SIBC), and 2. a subsequent comparison between the SIBC and OBC spectra. Here, 'semi-infinite' refers to a 1D lattice with only a single boundary.

1. The index theorem from spectral theory is employed to connect the SIBC spectrum to the PBC spectrum. According to this Theorem, the SIBC spectrum consists of the PBC spectral curve, in addition to all points enclosed by that curve for which the winding number is non-zero (see Fig. 1.1(c)). Here, the winding number around a reference point $E \in \mathbb{C}$ is defined as

$$W(E) := \int_0^{2\pi} \frac{dk}{2\pi i} \frac{d}{dk} \left[\log \det \left(H(k) - E\right)\right], \tag{1.17}$$

   with $H(k)$ being the Bloch Hamiltonian of H under the PBC. A negative (positive) winding about the point, E, indicates that the right (left) eigenstates are exponentially localized.

2. we begin with the following inclusion,

$$\sigma_{\mathrm{OBC}}(H) \subset \sigma_{\mathrm{SIBC}}(H), \tag{1.18}$$

   where σ denotes the spectrum, and $\subset$ represents a proper subset. Now, a similarity transformation modifies the SIBC spectrum, whereas it leaves the OBC spectrum unchanged, as the latter is defined through the infinite-volume limit of a finite-dimensional matrix. Consequently, the original OBC spectrum must be contained within the transformed SIBC spectrum. Such an inclusion can be considered for

an arbitrary imaginary gauge transformation V_r (Eq. (1.15)), we can deduce,

$$\sigma_{\mathrm{OBC}}(H) \subset \bigcap_{r\in(0,\infty)} \sigma_{\mathrm{SIBC}}\left(V_r^{-1}HV_r\right). \tag{1.19}$$

Here, $\bigcap_{r\in(0,\infty)}$ designates the intersection of all the $\sigma_{\mathrm{SIBC}}\left(V_r^{-1}HV_r\right)$ with r ranging from 0 to ∞.

If the PBC spectrum of $H(k)$ carries a non-trivial winding in the complex plane, one can identify an SIBC mode with energy $E \in \mathbb{C}$ located just inside the PBC spectral curve, which is exponentially localized near the boundary. Through the imaginary gauge transformation V_r with a suitable choice of r, this boundary-localized mode is mapped onto a plane-wave state. The energy E then lies on the boundary of $\sigma_{\mathrm{SIBC}}\left(V_r^{-1}HV_r\right)$, equivalently on the PBC spectrum of $V_r^{-1}HV_r$. As a result, the intersection $\sigma_{\mathrm{SIBC}}(H) \cap \sigma_{\mathrm{SIBC}}\left(V_r^{-1}HV_r\right)$ becomes strictly smaller than the original SIBC spectrum $\sigma_{\mathrm{SIBC}}(H)$. This construction can be iterated repeatedly until the right-hand side of the inclusion in Eq. (1.19) reduces to a spectral curve without winding. This reasoning ultimately implies that the OBC spectrum *cannot possess* non-zero winding (Fig. 1.1(c)). One may therefore conclude that whenever a system exhibits a non-trivial spectral winding, or a *point-gap topology* under PBC (Eq. (1.17)), the corresponding OBC spectral curve in the complex plane differs substantially from the PBC spectrum and the system necessarily displays NHSE.

Surprisingly, the same winding number that characterizes the skin modes identifies the topological boundary zero modes of a Hermitian TI [131]. The trick is to introduce an extended Hermitian Hamiltonian,

$$\tilde{H}_E := \begin{pmatrix} 0 & H-E \\ H^\dagger - E^* & 0 \end{pmatrix}, \tag{1.20}$$

where $E \in \mathbb{C}$ is a reference point. This extended Hamiltonian possesses an additional CS,

$$\Gamma \tilde{H}_E \Gamma^{-1} = -\tilde{H}_E \quad \text{with} \quad \Gamma = \begin{pmatrix} 1 & 0 \\ 0 & -1 \end{pmatrix}. \tag{1.21}$$

Within the AZ classification [15], the symmetry class characterized solely by CS is denoted as class AIII, for which the topological classification of insulating (gapped) phases is given by $\mathbb{Z}$. Here, the gapped nature of $\tilde{H}_E$ is defined through the condition $\det[H(k) - E] \neq 0$. In fact, the corresponding integer-valued topological invariant is exactly the winding number of the PBC spectral curve of H around a chosen reference point E, as defined in Eq. (1.17). Consequently, the same winding number simultaneously characterizes a class-AIII TI and the conventional NHSE. Notably, under this

correspondence, the Hatano–Nelson model, being the minimal model exhibiting the NHSE, can be naturally extended to the Hermitian SSH model. At first glance, the discussion above suggests the failure of the conventional BBC in the presence of the NHSE. However, the correspondence can be restored by introducing an appropriate topological invariant defined using the OBC bulk spectral information. Let us introduce the replacement of the BZ theory in systems where the BBC breaks down.

1.5.2 Generalized Brillouin Zone Theory

In the previous discussion, the connection between the non-trivial spectral winding of the PBC Hamiltonian and the emergence of NH skin modes under OBC was investigated, and a rigorous relationship between the two was established. This progress gave birth to a new concept: generalized Brillouin zone (GBZ) theory [45, 132, 133] or the non-Bloch theory [134]. This framework was proposed precisely to address the apparent breakdown of the BBC in NH systems. In this approach, the real Bloch wave vector k is replaced by a complex wave vector $k' = k - i \ln r$ (r being a real parameter). The GBZ is then defined in terms of k', allowing NH dynamics to be described as non-Bloch wave propagation characterized by a generalized phase factor $\beta = e^{ik'} = re^{ik}$. Unlike the conventional BZ, where the phase factor e^{ik} traces out a unit circle in the complex plane as k varies from $-\pi$ to π, the GBZ defined by β generally does not correspond to a unit circle, since r typically deviates from unity.

Let us now outline how the GBZ, commonly denoted by C_β, is constructed. In Hermitian systems, the parameter β is related to the Bloch wave number $k \in \mathbb{R}$ through the relation $\beta = \mathrm{e}^{ik}$. For a general NH Hamiltonian $\mathcal{H}(\beta)$, the characteristic equation can be expressed as

$$\det\left[\mathcal{H}\left(\beta\right) - E\right] = 0. \tag{1.22}$$

When k is real, the resulting bulk-band structure reproduces the spectrum of a long open chain. Extending this idea to NH systems requires selecting appropriate values of β such that the bands of $\mathcal{H}(\beta)$ faithfully reproduce those of a long open chain. For a finite system with OBC, the energy levels are discrete; as the system size increases, these levels become increasingly dense and asymptotically form continuum bands. Accordingly, determining the GBZ, C_β, amounts to analyzing the asymptotic distribution of eigenvalues in an open chain in the limit of large system size. In NH systems, the modulus $|\beta|$ is not constrained to unity, and the corresponding states may be localized near either boundary of the chain. As a result, these bands cannot be regarded as conventional bulk bands, but are instead referred to as *continuum bands* [134]. These are generated by continuously varying β along the contour C_β, as will be demonstrated later. If we number the solutions β_i ($i = 1, \cdots, 2M$) of Eq. (1.22) so as to satisfy $|\beta_1| \leq |\beta_2| \leq \cdots \leq |\beta_{2M-1}| \leq |\beta_{2M}|$,

then to get the continuum bands is given via the condition,

$$|\beta_M| = |\beta_{M+1}|\,. \tag{1.23}$$

The trajectory of β_M and β_{M+1} gives C_β. In Hermitian systems, the above equation becomes $|\beta_M| = |\beta_{M+1}| = 1$, and C_β is a unit circle. Rigorous analysis has further shown that although the GBZ forms a closed loop analogous to the conventional BZ, its mathematical properties are fundamentally different [133]. For instance, the GBZ encloses equal numbers of zeros and poles of the Hamiltonian when treated as a holomorphic function, such that their contributions cancel. As a result, irrespective of the choice of base point, the eigenvalue evaluated on the GBZ exhibits zero winding. This implies that the eigenvalue trajectories defined on the GBZ, or equivalently, the OBC spectrum of the Hamiltonian, do not form closed loops, but instead collapse into arcs or line segments. Such behavior is entirely consistent with the OBC spectra observed in the prototypical Hatano–Nelson model (see Fig. 1.1(a)). Thus, we have reviewed the origin of the NHSE from both mathematical and physical perspectives. In particular, clarifying the connection between the non-zero winding of the eigenvalues of an NH Hamiltonian under PBCs and the emergence of the NHSE under OBCs, established through the calculable GBZ framework, has yielded a complete formalism with a clear physical interpretation within a single theoretical setting. Owing to its consistency and explanatory power, this approach has become widely accepted and has recently been extended to higher-dimensional systems.

1.5.3 Higher-order Skin Effect

In recent years, higher-order counterparts of topological phases have been uncovered and studied in great detail [135–141]. Generally, spatial symmetries, such as inversion, mirror, and rotation symmetries, protect these higher-order topological phases. In 2D systems, higher-order topology gives rise to $\mathcal{O}(1)$ (Fig. 1.2(b)) zero modes localized at the corners, in stark contrast to the $\mathcal{O}(L)$ (Fig. 1.2(a)) chiral or helical edge modes associated with first-order topology. Likewise, in 3D systems, third-order topology produces $\mathcal{O}(1)$ zero modes confined to the corners, rather than the $\mathcal{O}(L^2)$ surface states characteristic of first-order TIs. The advent of higher-order topology naturally motivates the study of higher-order skin effect [142–145]. Higher-dimensional systems, therefore, provide a fertile arena in which topological phases and NHSE phenomena can coexist and intertwine. In 2D systems of size $L \times L$ with OBC along both directions, first-order NHSE is characterized by the accumulation of $\mathcal{O}(L^2)$ skin modes at generic boundaries (Fig. 1.2(c)). By contrast, in the case of a higher-order skin effect, only $\mathcal{O}(L)$ skin modes emerge, and these are localized at the corners (Fig. 1.2(d)). This behavior is

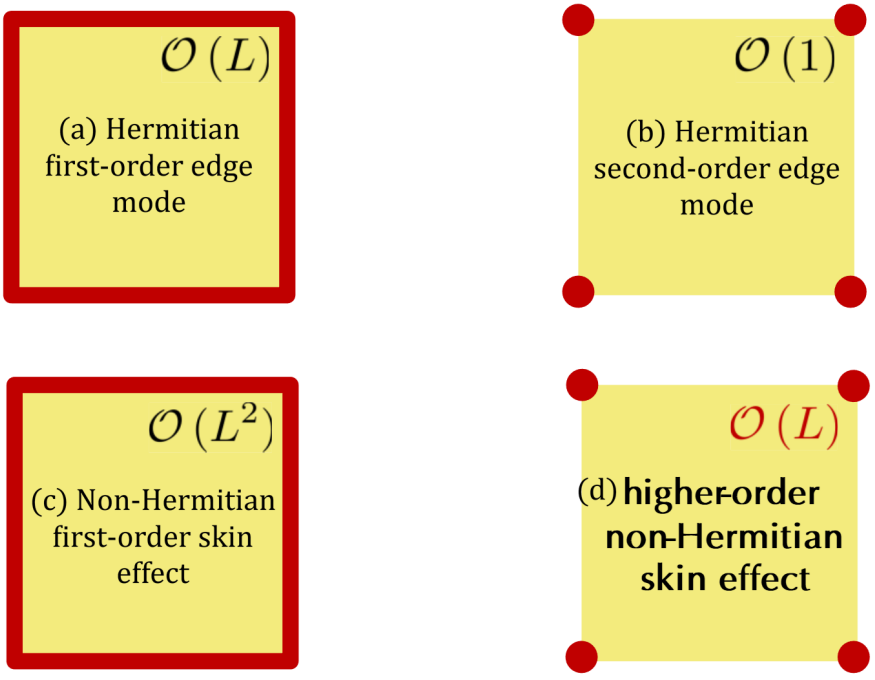

FIGURE 1.2: Boundary modes, illustrated via red lines or dots, are shown for a 2D system of size $L \times L$. (a) Hermitian first-order TI, where $\mathcal{O}(L)$ chiral or helical modes emerge along the edges of the system. (b) Hermitian higher-order TI, featuring $\mathcal{O}(1)$ zero modes localized at the corners. (c) First-order NHSE, in which intrinsic NH topology gives rise to $\mathcal{O}(L^2)$ skin modes accumulating at generic boundaries. (d) Second-order NHSE, where intrinsic NH topology leads to $\mathcal{O}(L)$ skin modes localized at the corners.

fundamentally different from all the previous cases, that is, Figs. 1.2(a), 1.2(b), and 1.2(c).

In purely Hermitian systems, higher-order topology arises from a non-trivial interplay between topological localization in two or more spatial directions, arranged so that the first-order topological polarizations cancel each other. In higher-dimensional NH systems, however, NHSE introduces an additional and fundamentally different localization mechanism. In this regard, the hybrid-skin topological (HST) effect is noteworthy as it represents a distinct interplay between NHSE and conventional topological phases, resulting in eigenstate localization at lower-dimensional boundaries, such as corners in 2D lattices. The concept of the HST effect was first proposed in 2019 by Lee, Li, and Gong [144], based on a 2D extension of the 1D NH SSH model exhibiting NHSE. In this construction, the model is formed by stacking the copies of the 1D system along a spatial direction and is characterized by four independent non-reciprocal parameters. In the absence of specific parameter constraints, a corner NHSE emerges for all bulk eigenstates. When the non-reciprocities are balanced, destructive interference occurs along one direction, giving rise to a line NHSE. By contrast, if the non-reciprocities cancel along both directions, the bulk states no longer exhibit NHSE along either axis;

nevertheless, a corner NHSE remains under OBC. This residual localization arises from first-order topological states that are unevenly distributed across sublattices. Such states do not undergo complete destructive interference due to non-reciprocity, allowing them to retain NHSE behavior and thereby form a new class of higher-order skin states.

1.6 Topolectrical Circuits

Having discussed the exceptional properties of the NH systems in detail, we shall now examine the feasibility of realizing these quantum systems on experimental platforms. Although topological phenomena were originally discovered in condensed matter physics, they have since attracted strong interest from a broad range of fields, including photonics, phononics, mechanics, spintronics, and electrical circuits. Among these platforms, electrical circuits have emerged as a compelling and accessible setting for investigating topological physics, introducing us to the concept of topolectrical circuits (TECs) [146]. Due to the high level of connection freedom, circuit networks have been used to create many novel states of matter, such as 2D topological states [147–153], 3D topological semimetals [3, 154–158], NH topological states [4, 103, 107, 159–163], higher-order topological states [164–169], and hyperbolic topological states [170–172]. The central idea underlying TECs is the exact correspondence between TB Hamiltonians in condensed matter systems and circuit Laplacians (admittance matrices). In particular, circuit implementations offer substantial freedom in engineering hopping amplitudes and on-site potentials, including their strengths, directions, and dimensions of a TB model. Moreover, TEC devices are well-suited for fabrication and miniaturization due to their compatibility with integrated circuit technology. These advantages make TECs an effective platform for probing exotic topological phenomena, advancing the understanding of topological phases, and demonstrating potential practical applications, as explored throughout this thesis.

The pioneering work, '*Topolectrical Circuit*' by Lee et al. [3] provided the first systematic formulation of the Laplacian framework and established the correspondence between a circuit Laplacian and a TB Hamiltonian. The early interest in TECs stems from their close analogy with quantum mechanics. In a TB Hamiltonian, electronic degrees of freedom are associated with lattice sites, whereas in a circuit, the node voltages play an equivalent role. In both cases, the governing matrix, the Hamiltonian for quantum systems, and the Laplacian for circuits, encodes the connectivity between these degrees of freedom. Despite this parallel, the two objects are not identical. A conventional Hamiltonian is Hermitian (though later we will consider NH extensions), satisfying $H = H^\dagger$. At the same time, the circuit Laplacian appears in an anti-Hermitian form, $\mathcal{L} = -\mathcal{L}^\dagger$, because the admittances of inductors and capacitors contribute an overall factor of i. Since this imaginary unit is standard to all elements of the Laplacian, one can factor it

out and work instead with $i\mathcal{L}$ (or equivalently $i\omega\mathcal{L}$, where ω is the driving frequency), a standard procedure in this field. The resulting matrix, often referred to as the normalized Laplacian, has real entries and is therefore more convenient for analyzing the system in direct analogy with a Hermitian TB Hamiltonian. In this representation, the eigenvalues are real, whereas the eigenvalues of the original Laplacian remain purely imaginary due to the overall prefactor of i. In a TEC, the existence or absence of a zero eigenvalue of the normalized Laplacian plays a central role. Using the TB correspondence, the normalized circuit Laplacian $\mathcal{L}$ satisfies an equation formally identical to the time-independent Schrödinger equation, $\mathcal{L}|\psi\rangle = E|\psi\rangle$, where $|\psi\rangle$ is an eigenvector of $\mathcal{L}$ with eigenvalue E. If the circuit Laplacian possesses a zero eigenvalue, the equation reduces to $\mathcal{L}|\psi_0\rangle = |0\rangle$, with $|0\rangle$ denoting the null vector of the same dimension as $\mathcal{L}$. Physically, the right-hand side indicates that there are no current sources at any node. Consequently, the eigenvector $|\psi_0\rangle$ corresponds to a voltage configuration across the circuit nodes that satisfies Kirchhoff's current law without requiring any external current injection. It is important to emphasize that this situation does not contradict energy conservation, since the circuit must be initially energized to establish such a voltage distribution. The essential correspondence here is between the eigenvector structure of $\mathcal{L}$ associated with a TEC, and the spatial structure of the eigenstate of a TB Hamiltonian. In particular, when topological zero modes exist in the non-trivial topological phase, and their eigenstates are exponentially localized at the boundaries, the voltage response of a suitably designed TEC must follow the same localization pattern. This correspondence constitutes one of the key signatures of TECs. We shall discuss methodologies and formalism, along with some examples, in the next chapter.

1.7 Thesis Overview

We now present a concise overview of the thesis, highlighting the main themes, the physical problems addressed, and the key results obtained during the course of this PhD work.

Chapter 1 presents a detailed account of the introduction.

Chapter 2 provides a brief discussion on the methodologies and the working principles of the TECs.

Chapter 3 examines an NH SSH model, highlighting the contrasting topological and localization behavior between $s\mathcal{PT}$ and non-$\mathcal{PT}$-symmetric ($n\mathcal{PT}$) regimes. In the $n\mathcal{PT}$ case, non-reciprocal hopping breaks the BBC, giving rise to NHSE, while the $s\mathcal{PT}$ system, realized via a complex staggered on-site potential, preserves the BBC and shows no NHSE. For the $n\mathcal{PT}$ system, we restore the BBC via the non-Bloch theory, and show

that the topological zero-energy edge modes among the skin modes can be characterized by the winding number, given via Eq. (1.17). While the topology resembles the Hermitian case for the $s\mathcal{PT}$ case, it exhibits spontaneous $\mathcal{PT}$-symmetry breaking as the imaginary potential strength varies, separating regions with real (unbroken) and complex (broken) eigenvalues. Surprisingly, the Hermitian winding number characterizes the topological edge modes. We have proposed TEC designs to realize the localization phenomena in both cases: the skin effect in the $n\mathcal{PT}$ case and topological edge modes in the $s\mathcal{PT}$ case. This chapter is based on the results obtained in Ref. [173].

Chapter 4 focuses on a quasi-1D NH model that captures the distinctive features of the NHSE. Extending its Hermitian counterpart into the NH regime yields two cases: a $s\mathcal{PT}$ model and a $n\mathcal{PT}$ model (which may or may not respect TRS). In the $s\mathcal{PT}$ case, spontaneous $\mathcal{PT}$-symmetry breaking divides the system into regions with real or complex eigenvalues. Although non-reciprocal hopping typically induces the NHSE, our analysis reveals that the $s\mathcal{PT}$ model (with non-reciprocal hopping) exhibits an intrinsic pseudo-skew-Hermitian character, which prevents the NHSE from occurring in the system. Overall, the model reveals three regimes controlled by the nature of non-reciprocity: (a) no NHSE for the $s\mathcal{PT}$ model and the $n\mathcal{PT}$ model without TRS, (b) standard NHSE for the $n\mathcal{PT}$ model with TRS, and (c) dual-edge NHSE for the $n\mathcal{PT}$ model respecting both TRS and particle-hole symmetry. We characterize the topology of these NH systems using the complex Berry phase. We have also designed TECs corresponding to the TB models and demonstrated the absence of NHSE in the non-reciprocal TEC through its impedance profile (IP). Additionally, we have computationally analyzed the admittance band structures to support these findings. The key results in this chapter appear in Refs. [174, 175].

Chapter 5 focuses on a disordered NH model, motivated by the inevitable presence of disorder, impurities, and defects in real materials. In this chapter, we investigate the interplay between the NHSE, driven by non-reciprocal hopping, and Anderson localization, induced by quasiperiodic disorder. Using a 1D NH Aubry-André model, we investigate the localization behavior and time evolution under single-site excitation, revealing quantum jumps between skin and Anderson-localized states. In the corresponding TEC, the excitation voltage remains localized near the driven node, unlike the NH jumps, predicted theoretically. The competition between Anderson localization and NHSE creates a tug-of-war, leading to partial delocalization of the output signal over a limited spatial range within the TEC. This chapter is based on the results obtained in Ref. [176].

Chapter 6 uncovers a competition between a TRS-preserving NH Bernevig-Hughes-Zhang model, which includes a spin-dependent gain/loss potential (γ), subjected to a TRS-breaking term, specifically an in-plane magnetic field, B_y. For an x-periodic nanoribbon, the magnetic field gaps out the helical edge states and produces higher-order topological corner modes, while increasing non-hermiticity restores the edge modes

when $\gamma > |B_y|$. Analysis of the NH projected spin spectrum shows that for corner modes ($\gamma \leq |B_y|$), the in-plane magnetic field enables spin-mixing channels. In contrast, stronger non-hermiticity ($\gamma > |B_y|$) suppresses spin scattering and delocalizes corner modes along the edges. We have also built TECs corresponding to the TB models and realized first- and higher-order topological models using the IP of the circuit. the key results in this chapter appear in Ref. [177].

In **Chapter 7**, we extend our investigation to higher-order skin effect, focusing on the HST effect by breaking the inversion symmetry of a square lattice. This is achieved by selectively removing vertical hopping terms, thereby transforming the lattice into a 2D brick-wall (stretched honeycomb) geometry. With the inclusion of non-hermiticity, the brick-wall lattice with OBC in both directions exhibits several striking and unconventional spectral features. The eigenvalues associated with the HST modes (or the corner skin modes) do not produce non-trivial windings in the complex energy plane. Instead, they form isolated, EP-like points; however, these are not actual EPs since they do not arise from the coalescence of eigenvectors. Among the corner skin modes, only two, originating from the topological corner states of the Hermitian brick-wall lattice, are localized at individual corners. The remaining corner skin modes accumulate at the opposite pair of corners. This spatial distribution is in sharp contrast to the second-order skin effect, in which the corner skin modes are more uniformly distributed. For both the NH square lattice and the NH brick-wall lattice, we have designed and implemented the corresponding TECs to visualize these HST modes directly.

We conclude the key findings from **Chapters 3-7** in **Chapter 8**, summarizing the critical results of our thesis.

Chapter 2

Fundamentals of Topolectrical Circuits

This chapter presents the fundamental circuit elements, underlying principles, and formalisms required to build TECs. In this section, we first present the fundamental circuit equations for basic electrical components, including resistors, inductors, varactors, and negative impedance converters with current inversion (INICs). Subsequently, we provide a detailed account of the construction principles of TECs, explaining how the circuit Laplacian can be mapped onto a TB Hamiltonian and how the circuit equations correspond to the Schrödinger equation. Finally, we describe practical methods for experimentally probing and identifying topological edge (and skin) modes via the electrical circuit implementation of selected TB models.

2.1 Basic Circuit Elements and Equations

Electric circuits are traditionally employed to control and manipulate the flow of electric charge. An electrical circuit consists of a network of closed loops formed by fundamental components such as sources, wires, switches, resistors (R), inductors (L), and capacitors (C), which together provide return paths for current flow [178]. The foundation of the world of electrical networks is built upon three fundamental laws, namely,

1. **Kirchhoff's current law (KCL)**: The sum of the currents into any circuit node is zero.

2. **Kirchhoff's voltage law (KVL)**: The sum of the voltage drops around any loop is zero, and

3. **voltage–current relation (VCR)**: The relationship between the current and voltage when the electric current goes through a component.

Based on KCL and KVL, two standard approaches to circuit analysis are nodal analysis and mesh analysis. These methods allow linear circuits to be systematically analyzed by formulating a set of simultaneous equations, which can then be solved to obtain the node voltages and loop currents. In Fig. 2.1(a), we illustrate the basic elements used in electrical circuits, including resistors, inductors, capacitors, and varactors. The voltage-current equations for these four components are written as

$$i = \frac{1}{R}v, \quad i = C\frac{dv}{dt}, \quad i = \frac{1}{L}\int_{-\infty}^{t} v dt, \quad i = C_j\frac{dv}{dt}, \tag{2.1}$$

where $C_j = \frac{C_0}{(V_b - V)^m}$ denotes the voltage-dependent diode capacitance. Here, C_0 is the capacitance in the absence of an applied voltage, V represents the applied voltage, V_b is the junction barrier voltage, and m is a material-dependent constant that can range from small fractional values to several hundred. Resistors, inductors, and capacitors form the building blocks of linear circuits, whereas the varactors are typically employed to introduce nonlinearity. In addition, memory effects can be incorporated into circuit models through elements such as memristors, memcapacitors, and meminductors. Fig. 2.1(b) shows the configuration of INIC. According to the properties of operational amplifiers (Op-Amps), one can write the voltage-current equations of this unit as,

$$\begin{pmatrix} I_1 \\ I_2 \end{pmatrix} = \frac{1}{Z_0}\begin{pmatrix} -\nu & \nu \\ -1 & 1 \end{pmatrix}\begin{pmatrix} V_1 \\ V_2 \end{pmatrix} \tag{2.2}$$

with $\nu = Z_-/Z_+$. Here, Z_-, Z_+, and Z_0 are impedances of the components shown in Fig. 2.1(b). Governed by Eq. (2.2), the unit behaves as a positive (negative) impedance when viewed from right to left (left to right), enabling the realization of non-reciprocal interactions as well as effective negative-impedance elements. In particular, this circuit element is exceptionally beneficial for designing TECs corresponding to NH TB models, as we shall see in the subsequent chapters. To illustrate how circuit equations are formulated, we consider a simple RLC circuit as an example, shown in Fig. 2.1(c). Using the nodal-analysis method, the response of this circuit is described by the following set

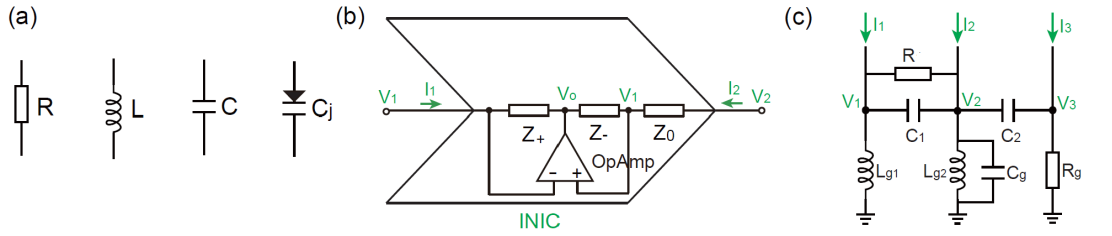

FIGURE 2.1: (a) Fundamental electrical components used in circuit designs, namely the resistor, inductor, capacitor, and varactor diode. (b) Schematic configuration of INIC. (c) A representative circuit diagram consisting of three interconnected nodes. The figures are adopted from Ref. [2].

of equations,

$$
\begin{aligned}
i_1 &= \frac{v_1 - v_2}{R} + C_1 \frac{d(v_1 - v_2)}{dt} + \frac{1}{L_{g1}} \int_{-\infty}^{t} v_1 dt, \\
i_2 &= -\frac{v_1 - v_2}{R} - C_1 \frac{d(v_1 - v_2)}{dt} + C_2 \frac{d(v_2 - v_3)}{dt} + C_g \frac{dv_2}{dt} + \frac{1}{L_{g2}} \int_{-\infty}^{t} v_2 dt, \\
i_3 &= -C_2 \frac{d(v_2 - v_3)}{dt} + \frac{v_3}{R_g}.
\end{aligned}
\tag{2.3}
$$

For a sinusoidal steady-state analysis, one can Fourier transform these equations involving time to the frequency space by assuming $v_n = V_n \exp(i\omega t)$ and $i_n = I_n \exp(i\omega t)$ $(n = 1, 2, 3)$ at frequency ω. The above equation can then be written as,

$$
\begin{pmatrix} I_1 \\ I_2 \\ I_3 \end{pmatrix} = \begin{pmatrix} G + i\omega C_1 + 1/(i\omega L_{g1}) & -G - i\omega C_1 & 0 \\ -G - i\omega C_1 & G + i\omega C_1 + i\omega C_2 + i\omega C_g + 1/(i\omega L_{g2}) & -i\omega C_2 \\ 0 & -i\omega C_2 & i\omega C_2 + G_g \end{pmatrix} \begin{pmatrix} V_1 \\ V_2 \\ V_3 \end{pmatrix}, \tag{2.4}
$$

with $G = 1/R$ and $G_g = 1/R_g$. The 3×3 matrix appearing in the above equation is the admittance matrix, commonly known as the circuit Laplacian [179].

2.2 Circuit Laplacian and the Schrödinger Equation

In TECs, nodal analysis is the primary analytical tool, as the focus is typically on node voltages rather than mesh currents. For a general linear circuit composed of RLC elements, one can introduce N-component vectors $\mathbf{V}$ and $\mathbf{I}$ to represent the voltages at the circuit nodes with respect to ground and the externally injected currents, respectively. The equations of motion for the circuit are then given by,

$$
\frac{d}{dt}\mathbf{I}(t) = \mathcal{C}\frac{d^2}{dt^2}\mathbf{V}(t) + \Sigma\frac{d}{dt}\mathbf{V}(t) + \mathcal{M}\mathbf{V}(t), \tag{2.5}
$$

where the $\mathcal{C}$, Σ, and $\mathcal{M}$ are the $N \times N$ real-valued matrices . The matrix elements of $\mathcal{C}$, Σ, and $\mathcal{L}$ correspond to the capacitances, inverse resistances, and inverse inductances

between pairs of nodes or between a node and ground. The circuit response at a driving frequency ω is governed by Kirchhoff's laws expressed in the frequency domain,

$$I(\omega) = J(\omega)V(\omega), \tag{2.6}$$

with

$$J(\omega) = i\omega\mathcal{C} + \Sigma + \frac{1}{i\omega}\mathcal{M} \tag{2.7}$$

being the circuit Laplacian. $J(\omega)$ can be written in the form $i\mathcal{L}$, where $\mathcal{L}$ plays a role analogous to a TB Hamiltonian in condensed matter physics. In this correspondence, the diagonal elements of $\mathcal{L}$ represent onsite potentials, while the off-diagonal elements describe hopping processes between sites. By diagonalizing the circuit Hamiltonian $\mathcal{L}$, one obtains the admittance spectrum j_n together with the associated eigenfunctions ϕ_n, where $n = 1, 2, 3, \ldots, N$ labels the eigenstates.

In analogy with the Schrödinger's equation, the homogeneous equations of Eq. (2.5) ($\mathbf{I} = 0$) can be rewritten as $2N$ differential equations,

$$-i\frac{d}{dt}\psi(t) = \mathcal{H}\psi(t), \tag{2.8}$$

with $\psi = [\dot{\mathbf{V}}(t), \mathbf{V}(t)]^T$ and the block Hamiltonian matrix being

$$\mathcal{H} = i\begin{pmatrix} \mathcal{C}^{-1}\Sigma & \mathcal{C}^{-1}\mathcal{M} \\ -\mathbb{I} & 0 \end{pmatrix}, \tag{2.9}$$

where $\mathbb{I}$ denotes the $N \times N$ identity matrix. Diagonalizing the second-quantized Hamiltonian in the above equation yields the frequency spectrum together with the corresponding voltage profile (VP). The time evolution of the n^{th} eigenmode is given by $\psi_n(t) = \psi_n e^{i\omega_n t}$ ($n = 1, 2, \ldots, 2N$), where the eigenfrequencies ω_n are determined by the roots of the admittance eigenvalues through the condition $j(\omega_n) = 0$. In practice, however, directly measuring the admittance spectrum of a circuit is challenging, since it would require continuously tuning the admittance by adjusting the inductors or capacitors connected to each node and to ground. By contrast, the frequency spectrum provides a more accessible alternative for probing band structure, as the driving frequency can be easily varied. This approach is particularly effective for detecting topological edge modes.

2.3 Observables in TECs

The most convenient way to visualize the circuit's response is to measure the *impedance* between two nodes. The eigenmodes and the impedance of the circuit are linked by the

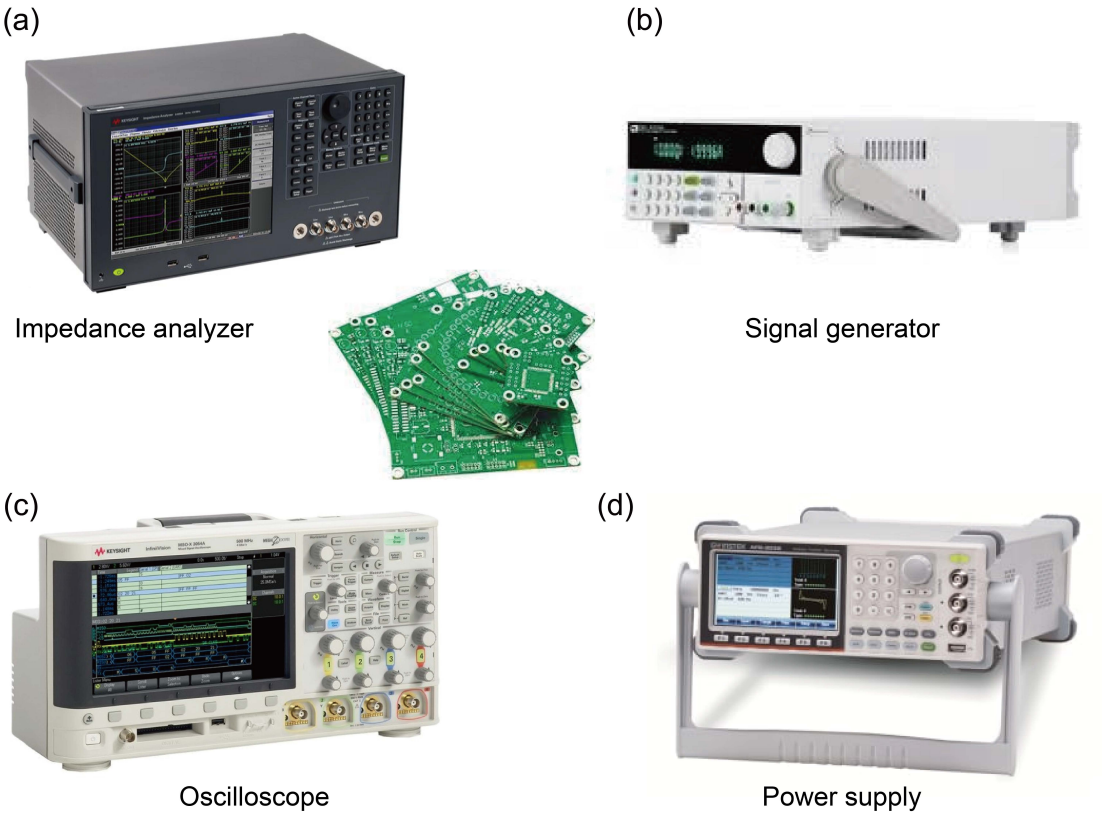

FIGURE 2.2: Instruments used in TEC experiments. (a) An impedance analyzer for measuring impedance. (b) Signal generator for producing voltage signals. (c) Oscilloscope for detecting voltage responses. (d) Power supply for powering the circuit network. The central image shows the printed circuit boards. The figures are adopted from the official websites of the respective instruments.

circuit's Green's function,

$$G = \sum_{j_n} \frac{1}{j_n} \phi_n \phi_n^{\dagger}, \tag{2.10}$$

with j_n being the n^{th} eigenvalue and ϕ_n being n^{th} eigenmode. One can characterize the topological edge modes using impedance measurements. The impedance between two nodes of a circuit is given by the formula [179],

$$Z_{ab} = \frac{V_a - V_b}{I_{ab}} = \sum_{i=a,b} \frac{G_{ai} I_i - G_{bi} I_i}{I} = G_{aa} + G_{bb} - G_{ab} - G_{ba} = \sum_{j_n} \frac{|\phi_{n,a} - \phi_{n,b}|^2}{j_n}, \tag{2.11}$$

where $|\phi_{n,a} - \phi_{n,b}|$ is the amplitude difference between a and b nodes of the n^{th} eigenmode. The impedance measured between node a and the ground is given by,

$$Z_{a,\text{ground}} = \sum_{j_n} \frac{|\phi_{n,a}|^2}{j_n}. \tag{2.12}$$

The above equation indicates that the impedance is highly sensitive to the wave-function distribution in the vicinity of $j_n = 0$, as it diverges at this point in the absence of dissipation. In realistic circuits, however, losses are unavoidable due to both the circuit components and the connecting wires. Interestingly, these losses introduce a small imaginary contribution to the admittance spectrum, regularizing the divergence and rendering the impedance finite. In experiments, the impedance can be measured by directly connecting the circuit nodes to the ports of a measurement instrument using wires. The IP is then obtained with an impedance analyzer, as illustrated in Fig. 2.2(a). Alternatively, static voltage responses can be measured by injecting an external current source to probe the eigenmodes, since the voltage distribution can be written as,

$$V = GI = \sum_{j_n} \frac{1}{j_n} \phi_n \phi_n^\dagger I. \tag{2.13}$$

Accordingly, the VP is predominantly determined by the eigenmodes in the vicinity of $j_n = 0$ through the factor j_n^{-1}. Static eigenmodes can thus be characterized either by impedance measurements or by static voltage measurements. However, such approaches are insufficient for resolving the dynamical propagation of edge states. To access their time evolution, one must measure the time-dependent voltage propagation in the circuit. Experimentally, this can be achieved by introducing a current signal using a waveform generator (Fig. 2.2(b)) at a chosen (sub) node and recording the voltage response at other nodes with oscilloscopes (Fig. 2.2(c)). In this way, the temporal propagation of voltage signals can be reconstructed. This technique is particularly crucial for identifying the chirality of the edge states in a TI (or hinge states in a higher-order TI). Fig. 2.2(d) shows a DC power supply, which is used to provide power to active components such as Op-Amps.

Up to this point, we have introduced the basics of TEC, including circuit elements, governing equations, and experimental devices. In the following, we shall present several examples of (NH) TIs and review how topological states and the NHSE are realized and explored in electrical circuit systems. We begin by recalling conventional topological states in circuits through the construction of a simple Hermitian SSH circuit [3]. Subsequently, we introduce non-Hermiticity by incorporating non-reciprocal intra-cell hopping and demonstrate the resulting breakdown of the BBC, together with the emergence of the NHSE, as revealed by the VP of the circuit [4]. Finally, we shall see an example of TEC realization of a periodically driven system.

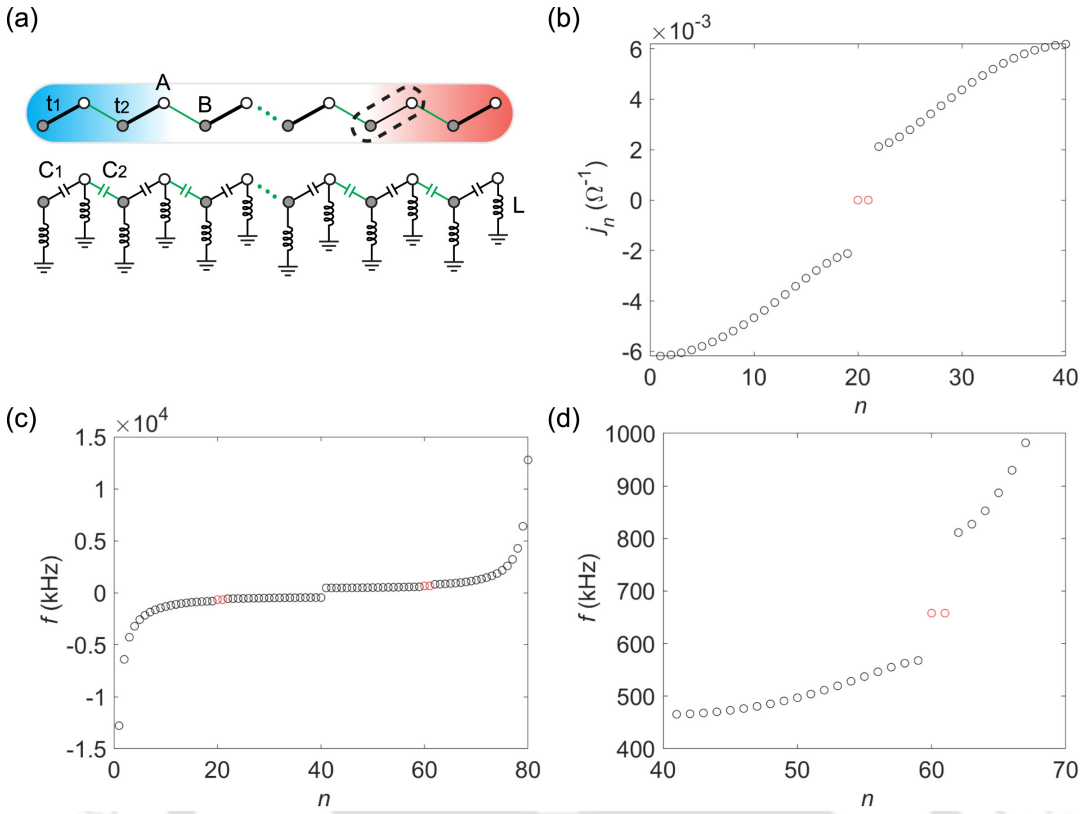

FIGURE 2.3: (a) SSH model (top) and its corresponding TEC realization (bottom). (b) The admittance spectrum for a system with $N = 20$ unit cells, where black and red circles denote bulk and edge modes, respectively. (c) Frequency spectrum of the circuit. (d) Enlarged view of the frequency spectrum shown in panel (c). The plots are adopted from Ref. [2].

2.4 Circuit Realization of an SSH Model

The SSH model [16] was initially introduced in the context of solitons in polyacetylene. Owing to its simple structure and non-trivial topology, it was later recognized as an effective minimal model for investigating topological states. The SSH model has played an important role in elucidating how symmetry and topology govern the electronic properties of materials and has significantly influenced the broader development of topological physics. To explicitly demonstrate the correspondence between circuit formulations and TB models, we take the SSH model as a representative example. As illustrated schematically in the upper panel of Fig. 2.3(a), the SSH lattice is characterized by alternating hopping amplitudes t_1 and t_2. The corresponding TB Hamiltonian reads,

$$H = \sum_{n=1}^{N} \left[t_1 \left(\hat{a}_n^\dagger \hat{b}_n + \hat{b}_n^\dagger \hat{a}_n \right) + t_2 \left(\hat{b}_n^\dagger \hat{a}_{n+1} + \hat{a}_{n+1}^\dagger \hat{b}_n \right) \right], \tag{2.14}$$

where t_1 (t_2) is the intra- (inter-) cell hopping of a unit cell for a system size of N unit cells. $\hat{a}_n(\hat{a}_n^\dagger)$ and $\hat{b}_n(\hat{b}_n^\dagger)$ are annihilation (creation) operators, corresponding to the sites at the A and the B sub-lattices, respectively, of the n^{th} unit cell. This SSH

Hamiltonian can be faithfully implemented using the LC circuit shown in the lower panel of Fig. 2.3(a). For this TEC realization, following Eq. (2.9), the capacitance and inductance matrices take the form,

$$\mathcal{C} = \begin{pmatrix} C_1+C_2 & -C_1 & 0 & 0 & 0 & 0 & 0 \\ -C_1 & C_1+C_2 & -C_2 & 0 & 0 & 0 & 0 \\ 0 & -C_2 & C_1+C_2 & -C_1 & 0 & 0 & 0 \\ 0 & 0 & -C_1 & C_1+C_2 & \cdots & 0 & 0 \\ \vdots & \vdots & 0 & \vdots & \ddots & -C_1 & 0 \\ 0 & 0 & 0 & 0 & -C_1 & C_1+C_2 & \end{pmatrix}_{N\times N}, \qquad \mathcal{M} = \frac{1}{L}\mathbb{I}_{N\times N}, \tag{2.15}$$

where $\mathcal{I}_{N\times N}$ is the identity matrix.

The corresponding circuit Laplacian is given by $J(\omega) = i\omega\mathcal{C} + \frac{1}{i\omega}\mathcal{M}$, which yields the effective circuit Hamiltonian $\mathcal{L}(\omega) = \omega\mathcal{C} - \frac{1}{\omega}\mathcal{M}$. In this mapping, the terms $-\omega C_1$ and $-\omega C_2$ directly play the roles of the hopping amplitudes t_1 and t_2, respectively. Let us define $t = \frac{C_1}{C_2}$. At the resonant frequency $\omega_0 = 1/\sqrt{L(C_1+C_2)}$, the diagonal components of $\mathcal{L}(\omega)$ vanish, resulting in an exact correspondence with the SSH TB Hamiltonian. For a concrete demonstration, we choose the parameters $C_1 = 0.5$ nF, $C_2 = 1$ nF, and $L = 39$ μH, which give a resonant frequency $f_0 = \omega_0/(2\pi) = 658$ kHz. Diagonalizing $\mathcal{L}(\omega)$ for a chain of $N = 20$ unit cells produces the admittance spectrum $j_n(\omega)$ shown in Fig. 2.3(b), where red symbols highlight the edge-localized modes. For the same circuit, the Schrödinger-like Hamiltonian takes the form,

$$\mathcal{H} = \begin{pmatrix} 0 & \mathcal{C}^{-1}\mathcal{L} \\ -\mathbb{I}_{N\times N} & 0 \end{pmatrix}, \tag{2.16}$$

with 0 denoting the $N \times N$ zero matrix. Diagonalization of $\mathcal{H}$ yields the frequency spectrum shown in Fig. 2.3(c), where each admittance eigenvalue j_n corresponds to a pair of frequencies $\pm f_n$ determined by the condition $j_n(\omega) = 0$. A magnified view of the spectrum reveals that the edge states are pinned near the resonant frequency, as displayed in Fig. 2.3(d). As a result, the eigenstates of the circuit Hamiltonian $\mathcal{L}(\omega)$ and those of the Schrödinger-type Hamiltonian $\mathcal{H}$ associated with positive frequencies exhibit a direct one-to-one correspondence. In constructing the circuit Hamiltonian, resistive losses in inductors and capacitors are neglected for simplicity. In realistic circuits, however, such losses introduce a small imaginary component into the admittance and frequency spectra, which manifests experimentally as a finite linewidth and broadens the impedance spectrum.

Let us now examine how the IP of the circuit changes as the capacitor values are varied. It is clear from Eq. (2.11) that the VP of the circuit is determined by the eigenvalue, $j_n = 0$, or j_0, also referred to as the mid-gap eigenvalue. The mid-gap state can be directly

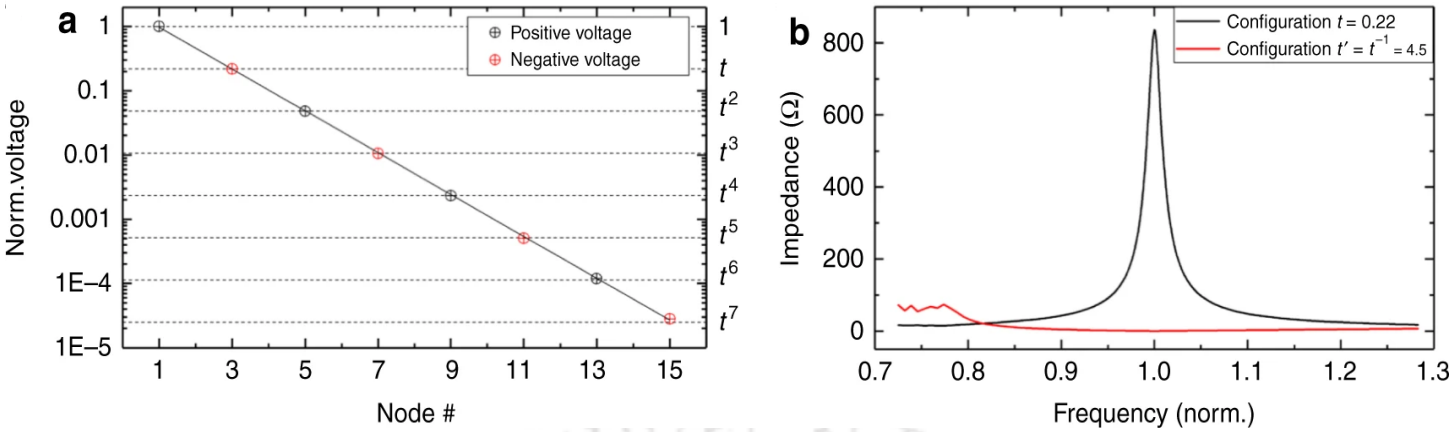

FIGURE 2.4: (a) Measurement of the mid-gap normalized voltage eigenmode $V(n)$, showing excellent agreement with the theoretical prediction, namely $V(n) \propto ((-t)^N, 0)$. Here, $\frac{C_1}{C_2} = \frac{V_2}{V_1} = t$ for the n^{th} two-site unit cell counted from the left. (b) Impedance measurements for the configurations $t = 0.22$ and $t = 1/4.5$. Although serial resistance and component non-uniformities are non-negligible, a pronounced SSH mid-gap impedance peak is clearly observed for $t = 0.22$, while it is absent in the $t = 1/4.5$ configuration. The plots are adopted from Ref. [3].

detected through impedance measurements. Let V_1 and V_2 be the voltage differences across C_1 and C_2, respectively, and satisfy the condition, $Q = C_1V_1 = C_2V_2$. For $C_1 < C_2$, this implies that the voltage drop across C_1 is greater than that across each C_2. This further implies that $t = V_2/V_1 = C_1/C_2 < 1$, indicating that the TEC is in the topological phase. When an AC source drives the circuit, the potentials V_1 and V_2 oscillate out of phase, giving rise to a spatial voltage configuration of the form, $V(n) \propto (1, 0, -\frac{V_2}{V_1}, 0, (\frac{V_2}{V_1})^2, 0, -(\frac{V_2}{V_1})^3, 0, \ldots (-\frac{V_2}{V_1})^n, 0)$, where the index n runs through the two-node unit cells [3]. This alternating pattern is reflected in the normalized VP shown in Fig. 2.4(a). Likewise, for $t < 1$, namely in the regime where j_0 exists, the circuit displays a strongly enhanced, divergent impedance response at the resonant frequency $\omega_0 = 1/\sqrt{L(C_1 + C_2)}$, as illustrated in Fig. 2.4(b). In contrast, no such divergent impedance behavior is observed for $t > 1$.

2.5 NHSE realized through Circuits

In this section, we review the experiment done by T. Helbig *et al.* in 2020, to observe skin effect in an NH SSH model with nonreciprocal intra-cell hopping [4]. The Hamiltonian of the NH SSH model is given in Eq. (2.14), with a minor change in notation where the hopping parameters are identified as $t_1 \equiv v$ and $t_2 \equiv r$, as illustrated in Fig. 2.5(a). Nonreciprocity was introduced through the parameter γ in the intra-cell hopping amplitude v. A circuit chain consisting of $N = 10$ unit cells was constructed, as shown in Fig. 2.5(b). The detailed circuit elements forming a single unit cell are specified in Fig. 2.5(c), and

a picture of a fabricated unit-cell board cutout is displayed in Fig. 2.5(d). The key components of Fig. 2.5(d) are:

1. An LC resonator formed by two parallel surface-mounted device capacitors ($C_1 = 2 \times 150\,\mathrm{nF}$) and a high-current surface-mounted device inductor on the backside ($L_1 = 10.1\,\mu\mathrm{H}$), which together realize $v(\omega)$.

2. An INIC consisting of an surface-mounted device capacitor ($C_3 = 47\,\mathrm{nF}$), a nulling potentiometer ($R_{\mathrm{null}} = 5\,\mathrm{k}\Omega$), jumpers (short, conductive wires that bridge, complete, or configure circuits without permanent soldering) for grounding the Op-Amp inputs during nulling, auxiliary impedance-conversion elements (two identical pairs of an surface-mounted device capacitor $C_{\mathrm{aux}} = 470\,\mathrm{nF}$ and a metal-film resistor $R_{\mathrm{aux}} = 20\,\Omega$), the Op-Amp LT1363, and radio-frequency bypass capacitors (100 nF) for the positive and negative supply voltages on the backside, collectively generating γ.

3. An auxiliary intra-cell resistor ($10\,\Omega$, not utilized).

4. The grounding network for sub-lattice A, comprising a trimmer resistor R_0 (set to $20\,\Omega$), a shielded wire-wound inductor $L_0 \approx 33\,\mu\mathrm{H}$ on the backside, and two parallel surface-mounted device capacitors $C_0 = 2 \times 47\,\mathrm{nF}$.

5. The grounding network for sub-lattice B, identical to 4. except for the capacitor configuration; and 6. intercell coupling r realized using parallel surface-mounted device capacitors ($C_2 = 2 \times 47\,\mathrm{nF}$).

For a given AC input current of frequency $\omega = 2\pi f$, when $\gamma \neq 0$, the intra-cell coupling becomes effectively non-reciprocal, giving rise to a non-reciprocal SSH circuit. For each driving frequency f, the voltage amplitudes $|V_n|$ of the n^{th} eigenvector under OBC are plotted as functions of the node index x in Fig. 2.5(e). The green and blue curves denote skin modes and topological edge modes, respectively. As illustrated in panels (i) and (ii) ((iv) and (v)), when $v(\omega) < 0$ ($v(\omega) > 0$), all voltage modes accumulate at the left (right) boundary of the circuit, demonstrating NHSE within the TEC. At the itinerant transition point $v = 0$, occurring at a frequency $f \sim \left(\frac{2\pi}{\sqrt{L_1 C_1}}\right)$ and shown in panel (iii), the bulk modes exhibit no localization. To analyze the topological nature of the circuit, the OBC Laplacian is subsequently mapped onto an effective reciprocal lattice model that restores the BBC. To enable a direct comparison between theoretical predictions and experimental observations, the effective description was refined into a full-scale fitting model that incorporates parasitic resistances in the inductive couplings, which constitute the dominant experimental imperfections. Specifically, the inductances were modified according to $L_j \to L_j + R_{L_j}/(i\omega)$, where R_{L_j} denotes the series resistance associated with the inductor L_j. This procedure leads to a complexification of the intra-cell coupling, such that $v(\omega)$ is renormalized to $v(\omega) \to v_R + iv_I$ within the effective

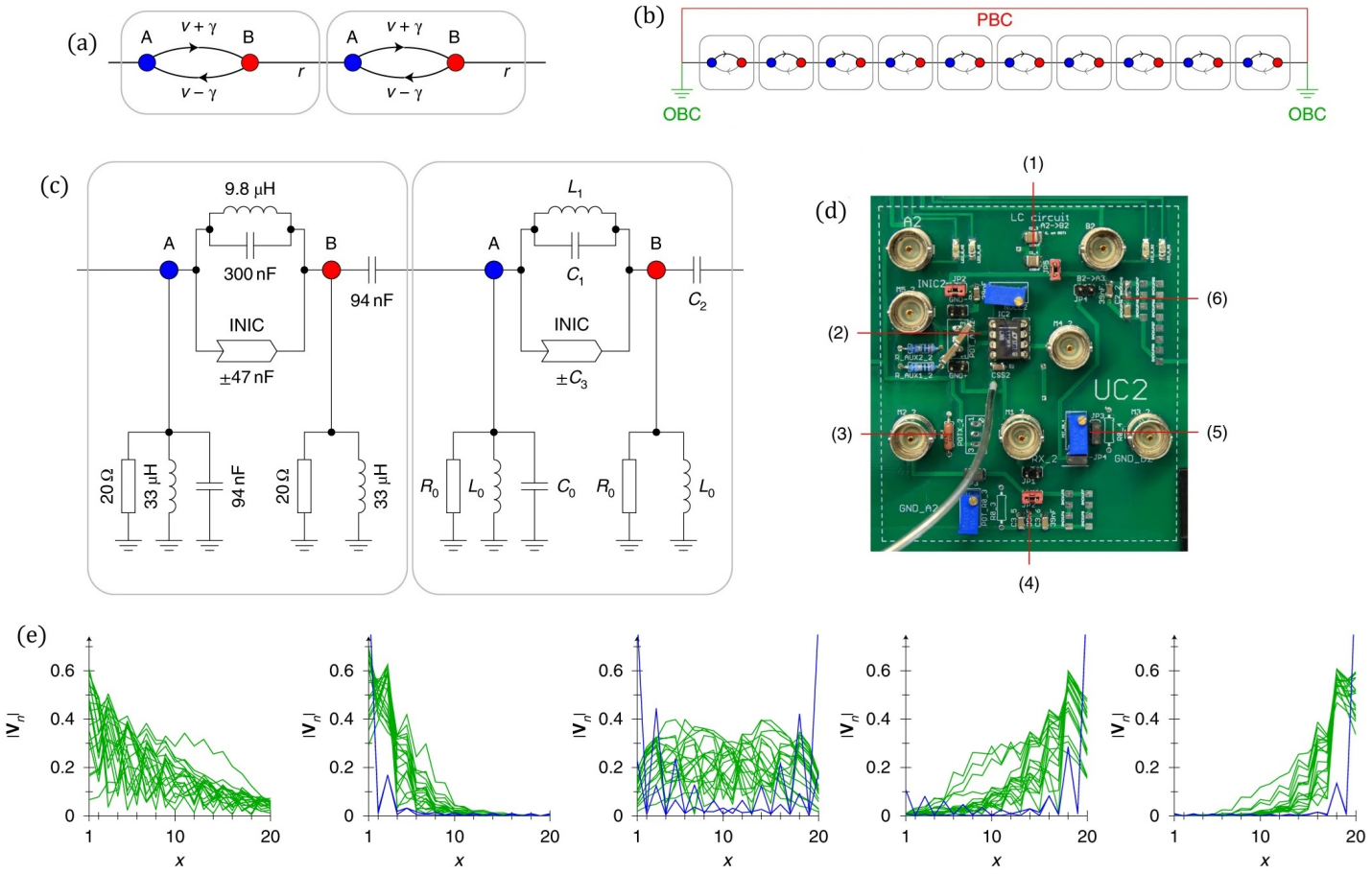

FIGURE 2.5: (a) Asymmetric intra-cell couplings $v \pm \gamma$ give rise to an NH non-reciprocal TB model. (b) Schematic of the complete circuit configuration composed of $N = 10$ unit cells, illustrating periodic (red) and open (green) boundary conditions. (c) TEC setup of the non-reciprocal circuit model corresponding to panel (a). The parameter γ is implemented using INICs, while an intra-cell LC resonator is employed to tune $v(\omega)$. (d) Photograph of a circuit-board cutout corresponding to a single unit cell. All circuit modules can be connected or disconnected independently using jumpers. (e) NHSE observed in the TEC for different driving frequencies, f. The images and plots are adapted from Ref. [4].

model. Subsequently, the OBC Laplacian was transformed via a similarity transformation, $\mathcal{L}' = S^{-1}\mathcal{L}S$, where $S = \mathrm{diag}(1, \alpha, \alpha^2, \alpha^3, \ldots, \alpha^N)$ for a system consisting of N unit cells. The resulting Laplacian $\mathcal{L}'$ supports topological zero-energy edge modes, which are indicated by the blue curves in Fig. 2.5(e).

2.6 Building a Circuit for periodically Driven Systems

While the exploration of NH topological systems has already unveiled a multitude of exotic physical phenomena, a further dimension of control and novelty can be achieved by extending these studies beyond static scenarios. In this context, Floquet engineering [180–183] has emerged as a powerful technique, offering an elegant and systematic

framework for tailoring and manipulating topological properties in out-of-equilibrium scenarios. By periodically modulating system parameters, Floquet theory reveals that additional non-trivial states of matter can be realized beyond their static analogues, such as the emergence of π-modes [184] and drive-induced longer-range interactions. This has been convincingly demonstrated in various experimental platforms, including ultracold atoms trapped in optical lattices, photonic waveguide arrays [185–188], etc. In this section, we explore a periodically driven model and demonstrate how NHSE may emerge even in the absence of non-reciprocity. The primary motivation is to realize such a driven system within a TEC framework [189].

Let us now discuss the advantages of analyzing the Floquet drive in the frequency domain. We begin with a sinusoidally driven system described by the Hamiltonian $H(t) = H_0 + V_0 \cos \omega t$, where V_0 and ω denote the amplitude and frequency of the driving term, respectively, and H_0 is a generic static Hamiltonian. Floquet theory allows the time-dependent Schrödinger equation to be solved using the ansatz $|\psi(t)\rangle = e^{-iEt} |u(t)\rangle$, where $|u(t+T)\rangle = |u(t)\rangle$ denotes the time-periodic Floquet modes and E represents the Floquet quasi-energies. In close analogy with the quasi-momentum in crystals, the quasi-energies are defined modulo $2\pi/T$, i.e., within the Floquet Brillouin zone $E \in [-\pi/T : \pi/T]$. From this perspective, the Floquet modes can be interpreted as the eigenstates of the stroboscopic time-evolution operator,

$$\begin{aligned} \hat{U}(T) |\psi(0)\rangle &= |\psi(T)\rangle , \\ \hat{U}(T) |u(0)\rangle &= e^{-iET} |u(T)\rangle = e^{-iET} |u(0)\rangle . \end{aligned} \tag{2.17}$$

Hence, the Floquet stroboscopic time evolution operator is,

$$\hat{U}(T) = \mathcal{T} \exp[-i \int_0^T H(t) dt] = e^{-iH_{\text{eff}}T}. \tag{2.18}$$

$\mathcal{T}$ denotes the time ordering product and H_{eff} is the effective time-independent Hamiltonian. One can obtain E and $|u(t)\rangle$ by solving the Floquet-Bloch equation,

$$[H(t) - i\partial_t] |u_k(t)\rangle = E |u_k(t)\rangle . \tag{2.19}$$

The operator $H(t) - i\partial_t = H_F$ is called the Floquet Hamiltonian. Because of the time periodicity, it is convenient to consider the composite Hilbert space $R \otimes T$ where R is the usual Hilbert space with a complete set of orthogonal basis, and T is the space of time periodic functions spanned by $\{e^{-im\omega t}\}$. This yields the following form of H_F,

$$H_F = \sum_{m,m'} \Big(m\omega \delta_{m,m'} + \frac{1}{T} \int_0^T dt H(t) e^{-i(m-m')\omega t} \Big). \tag{2.20}$$

This leads to a situation in which we can split the driven spectrum into an infinite number

of copies of the static Hamiltonian, each separated from the other by $m\omega$, where the index m defines a subspace called the m^{th} Floquet replica. A general representation of the Floquet Hamiltonian can thus be represented as,

$$H_F = \begin{bmatrix} \ddots & \vdots & \vdots & \vdots & \vdots & \vdots & \iddots \\ \dots & H_0 - 2\omega & H_{-1} & H_{-2} & H_{-3} & H_{-4} & \dots \\ \dots & H_1 & H_0 - \omega & H_{-1} & H_{-2} & H_{-3} & \dots \\ \dots & H_2 & H_1 & H_0 & H_{-1} & H_{-2} & \dots \\ \dots & H_3 & H_2 & H_1 & H_0 + \omega & H_{-1} & \dots \\ \dots & H_4 & H_3 & H_2 & H_1 & H_0 + 2\omega & \dots \\ \iddots & \vdots & \vdots & \vdots & \vdots & \vdots & \ddots \end{bmatrix}, \tag{2.21}$$

where the elements $H_{\pm m} = \frac{1}{T}\int_0^T H(t)e^{\pm im\omega t}dt$ get rid of the explicit time dependence of the system. The Hamiltonian H_F is termed the Shirley-Floquet Hamiltonian. The elements of the Floquet Hamiltonian can be represented as,

$$\langle m| H_F |m'\rangle = m\omega\delta_{m,m'} + E_0\delta_{m,m'} + H_{m-m'}, \tag{2.22}$$

where E_0 is the energy of the static Hamiltonian, and the Fourier elements $H_{\pm m}$ are expressed as the second term in the right-hand side of the above equation. The elements $H_{|m|}$, except for $m = 0, \pm 1$, vanish owing to the mathematical form of the drive.

To implement a driving protocol in a system that demonstrates topological modes and may have non-hermiticity-induced standard features, we consider a Creutz ladder [190] as a paradigmatic model. Let us briefly mention the basic properties of a Creutz ladder. It is composed of two parallel chains (or 'rungs') of lattice sites, interconnected via diagonal (t_D), vertical (t_V), and horizontal (t_H) hopping amplitudes, as illustrated in Fig. 2.6. A distinctive feature of this model is the presence of a magnetic flux threading the ladder, thereby introducing an additional degree of freedom through the Peierls phase (ϕ) associated with horizontal hopping. Each unit cell contains two sub-lattice sites, denoted by a_n and b_n. The corresponding Hamiltonian in momentum space takes the form,

$$H_0 = \sum_n \left[t_H \left(e^{i\phi} a_n^\dagger a_{n+1} + e^{-i\phi} b_n^\dagger b_{n+1} \right) + t_D \left(a_n^\dagger b_{n+1} + a_{n+1}^\dagger b_n \right) + t_V a_n^\dagger b_n \right] + H.c., \tag{2.23}$$

The magnetic flux ϕ threads each plaquette of the ladder, which is related to the hopping phase via $2\phi = \frac{\Phi}{\Phi_0}$, with Φ_0 denoting the magnetic flux quantum. The static model exhibits a topological phase transition at $t_V = 2t_D$. The system shows nontrivial behavior for $\frac{t_V}{2t_D} < 1$ and trivial behavior for $\frac{t_V}{2t_D} > 1$. For the driven scenario, when the driving frequency, ω (Eq. (2.20)), is larger than the bandwidth of the system, D, (defined as $D = 2(|t_V| + 2|t_D|)$, higher-order couplings ($|m| > 1$) are strongly suppressed, so that keeping only a few replicas suffices to capture the essential physics. Thus, Eq. (2.21) reduces to a 3×3 matrix, with diagonal entries as $H_0 - \omega$, H_0, and $H_0 + \omega$.

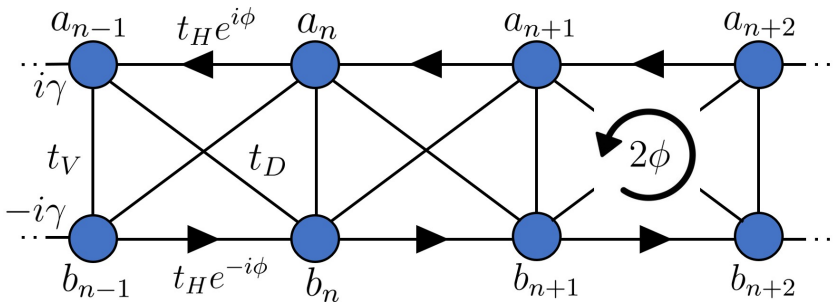

FIGURE 2.6: Schematic representation of the quasi-1D Creutz ladder, where a_n and b_n denote the two distinct sub-lattices. The different hopping amplitudes, t_H, t_V, t_D, denote the horizontal, vertical, and diagonal hoppings, respectively.

We next examine the impact of adding a sub-lattice-dependent imaginary onsite potential, represented by the term,

$$H_\gamma = \sum_n i(\gamma_A \, a_n^\dagger a_n + \gamma_B \, b_n^\dagger b_n). \tag{2.24}$$

With the introduction of H_γ to the Hermitian Hamiltonian H in Eq. (2.23), the total Hamiltonian of the system can be written as,

$$H_0 = H + H_\gamma \tag{2.25}$$

Subsequently, as a driving protocol, a harmonic modulation of the vertical hopping term is introduced via

$$t_V(t) = (2V_0 \cos \omega t + t_V). \tag{2.26}$$

Here, V_0 is the driving strength and $\omega = 2\pi/T$ is the driving frequency with T being the time period.

For better comprehension, let us briefly go through the theoretical results obtained for a driven NH Creutz ladder, described via a combination of Eqs. (2.25) and (2.26). Interestingly, when a staggered configuration is imposed, specifically, $\gamma_A = -\gamma_B = \gamma$, and the pseudo-spin basis is rotated as $\sigma_y \to \sigma_z \to -\sigma_y$., an effective asymmetry emerges in the intra-cell hopping terms involving t_V and γ. This asymmetry mimics that found in non-reciprocal extensions of the SSH model [45, 173], thereby enabling the onset of NHSE in the Creutz ladder. As shown in Fig. 2.7(a), for positive values of t_V, the upper diagonal elements are fully occupied, leading to all the eigenstates being localized at the left edge of the system. Conversely, when t_V is negative (Fig. 2.7(b)), the lower diagonal elements become completely occupied, resulting in all eigenstates being localized at the right edge. Although examining the geometric winding in either of the symmetric time frames provides insight into the system's topological characteristics, it does not provide a complete description of the number or type of edge modes present. Depending on the periodic table of Floquet TIs [191], each non-trivial phase in the system can then be

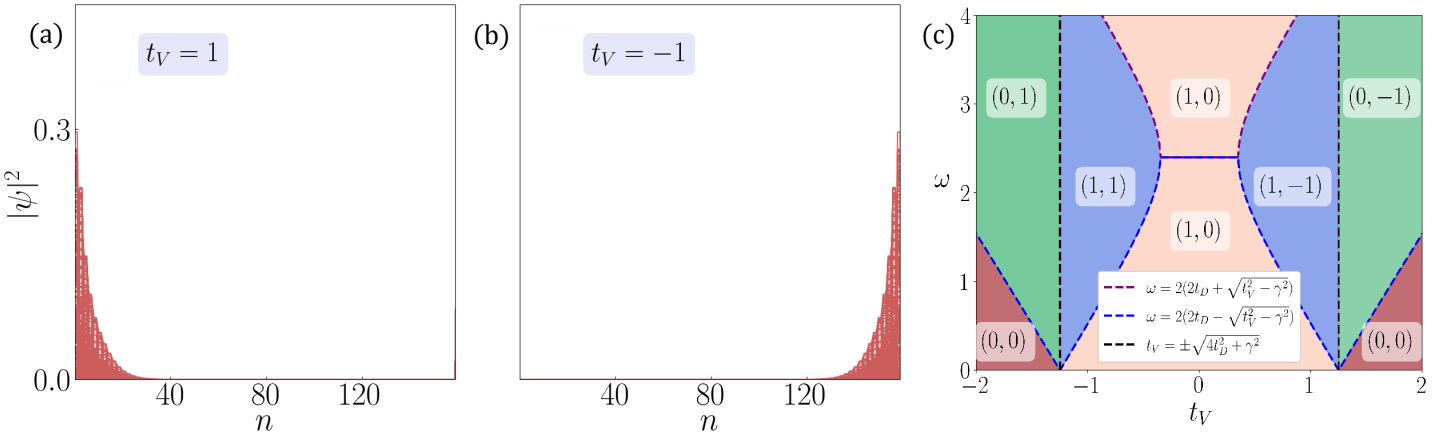

FIGURE 2.7: Panels (a) and (b) denote the distribution of the NH skin modes at the edges corresponding to positive ($t_V = 1$) and negative ($t_V = -1$) values of t_V, respectively. (c) Topological phase diagram in the ω–t_V plane characterized by the pair (ν_0, ν_π). The phase boundaries are determined by solving the gap-closing conditions of the effective Hamiltonian H_{eff} derived using high-frequency expansion. The other parameters have been chosen as $t_H = t_D = 0.6$, $V_0 = 0.3$, $\omega = 1$, and $\gamma = 0.4$.

characterized by a pair of winding numbers, ν_0 and ν_π given as,

$$\nu_0 = \frac{\nu_1 + \nu_2}{2}, \quad \nu_\pi = \frac{\nu_1 - \nu_2}{2}, \tag{2.27}$$

where ν_1 and ν_2 denote the conventional definition of winding numbers [17, 192] associated with the effective Hamiltonians in the two symmetric time frames, with the integration being carried out along the GBZ contour obtained from analyzing the NH setting of the model [189]. Fig. 2.7(c) illustrates these phase boundaries in the $\omega - t_V$ plane. Evidently, these three distinct boundaries divide the parameter space into eight subregions (as shown in Fig. 2.7(c)). Furthermore, via analyzing the quasienergy spectrum and evaluating the two invariants at representative points within these regions, one can classify each subregion as a distinct nontrivial phase characterized by its corresponding pair of ν_0 and ν_π values.

Having understood the basics, let us now design a TEC capable of faithfully mimicking the Floquet NH Creutz ladder. The goal is not merely to simulate a quantum phenomenon in an electrical setting, but to directly visualize the localization behavior predicted by the TB model within the TEC framework. The voltage and impedance profiles, being the key measurable quantities in such circuits, will serve as direct probes of the TB model's features. The Hermitian Creutz ladder (Eq. (2.23)), is emulated by an equivalent electrical circuit, shown in Fig. 2.8(a), whose Laplacian is denoted by $\mathcal{L}$. Positive hopping amplitudes are achieved using capacitors, resulting in a positive imaginary admittance without dissipation under AC driving. In particular, the diagonal (vertical) hopping amplitude t_D (t_V) in Fig. 2.6 is implemented via a capacitor C_D (C_V) as shown in Fig. 2.8(a). The admittance of C_D (C_V) is given by $i\omega_R C_D$ ($i\omega_R C_V$) and

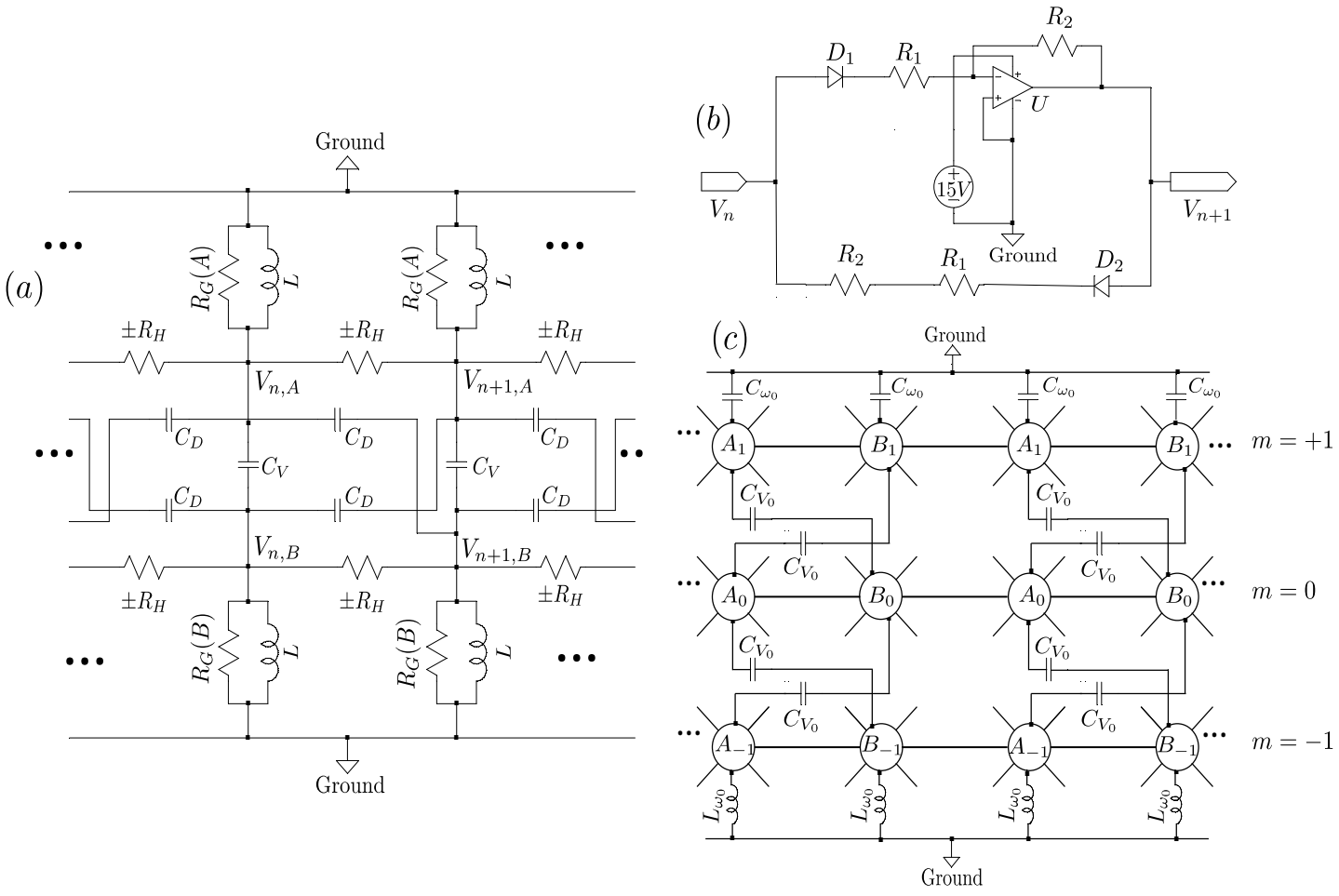

FIGURE 2.8: (a) The TEC diagram corresponding to the NH Creutz ladder. The output voltage at the subnode A/B of the n^{th} node is denoted by $V_{n,A/B}$. The circuit elements $\pm R_H$, C_D, and C_V represent the hopping amplitudes $\pm it_H$, t_D, and t_V, respectively. Further, the resistors $R_G(A/B)$ encode the NH onsite potentials $\pm i\gamma$. A grounded inductor L is included at each subnode to tune the diagonal terms of the TEC Laplacian at the resonating frequency, ω_R. (b) Circuit implementation of $\pm R_H$ between two adjacent nodes n and $n+1$. A unidirectional current passing through diode D_1, from node n to $n+1$, experiences an effective negative resistance of $-(R_1+R_2) = -R_H$ due to the π phase shift in the output voltage V_{n+1}, generated by the inverting amplifier configuration of the Op-Amp U. However, when flowing in the reverse direction, that is, from $n+1$ to n, the current experiences a positive resistance of $(R_1+R_2) = R_H$. (c) The TEC diagram corresponding to the NH Creutz ladder under a harmonic drive applied to the vertical hopping. The diagram illustrates three replicas of the original TEC, corresponding to Floquet indices $|m| = 0, 1$, interconnected by capacitors C_{V_0}. These capacitors simulate the Floquet drive by coupling adjacent Floquet layers.

must satisfy the condition,

$$|i\omega_R C_D| = t_D \quad \text{and} \quad |i\omega_R C_V| = t_V. \tag{2.28}$$

The value of the grounded inductor, L, is chosen to satisfy the following relation,

$$i\omega_R(C_V + 2C_D) + \frac{1}{i\omega_R L} = 0, \tag{2.29}$$

at the resonating frequency, ω_R. The remaining terms in H (Eq. (2.23)) correspond to horizontal hopping modified by the Peierls phase $t_H e^{\pm i\phi}$, with $\phi = \pi/2$. These terms are implemented using resistors, which introduce dissipative impedance into the circuit. Note that the values must satisfy the condition,

$$\left|\mp\frac{i}{R_H}\right| = |\pm it_H|. \tag{2.30}$$

This negative resistance, $-R_H$, is implemented using an inverting Op-Amp configuration, which functions as an amplifier with fixed negative gain, producing an output voltage of opposite polarity. In Fig. 2.8(b), if V_n (V_{n+1}) is taken as the input (output) voltage, assuming current flows only from V_n to V_{n+1}, the effective impedance is given by $-(R_1 + R_2)$, where $R_1 + R_2 = R_H$. This is equivalent to $-it_H$ in the TB model. The configuration is implemented by placing a diode (D_1) at the inverting output of the Op-Amp (U), ensuring unidirectional current flow from the n^{th} to the $(n+1)^{\text{th}}$ node, which effectively generates negative resistance for currents in the intended direction. To realize the hopping term $+it_H$ (the Hermitian conjugate of $-it_H$), a parallel path is added between the n^{th} and $(n+1)^{\text{th}}$ nodes, consisting of a series connection of R_1, R_2, and a diode (D_2) oriented opposite to D_1, as shown in Fig. 2.8(b). To realize the onsite imaginary potential, $\pm i\gamma$, given via Eq. (2.24), within the TEC, resistors $R_G(A)$ and $R_G(B)$ at the subnodes A_n and B_n, respectively, are placed such that their magnitudes are equal. Still, their signs are opposite, consistent with the relation $\gamma_A = -\gamma_B = \gamma$. Thus, depending upon the sub-lattice index (a_n or b_n) as illustrated in Fig. 2.6, the corresponding resistors must exhibit positive or negative resistance (A_n or B_n), as shown in Fig. 2.8(a). The values of $R_G(A)$ and $R_G(B)$ is given by,

$$R_G(A) = -R_G(B) = \frac{1}{|\gamma|}. \tag{2.31}$$

The negative resistance, $-R_G(B)$, is implemented using the same configuration as $-R_H$. Let us derive the Laplacian $\mathcal{L}$ of the TEC with a total number of N_0 nodes, driven at an arbitrary angular frequency ω_a. The analytical details behind the formulation of the Laplacian and its equivalence to the Hamiltonian of the TB model at the resonant angular frequency, ω_R, are thoroughly discussed in Appendix B.

Let us now simulate the Floquet Hamiltonian using TECs. The design consists of multiple interconnected circuit layers, each representing a specific Fourier mode, as shown in Ref. [193] for a driven Hermitian SSH TEC. Nevertheless, one can still opt for a real-time implementation with dynamically varying circuit parameters as suggested in Refs. [194, 195], which offer a direct way to probe Floquet physics. In the context of the driven NH Creutz ladder, the mathematical form of the drive associated with the vertical hopping t_V ensures that only the Fourier components with $m = 0$ and $|m| = 1$ contribute significantly to the Floquet expansion. In Fig. 2.8(c), the circuit diagram corresponding to the driven NH Creutz ladder is presented schematically. The diagonal blocks $H \pm \omega$ in Eq. (2.21) are implemented using grounded inductors (L_ω) and capacitors (C_ω) connected to each subnode, depending on the sign of the shift, and the following relations must be satisfied,

$$|i\omega_R C_\omega| = \frac{1}{|i\omega_R L_\omega|} = \omega, \quad \text{and} \quad |i\omega_R C_{V_0}| = V_0. \tag{2.32}$$

The non-zero off-diagonal couplings between the adjacent Floquet replicas ($|m| = 0,\ 1$) are realized using capacitors of value C_{V_0}, corresponding to a driving amplitude V_0. Thus, Fig. 2.8(c) provides the complete TEC-based realization of the driven NH Creutz ladder. For convenience, the following parameter values are fixed, $C_D = 0.6\,\mu\text{F}$ ($t_D = 0.6$), $C_\omega = 3\,\mu\text{F}$ ($\omega = 3$), $C_{V_0} = 0.3\,\mu\text{F}$ ($V_0 = 0.3$), $R_H = \frac{5}{3}\,\Omega$ ($t_H = 0.6$) and $R_G(A) = 2.5\,\Omega$ ($\gamma = 0.4$).

Let us first analyze the TEC corresponding to the static Hermitian Creutz ladder. For the Hermitian model, the topological phase transition is governed by the vertical and diagonal hoppings in Eq. (2.23), in particular by the ratio $\frac{t_V}{2t_D}$. As shown in Fig. 2.8(a), setting $R_G(A) = R_G(B) \to \infty$ effectively removes the connection, yielding $\gamma = 0$. Fig. 2.9(a) shows the IP of the Hermitian Creutz TEC, using Eq. (2.11). In the topological regime, that is, for $C_V < 2C_D$, two topological edge modes emerge, resulting in a substantial increase in the circuit impedance. This manifests as two prominent edge IPs. The first port is fixed at the first (last) node, while the second port is swept across all nodes to obtain the second (first) edge IP. Each node is connected to two C_D capacitors and one C_V capacitor, and for a fixed amount of charge Q, this asymmetry leads to significant potential differences.

For the driven case, the IP of the Hermitian Creutz TEC is constructed according to Fig. 2.8(c), with the values of the circuit elements kept unchanged. As shown in Fig. 2.9(b), the IP exhibits localization at the edges of each Floquet replica ($|m| = 0, 1$). Specifically, the first (second) edge IP is predominantly localized at the left (right) edge of the central Floquet replica ($m = 0$), consistent with the spatial probability distribution of the topological edge modes in the corresponding TB model. To construct the NH Floquet Creutz TEC, the resistors $R_G(A/B)$, with $R_G(A) = -R_G(B) = 2.5\,\Omega$, are being

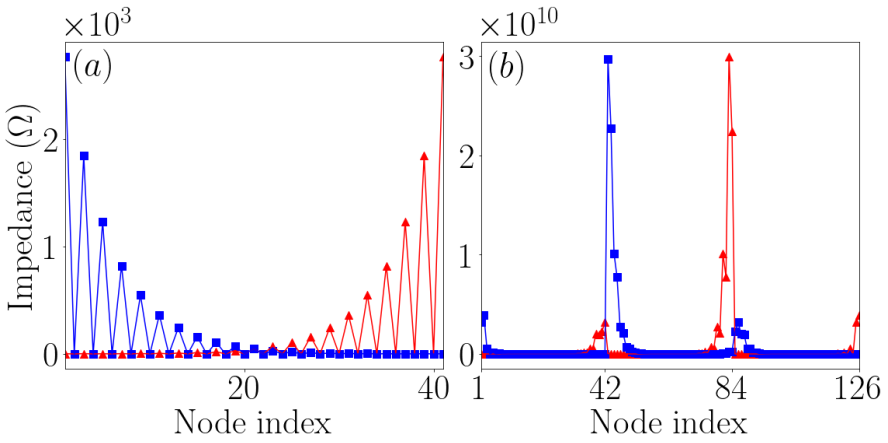

FIGURE 2.9: (a) The IP of the Hermitian Creutz ladder TEC, consisting of 21 unit cells, is shown for both the trivial and topological regimes. The first and second edge IPs are represented by red triangles and blue squares, respectively. (b) The IP of the driven Creutz TEC, incorporating three Floquet replicas ($|m| = 0, 1$), is presented. In this case, the first edge IP is predominantly localized near the right edge of the $m = 0$ ladder (84^{th} node), while the second edge IP localizes near its left edge (43^{rd} node). Additionally, each edge IP exhibits minor localization near the adjacent edges to its primary localization node. The topological phase, which is evident from the presence of edge modes in the IP, is achieved by setting $C_V = 0.4\,\mu\text{F} < 2C_D$.

included. As demonstrated via Figs. 2.7(a) and 2.7(b), the staggered imaginary onsite potential $\pm i\gamma$ induces the NHSE in the driven NH Creutz ladder. This phenomenon manifests in the TEC as shown in Fig. 2.10(a), where the absolute values of all the eigenmodes of the Laplacian are plotted against the node index. The localization at the edges clearly indicates the presence of NHSE, as shown by theoretical simulations of the TEC setup. To experimentally probe NHSE in such a setup, one must excite the TEC at a randomly chosen node and measure the resulting VP. Fig. 2.10(b) illustrates this situation, where a specific node, namely, the 66^{th} node, is excited using a current source, and the voltage at each node is recorded accordingly. As demonstrated for the TB model, reversing the sign of t_V alters the direction of NHSE, resulting in the localization of bulk modes at the opposite edge of the system (see Figs. 2.7(a) and 2.7(b)). To implement this sign reversal of t_V within the TEC, one must effectively reverse the sign of the vertical hopping, which requires replacing the capacitor C_V with an inductor L_V of the same magnitude. The value of L_V must satisfy the relation, $\frac{1}{|i\omega_R L_V|} = t_V$, and a corresponding adjustment must be made to the grounded inductor L. It has previously been demonstrated that an onsite potential can induce NHSE even in the absence of non-reciprocity in static cases [107] via TECs. This clearly demonstrates that one can control the direction and amplitude of voltage localization in the TEC by switching between vertical capacitors and inductors, an analogue of which has been elaborately discussed in the TB model.

We now explore the topological zero and π-modes, as illustrated in Fig. 2.7(c). To demonstrate this, three representative points from distinct regions of the phase diagram

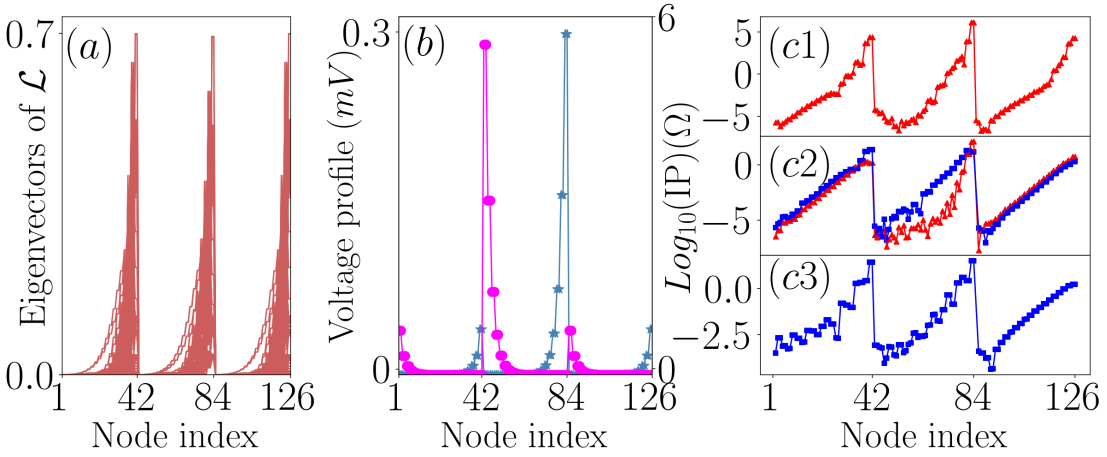

FIGURE 2.10: (a) The eigenmodes of the Laplacian for the driven NH Creutz ladder TEC with $R_G(A) = 2.5\,\Omega$ exhibit localization near the edges of the Floquet replicas, signaling the emergence of NHSE in the TEC. The value of C_V is chosen to be $0.3\,\mu$F. (b) A random node (node 66 in this case) is excited using a current source of amplitude $1\,\mu A$, and the resulting VP is plotted against the node index. The circles (peak at the 43^{rd} node) and stars (peak at the 84^{th} node) correspond to the cases with capacitors ($C_V = 1\,\mu$F) and inductors ($L_V = 1\,\mu$H), respectively. The IP in the log_{10} scale are plotted for three different cases, (c1) $C_V = 0.3\,\mu$F, (c2) $C_V = 0.7\,\mu$F, and (c3) $C_V = 1.7\,\mu$F. The red triangles (blue squares) correspond to the IP for the realization of the zero (π) energy modes via the TEC.

in Fig. 2.7(c), characterized by the following winding numbers, 1. $\nu_0 = 1, \nu_\pi = 0$, 2. $\nu_0 = 1, \nu_\pi = -1$, 3. $\nu_0 = 0, \nu_\pi = -1$, are being considered. For the first case, corresponding to $\nu_0 = 1$, the logarithm of the IP is plotted in Fig. 2.10(c1). The impedance exhibits peaks at the right edges of each circuit row, indicating the presence of zero-energy modes. In the second case ($\nu_0 = 1, \nu_\pi = -1$), both zero and π modes are predicted by the TB model. However, since the π modes have non-zero energies $\pm\frac{\omega}{2}$, they do not lead to impedance divergence in the conventional setup used to detect zero modes. As a result, the π modes are not directly visible in the standard IP measurement. To detect the π-modes in the TEC, an effective chemical potential shift of $\mp\frac{\omega}{2}$ must be introduced. This can be achieved by incorporating additional capacitors (to add $+\frac{\omega}{2}$) or inductors (to add $-\frac{\omega}{2}$) [193]. This adjustment ensures that the circuit impedance diverges at eigenenergies of the Laplacian corresponding to the π-mode energies of the TB model. Accordingly, Fig. 2.10(c2) shows two configurations: one without added inductors (capturing the zero modes), and another with inductors that simulate the required chemical potential ($-\frac{\omega}{2}$), enabling the detection of the π-modes. In both the cases, the IP exhibits maxima at the right edges of the circuit rows, signaling the presence of both zero and π modes in the TEC. Finally, Fig. 2.10(c3) corresponds to the third region ($\nu_0 = 0, ; \nu_\pi = -1$), where only π-modes are present, with no accompanying zero modes. This is consistent with the phase diagram in Fig. 2.7(c).

Chapter 3

Exploring $\mathcal{PT}$ Symmetry in Non-Hermitian SSH Model

The topological properties of the SSH model [16] have already been discussed briefly in Section 2.4 of the previous chapter. It comprises two atoms per unit cell. When the intra-cell hopping amplitude is weaker than the inter-cell hopping, the system encodes a topological phase characterized by two doubly degenerate zero-energy modes at both edges of an open chain. These edge states are quantified by winding number [196]. In the Hermitian SSH model, the winding number is zero in the topologically trivial phase and unity in the non-trivial phase. In this chapter, we investigate a generalized 1D NH SSH model. Specifically, we demonstrate two NH versions of the SSH model, namely the $s\mathcal{PT}$ and $n\mathcal{PT}$ SSH models, based on the protocol of incorporating non-hermiticity. The $n\mathcal{PT}$ SSH model is achieved via non-reciprocal hopping integrals (both within and across unit cells), while the $s\mathcal{PT}$ SSH model is realized through the inclusion of complex staggered on-site potential. We compare and contrast the corresponding topological phases, NHSE, and the structure of the EPs in each case. For the $n\mathcal{PT}$ SSH model, we employ the non-Bloch theory [134] to distinguish the topological phases of the model. For each model, we propose a TEC design and show the impedance (voltage) profile to realize the topological zero-energy (skin) modes. This chapter is organized as follows. We introduce the Hamiltonians corresponding to the $s\mathcal{PT}$, and the $n\mathcal{PT}$ cases in Section 3.1. We discuss the $n\mathcal{PT}$ SSH model in Section 3.2, and explore the conditions for the EPs and NHSE in the model. We then construct the GBZ for the model, calculate the winding number, which is defined specifically for this model, and

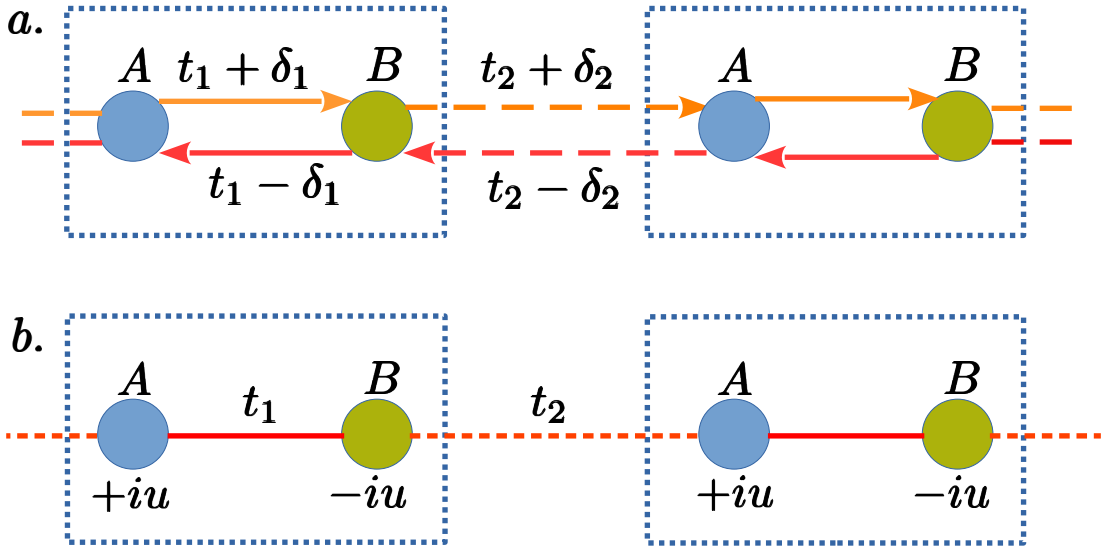

FIGURE 3.1: (a) NH SSH model with non-hermiticity induced in the intra-cell (t_1) and the inter-cell (t_2) hopping amplitudes. (b) NH SSH model with imaginary potential, u. The box represents a single unit cell.

propose the TEC design. In Section 3.3, we study the topology of the $s\mathcal{PT}$ SSH model. Finally, we conclude with a brief summary of our results in Section 3.4.

3.1 Model Hamiltonians and Symmetries

The Hamiltonian of the Hermitian SSH model is given by Eq. (2.14) of the previous chapter. First, we consider a model with non-reciprocity in both the intra-cell and the inter-cell hopping energies, which are pictorially shown in Fig. 3.1(a). The corresponding Hamiltonian can be written as,

$$\hat{H}_1 = \sum_{n=1}^{N} \left[(t_1 - \delta_1)\, \hat{a}_n^\dagger \hat{b}_n + (t_1 + \delta_1)\, \hat{b}_n^\dagger \hat{a}_n + (t_2 - \delta_2)\, \hat{b}_n^\dagger \hat{a}_{n+1} + (t_2 + \delta_2)\, \hat{a}_{n+1}^\dagger \hat{b}_n \right] \quad (3.1)$$

where, δ_1 (δ_2) is the non-reciprocity in t_1 (t_2). An alternative NH model can be obtained by including a staggered imaginary on-site potential within the Hermitian SSH model, while keeping the hopping parameters unaltered. This Hamiltonian can be written as,

$$\hat{H}_2 = \sum_{n=1}^{N} \left[iu \left(\hat{a}_n^\dagger \hat{a}_n - \hat{b}_n^\dagger \hat{b}_n \right) + t_1 \left(\hat{a}_n^\dagger \hat{b}_n + \hat{b}_n^\dagger \hat{a}_n \right) + t_2 \left(\hat{b}_n^\dagger \hat{a}_{n+1} + \hat{a}_{n+1}^\dagger \hat{b}_n \right) \right] \quad (3.2)$$

where u is the strength of the imaginary on-site potential. The system can be visualized as presented in Fig. 3.1(b).

Next, we Fourier transform $\hat{H}_j$ $(j = \{1, 2\})$ and write them in the Bloch form as,

$$H_j = \sum_k \begin{pmatrix} \hat{a}_k^\dagger & \hat{b}_k^\dagger \end{pmatrix} h_j(k) \begin{pmatrix} \hat{a}_k \\ \hat{b}_k \end{pmatrix}, \tag{3.3}$$

where,

$$h_1(k) = \begin{pmatrix} 0 & (t_1 - \delta_1) + (t_2 + \delta_2)e^{-ik} \\ (t_1 + \delta_1) + (t_2 - \delta_2)e^{ik} & 0 \end{pmatrix}, \tag{3.4}$$

and,

$$h_2(k) = \begin{pmatrix} iu & t_1 + t_2 e^{-ik} \\ t_1 + t_2 e^{ik} & -iu \end{pmatrix}. \tag{3.5}$$

Both Eqs. (3.4) and (3.5) can be expressed in the form of the standard Dirac Hamiltonian as $H_j = \vec{d_j} \cdot \sigma$, where $\vec{d_j}$ denotes vectors in the complex plane, and σ denotes the Pauli matrices. Further, the components of the $\vec{d_j}$ are written as,

$$\begin{aligned} d_1^{\mathrm{R}} &\equiv (d_{1x}^{\mathrm{R}},\ d_{1y}^{\mathrm{R}},\ d_{1z}^{\mathrm{R}}) = (t_1 + t_2 \cos k,\ t_2 \sin k,\ 0); \\ d_1^{\mathrm{I}} &\equiv (d_{1x}^{\mathrm{I}},\ d_{1y}^{\mathrm{I}},\ d_{1z}^{\mathrm{I}}) = (-\delta_2 \sin k,\ -\delta_1 + \delta_2 \cos k,\ 0), \end{aligned} \tag{3.6}$$

and

$$\begin{aligned} d_2^{\mathrm{R}} &\equiv (d_{2x}^{\mathrm{R}},\ d_{2y}^{\mathrm{R}},\ d_{2z}^{\mathrm{R}}) = (t_1 + t_2 \cos k,\ t_2 \sin k,\ 0); \\ d_2^{\mathrm{I}} &\equiv (d_{2x}^{\mathrm{I}},\ d_{2y}^{\mathrm{I}},\ d_{2z}^{\mathrm{I}}) = (0,\ 0,\ u), \end{aligned} \tag{3.7}$$

where, d_j^{R}, d_j^{I} $(j = \{1, 2\})$ represent the real and the imaginary parts of $\vec{d_j}$ respectively. The eigenvalues of these Hamiltonians are given by,

$$E_j = \pm |\vec{d_j}|. \tag{3.8}$$

Let us examine the symmetries of the Hamiltonians, h_j. $h_1(k)$ clearly has the CS,

$$\sigma_z\ h_1(k)\ \sigma_z = -h_1(k), \tag{3.9}$$

as the CS operator, Γ, is σ_z for this system [197]. However, it does not possess the $\mathcal{PT}$ symmetry, that is,

$$\sigma_x\ h_1^*(k)\ \sigma_x \neq h_1(k), \tag{3.10}$$

as the $\mathcal{PT}$ operator is given via $\sigma_x K$, with K being the complex conjugation operator [17]. While the opposite happens for $h_2(k)$, that is, $\mathcal{PT}$ symmetry exists,

$$\sigma_x\ h_2^*(k)\ \sigma_x = h_2(k), \tag{3.11}$$

however, CS is lost,

$$\sigma_z \; h_2(k) \; \sigma_z \neq -h_2(k). \tag{3.12}$$

To make the preceding discussion more structured, in the following section, we separate the discussion of our results into those for the case with absent $\mathcal{PT}$ symmetry and those for the case with $\mathcal{PT}$ symmetry. While doing so, we have considered two cases corresponding to the topological and trivial phases of the Hermitian SSH model, namely $t_1 < t_2$ and $t_1 > t_2$, respectively, to compare the results obtained from the NH settings to those with the Hermitian model. Specifically, we consider $t_1 = 1$, and fix t_2 at 2 and 0.5 throughout the chapter to maintain the consistency.

3.2 $n\mathcal{PT}$ SSH Model

Since the NH Hamiltonians for both cases can be written in terms of $\vec{d_j} \cdot \sigma$ ($j = \{1, 2\}$), it may be instinctive to obtain a detailed structure of $\vec{d_j}$, which inevitably acquires a complex form, which we elucidate below. In the $n\mathcal{PT}$ case, the components of the $\vec{d_1}$ can be expressed via a complex angle ϕ, which is defined by,

$$\tan\phi = \frac{d_{1y}}{d_{1x}} = \frac{d_{1y}^{\mathrm{R}} + i d_{1y}^{\mathrm{I}}}{d_{1x}^{\mathrm{R}} + i d_{1x}^{\mathrm{I}}}, \tag{3.13}$$

with $d_{1x}^{\mathrm{R}} = \mathrm{Re}(d_{1x})$, $d_{1x}^{\mathrm{I}} = \mathrm{Im}(d_{1x})$, $d_{1y}^{\mathrm{R}} = \mathrm{Re}(d_{1y})$ and $d_{1y}^{\mathrm{I}} = \mathrm{Im}(d_{1y})$. ϕ can be termed as an angle between the components (d_{1x}, d_{1y}), and can be expressed as,

$$\phi = \phi_{\mathrm{R}} + i\phi_{\mathrm{I}}, \tag{3.14}$$

where ϕ_{R} and ϕ_{I} denote the real and the imaginary parts of ϕ. These components can further be expressed in terms of the components of $\vec{d_1}$ [198],

$$e^{2i\phi_{\mathrm{R}}} = \left(\frac{d_{1+}}{d_{1-}}\right) \Bigg/ \left|\frac{d_{1+}}{d_{1-}}\right|, \quad \text{and} \quad e^{-2\phi_{\mathrm{I}}} = \left|\frac{d_{1+}}{d_{1-}}\right|, \tag{3.15}$$

which, in turn, can be simplified into,

$$\tan 2\phi_{\mathrm{R}} = \mathrm{Im}\left(\frac{d_{1+}}{d_{1-}}\right) \Bigg/ \mathrm{Re}\left(\frac{d_{1+}}{d_{1-}}\right). \tag{3.16}$$

Here, $d_{1\pm}$ are defined by,

$$d_{1+} = d_{1x}^{\mathrm{R}} - d_{1y}^{\mathrm{I}} + i(d_{1y}^{\mathrm{R}} + d_{1x}^{\mathrm{I}}); \quad d_{1-} = d_{1x}^{\mathrm{R}} + d_{1y}^{\mathrm{I}} - i(d_{1y}^{\mathrm{R}} - d_{1x}^{\mathrm{I}}). \tag{3.17}$$

Let us now focus on finding the EPs of this system. The eigenvalues given by Eq. (3.8) will coalesce when $E_{1\pm} = 0$, that is, when the following condition is satisfied,

$$(d_{1x}^{\mathrm{R}} + id_{1x}^{\mathrm{R}})^2 + (d_{1y}^{\mathrm{R}} + id_{1y}^{\mathrm{I}})^2 = 0. \tag{3.18}$$

From the above equation, it is evident that the real part of the energy, E_1, will be zero when

$$d_{1x}^{\mathrm{R}} = \pm d_{1y}^{\mathrm{I}} \qquad \text{and} \qquad d_{1y}^{\mathrm{R}} = \mp d_{1x}^{\mathrm{I}}, \tag{3.19}$$

and the imaginary part becomes zero when the hopping amplitudes satisfy,

$$\frac{t_1}{t_2} = -\frac{\delta_1}{\delta_2}. \tag{3.20}$$

Following Eq. (1.1) of Chapter 1, the right eigenvector of the Hamiltonian, $h_1(k)$, is given by,

$$\left|\Psi_{1\pm}^{\mathrm{RE}}\right\rangle = \sqrt{\frac{M_1}{M_1+M_2}}\, e^{i\xi} \begin{pmatrix} \pm\sqrt{\frac{M_1}{M_2}}\, e^{-i(\alpha_1+\alpha_2)/2} \\ 1 \end{pmatrix} \tag{3.21}$$

with $e^{i\xi}$ being a phase factor. Further,

$$M_1 = \left|(t_1-\delta_1) + (t_2+\delta_2)e^{ik}\right|, \quad M_2 = \left|(t_1+\delta_1) + (t_2-\delta_2)e^{-ik}\right|, \quad \text{and}$$
$$\alpha_1 = \tan^{-1}\left[\frac{(t_2+\delta_2)\sin k}{(t_1-\delta_1)+(t_2+\delta_2)\cos k}\right], \quad \alpha_2 = \tan^{-1}\left[\frac{(t_2-\delta_2)\sin k}{(t_1+\delta_1)+(t_2-\delta_2)\cos k}\right].$$

Now the coalescence of the eigenvectors at the EPs demands that M_1 has to vanish. This is equivalent to the condition,

$$|\delta_1 - \delta_2| = t_1 + t_2 \quad \text{and} \quad |\delta_1 + \delta_2| = |t_1 - t_2|, \tag{3.22}$$

at $k = \pm\pi$ and $k = 0$ respectively. Hence, the location of the EPs is given by Eq. (3.19) along with the criteria laid down in Eq. (3.22).

Let us turn towards the discussion on the spectral properties of the system. For the time being, we shall proceed with the BZ theory, that is, we employ the momentum space Hamiltonian, $h_1(k)$ (Eq. (3.4)). Diagonalizing $h_1(k)$, we get the expression for the energy, $E_1(k)$, in terms of Bloch momenta k,

$$E_{1\pm}(k) = \pm\sqrt{t_1^2 + t_2^2 - \delta_1^2 - \delta_2^2 + 2(t_1t_2 + \delta_1\delta_2)\cos k - 2i(t_1\delta_2 + t_2\delta_1)\sin k}. \tag{3.23}$$

Since the model possesses chiral symmetry, that is, the Hamiltonian in Eq. (3.1) satisfies Eq. (3.9), each eigenvalue E is always accompanied by a chiral partner $-E$. The PBC spectra for the parameter set $t_2 = 2$, $\delta_1 = 0.3$, $\delta_2 = 0.2$ are shown in Fig. 3.2(a); the motivation for choosing these values will be clarified shortly. The PBC spectrum is

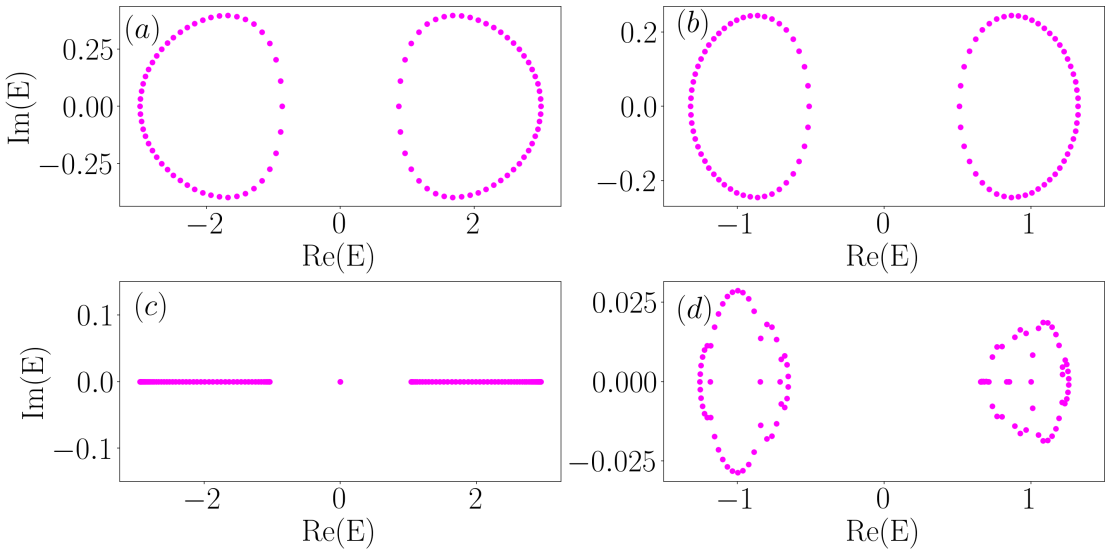

FIGURE 3.2: The upper and the lower panels represent $\mathrm{Re}(E_1)$ vs $\mathrm{Im}(E_1)$ plots for the PBC and the OBC spectra, respectively. The parameters are, for (a) & (c) $t_2 = 2$, $\delta_1 = 0.3$, $\delta_2 = 0.2$, and for (b) & (d) $t_2 = 0.5$, $\delta_1 = -0.3$, $\delta_2 = 0.4$.

composed of two well-separated bounded regions, each corresponding to a *non-trivial point-gap* topology, thereby signaling the presence of the NHSE [45] in the system. In contrast, the OBC spectrum for the same parameters, displayed in Fig. 3.2(c), consists entirely of real eigenvalues and features a pair of zero-energy modes ($\mathrm{Re}(E_1) = 0$). This behavior indicates that, for this specific parameter choice, the Hamiltonian $\hat{H}_1$ can be mapped to an effective Hermitian Hamiltonian, analogous to the situation encountered for the real-space Hatano–Nelson Hamiltonian (see Eq. (1.15)), previously discussed in Section 1.5 of Chapter 1.

A qualitatively different situation arises for the parameter set $t_2 = 0.5$, $\delta_1 = -0.3$, $\delta_2 = 0.4$. In this case, the OBC spectrum shown in Fig. 3.2(d) becomes complex, whereas the corresponding PBC spectrum in Fig. 3.2(b) remains largely similar to that in Fig. 3.2(a). Notably, the pair of zero-energy modes present in Fig. 3.2(c) is absent in Fig. 3.2(d), highlighting a clear distinction between these two regimes. The probability distribution of the wavefunctions, exhibiting NHSE, is depicted in Fig. 3.3. Fig. 3.3(a) shows that nearly all the eigenstates for both cases are localized at the edges of the system, with the zero energy modes present for the choice of parameters as in Fig. 3.2(a). However, these are absent in Fig. 3.3(b), bearing signatures of trivial phases, where the parameters are kept the same as in Fig. 3.2(b).

3.2.1 Non-Bloch Band Theory for the $n\mathcal{PT}$ SSH Model

Let us now discuss the topology of the BBC-broken $n\mathcal{PT}$ system with the help of the non-Bloch theory [134], as reviewed earlier in Section 1.5.2 of Chapter 1, which helps

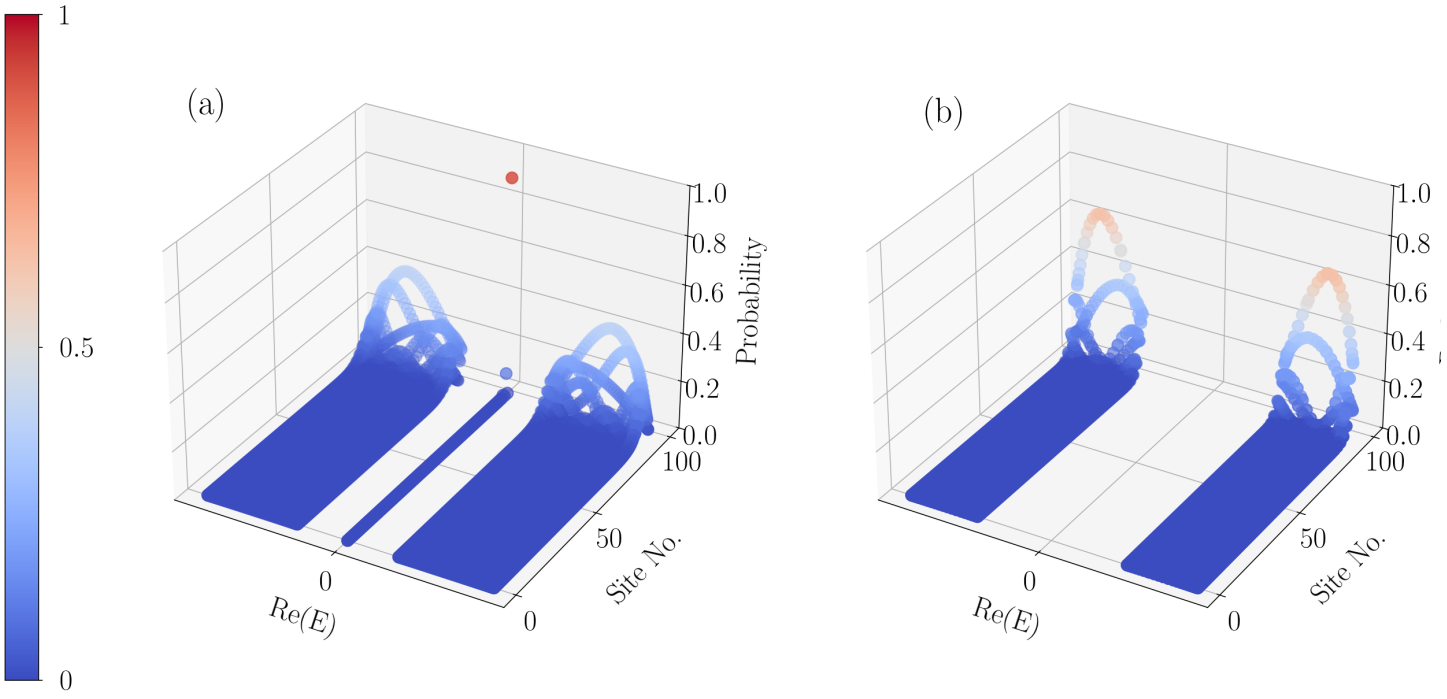

FIGURE 3.3: Occurrence of NHSE in the $n\mathcal{PT}$ SSH model is shown. The parameters are, (a) $t_2 = 2,\ \delta_1 = 0.3,\ \delta_2 = 0.2$, (b) $t_2 = 0.5,\ \delta_1 = -0.3,\ \delta_2 = 0.4$.

correctly enumerate the topological phases and their invariants. The following discussion on obtaining the topological phases (and invariant) should be made with caution, since the Bloch momentum, k, no longer remains real as a result of the breakdown of the BBC, and hence the notion of a standard BZ in principle does not exist. To this end, we replace the Bloch factor by $\beta = e^{ik}$. For Hermitian systems, the GBZ reduces to the conventional BZ, where C_β forms a unit circle in the complex plane, since $|\beta| = |e^{ik}| = 1$. In contrast, for NH systems, this condition is generally violated. Following the procedure outlined in Ref. [134], we therefore rewrite Eq. (3.4) explicitly in terms of the complex parameter β. Thus, we get,

$$h_1(\beta) = R_+(\beta)\sigma_+ + R_-(\beta)\sigma_-, \tag{3.24}$$

where,

$$R_+(\beta) = (t_2 + \delta_2)\beta^{-1} + (t_1 - \delta_1), \quad R_-(\beta) = (t_1 + \delta_1) + (t_2 - \delta_2)\beta, \tag{3.25}$$

with $\sigma_\pm = \frac{\sigma_x \pm i\sigma_y}{2}$. To some extent, $R_+(\beta)$ and $R_-(\beta)$ corresponds to d_{1+} and d_{1-} in Eq. (3.17) in the GBZ setting. The first step toward constructing the GBZ, denoted by C_β, is to solve the characteristic equation of the $n\mathcal{PT}$ SSH model,

$$\det[h_1(\beta) - E] = 0, \tag{3.26}$$

together with the constraint specified in Eq. (1.23) of Chapter 1. Consequently, the characteristic equation, in terms of $R_+(\beta)$ and $R_-(\beta)$, becomes,

$$R_+(\beta)\, R_-(\beta) = E^2. \tag{3.27}$$

This is a quadratic equation in terms of β, and hence only has two solutions for β, which are given by,

$$\beta_{1,2} = \frac{-(t_1^2+t_2^2-\delta_1^2-\delta_2^2-E^2) \pm \sqrt{(t_1^2+t_2^2-\delta_1^2-\delta_2^2-E^2)^2 - 4(t_1-\delta_1)(t_2-\delta_2)(t_1+\delta_1)(t_2+\delta_2)}}{2(t_1-\delta_1)(t_2-\delta_2)}. \tag{3.28}$$

Now, imposing the condition, $|\beta_1| = |\beta_2|$, to get the continuum bands [134], we get the following condition,

$$(t_1^2+t_2^2-\delta_1^2-\delta_2^2-E^2)^2 - 4(t_1-\delta_1)(t_2-\delta_2)(t_1+\delta_1)(t_2+\delta_2) = 0. \tag{3.29}$$

Solving the above equation for E^2, we get,

$$E^2 = \left(\sqrt{t_1^2-\delta_1^2} \pm \sqrt{t_2^2-\delta_2^2}\right)^2. \tag{3.30}$$

Putting the above expression for E^2 in Eq. (3.28) along with the condition in Eq. (3.29), we get the branch point values of βs in the locus of the GBZ curve, C_β,

$$\beta = \pm\sqrt{\left(\frac{t_1+\delta_1}{t_1-\delta_1}\right)\left(\frac{t_2+\delta_2}{t_2-\delta_2}\right)}. \tag{3.31}$$

We next determine the remaining values of β in the form $|\beta|e^{ik}$, with $k \in [-\pi, \pi]$, and plot them in Figs. 3.4(a) and 3.4(b), corresponding to the two parameter sets used in Figs. 3.3(a) and 3.3(b), respectively. Note that when $|\beta| = 1$, that is, $(t_1+\delta_1)(t_2+\delta_2) = (t_1-\delta_1)(t_2-\delta_2)$, the system reduces to a Hermitian Hamiltonian. It is worth emphasizing that, for the $n\mathcal{PT}$ SSH model, the modulus $|\beta|$ is constant and does not explicitly depend on the energy E. In more general NH systems, however, β typically takes the form $\beta = \rho(E)e^{ik}$, where the factor $\rho(E)$ depends on the energy. In such cases, $\rho(E)$ must be determined for each value of k by solving the characteristic equation $\det[\mathcal{H}(\beta) - E] = 0$ (Eq. (1.22) of Chapter 1), together with the condition for forming continuum bands, namely $|\beta_M| = |\beta_{M+1}|$ (Eq. (1.23) of Chapter 1). Substituting $|\beta|$ from Eq. (3.31) in Eq. (3.25), $R_\pm(\beta)$ can be expressed as,

$$\begin{aligned} R_+(\beta) &= \frac{\sqrt{(t_1^2-\delta_1^2)\,(t_2^2-\delta_2^2)}}{(t_1+\delta_1)}\, e^{ik} + (t_1-\delta_1), \\ R_-(\beta) &= \frac{\sqrt{(t_1^2-\delta_1^2)\,(t_2^2-\delta_2^2)}}{(t_1-\delta_1)}\, e^{ik} + (t_1+\delta_1). \end{aligned} \tag{3.32}$$

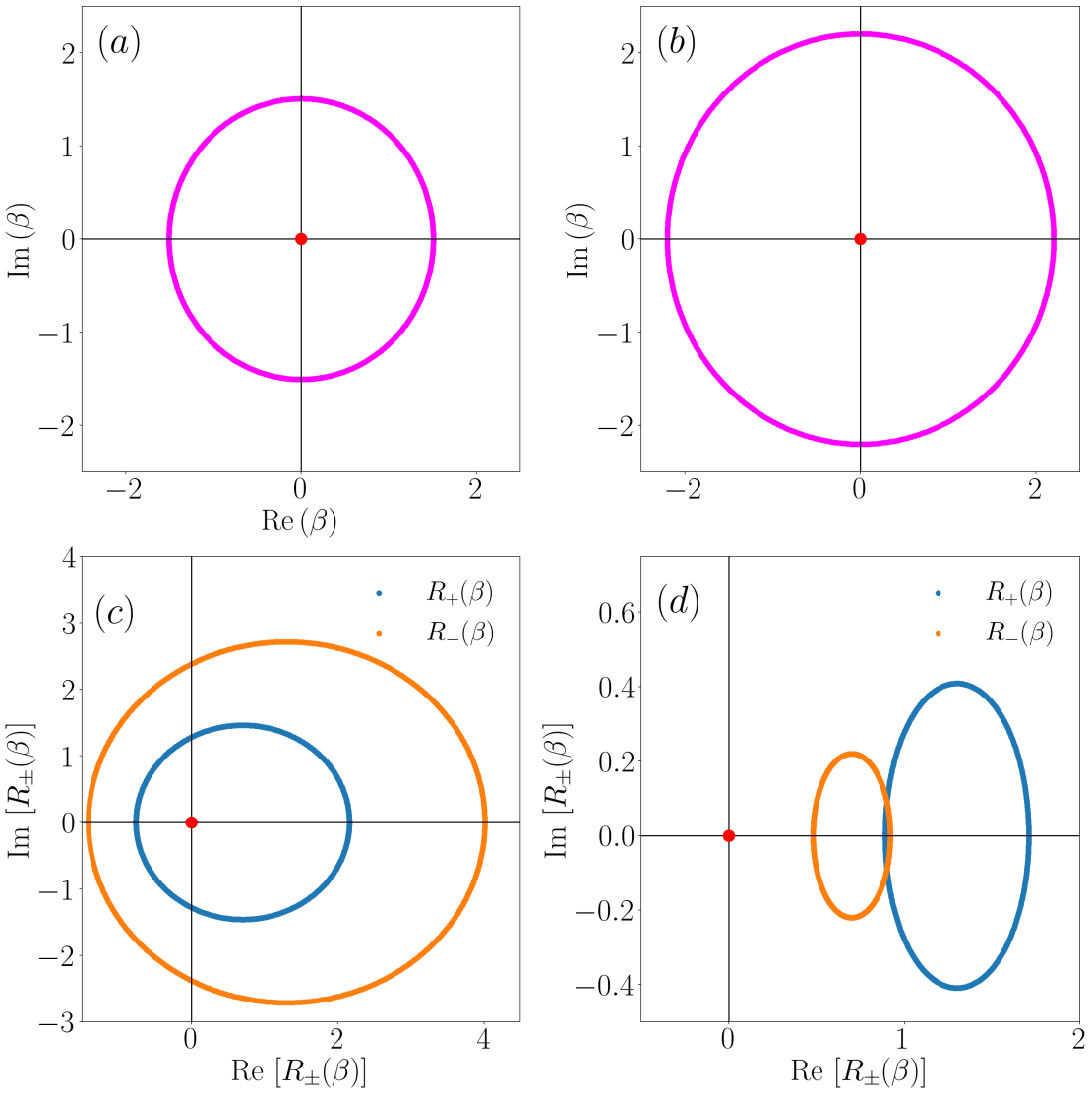

FIGURE 3.4: The GBZ, denoted by C_β, in the complex plane, corresponding to cases (a) $t_2 = 2,\ \delta_1 = 0.3,\ \delta_2 = 0.2$, and (b) $t_2 = 0.5,\ \delta_1 = -0.3,\ \delta_2 = 0.4$. It may be noted that the radii are greater than unity, as opposed to the Hermitian case, where it is always 1. (c) & (d) winding of $R_+(\beta)$ and $R_-(\beta)$ in the complex plane corresponding to the GBZ in (a) & (b), respectively. The red dot in each case denotes the origin.

These equations represent that $R_+(\beta)$ and $R_-(\beta)$ traces a circle with radius $\frac{\sqrt{(t_1^2-\delta_1^2)(t_2^2-\delta_2^2)}}{(t_1+\delta_1)}$ and $\frac{\sqrt{(t_1^2-\delta_1^2)(t_2^2-\delta_2^2)}}{(t_1-\delta_1)}$ with centers at $[(t_1-\delta_1),\ 0]$ and $[(t_1+\delta_1),\ 0]$, respectively, in the complex plane. Thus the circle traced out by $R_+(\beta)$ or $R_-(\beta)$, shown in Figs. 3.4(c) and 3.4(d), contains the origin (marked by the red dot), only when $\sqrt{t_1^2-\delta_1^2} \leq \sqrt{t_2^2-\delta_2^2}$.

Following the expression for the winding number, w, given in Ref. [134], defined for the BBC-broken systems,

$$w = -\frac{(w_+ - w_-)}{2}, \quad \text{where} \quad w_\pm = \frac{1}{2\pi}[\arg\, R_\pm(\beta)]_{C_\beta}, \tag{3.33}$$

we compute the winding number, w, for our system. In the above equation, $w = 1$, or equivalently $w_{\pm} = \mp 1$, and that is only possible when the curves traced by $R_+(\beta)$ or $R_-(\beta)$ contain the origin. Fig. 3.4(c) illustrates the winding of $R_+(\beta)$ (blue curve) and $R_-(\beta)$ (orange curve) for the parameter set used in Fig. 3.3(a). Both the trajectories encircle the origin, yielding $w_{\pm} = \mp 1$ and hence a total winding number $w = 1$ for the choice $t_2 = 2$, $\delta_1 = 0.3$, $\delta_2 = 0.2$ $\left(\sqrt{t_1^2 - \delta_1^2} \leq \sqrt{t_2^2 - \delta_2^2}\right)$. The same parameters were employed in Figs. 3.2(c) and 3.3(a), to show the appearance of topological zero-energy edge modes in the spectral plot and the probability density of the system, respectively. By contrast, for $\sqrt{t_1^2 - \delta_1^2} \geq \sqrt{t_2^2 - \delta_2^2}$, the trajectories of $R_+(\beta)$ (blue) and $R_-(\beta)$ (orange) do not enclose the origin, as shown in Fig. 3.4(d). Consequently, w vanishes, and no topological zero-energy edge modes appear in Figs. 3.2(d) and 3.3(b), indicating that the system is topologically trivial in this regime. Thus, the condition to get a topological phase transition, is,

$$\sqrt{t_1^2 - \delta_1^2} = \sqrt{t_2^2 - \delta_2^2}; \qquad t_1 \neq \delta_1. \tag{3.34}$$

Therefore, although the conventional BBC breaks down in the $n\mathcal{PT}$ case, the topological characterization of the model is recovered within the non-Bloch framework, specifically through the generalized definition of the winding number for NH systems given by Eq. (3.33).

3.2.2 TEC Construction of the $n\mathcal{PT}$ SSH Model

Having explored the TB model and its associated symmetries, let us now shift our focus to constructing a corresponding electric circuit. The procedure involves substituting the atoms in a unit cell of the TB model with nodes or junctions in the TEC, as shown in the formalism and examples of the previous chapter. Writing KVL, KCL, and VCR (illustrated in the previous chapter) for any random node, i, we shall have the following relation,

$$\mathcal{L}_{ij} = X_{ij} + \delta_{ij} W_i, \quad \text{where} \quad W_i = \sum_j X_{ij} + X_i, \quad \text{and} \quad i = 1, 2, 3, \ldots 2L_0, \tag{3.35}$$

where X_{ij} is the conductance between two distinct nodes i and j, and L_0 is number of total unit cells of the TEC. V_i and I_i denote the voltage and the current flowing into node i from the source placed elsewhere. Note that the term X_{ii} bears no meaning and can be set to zero, whereas X_i is the resultant conductance between node i and the ground. The TEC corresponding to the Hermitian SSH model and its Laplacian was previously introduced in Section 2.4 of the previous chapter. In that circuit, the intra- and inter-cell hopping amplitudes, t_1 and t_2, are implemented using capacitors C_1 and C_2, respectively, which are kept the same for this TEC also, as illustrated in Fig. 3.5(a). Additionally, the non-reciprocal components of the hoppings, denoted by δ_1 and δ_2 for

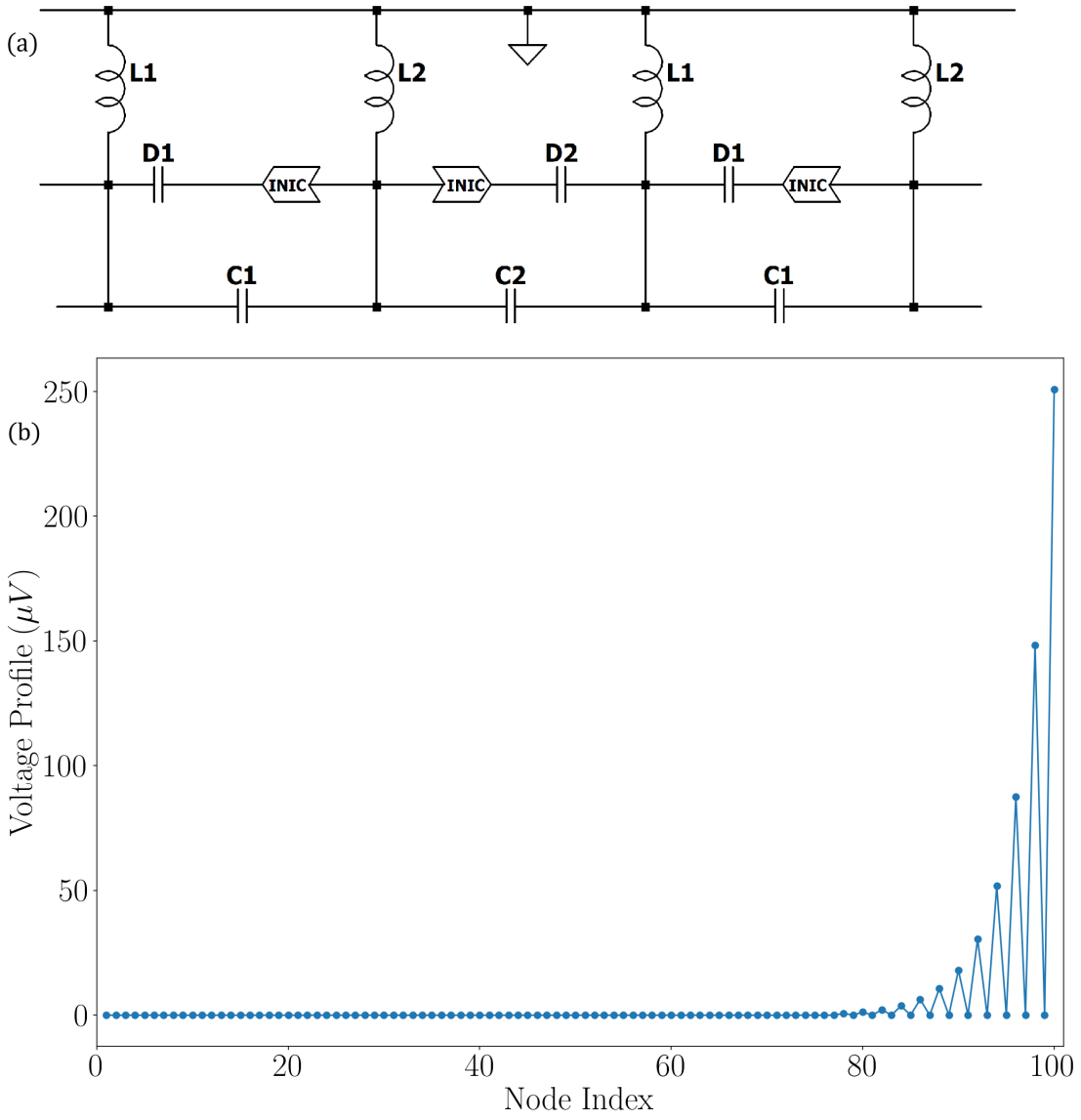

FIGURE 3.5: (a) TEC design for the $n\mathcal{PT}$ SSH model. (b) The VP of the TEC is plotted at the node indices, which shows a voltage localization at the right edge. The output is a direct visualization of Fig. 3.3(a). The number of nodes considered here is 100.

the TB model (Eq. (3.1)), are realized through the capacitors $D1$ and $D2$, along with INICs (see Fig. 2.1(b) of the previous chapter), connected in series with them. The circuit parameters are chosen as $C_1 = 1\,\mu$F, $C_2 = 2\,\mu$F, $D1 = 0.3\,\mu$F, and $D2 = 0.2\,\mu$F to maintain the consistency with the values of the parameters (t_1, t_2, δ_1, and δ_2) used in the TB model. L_1 and L_2 are the grounded inductors, kept for tuning the diagonal elements of the Laplacian of the TEC [3]. The TEC is operated at a driving frequency of $f = 1/(2\pi)$ MHz. We hence probe the VP of the TEC by exciting it with a current, $I = 1\,\mu$A, at a random node. For voltage measurements, one terminal of the measuring instrument (e.g., a multimeter) is kept fixed, while the voltage at each node is recorded by varying the other terminal. The resulting VP, shown in Fig. 3.5(b), reveals voltage

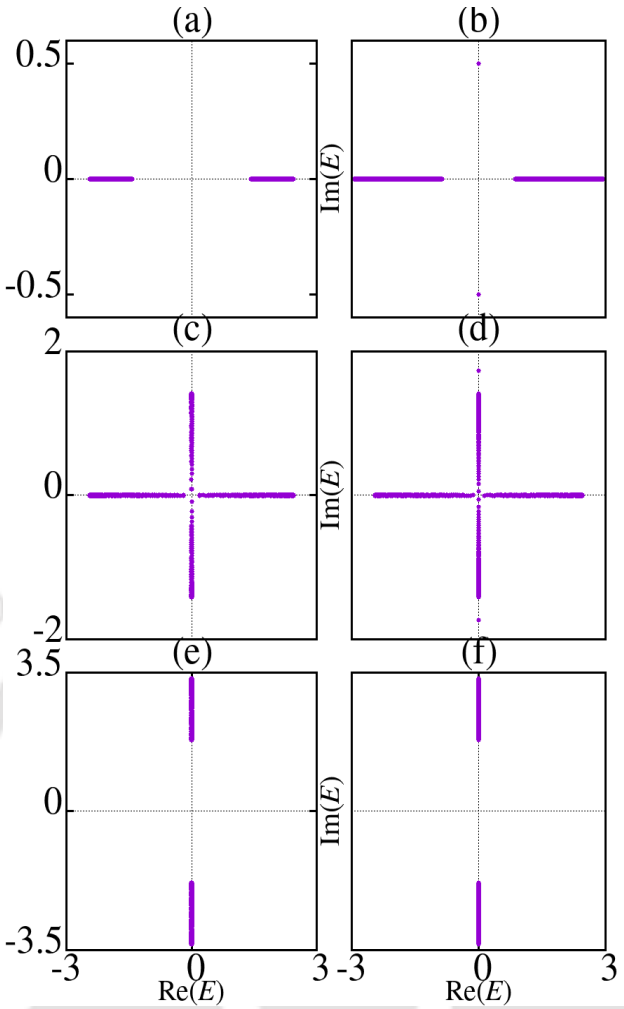

FIGURE 3.6: Re(E) vs Im(E) with PBC (left column) and OBC (right column) for three cases: (a) and (b) correspond to $u = 0.5$, (c) and (d) correspond to $u = 2$, (e) and (f) correspond to $u = 3.5$, keeping $t_2 = 2$.

accumulation at the right boundary of the circuit, thereby confirming the right-edge localization characteristic of the NHSE depicted in Fig. 3.3.

3.3 $s\mathcal{PT}$ SSH Model

In this section, we shall explore an alternate route for rendering non-hermiticity to our dimerized Hamiltonian, which is achieved via the inclusion of an imaginary potential, u. The Bloch Hamiltonian is given by $h_2(k)$ in Eq. (3.5), and its eigenvalues by,

$$E_{2\pm} = \pm\sqrt{|t_1 + t_2 e^{-ik}|^2 - u^2}, \tag{3.36}$$

using Eq. (3.8). Using the above expression, we plot energy spectra in the complex plane for both the PBC and the OBC corresponding to $t_1 < t_2$ in Fig. 3.6. Due to $\mathcal{PT}$ symmetry (obeys Eq. (3.11)), the energy eigenvalues always occur in complex conjugate

pairs, that is, there must be an E^* for every E. For $t_1 < t_2$ with OBC (right column of Fig. 3.6, two edge modes exist with $E = \pm iu$ for all values of u, a scenario that is absent for $t_1 > t_2$ (not shown here). The energy eigenvalues remain purely real (except the points $E = \pm iu$ in Fig. 3.6(b)) until the parameter u satisfies $u = |t_1 - t_2|$, as shown in Figs. 3.6(a) and 3.6(b). Beyond that, the number of purely imaginary eigenvalues increases with u, until $u = t_1 + t_2$ (Figs. 3.6(c) and 3.6(d)). Finally, all the energies become purely imaginary for larger values of u, as demonstrated via Figs. 3.6(e) and 3.6(f). So, $u = |t_1 - t_2|$ can be thought of as the transition point between the $\mathcal{PT}$-broken and the unbroken regions, prior to which the $\mathcal{PT}$ symmetry is unbroken, while beyond $u = |t_1 - t_2|$, it is broken (Table 3.1). Furthermore, the PBC spectra do not exhibit

Range of u	**$\mathcal{PT}$ symmetry**	**Eigenvalue nature**
$0 \leq u < \lvert t_1 - t_2 \rvert$	$\mathcal{PT}$-unbroken	Purely real
$\lvert t_1 - t_2 \rvert < u < t_1 + t_2$	$\mathcal{PT}$-breaking phase	Complex
$u > t_1 + t_2$	$\mathcal{PT}$-broken	Purely imaginary

TABLE 3.1: The $\mathcal{PT}$-broken and the unbroken regions of the $s\mathcal{PT}$ SSH model are shown as a function of the imaginary potential, u. The phase transition between the $\mathcal{PT}$-unbroken phase with purely real eigenvalues and $\mathcal{PT}$-breaking phase with complex eigenvalues happens at $u = |t_1 - t_2|$. Similarly, the phase transition between the $\mathcal{PT}$-breaking phase with complex eigenvalues and $\mathcal{PT}$-broken phase purely imaginary eigenvalues happens at $u = t_1 + t_2$.

any non-trivial winding in the complex energy plane, implying the absence of point-gap topology (and hence the absence of NHSE within the system).

Let us now examine the topological aspects of the system. The right eigenvectors of $h_2(k)$ are given by,

$$\left|\Psi_{2+}^{RE}\right\rangle = \begin{pmatrix} e^{-i\phi_k}\cos\theta_k \\ \sin\theta_k \end{pmatrix} \quad \text{and} \quad \left|\Psi_{2-}^{RE}\right\rangle = \begin{pmatrix} -e^{-i\phi_k}\sin\theta_k \\ \cos\theta_k \end{pmatrix}, \tag{3.37}$$

where, $\phi_k = i\ln\left|\frac{t_1+t_2e^{-ik}}{|t_1+t_2e^{-ik}|}\right|$ and $\theta_k = \tan^{-1}\left(\sqrt{\frac{E_+-iu}{E_++iu}}\right)$. As the BBC of the system is preserved, the topological invariant for the $s\mathcal{PT}$ SSH model is considered as the winding number for the Hermitian systems. The winding number, ν, is represented by [33],

$$\nu = \frac{1}{2\pi}\oint_C \partial_k\phi(k)\, dk, \tag{3.38}$$

where $\phi(k)$ is the argument of $\vec{d_2}$, that is $\phi(k) = \tan^{-1}(d_{2y}/d_{2x})$, given via Eqs. (3.7). The contour C denotes the BZ, that is, k goes from $-\pi$ to π. There are no zero energy modes ($|E| = 0$) as long as $u \neq 0$. However, for $t_1 < t_2$, we still get $\nu = 0$ for $t_1 > t_2$, and $\nu = 1$ for $t_1 < t_2$ irrespective of the values of u, which is similar to the Hermitian SSH model. This simply means that the energies of edge modes are now raised to $E = \pm iu$ from zero energy due to the introduction of the imaginary potential, $\pm iu$. Now, let us focus on finding the EPs of this system. The energy eigenvalues coalesce when $E_{2\pm}$

become zero, which leads to,

$$|t_1 + t_2 e^{-ik}|^2 = u^2. \tag{3.39}$$

The coalescence of the eigenvectors also demands Eq. (3.39) to be satisfied, and thus is in contrast with the $n\mathcal{PT}$ case, where the conditions corresponding to the coalescence of the eigenvalues and the eigenvectors are distinct. In terms of components of $\vec{d}_2$ (Eq. (3.7)), Eq. (3.39) can be written as,

$$(d_{2x}^{\mathrm{R}})^2 + (d_{2y}^{\mathrm{R}})^2 = u^2, \tag{3.40}$$

which is the equation of a circle with radius u in a space spanned by $d_{2x}^{\mathrm{R}} - d_{2y}^{\mathrm{R}}$. Consequently, the EPs are arranged on the circumference of a circle of radius u, constituting an exceptional contour [98].

3.3.1 TEC Construction of the $s\mathcal{PT}$ SSH Model

Following the procedure outlined in Section 3.2.2, we construct a TEC corresponding to the $s\mathcal{PT}$ SSH model. A crucial aspect of this construction is the implementation of the staggered imaginary on-site potential $\pm iu$ within the circuit. The negative imaginary potential $(-iu)$ can be readily realized by introducing a resistor R, which serves as a dissipative element, in parallel with the grounded inductor L_1 (Fig. 3.7(a)). In contrast, generating the positive imaginary potential $(+iu)$ requires the use of an INIC connected in series with a resistor R, in parallel with the grounded inductor L_2. While the primary role of the INIC is to introduce non-reciprocal current flow between nodes, its impact on the circuit's Laplacian becomes negligible when one of the connected nodes is grounded, as is the case in our setup. This can be understood as follows. An INIC, placed in series with an impedance, introduces a positive impedance in one direction and a negative impedance of equal magnitude in the opposite direction, thereby breaking reciprocity. When placed in series with an impedance that connects a node to ground, the impedance seen from that particular node becomes negative. However, relative to the ground, the impedance remains positive. Since the Laplacian is constructed by applying KCL at each node (excluding the ground), only the impedance as viewed from the node is relevant. Therefore, despite breaking reciprocity, the use of INICs still allows us to realize negative impedance in an anticipated manner, thereby eliminating non-reciprocal effects. Note that reversing the sign of iu does not alter the results of the corresponding TB model. Likewise, in the TEC implementation, the specific placement of the INIC, whether in series with L_1 or with L_2, does not affect the resulting behavior. To realize topological (non-zero-energy) modes, we choose the circuit parameters as $C_1 = 1\,\mu\mathrm{F}$, $C_2 = 2\,\mu\mathrm{F}$, and $R = 1\,\Omega$, which correspond to $t_1 = 1$, $t_2 = 2$, and $u = 1$ in the TB model. The procedure to obtain the IP of the TEC is the same as demonstrated in Section 3.2.2, that is, the circuit is excited with a current source, $I = 1\,\mu\mathrm{A}$, at a random node, and then keeping

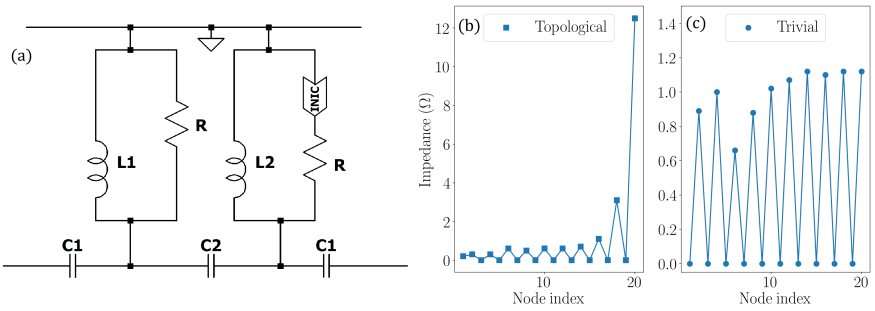

FIGURE 3.7: (a) TEC design for the $s\mathcal{PT}$ SSH model. The IP of the TEC is plotted at the node indices in the (b) topological region and (c) trivial region. The total number of nodes in this case is kept fixed at 20.

one terminal of the measuring instrument (e.g., a multimeter) fixed at the left end of the TEC, the voltage at each node is recorded by varying the other terminal. Fig. 3.7(b) displays the IP of the $s\mathcal{PT}$ SSH circuit, obtained via Eq. (2.11) of the previous chapter. The edge localization of the IP at the right end of the circuit closely reproduces one of the two topological edge modes predicted by the TB model. Note that the other edge mode would be localized at the left end of the circuit, which is not shown here, and would only require fixing one terminal of the measuring instrument at the right end (instead of the left) of the TEC. When the value of C_2 is modified and set to $C_2 = 0.5\,\mu$F, the edge localization in the IP disappears. Instead, the IP exhibits fluctuating behavior characteristic of the trivial regime ($C_1 > C_2$), as shown in Fig. 3.7(c).

3.4 Summary

In this chapter, we have investigated the NH SSH model and examined two cases, namely the $s\mathcal{PT}$ case (modeled by a complex on-site potential) and the $n\mathcal{PT}$ case (modeled by breaking reciprocity in the hopping amplitudes). The topological properties of the $n\mathcal{PT}$ system are obtained via the non-Bloch (GBZ) theory due to the breakdown of the BBC. Consequently, the PBC spectra (corresponding to BZ theory) exhibit a point-gap topology in the complex plane. The conditions for EPs, in a more general sense, have also been provided. For the $s\mathcal{PT}$ case, the eigenvalues are either purely real ($\mathcal{PT}$-unbroken region) or purely imaginary ($\mathcal{PT}$-broken region). This model does not show NHSE; instead, only two non-zero-energy topological edge modes, characterized via the winding number, are observed for $t_1 < t_2$. The scenario is similar to the Hermitian SSH model Also, we observe the emergence of an exceptional contour rather than EPs. The localization phenomena (NHSE for the $n\mathcal{PT}$ case and topological edge modes for the $s\mathcal{PT}$ case) are correctly captured in the corresponding TEC setups.

Chapter 4

Unraveling Skin Effect in a Non-Hermitian Quasi-1D System

Having studied the NH SSH model along with its TEC analogues in the previous chapter, we explore the topological properties of another, and somewhat unconventional system, namely, an NH quasi-1D model, comprising spinless fermions residing at A and B atoms within a unit cell, in this chapter. We introduce non-hermiticity into the Hermitian model in the same way as in the previous chapter, namely, via staggered onsite imaginary potential and non-reciprocal hopping amplitudes. Hence, we classify such NH systems based on their adherence to the $\mathcal{PT}$ symmetry. Furthermore, we observe the existence of BBC [199] within a distinct non-reciprocal model, suggesting that NHSE does not occur in this specific system. To explore the topological properties of the model, we proceed to calculate the topological invariant, which is the complex Berry phase [200], and the inverse participation ratio (IPR) to observe the behavior of the edge modes. Additionally, we identify a different kind of non-reciprocal system that exhibits both the conventional NHSE and the NHSE appearing at both edges. Subsequently, we propose TEC designs for each TB model. This chapter is organized as follows. In section 4.1, we provide a concise introduction to the Hermitian model and its representations in real and momentum space. This is followed by a systematic presentation of the results from the Hermitian model, including analyses of IPR, energy spectra, and the topological invariant, the Berry phase. In section 4.2, we introduce the two $n\mathcal{PT}$ NH models, categorizing them based on the presence and absence of TRS. In section 4.3, we discuss the $s\mathcal{PT}$ NH model, characterized by non-reciprocal

hopping amplitudes. The non-existence of NHSE is carefully scrutinized in this case. The corresponding TEC setups are explored following the discussion of each TB model. In section 4.4, we summarize the results obtained in this chapter.

4.1 Hermitian Model

We begin by discussing a 1D ladder model comprising A and B atoms in a unit cell. The Hamiltonian of the system is given by,

$$H_0 = \sum_{i=1}^{L}\left[\epsilon_A \hat{a}_i^\dagger \hat{a}_i + \epsilon_B \hat{b}_i^\dagger \hat{b}_i\right] - \sum_{i=2}^{L} t_{AB}\hat{a}_i^\dagger \hat{b}_{i-1} + \sum_{i=1}^{L-1}\left[-t_A \hat{a}_i^\dagger \hat{a}_{i+1} + t_B \hat{b}_i^\dagger \hat{b}_{i+1} + t_{AB}\hat{a}_i^\dagger \hat{b}_{i+1}\right] + \text{H.c.}, \tag{4.1}$$

where ϵ_A and ϵ_B are the onsite potentials corresponding to the A and B atoms, $-t_A$ (t_B) and t_{AB} ($-t_{AB}$) being the hopping strengths for $A^{i-1} \leftrightarrow A^i$ ($B^{i-1} \leftrightarrow B^i$) and $A^{i-1} \leftrightarrow B^i$ ($B^{i-1} \leftrightarrow A^i$), respectively (double-headed arrows denote the Hermitian case). A^i and B^i suggest A and B atoms at i^{th} unit cell respectively and L denotes the total number of unit cells. $\hat{a}_i$ ($\hat{a}_i^\dagger$) and $\hat{b}_i$ ($\hat{b}_i^\dagger$) are annihilation (creation) operators for spinless fermions pertaining to the A and B atoms of the i^{th} unit cell respectively. Under PBC, the Hamiltonian in Eq. (4.1) can be written in the following Bloch form in momentum space as,

$$H_0(k) = \sum_k \begin{pmatrix}\hat{a}_k^\dagger & \hat{b}_k^\dagger\end{pmatrix} h_0(k) \begin{pmatrix}\hat{a}_k \\ \hat{b}_k\end{pmatrix}, \tag{4.2}$$

with $h_0(k)$ being the Bloch Hamiltonian which has a form,

$$h_0(k) = \begin{pmatrix}\epsilon_A - t_A e^{-ik} - t_A^* e^{ik} & 2it_{AB}\sin k \\ -2it_{AB}\sin k & \epsilon_B + t_B e^{-ik} + t_B^* e^{ik}\end{pmatrix}. \tag{4.3}$$

Before going to the NH versions of the system described by Eq. (4.1), first, we need to understand the properties of the Hermitian counterpart. For this, we shall study a special case of this Hamiltonian by setting $\epsilon_A = -\epsilon_B = \epsilon$ and $t_A = t_B = t_A^* = t_B^* = t$. With this simplification, the model Hamiltonian in real space can be written as,

$$H_1 = \sum_{i=1}^{L}\left[\epsilon(\hat{a}_i^\dagger \hat{a}_i - \hat{b}_i^\dagger \hat{b}_i)\right] - \sum_{i=2}^{L} t_{AB}\hat{a}_i^\dagger \hat{b}_{i-1} + \sum_{i=1}^{L-1}\left[-t(\hat{a}_i^\dagger \hat{a}_{i+1} - \hat{b}_i^\dagger \hat{b}_{i+1}) + t_{AB}\hat{a}_i^\dagger \hat{b}_{i+1}\right] + \text{H.c.} \tag{4.4}$$

after the Fourier transformation of Eq. (4.4), the Bloch Hamiltonian takes the form,

$$h_1(k) = \begin{pmatrix}\epsilon - 2t\cos k & 2it_{AB}\sin k \\ -2it_{AB}\sin k & -\epsilon + 2t\cos k\end{pmatrix}. \tag{4.5}$$

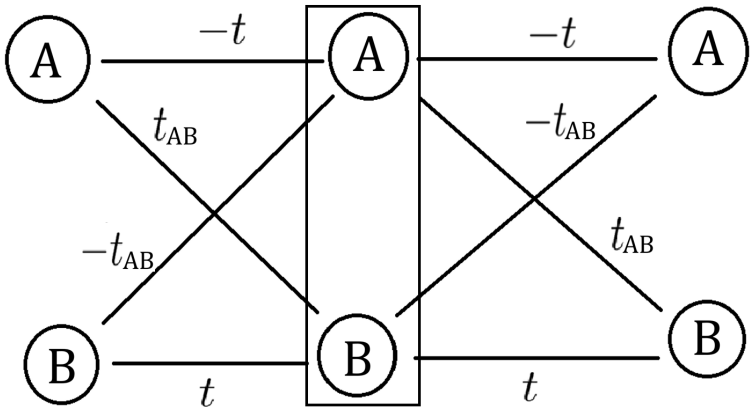

FIGURE 4.1: Pictorial representations of the simplified version (H_1, given by Eq. (4.4)) of the Hermitian quasi-1D system. The rectangular box represents a unit cell.

This implies a staggered potential of strength $\pm\epsilon$ at each of the atoms A and B, hopping amplitudes of $\pm t$ ($A^i \leftrightarrow A^{i+1}$, $B^i \leftrightarrow B^{i+1}$) and $\pm t_{AB}$ ($A^i \leftrightarrow B^{i+1}$ and $A^i \leftrightarrow B^{i-1}$), shown in Fig. 4.1. Let us discuss the symmetries of H_1. The system has TRS [192], as the Bloch Hamiltonian, $h_1(k)$, satisfies the following relation,

$$\mathcal{T}_+ h_1(k) {\mathcal{T}_+}^{-1} = h_1(-k); \quad \text{with} \quad \mathcal{T}_+ \mathcal{T}_+^* = \pm 1, \tag{4.6}$$

where $\mathcal{T}$ ($= U_T \mathcal{K}$, U_T being a unitary matrix) is the TRS operator that is anti-unitary in nature. For systems consisting of spinless fermions, $\mathcal{T}$ is nothing but the complex conjugation operator $\mathcal{K}$ and $\mathcal{T}^2 = 1$. The system also possesses PHS [15], which is written as,

$$\mathcal{C} h(k) \mathcal{C}^{-1} = -h(-k); \quad \text{with} \quad \mathcal{C}^2 = \pm 1. \tag{4.7}$$

The anti-unitary PHS operator $\mathcal{C} = U_C \mathcal{K}$ (U_C is unitary) anti-commutes with the Bloch Hamiltonian $h_1(k)$ with $U_C = \sigma_x$. Thus, the eigenvalues come in pairs, $\pm E$, with corresponding eigenvectors being $|\psi\rangle$ and $\mathcal{C}|\psi\rangle$. The presence of CS [15] is also noted, as the CS operator (Γ) is nothing but $\Gamma = \mathcal{T} \cdot \mathcal{C}$. These characteristics lead us to classify the system within the class BDI in AZ symmetry class [15].

Next, we explore the topological properties and edge-states of this model with OBC and calculate the topological invariants for each PBC model. First, we take the Hermitian model represented by Eq. (4.4) for a 1D chain of length L. In Fig. 4.2(a), we have presented the real-space eigenspectra with the onsite energy ϵ being varied from 0 to $4t$. Here, we have set $t = t_{AB} = 1$ and, in most cases, set the energy scale to a unit of t. The existence of a two-fold degenerate zero energy edge state till $\epsilon = 2t$ and their disappearance beyond that point suggest a topological phase transition at that point. Thus, for $\epsilon < 2t$ ($\epsilon > 2t$), the model is topological (trivial). To ascertain the localization of the zero energy edge states, we use the familiar approach of computing the IPR [201],

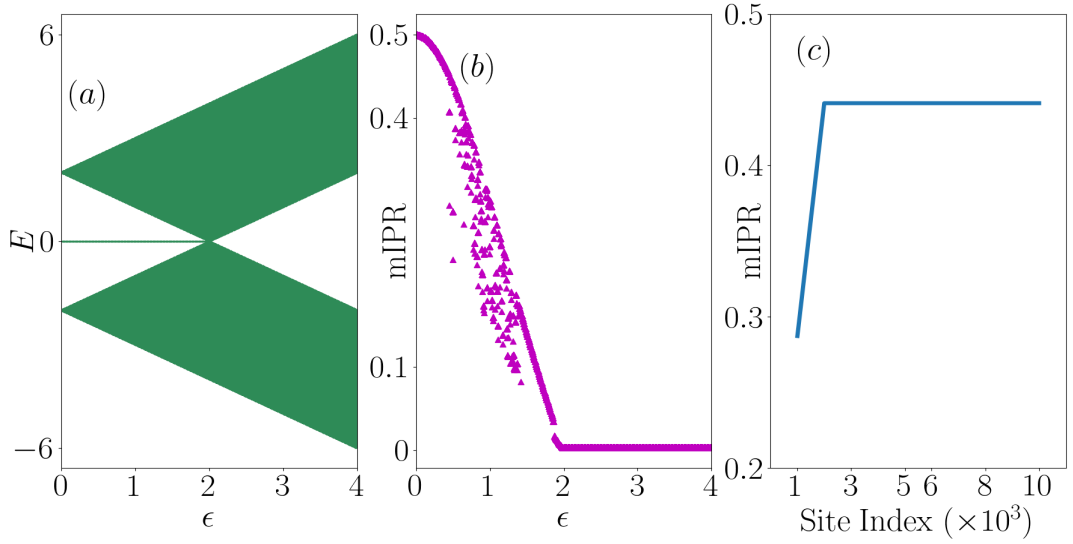

FIGURE 4.2: (a) Eigenvalues of H_1 (Eq. (4.4)) vs ϵ, showing the appearance (disappearance) of the zero energy eigenstates prior to (beyond) $\epsilon = 2t$, (b) mIPR vs ϵ is shown, suggesting that the edge states vanish beyond the point $\epsilon = 2t$, and (c) system size effects on mIPR is shown with $\epsilon = 0.5t$.

defined via,

$$\text{IPR}^{(i)} = \frac{\sum_n |\psi_n^i|^4}{\left(\sum_n |\psi_n^i|^2\right)^2}, \tag{4.8}$$

where $\text{IPR}^{(i)}$ is the IPR of the i^{th} eigenstate and n denotes site index. IPR of a particular state varies inversely with the system size ($\sim L^{-1}$) when it is extended. In contrast, the IPR becomes independent of system size for localized states and approaches 1 (in the thermodynamic limit) when they are completely localized at a given site. Here, the maximum IPR (mIPR) represents the IPR of the topological edge modes. Further, it denotes the highest IPR among all eigenstates in the trivial phase, which lacks topological edge modes. It is plotted as a function of the potential, ϵ, in Fig. 4.2(b). The non-zero values suggest that the edge states exist until $\epsilon = 2t$ and vanish afterwards. As the value of the IPR (or mIPR) is sensitive to the total number of unit cells, we also investigate the system-size effect on mIPR. Fig. 4.2(c) shows the corresponding plot, suggesting that it is independent of the system size beyond a critical system size of $L \sim 1000$. Thus, we have fixed the number of unit cells at 1000 for the numerical analysis of mIPR.

We select the topological invariant as the Berry phase [202] in our case. It is a geometric phase acquired by the eigenstates during an adiabatic cycle in parameter space, such as time, position, or momentum. The definition of the Berry phase is given via

$$\gamma_\pm = i \oint_{BZ} \langle \psi_\pm(k) | \nabla_k | \psi_\pm(k) \rangle \, dk, \tag{4.9}$$

where $|\psi_+(k)\rangle$ ($|\psi_-(k)\rangle$) is the eigenvector corresponding to the upper (lower) band of the Bloch Hamiltonian, and $\pm$ signs label the band index. Generally, the Berry phase

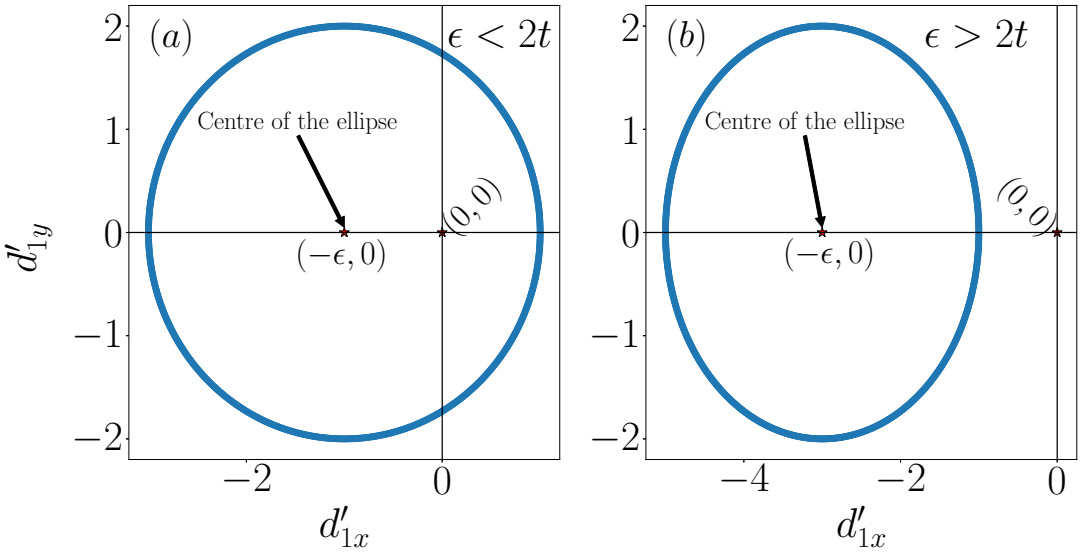

FIGURE 4.3: The locus of $\vec{d'_1}$ (an ellipse) in $d'_{1x} - d'_{1y}$ plane for the two cases, namely, (a) $\epsilon < 2t$, where the origin $(0, 0)$ is inside the closed loop, and (b) $\epsilon > 2t$, where the origin is outside the ellipse. The center of the ellipse is at $(-\epsilon, 0)$.

is an integer (positive or negative) in the unit of π. Let us now discuss the properties of the momentum space Hamiltonian, $h_1(k)$ (Eq. (4.5)). $h_1(k)$ can be written as a Dirac Hamiltonian, $h_1(k) = \vec{d_1} \cdot \sigma$, where $\vec{d_1} \equiv (0, -2t_{AB} \sin k, \epsilon - 2t \cos k)$ and σ denote the Pauli matrices. The presence of the d_{1z} term in $\vec{d_1}$ poses a challenge for computing the Berry phase from Eq. (4.9). Hence, to make d_{1z} zero, we shall perform a unitary transformation on $h_1(k)$. This is achieved via a unitary matrix U, such that,

$$h'_1(k) = U^\dagger h_1(k) U; \quad \text{where,} \quad U = \frac{1}{\sqrt{2}} \begin{pmatrix} 1 & -1 \\ 1 & 1 \end{pmatrix}, \tag{4.10}$$

which yields,

$$h'_1(k) = \begin{pmatrix} 0 & -\epsilon + 2t \cos k \quad +2it_{AB} \sin k \\ -\epsilon + 2t \cos k - 2it_{AB} \sin k & 0 \end{pmatrix}, \tag{4.11}$$

The Dirac form for $h'_1(k)$ is given as, $h'_1(k) = \vec{d'_1} \cdot \sigma$ with $\vec{d'_1} \equiv (-\epsilon + 2t \cos k, -2t_{AB} \sin k, 0)$. The unitary transformation interchanges the x and the z components of $\vec{d_1}$ in addition to rendering a negative sign, that is, $d'_{1x} = -d_{1z}$ and $d'_{1z} = -d_{1x}$. Now that we have $d'_{1z} = 0$, we shall use the eigenvectors of $h'_1(k)$ corresponding to the eigenvalues $E_{1\pm}(k)$, which are given by,

$$|\psi'_{1\pm}(k)\rangle = \pm \frac{1}{\sqrt{2}} e^{\pm i\zeta} \begin{pmatrix} e^{-i\phi_{1k}} \\ 1 \end{pmatrix}, \tag{4.12}$$

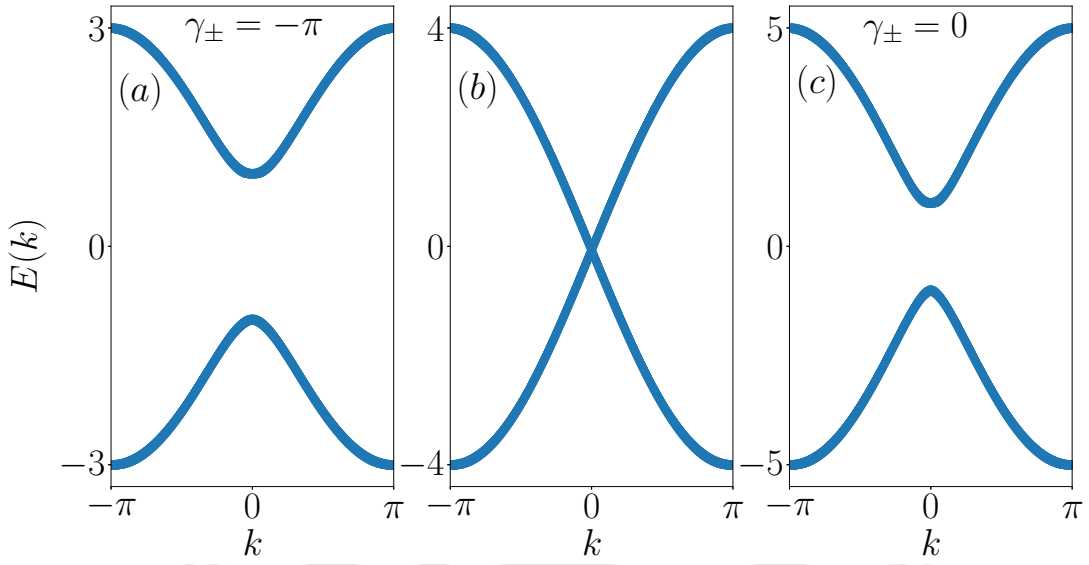

FIGURE 4.4: The energy dispersion corresponding to $h_1(k)$ shown for the three cases, namely, (a) $\epsilon < 2t$ (gapped), (b) $\epsilon = 2t$ (where the spectral gap closes), and (c) $\epsilon > 2t$ (gap reopens) keeping $t = t_{AB} = 1$. (a) and (c) imply the topological and the trivial phases of H_1, whereas (b) shows a gap closing (phase transition) point.

where ζ is independent of k and ϕ_{1k} is given by,

$$\phi_{1k} = \tan^{-1}\left(\frac{-2t_{AB}\sin k}{-\epsilon + 2t\cos k}\right). \tag{4.13}$$

Putting $|\psi'_{1\pm}(k)\rangle$ in Eq. (4.9), we will get the expression of the Berry phase, $\gamma_\pm$, given via,

$$\gamma_\pm = \frac{1}{2}\oint_{BZ}\frac{\partial\phi_{1k}}{\partial k}\,dk = \frac{1}{2}\oint_{BZ}\frac{2t_{AB}(\epsilon\cos k - 2t)}{(-\epsilon + 2t\cos k)^2 + 4t_{AB}^2\sin^2 k}\,dk. \tag{4.14}$$

The Berry phase depends on the values of ϵ and t; however, it is independent of t_{AB}. For $\epsilon < 2t$, the Berry phase acquires the value $-\pi$, and for $\epsilon > 2t$ it vanishes, marking the topologically non-trivial and trivial regimes, respectively. These are reminiscent of the appearance and disappearance of two zero-energy edge states (shown in Fig. 4.2(a)).

The transformed Bloch Hamiltonian $h'_1(k)$ (Eq. (4.11)) falls under the same symmetry class, namely **BDI**, which ensures that it has all the symmetries which the original model (represented by $h_1(k)$) possesses. As shown in Fig. 4.3, in the $d'_{1x} - d'_{1y}$ plane, $\vec{d'_1}$ forms a loop as k goes from $-\pi$ to $+\pi$ in the BZ and includes the origin $(0, 0)$, about which the trajectory of $\vec{d'_1}$ can be seen to look for the topological properties. For the case $\epsilon < 2t$, the EP is enclosed (Fig. 4.3(a)) and excluded (Fig. 4.3(b)) when $\epsilon > 2t$, indicating topologically non-trivial and trivial phases, respectively. The expression for the energy, $E_1(k)$ corresponding to Bloch Hamiltonians $h_1(k)$ or $h'_1(k)$, is given by,

$$E_{1\pm}(k) = \pm\sqrt{(-\epsilon + 2t\cos k)^2 + 4t_{AB}^2\sin^2 k}, \tag{4.15}$$

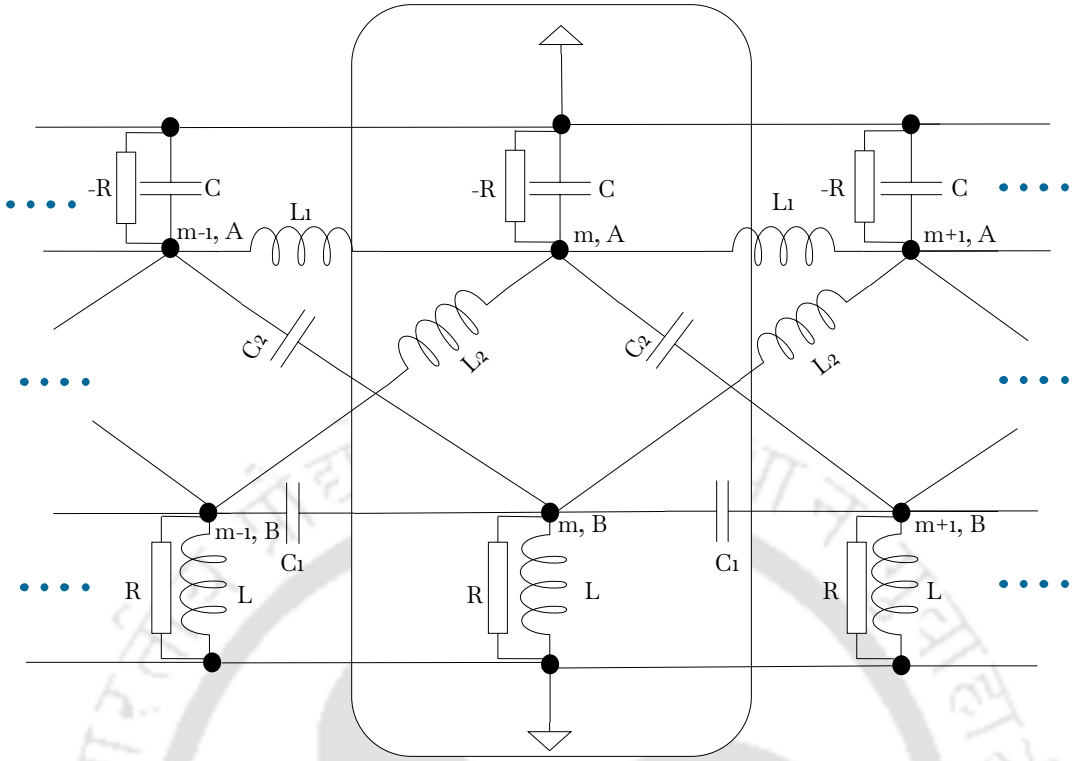

FIGURE 4.5: Circuit diagram for 3 consecutive unit cells corresponding to the Hermitian model in Eq. (4.4). The unit cells and the atomic degrees of freedom are denoted by m and A/B, respectively. The rectangular box represents a particular unit cell. The black dots represent all the connections (or junctions). The expressions (and values) of all the remaining circuit elements are mentioned in the text.

and is plotted in Fig. 4.4. Figs. 4.4(a) and Fig. 4.4(c) show gapped eigenspectra corresponding to the cases $\epsilon < 2t$ and $\epsilon > 2t$, respectively, but with different values of the Berry phase, which are $-\pi$ and 0, respectively. They correspond to the scenario depicted in Fig. 4.3(a) and Fig. 4.3(b), respectively. The spectral gap vanishes at $k = 0$ in Fig. 4.4(b), which corresponds to $\epsilon = 2t$, which is the case when the EP $(0, 0)$ lies on the locus of $\vec{d_1}$.

4.1.1 Circuit Realization of the Hermitian Model

Having explored the TB model and its associated symmetries, let us now shift our focus to constructing a corresponding electric circuit. The procedure involves substituting the atoms in a unit cell of the TB model with nodes or junctions in the TEC, as shown in the formalism and examples of Chapter 2. The relationship between the Hamiltonian characterizing the TB model, delineated by Eq. (4.4), and the Laplacian pertaining to the analogous circuit portrayed in Fig. 4.5, can be elucidated through the following elaboration. The hopping parameters t $(-t)$ and t_{AB} $(-t_{AB})$ of the TB model are embodied by the capacitors (and inductors) denoted as C_1 (and L_1) and C_2 (and L_2),

as shown in Fig. 4.5. Furthermore, the modulation of the onsite potential, denoted by $\pm\epsilon$, is achieved by utilizing elements C_3 and L_3. Note that the circuit elements C (and L), which are connected to the ground, are parallel combinations of C_1, C_2 and C_3 (and L_1, L_2 and L_3), respectively, which yields $C = 3C_1 - C_2 - C_3$ $\left(\text{and } \frac{1}{L} = \frac{3}{L_1} - \frac{1}{L_2} - \frac{1}{L_3}\right)$. For the present case, we set $|R| = \infty$, which implies that the connection is disjunctive there. Consider the Laplacian of the Hermitian circuit denoted as J_{H_1}. This Laplacian can be expressed as follows,

$$J_{H_1}(\omega) = \begin{pmatrix} -\frac{1}{i\omega}(\frac{2}{L_1}+\frac{1}{L_2}) - i\omega(C_2+C) & 0 & \frac{1}{i\omega L_1} & i\omega C_2 & 0 & \cdots & & \\ 0 & -i\omega(2C_1+C_2) - \frac{1}{i\omega}(\frac{1}{L}+\frac{1}{L_2}) & \frac{1}{i\omega L_2} & i\omega C_1 & 0 & \cdots & & \\ \frac{1}{i\omega L_1} & \frac{1}{i\omega L_2} & -\frac{1}{i\omega}(\frac{2}{L_1}+\frac{1}{L_2}) - i\omega(C_2+C) & 0 & \frac{1}{i\omega L_1} & i\omega C_2 & 0 & \cdots \\ i\omega C_2 & i\omega C_1 & 0 & -i\omega(2C_1+C_2) - \frac{1}{i\omega}(\frac{1}{L}+\frac{1}{L_2}) & \frac{1}{i\omega L_2} & i\omega C_1 & 0 & \cdots \\ 0 & 0 & \frac{1}{i\omega L_1} & \frac{1}{i\omega L_2} & -\frac{1}{i\omega}(\frac{2}{L_1}+\frac{1}{L_2}) - i\omega(C_2+C) & 0 & \frac{1}{i\omega L_1} & i\omega C_2 \quad 0 \quad \cdots \\ \vdots & \vdots & \vdots & \vdots & \vdots & \ddots & & \end{pmatrix} \tag{4.16}$$

The Laplacian, $J_{H_1}(\omega_0)$, replicates the Hamiltonian H_1 (Eq. (4.4)) at a resonance angular frequency ω_0, defined via,

$$\omega_0 = 2\pi f_0 = \frac{1}{\sqrt{L_1 C_1}} = \frac{1}{\sqrt{L_2 C_2}} = \frac{1}{\sqrt{L_3 C_3}}. \tag{4.17}$$

The next task is to obtain the IP of the TEC, in which one port remains anchored at the edge of the circuit while the other is systematically connected to each node within the network. Fig. 4.6 demonstrates the IP of the TEC at the resonance frequency ω_0. The first port is fixed at the first (last) node to obtain the second (first) edge mode. We have kept the values of C_1, L_1, C_3 and L_3 fixed at 22 μF, 27 μH, 6.8 μF and 87 μH, respectively. The resonance frequency of the circuit is $f_0 \approx 6.53\ kHz$. Notably, the IP observed, corresponding to the topological scenario in which $C_2 + C_3 < 3C_1$, remarkably mirrors the exponentially decaying probability distribution (blue and orange curves). This is a direct visualization of the doubly-degenerate zero-energy boundary modes observed in the corresponding TB model (see Fig. 4.2(a)). For the trivial case ($C_2 + C_3 > 3C_1$), we have kept the values of C_2 and L_2 fixed at 68 μF and 8.7 μH, while for topological case ($C_2 + C_3 < 3C_1$), those have values 33 μF and 18 μH, respectively. Consequently, the topological phase transition, that is, an emergence of a trivial phase in our TEC, manifests at the critical condition $C_2 + C_3 = 3C_1$. This equivalence can

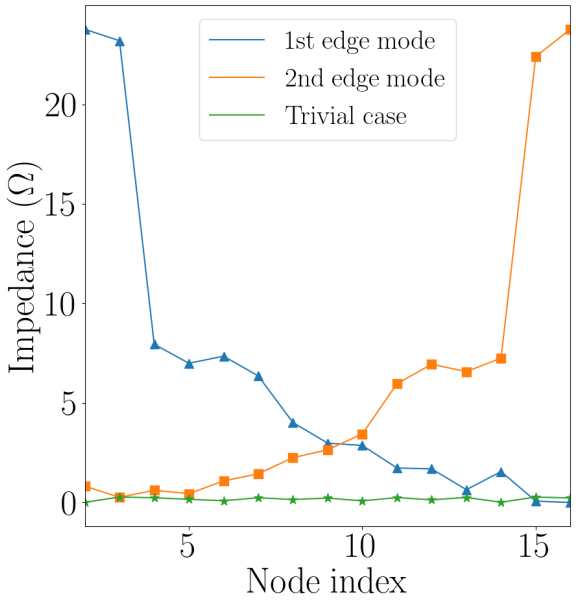

FIGURE 4.6: The IP of the Hermitian circuit, comprising of eight unit cells, for both the trivial and the topological cases. The TEC comprises 16 nodes.

be understood as follows: the TB potential, ϵ, is expressed as $\epsilon \equiv C_2 + C_3 - C_1$, and $t \equiv C_1$, as mentioned before, and the spectral-gap-closing scenario that occurs for the TB model at $\epsilon = 2t$ (Fig. 4.4). Within the trivial regime, the entire IP hovers near zero, indicating an extended eigenmode in the corresponding TB model.

4.2 $n\mathcal{PT}$ NH Models

Next, we explore the NH extensions of the Hermitian model described by Eq. (4.4). Following the method described in the previous chapter to break the hermiticity of a model, we employ the following techniques,

1. introduce imaginary onsite potential.
2. break the reciprocity in the hopping strengths between the lattice sites.

We shall explore models that lack the $\mathcal{PT}$ symmetry in the subsequent subsections. Furthermore, we have categorized $n\mathcal{PT}$ NH models into two groups, namely, those with and without TRS, and examined their topological and localization properties in detail.

4.2.1 *nPT* NH Model without TRS

In this section, we introduce a staggered imaginary onsite potential in the system. This will result in a Hamiltonian of the form given by,

$$H_2 = \sum_{i=1}^{L}\left[i\epsilon(\hat{a}_i^\dagger\hat{a}_i - \hat{b}_i^\dagger\hat{b}_i)\right] - \sum_{i=2}^{L} t_{AB}\hat{a}_i^\dagger\hat{b}_{i-1} + \sum_{i=1}^{L-1}\left[-t(\hat{a}_i^\dagger\hat{a}_{i+1} - \hat{b}_i^\dagger\hat{b}_{i+1}) + t_{AB}\hat{a}_i^\dagger\hat{b}_{i+1}\right] + \text{H.c.}, \tag{4.18}$$

where ϵ is real. The corresponding Bloch Hamiltonian is given by,

$$h_2(k) = \begin{pmatrix} i\epsilon - 2t\cos k & 2it_{AB}\sin k \\ -2it_{AB}\sin k & -i\epsilon + 2t\cos k \end{pmatrix}. \tag{4.19}$$

The $i\epsilon$ term will break TRS and hence will not possess $\mathcal{PT}$ symmetry, which can be realized via,

$$(\mathcal{PT})h_2(k)(\mathcal{PT})^{-1} = -h_2^*(k) \neq h_2(k),$$

where the $\mathcal{PT}$ operator is equal to $\sigma_x\mathcal{K}$ (σ_x : x component of Pauli matrices and $\mathcal{K}$: complex conjugation operator). It is known that in NH systems, there exists an **AZ†** symmetry class [34], apart from the **AZ** symmetry class, since $H^* \neq H^T$. Thus, this

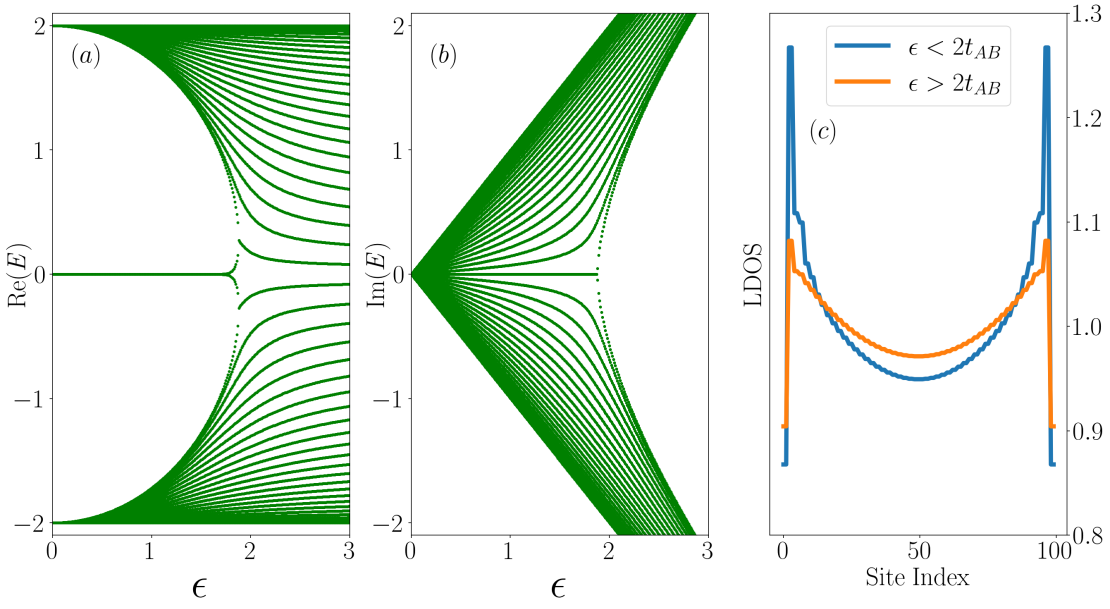

FIGURE 4.7: The (a) real part and (b) imaginary part of the eigenvalues of H_2 are plotted as a function of ϵ for 100 unit cells. (b) shows the absence of purely real eigenvalues and hence is suggestive of a $n\mathcal{PT}$ scenario. (a) and (b) show the appearance (disappearance) of doubly degenerate absolute zero energy edge modes, that is, both the real and imaginary parts of the eigenvalues being zero, for $\epsilon < 2t_{AB}$ ($\epsilon > 2t_{AB}$). (c) LDOS is calculated for both the topological and the trivial phases. The plot confirms the absence of NHSE.

system possesses another symmetry TRS† from the **AZ†** class, which demands,

$$\mathcal{C}_+ h^T(k)\mathcal{C}_+^{-1} = h(-k); \quad \text{with} \quad \mathcal{C}_+\mathcal{C}_+^* = \pm 1, \tag{4.20}$$

for any $h(k)$, with $\mathcal{C}_+$ being an unitary matrix. Further, $h_2(k)$ satisfies $h_2^T(k) = h_2(-k)$. So, the present model falls in the class **AI†** in the real **AZ†** symmetry classification due to the TRS† symmetry present in the system.

We now analyze the topological and localization properties of the edge modes of this model. The potential $\pm i\epsilon$ on the A and B atoms in the Hamiltonian H_2 physically implies 'gain' and 'loss' of energy that the system experiences due to the non-hermiticity. Fig. 4.7(a) suggests that doubly degenerate zero energy edge modes exist till $\epsilon = 2$ (in units of t_{AB}), and disappear beyond that. The presence of non-zero imaginary parts in the energy spectrum depicted in Fig. 4.7(b) serves as evidence for the absence of $\mathcal{PT}$ symmetry of the system. Figs. 4.7(a) and 4.7(b) demonstrate that the energy eigenvalues, E, appear in pairs, that is $\pm E$, which is a manifestation of PHS. In Fig. 4.7(c), we have shown the local density of states (LDOS), which can be obtained from the expression,

$$\text{LDOS}^{(n)} = \sum_{i=1}^{2L} |\psi_n^i|^2,$$

corresponding to the n^{th} lattice site, where the summation index, i, runs over all eigenvalues. Higher values of LDOS at the edges of the system for the case $\epsilon < 2t_{AB}$ support the existence of the two localized edge modes, which contrasts with the case corresponding to $\epsilon > 2t_{AB}$. It is clear from Fig. 4.7(c) that the NHSE is absent in this system as LDOS is non-zero at the interior of the system. The IPR is given by the same formula as

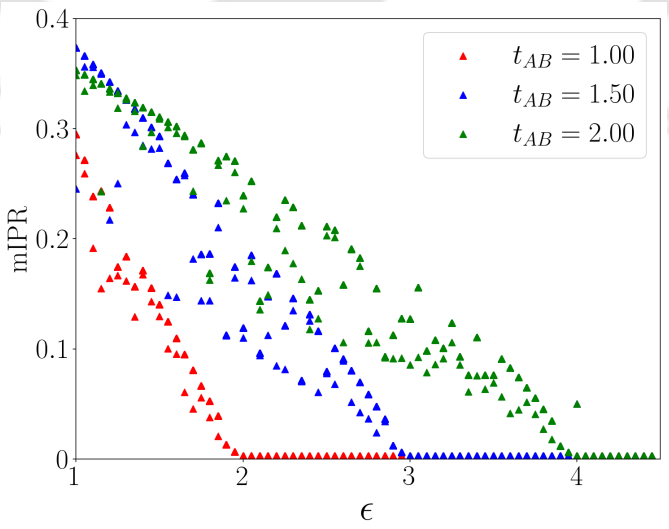

FIGURE 4.8: mIPR versus ϵ is plotted here for different values of t_{AB} keeping $t = 1$. The plot suggests that the existence of the edge states now depends on t_{AB}. The scenario is unlike the Hermitian model, where it depends on t.

in Eq. (4.8), except that the right eigenvectors, determined via Eq. (1.1) of Chapter 1, will have to be used for this case. The mIPR, defined in the previous section, is computed as a function of ϵ for three different values of t_{AB}, namely, $t_{AB} = 1$, 1.5, 2.0, and is shown in Fig. 4.8. The presence of the zero-energy edge states for the model depends on t_{AB}. The mIPR is non-zero (edge states) for values of ϵ lower than $2t_{AB}$, and beyond that, it is zero, implying that the edge states exist till $\epsilon = 2t_{AB}$, and disappear beyond that.

It may be noted that, owing to the fact that BBC is preserved in this case (absence of NHSE), involving the non-Bloch band theory [134] is superfluous. Thus, we proceed to analyze the PBC scenario with standard BZ theory. We perform the same unitary transformation as done in the previous section, given in Eq. (4.10), on the Bloch Hamiltonian, $h_2(k)$ in Eq. (4.19), which yields,

$$h_2'(k) = \begin{pmatrix} 0 & -i\epsilon + 2t\cos k + 2it_{AB}\sin k \\ -i\epsilon + 2t\cos k - 2it_{AB}\sin k & 0 \end{pmatrix}, \tag{4.21}$$

which can be written in a Dirac form as, $h_2'(k) = \vec{d_2'}\cdot\sigma$ with $\vec{d_2'} \equiv (-i\epsilon + 2t\cos k,\ -2t_{AB}\sin k,\ 0)$. $\vec{d_2'}$ has all the symmetries, that is, both PHS and TRS†. Evidently, $\vec{d_2}$ and $\vec{d_2'}$ have the same eigenspectra, and are given by,

$$E_{2\pm}(k) = \pm\sqrt{(-i\epsilon + 2t\cos k)^2 + 4t_{AB}^2\sin^2 k}. \tag{4.22}$$

The left ($|\lambda_{2\pm}'(k)\rangle$) and the right ($|\psi_{2\pm}'(k)\rangle$) eigenfunctions of $h_2'(k)$ are given by,

$$|\lambda_{2\pm}'(k)\rangle = \frac{1}{\sqrt{2}}e^{\pm i\eta^*}\begin{pmatrix} \pm e^{-i\phi_{2k}^*} \\ 1 \end{pmatrix};\quad |\psi_{2\pm}'(k)\rangle = \frac{1}{\sqrt{2}}e^{\pm i\eta}\begin{pmatrix} \pm e^{-i\phi_{2k}} \\ 1 \end{pmatrix}. \tag{4.23}$$

Here η is a constant (and independent of k and ϕ_{2k}), and ϕ_{2k} is given by,

$$\phi_{2k} = \tan^{-1}\left(\frac{-2t_{AB}\sin k}{-i\epsilon + 2t\cos k}\right).$$

With the help of a bit of algebra, one can show that the locations of the two EPs in a space spanned by $d_{2x}'^{\mathrm{R}} - d_{2y}'^{\mathrm{R}}$ are at $(d_{2y}'^{\mathrm{I}}, -d_{2x}'^{\mathrm{I}})$ and $(-d_{2y}'^{\mathrm{I}}, d_{2x}'^{\mathrm{I}})$ [173, 198] which are $(0, \epsilon)$ and $(0, -\epsilon)$ respectively, where $d_{2x}'^{\mathrm{R}}$ ($d_{2y}'^{\mathrm{R}}$) and $d_{2x}'^{\mathrm{I}}$ ($d_{2y}'^{\mathrm{I}}$) represent the real and the imaginary parts of d_{2x}' (d_{2y}') respectively. At these EPs, for $k = \frac{\pi}{2}$, $E_2(k)$ vanish and $\langle\lambda_{2\pm}'(k)|\psi_{2\pm}'(k)\rangle$ becomes ill-defined. The locus of the real part of $\vec{d_2'}$ constitutes an ellipse with the center at $(0,0)$ in the $d_{2x}'^{\mathrm{R}} - d_{2y}'^{\mathrm{R}}$ plane as shown in Figs. 4.9(a) and 4.9(b) corresponding to two representative values of ϵ, namely, $\epsilon = 1.5$ and $\epsilon = 2.5$ respectively. The EPs are inside (outside) the ellipse in Fig. 4.9(a) (Fig. 4.9(b)) for $\epsilon < 2t_{AB}$ ($\epsilon > 2t_{AB}$). Thus, Fig. 4.9(a) is referred to as the topological phase with two zero-energy edge modes, while Fig. 4.9(b) is in the trivial phase. Further, Figs. 4.9(c)

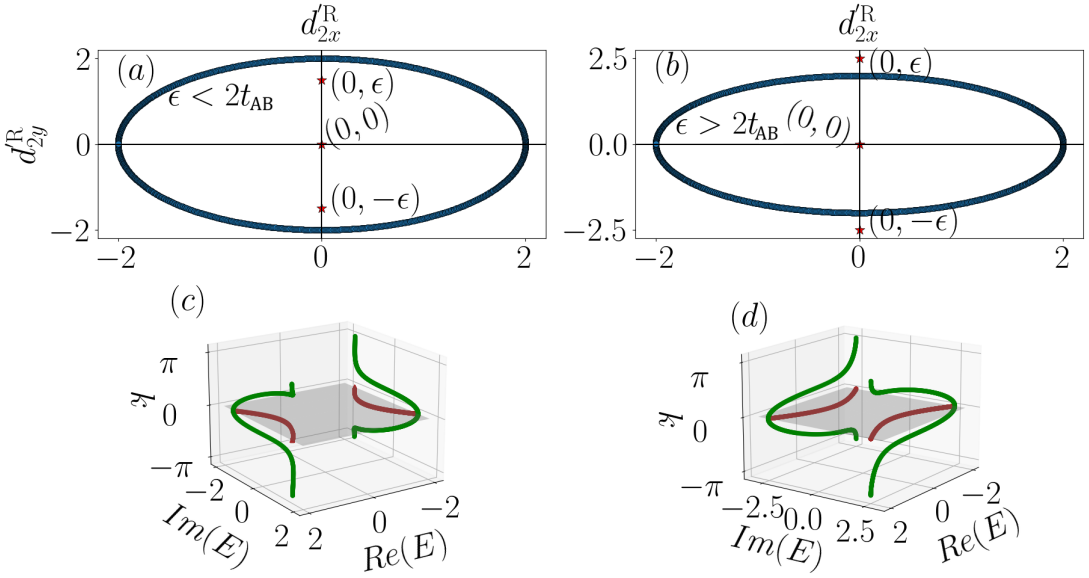

FIGURE 4.9: Real part of $\vec{d_2'}$ is drawn in a plane spanned by $d_{2x}^{\prime R} - d_{2y}^{\prime R}$ for the parameters $t = 1$, $t_{AB} = 1$, and (a) $\epsilon = 1.5$, where the ellipse encloses the EPs (topological case), and (b) $\epsilon = 2.5$, where it excludes the EPs (trivial case). (c) and (d) represent 3D plots of the band structures ($E_{2\pm}(k)$ vs k) with the real and the imaginary parts of the energy being plotted along the x and y axis, respectively. At the same time, the momentum k is along the z direction. The points in green and brown denote the actual data points and their 2D projections, respectively.

and 4.9(d) are the band structures for the same parameters as used in Figs. 4.9(a) and 4.9(b), respectively. The plot shown in green color denotes $E_{2\pm}(k)$ as a function of k, and the one in brown color represents the 2D projection of the same in the complex plane. Fig. 4.9(c), which corresponds to the topological phase, shows that there is a real line gap in the band structure as $\mathrm{Re}(E_2(k)) \neq 0 \ \forall \ k$. The base axis is the imaginary axis, with the projected $E_2(k)$ lying on either side. At $\epsilon = 2t_{AB}$, the two bands are intertwined at the points, $-\frac{\pi}{2}$, 0 and $\frac{\pi}{2}$, in the BZ. Thus, the Hamiltonian becomes gapless at these points, where the topological to the trivial phase transition occurs. In contrast, in Fig. 4.9(d), for $\epsilon > 2t_{AB}$, the line gap becomes imaginary, with the base axis now being replaced by the real axis, and the system is in a trivial phase. The absence of non-trivial point-gap topology in this system is reminiscent of the absence of NHSE.

We have also computed the complex Berry phase [197, 200], the NH version of the Berry phase, given via Eq. (4.9), to characterize the topological phases in the system. It encodes both geometric phase (real part) and geometric amplification or decay (imaginary part), revealing how topology survives and is reshaped by the non-hermiticity. The origin of this topological invariant remains the same as in the Hermitian case, with the only difference that both left and right eigenvectors, defined via Eq. (1.1) of Chapter 1, must now be employed for computation. Thus, the definition becomes,

$$\gamma_{\pm} = i \oint_{BZ} \langle \lambda(k)| \nabla_k |\psi(k)\rangle \ dk, \tag{4.24}$$

for the left (right) eigenvector $\langle\lambda(k)|$ ($|\psi(k)\rangle$) of any general NH Hamiltonian. Substituting the expressions of $|\lambda'_{2\pm}(k)\rangle$ and $|\psi'_{2\pm}(k)\rangle$ (Eq. (4.23)) in Eq. (4.24), we get the expression as,

$$\gamma_{\pm} = \frac{1}{2}\oint_{BZ} \frac{\partial\phi_{2k}}{\partial k}\, dk = \frac{1}{2}\oint_{BZ} \frac{2t_{AB}(i\epsilon\cos k - 2t)}{(-i\epsilon + 2t\cos k)^2 + 4t_{AB}^2\sin^2 k}\, dk. \tag{4.25}$$

From the above equation, we get that while the complex Berry phase is independent of t, it changes value from $-\pi$ to 0 at $\epsilon = 2t_{AB}$, denoting that these are the topological and the trivial phases, respectively. Thus, a phase transition occurs at $\epsilon = 2t_{AB}$. These phenomena are almost the same as the Hermitian case, except for the fact that the roles of t and t_{AB} are interchanged with regard to the topological phase transitions.

4.2.2 TEC Realization of the $n\mathcal{PT}$ Model (without TRS)

The creation of an analogous electric circuit is accomplished by incorporating both positive and negative resistive components ($\pm R$), as illustrated in Fig. 4.5, with R being finite for this case. They are strategically connected between the circuit nodes and the reference ground. Furthermore, we have set $C = 2C_1$ and $L = \frac{L_1}{2}$ to cancel out any additional terms in the onsite potential other than $\pm R$. This makes the scenario completely equivalent to the imaginary onsite potential, $\pm i\epsilon$, in the corresponding TB model. It is important to note that negative impedance is implemented via INIC. The construction and working principle of INIC is already discussed in Chapter 2 (Fig. 2.1(b)). In

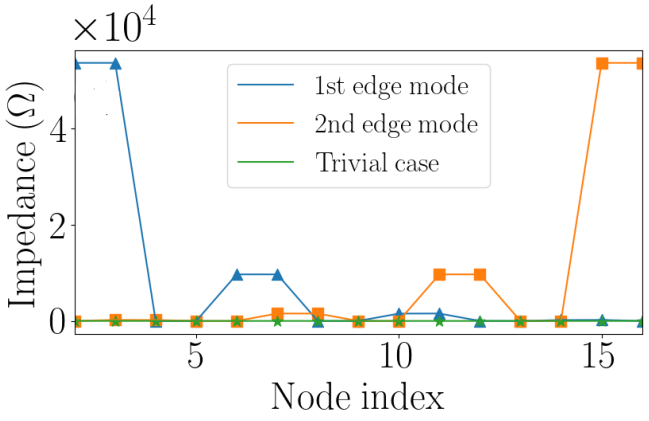

FIGURE 4.10: The IP of the $n\mathcal{PT}$ NH circuit, constituting of eight unit cells. The trivial and the topological cases correspond to the values of R being 10 Ω and 100 Ω, respectively.

Fig. 4.10, we present the IP for the $n\mathcal{PT}$ NH circuit, which has been achieved within both the trivial and topological regions employing the method expounded in the previous section. The resonance frequency of the circuit is approximately $f_0 = \frac{\omega_0}{2\pi} \approx 206.5\ kHz$.

The criterion for the topological phase transition in this scenario is succinctly expressed as $R = \frac{1}{2\omega_0 C_2} \approx 11.68\ \Omega$, which is equivalent to $\epsilon = 2t_{AB}$ for the TB model.

4.2.3 $n\mathcal{PT}$ NH Model with TRS

We proceed to construct another type of NH model that lacks $\mathcal{PT}$ symmetry but retains TRS. To accomplish this, we fabricate a model where the non-reciprocity term is included in the $A^i \leftrightarrow A^{i+1}$ and $B^i \leftrightarrow B^{i+1}$ hopping. The Hamiltonian in real space is given by,

$$H_3 = H_1 - \sum_{i=1}^{L-1} \left[\Delta(\hat{a}_i^\dagger \hat{a}_{i+1} - \hat{a}_{i+1}^\dagger \hat{a}_i) + \tilde{\Delta}(\hat{b}_i^\dagger \hat{b}_{i+1} - \hat{b}_{i+1}^\dagger \hat{b}_i)\right], \tag{4.26}$$

where Δ ($\tilde{\Delta}$) is the non-reciprocity in the hopping between A (B) atoms, and H_1 is given by Eq. (4.4). The corresponding Bloch Hamiltonian can be written as,

$$h_3(k) = \begin{pmatrix} \epsilon - 2t\cos k + 2i\Delta \sin k & 2it_{AB}\sin k \\ -2it_{AB}\sin k & -\epsilon + 2t\cos k + 2i\tilde{\Delta}\sin k \end{pmatrix}. \tag{4.27}$$

Now, we discuss two special cases of the above equation, namely, (i) $\Delta = \tilde{\Delta}$ and (ii) $\Delta = -\tilde{\Delta}$. It becomes evident that the Hamiltonian $h_3(k)$ possesses TRS regardless of the relationship between Δ and $\tilde{\Delta}$. As a result, the eigenvalues appear in complex conjugate pairs. However, $h_3(k)$ lacks inversion (parity) symmetry, thereby classifying it as an $n\mathcal{PT}$ model. Additionally, $h_3(k)$ holds the following relations,

$$\mathcal{C}_- h_3^T(k, \Delta = \tilde{\Delta})\mathcal{C}_- = -h_3(-k, \Delta = \tilde{\Delta}), \quad \mathcal{C}_-\mathcal{C}_-^* = \pm 1;$$
$$\mathcal{T}_- h_3^*(k, \Delta = -\tilde{\Delta})\mathcal{T}_-{}^{-1} = -h_3(-k, \Delta = -\tilde{\Delta}); \quad \mathcal{T}_-\mathcal{T}_-^* = \pm 1,$$

where $\mathcal{C}_- = \mathcal{T}_- = \sigma_x$. Based on these conditions, we can conclude that the model possesses PHS (PHS†) when $\Delta = \tilde{\Delta}$ ($\Delta = -\tilde{\Delta}$), and fall in the **BDI** (**D**†) class in AZ ($AZ^\dagger$) symmetry classification.

From now on, we work in real space, that is, a finite chain, for this case. To begin with, the localization phenomena are investigated by computing the LDOS. As depicted in Fig. 4.11, the LDOS exhibits pronounced accumulation either at one edge or both edges of the 1D chain, contingent upon the specific relationship between Δ and $\tilde{\Delta}$. This indicates the presence of NHSE in both scenarios. For $\Delta = -\tilde{\Delta}$, represented by orange circles in Fig. 4.11, the LDOS appears to have a higher value at the left edge, indicating that a majority of the bulk wave functions are localized at this edge. This observation elucidates the usual NHSE, with the accumulation of the states at the left edge. In contrast, when $\Delta = \tilde{\Delta}$, there are higher values of LDOS at both edges, suggesting that most of the bulk eigenstates are localized at both edges simultaneously. This can be understood as follows. As demonstrated in Ref. [203], PHS compels two *particle-hole*

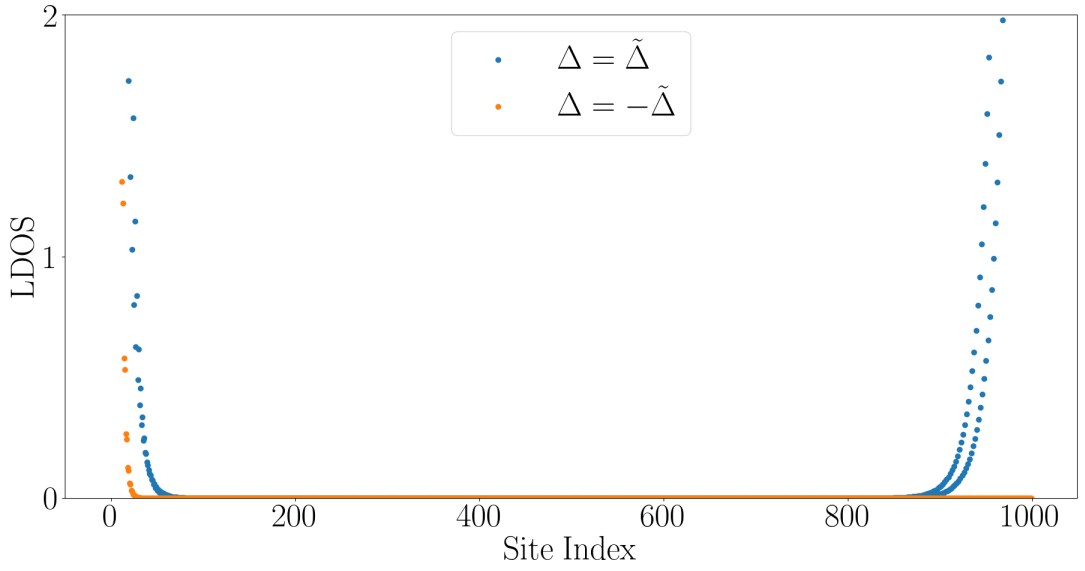

FIGURE 4.11: NHSE at left and at both edge(s) for the cases $\Delta = \pm\tilde{\Delta}$, respectively. The LDOS for both cases vanishes inside the chain and has finite value only at the edges.

partner skin modes to localize at opposite boundaries. These skin modes, although localized at different boundaries and connected by PHS, are not degenerate and instead exhibit different eigenvalues. Our $n\mathcal{PT}$ NH model having TRS ($\Delta = \tilde{\Delta}$), also adheres to PHS. This particular symmetry leads to non-degenerate skin modes localized at both edges, which are related by the PHS. When $\tilde{\Delta}$ changes sign, the system forfeits PHS, but acquires another symmetry, namely, PHS†, resulting in NHSE to occur exclusively on one edge (left edge here). It is noteworthy to mention that this phenomenon is very similar to the bidirectional NHSE [204], which requires the system to have TRS†. However, unlike our case, the skin modes are degenerate and localized at both edges. It is intriguing how a simple change in the sign of the non-reciprocity parameter, $\tilde{\Delta}$, can drive the system from normal NHSE to NHSE at both the edges.

4.2.4 TEC Realization

We now construct the TEC corresponding to the TB model defined in Eq. (4.26). The Hermitian version of the circuit is shown in Fig. 4.5, where $R \to \infty$ (i.e., the resistor is disconnected). To incorporate non-reciprocity Δ ($\tilde{\Delta}$) on the nodes $m, A \leftrightarrow m+1, A$ ($m, B \leftrightarrow m+1, B$), as illustrated in Fig. 4.12, we introduce INIC elements $D1$ ($D2$) connected in parallel with L_1 (C_1). The internal structure of $D1$ contains a capacitor whose value encodes the strength of the non-reciprocity parameter Δ. We keep $D1$ fixed. However, when $\Delta = \tilde{\Delta}$, the INIC $D2$ is implemented using a capacitor, whereas for $\Delta = -\tilde{\Delta}$ it is implemented using an inductor. All remaining circuit components retain

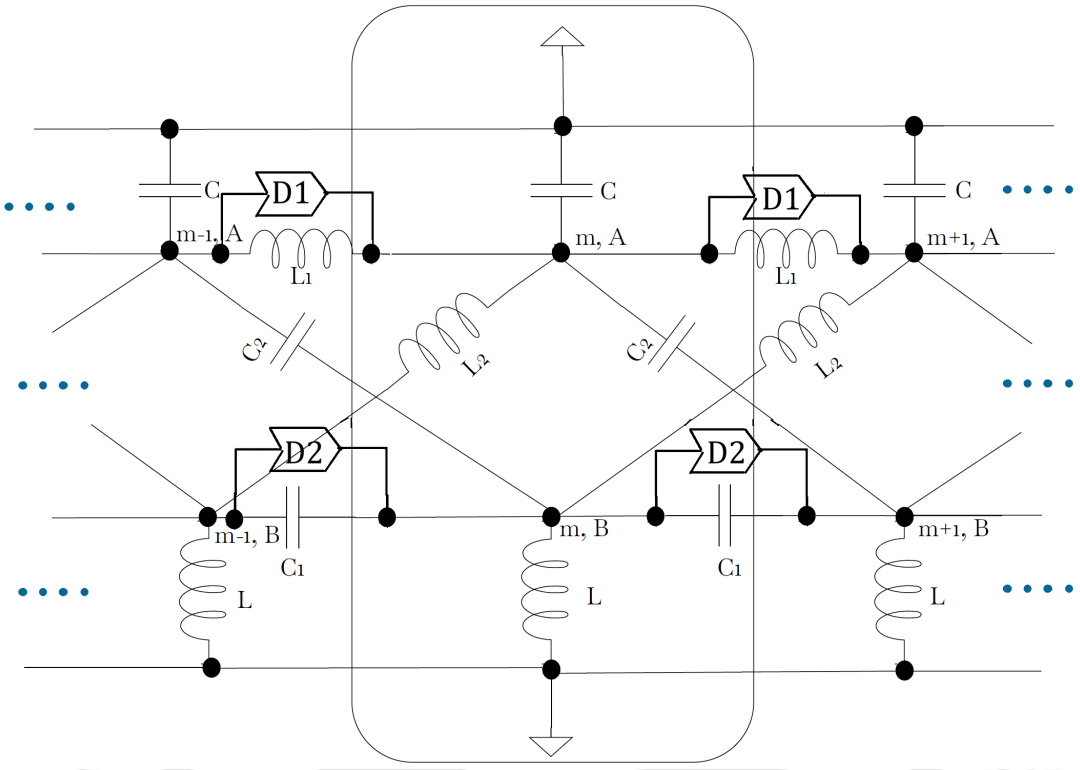

FIGURE 4.12: Circuit diagram for 3 subsequent unit cells corresponding to the Hermitian model in Eq. (4.26).

the same values as those in Fig. 4.5; however, the values of the grounded capacitors (C) and inductors (L) are adjusted accordingly to accommodate the chosen non-reciprocity.

In general, the NHSE in a TEC is identified by examining the VP, as demonstrated in Section 3.2.2 of the previous chapter for the $n\mathcal{PT}$ SSH circuit. In the present case, however, the system exhibits NHSE not only in its conventional form but also simultaneously at both edges, arising from the condition $\Delta = \pm\tilde{\Delta}$, as shown in Fig. 4.11. Consequently, instead of the VP, we analyze the IP of the TEC to capture both these scenarios. Fig. 4.13 shows the resulting IP of the TEC for the case $D1 \equiv \pm D2$. When $D1 \equiv -D2$, indicated by orange circles, the IP accumulates at the left boundary, signaling behavior analogous to the conventional NHSE within the TEC. By contrast, when $D1 \equiv D2$, represented by blue squares, enhanced IP localization appears at both edges. This indicates that the impedance is simultaneously localized at the two boundaries, corresponding to the NHSE occurring at both edges of the TEC. Interestingly, the IP has lower values at B subnodes compared to A subnodes. The same phenomenon was observed for the Hermitian SSH circuit (see Fig. 2.4(a) of Chapter 2) and can be understood as follows. Let V_1 and V_2 be the voltage differences across the adjacent nodes. When the circuit is driven by an AC source, the potentials V_1 and V_2 oscillate out of phase due to the setting, $D1 \equiv D2$, giving rise to a spatial voltage configuration of the form, $V(n) \propto (1, 0, -\frac{V_2}{V_1}, 0, (\frac{V_2}{V_1})^2, 0, -(\frac{V_2}{V_1})^3, 0, \ldots (-\frac{V_2}{V_1})^n, 0)$, where the index n runs

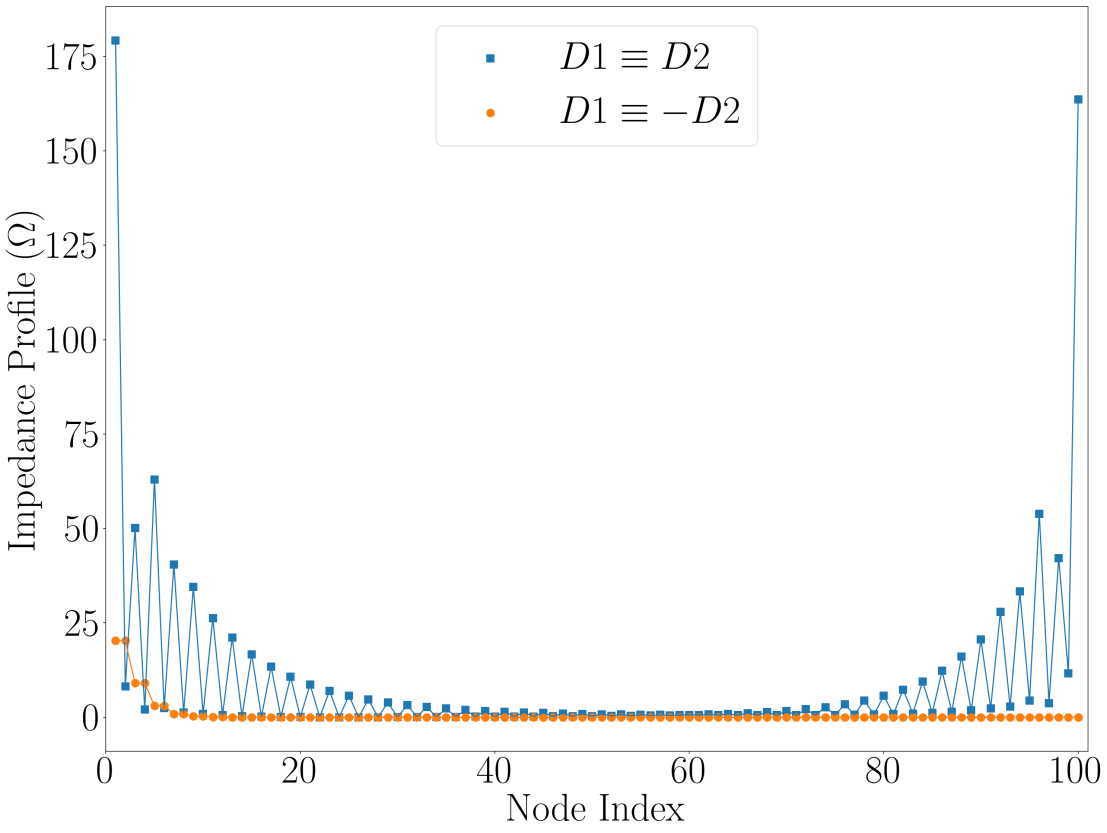

FIGURE 4.13: Normal NHSE and NHSE at both edges are being realized in TEC for different setups of $D2$, that is, whether it contains an inductor or a capacitor. The impedance values at the edges are significantly larger for $D1 \equiv D2$ than for $D1 \equiv -D2$.

through the two-node unit cells. This alternating pattern is reflected in the IP (blue squares). In the case $D1 \equiv -D2$, the voltages V_1 and V_2 oscillate in phase, and consequently, no alternating pattern is manifested in the IP of the TEC (orange circles). This enhancement indicates greater TEC sensitivity to circuit perturbations when the NHSE occurs simultaneously at both boundaries.

4.3 $s\mathcal{PT}$ NH Model

Now we break the Hermiticity of H_1 (Eq. (4.4)) by including a non-reciprocity parameter, δ, in the hopping term (t_{AB}) among the A and B atoms from neighbouring unit cells. The new Hamiltonian takes the form,

$$H_4 = H_1 + \delta \left[\sum_{i=1}^{L-1} (\hat{a}_i^\dagger \hat{b}_{i+1} - \hat{b}_{i+1}^\dagger \hat{a}_i) - \sum_{i=2}^{L} (\hat{a}_i^\dagger \hat{b}_{i-1} - \hat{b}_{i-1}^\dagger \hat{a}_i) \right], \tag{4.28}$$

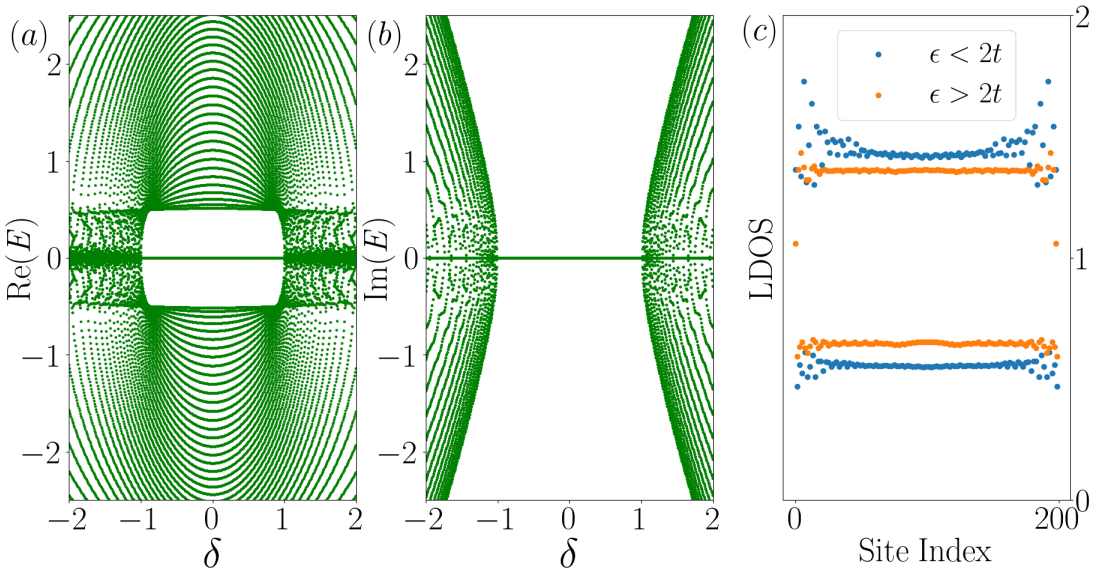

FIGURE 4.14: The (a) real part, and the (b) imaginary part of eigenspectra plotted as a function of the non-reciprocity parameter, δ, with $\epsilon = 1.5t$, $t = 1$, $t_{AB} = 1.5$. (c) The LDOS is calculated for $\epsilon = 1.5$ ($< 2t$) and $\epsilon = 3$ ($> 2t$). The LDOS plot confirms the absence of NHSE.

with the Bloch Hamiltonian, $h_4(k)$, given by,

$$h_4(k) = \begin{pmatrix} \epsilon - 2t\cos k & 2i(t_{AB} + \delta)\sin k \\ -2i(t_{AB} - \delta)\sin k & -\epsilon + 2t\cos k \end{pmatrix}, \tag{4.29}$$

which indicates that the forward ($A^i \to B^{i+1}$) and the backward ($A^i \leftarrow B^{i+1}$) hopping amplitudes between A^i and B^{i+1} are $t_{AB} - \delta$ and $t_{AB} + \delta$, respectively. The non-reciprocity term does not affect the TRS or the PHS (relevant to this case), as $h_4(k)$ satisfies,

$$\mathcal{C}_- h_4^T(k)\mathcal{C}_-^{-1} = -h_4(-k); \quad \text{with} \quad \mathcal{C}_-\mathcal{C}_-^* = \pm 1,$$
$$\mathcal{T}_+ h_4^*(k){\mathcal{T}_+}^{-1} = h_4(-k); \quad \text{with} \quad \mathcal{T}_+\mathcal{T}_+^* = \pm 1,$$

where $\mathcal{C}_-$ is σ_x, and $\mathcal{T}_+$ is the complex conjugation operator, $\mathcal{K}$. Hence, $h_4(k)$ has CS but does not have sub-lattice symmetry, which is defined via, $\mathcal{S}h(k)\mathcal{S}^{-1} = -h(k)$; with $\mathcal{S}^2 = 1$, for any $h(k)$. Here, $\mathcal{S}$ denotes a unitary matrix. While CS and sub-lattice symmetry are identical for a Hermitian system, they differ for NH systems [35]. For NH systems, the CS operator, Γ demands, $\Gamma h^\dagger(k)\Gamma^{-1} = -h(k)$; with $\Gamma^2 = 1$, for any $h(k)$. Thus, the system falls in class BDI in real AZ symmetry class due to the presence of all three symmetries, namely, TRS, PHS, and CS. In addition, the model also has $\mathcal{PT}$ symmetry, as we shall see later.

We now explore the evolution of the properties as we vary the parameters ϵ (onsite potential) and δ (non-reciprocity). The eigenvalues of H_4 (Eq. (4.28)) are plotted in

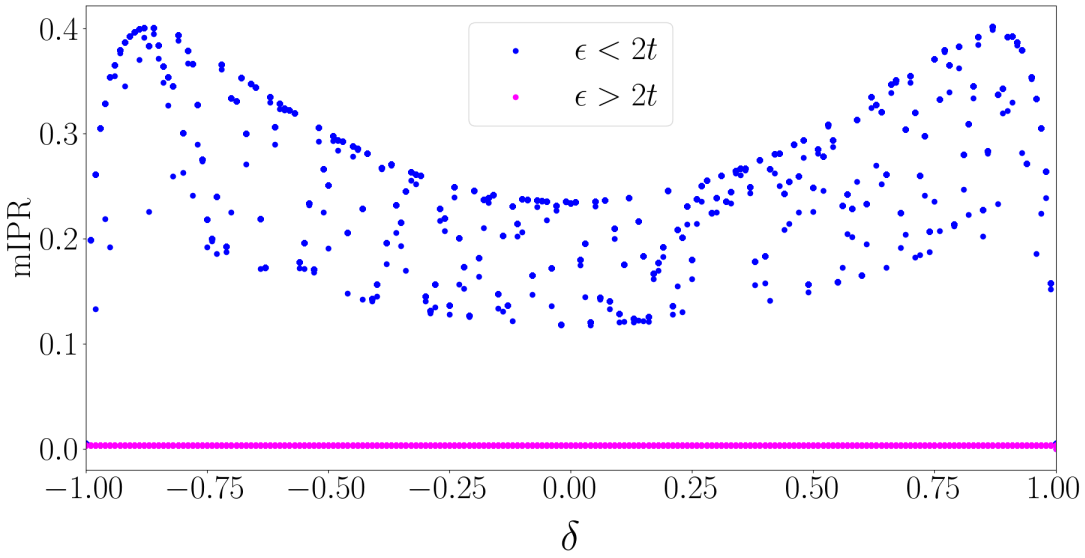

FIGURE 4.15: The mIPR is shown as a function of δ for $t = t_{AB} = 1$ corresponding to the cases $\epsilon = 1.2$ ($< 2t$) and $\epsilon = 2.6$ ($> 2t$), respectively.

Figs. 4.14(a) and 4.14(b) for $\epsilon < 2t$. The imaginary part of E is zero as long as the condition $|\delta| \leq t_{AB}$ is satisfied, suggesting that this regime belongs to the $\mathcal{PT}$-unbroken phase [41], and beyond that ($|\delta| > t_{AB}$), the system enters a $\mathcal{PT}$-broken phase. Fig. 4.14(c) represents the LDOS plots via two pairs of (almost) flat lines corresponding to $\epsilon < 2t$ (lines in blue) and $\epsilon > 2t$ (orange lines). These lines denote discrete LDOS values at lattice sites and oscillate from one site to the next. The LDOS has finite values at the interior of the system, leading to a unique phenomenon: *the absence of NHSE in a non-reciprocal system.* The explanation and the analyses behind this surprising incident are discussed in Appendix B in detail via pseudo-hermiticity [43] and the non-Bloch band theory [134]. Further, for $\epsilon < 2t$, the blue lines demonstrate the existence of edge modes via higher values at the edges, while the orange ones do not have any such signature. The degree of localization of these edge states, measured by mIPR, is shown in Fig. 4.15 as a function of the non-reciprocity parameter, δ, in the range $[-1 : 1]$. The mIPR is non-zero for $\epsilon < 2t$ and indicates the presence of edge states, suggesting that this is a topological phase. These edge modes, along with the mIPR, vanish as soon as ϵ becomes larger than $2t$ when all the eigenstates become extended. Thus, a phase transition occurs at $\epsilon = 2t$.

Since the BBC is preserved in this system (NHSE is absent), we shall analyze it in the momentum space using the standard BZ theory to characterize its topological properties. We shall proceed in the same manner as in the previous sections, that is, the basis of the Bloch Hamiltonian, $h_4(k)$, will be rotated via a unitary operator, U, given in Eq. (4.10).

The resultant Bloch Hamiltonian, let us call it as $h_4'(k)$, is given by,

$$h_4'(k) = \begin{pmatrix} 2i\delta \sin k & -\epsilon + 2t\cos k + 2it_{AB}\sin k \\ -\epsilon + 2t\cos k - 2it_{AB}\sin k & -2i\delta \sin k \end{pmatrix}, \tag{4.30}$$

with $\vec{d_4'} \equiv (-\epsilon + 2t\cos k,\ -2t_{AB}\sin k,\ 2i\delta \sin k)$, suggesting that all, but the z component of $\vec{d_4'}$ is real, that is,

$$d_{4x}'^{\mathrm{R}} = -\epsilon + 2t\cos k,\ d_{4y}'^{\mathrm{R}} = -2t_{AB}\sin k,\ d_{4z}'^{\mathrm{R}} = 0; d_{4x}'^{\mathrm{I}} = 0,\ d_{4y}'^{\mathrm{I}} = 0,\ d_{4z}'^{\mathrm{I}} = 2i\delta \sin k,$$

where the notations bear a similar meaning to those given in the previous section. It is clear that $h_4'(k)$ commutes with the $\mathcal{PT}$ operator given by $\sigma_x\mathcal{K}$ and hence preserves $\mathcal{PT}$ symmetry. The expression for the band structure is given by,

$$\begin{aligned} E_{4\pm}(k) &= \pm\sqrt{(d_{4x}'^{\mathrm{R}} + id_{4x}'^{\mathrm{I}})^2 + (d_{4y}'^{\mathrm{R}} + id_{4y}'^{\mathrm{I}})^2 + (d_{4z}'^{\mathrm{R}} + id_{4z}'^{\mathrm{I}})^2}. \\ &= \pm\sqrt{(-\epsilon + 2t\cos k)^2 + 4(t_{AB}^2 - \delta^2)\sin^2 k}. \end{aligned} \tag{4.31}$$

Moreover, the left and the right eigenvectors of $h_4'(k)$ are obtained as,

$$|\lambda_{4\pm}'(k)\rangle = \pm\frac{1}{\sqrt{2}}\beta_1 e^{\pm i\alpha^*}\begin{pmatrix} \frac{\sin\theta_k^* e^{-i\phi_{4k}}}{\pm 1+\cos\theta_k^*} \\ 1 \end{pmatrix}; \quad |\psi_{4\pm}'(k)\rangle = \pm\frac{1}{\sqrt{2}}\beta_2 e^{\pm i\alpha}\begin{pmatrix} \frac{\sin\theta_k e^{-i\phi_{4k}}}{\pm 1-\cos\theta_k} \\ 1 \end{pmatrix}, \tag{4.32}$$

where α is independent of k and ϕ_{4k} and θ_k are given by,

$$\phi_{4k} = \tan^{-1}\left[\frac{-2t_{AB}\sin k}{-\epsilon + 2t\cos k}\right]; \quad \theta_k = \tan^{-1}\left[\frac{\sqrt{(-\epsilon + 2t\cos k)^2 + 4t_{AB}^2\sin^2 k}}{2i\delta \sin k}\right].$$

β_1 and β_2 satisfy the relation,

$$\beta_1^*\beta_2 = \frac{1}{2}(1 - \cos\theta_k),$$

and are periodic functions of k. Putting $|\lambda_{4\pm}'(k)\rangle$ and $|\psi_{4\pm}'(k)\rangle$ from Eq. (4.32) into Eq. (4.24), we get an expression as,

$$\begin{aligned} \gamma_\pm &= \frac{1}{2}\oint_{BZ}\frac{\partial\phi_{4k}}{\partial k}\ (1 + \cos\theta_k)\ dk \\ &= \frac{1}{2}\oint_{BZ}\frac{2t_{AB}\ (\epsilon\cos k - 2t)}{(-\epsilon + 2t\cos k)^2 + 4t_{AB}^2\sin^2 k}\ \left(1 + \frac{2i\delta\sin k}{E_{4+}(k)}\right)dk. \end{aligned}$$

From the above equation, the complex Berry phase takes a value of $-\pi$ (0) for $\epsilon < 2t$ $(\epsilon > 2t)$, hinting that the topological phase transition occurs at $\epsilon = 2t$. The energy $E_{4\pm}(k)$ in Eq. (4.31) becomes zero when $d_{4x}'^{\mathrm{R}} = 0$ and $d_{4y}'^{\mathrm{R}} = |d_{4z}'^{\mathrm{I}}|$. These two conditions

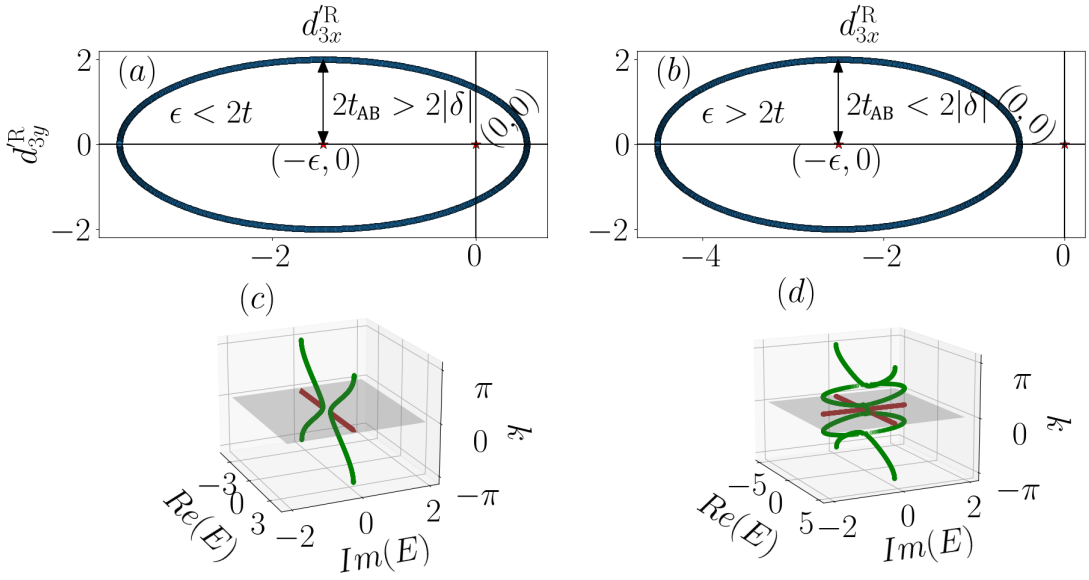

FIGURE 4.16: The locus of $\vec{d}'_4$ is plotted in a plane spanned by $d'^{\mathrm{R}}_{4x} - d'^{\mathrm{R}}_{4y}$ for the parameters $t = 1$, $t_{AB} = 1$ and (a) $\epsilon = 1.5$, where the ellipse contains the origin $(0, 0)$ (topological case) and (b) $\epsilon = 2.5$, where it excludes the origin (trivial case). (c) and (d) represent 3D figures of the band structures. The parameters are the same as those of (a) and (b). The green and the brown points are the actual data points and their 2D projections, respectively.

are for an EP. Putting these conditions in Eq. (4.32), we see that,

$$\langle \lambda'_{4\pm}(k) | \psi'_{4\pm}(k) \rangle = 0.$$

This shows that the biorthonormality condition is violated at the EP, and that the left and right eigenvectors subsequently become self-orthogonal, as discussed in Section 1.4 of Chapter 1.

Figs. 4.16(a) and 4.16(b) represent the trajectory of $\vec{d}'_4$, which is an ellipse in a plane spanned by $d'^{\mathrm{R}}_{4x} - d'^{\mathrm{R}}_{4y}$ for two values of ϵ, namely, $\epsilon = 1.5$ and $\epsilon = 2.5$, respectively. In Fig. 4.16(a), the origin $(0, 0)$ is inside the ellipse, that is, $\epsilon < 2t$, suggesting that it denotes a topological phase. On the other hand, Fig. 4.16(b) describes the trivial phase as the ellipse excludes the origin when $\epsilon > 2t$. Similar to the $n\mathcal{PT}$ case (without TRS), the energy gap, in this case, too, represents a line gap. However, due to the presence of $\mathcal{PT}$ symmetry, the eigenvalues are either purely real or purely imaginary (Figs. 4.16(c) and 4.16(d)) in this case Note that the $\mathcal{PT}$-broken-unbroken phase transition has an analytic dependence on the parameters given by,

$$\epsilon_0 = 2\sqrt{\delta^2 + t^2 - t_{AB}^2}. \tag{4.33}$$

Fig. 4.16(c) shows the case where $\mathcal{PT}$ symmetry is still unbroken since the condition $\epsilon > \epsilon_0$ is satisfied, resulting in the eigenspectra to be purely real. When the value of ϵ

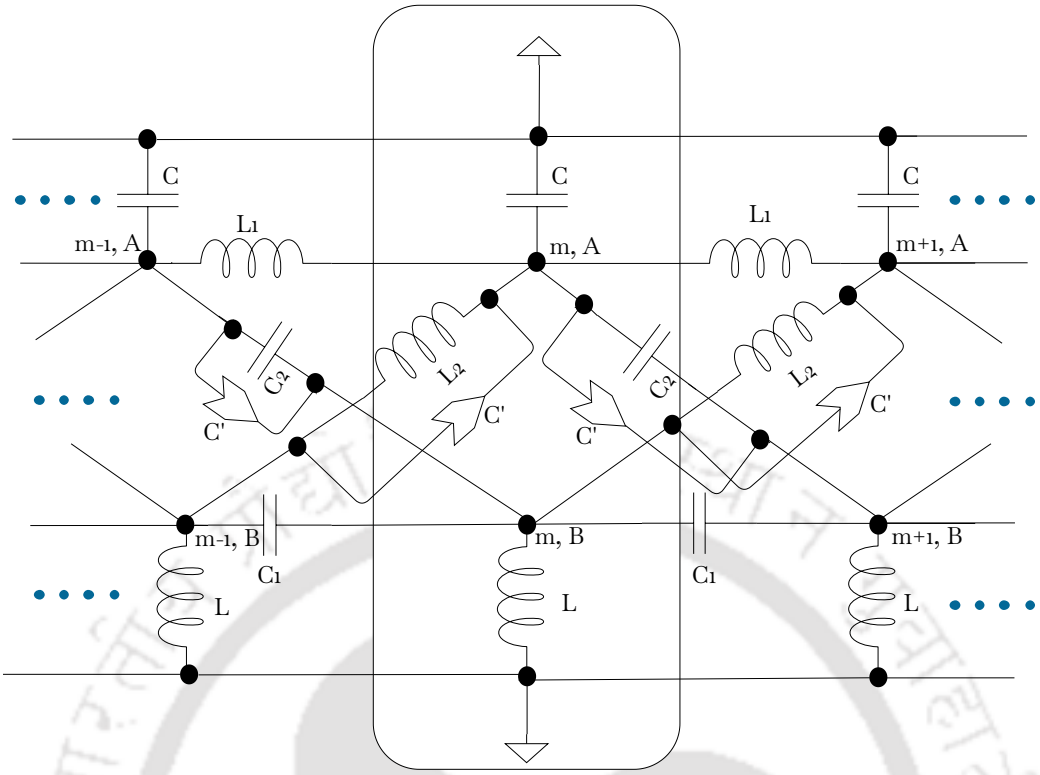

FIGURE 4.17: Circuit diagram for the $s\mathcal{PT}$ circuit. The INICs are denoted by the arrowheads, which offer an impedance $C' = C_x$ and $C' = -C_x$ for the forward $(m-1,\ A/B \rightarrow m,\ B/A)$ and backward $(m,\ A/B \rightarrow m-1,\ B/A)$ flow of current, respectively. The expressions (or values) for the remaining circuit elements are the same as for the Hermitian case.

falls below the critical value, ϵ_0, it corresponds to the $\mathcal{PT}$-breaking phase; that is, the system has not yet entered the $\mathcal{PT}$-broken phase. This phase is depicted in Fig. 4.16(d), where some of the eigenvalues become purely imaginary. Finally, for large values of $|\delta|$, all the eigenvalues become imaginary and appear in pairs with an imaginary line gap. The absence of the non-trivial point gap in Figs. 4.16(c) and 4.16(d) also suggests that the BBC is preserved for this system, and hence GBZ theory is not performed here. To provide a lucid description, we present Table 4.1 to summarize localization phenomena across different NH models, highlighting their unique features and enumerating the presence or absence of NHSE and its variants.

4.3.1 TEC Realization

The inclusion of non-reciprocity in a circuit is achieved via the INICs, connected in parallel with C_2 and L_2 between the nodes, as shown in Fig. 4.17. They provide a capacitance $C' = \pm C_x$, equivalent to $\pm\delta$ in the corresponding TB model. The expressions for C and L remain unchanged from those in the Hermitian circuit (Fig. 4.5). The IP,

Cases	1	2	3	4
NH models	$n\mathcal{PT}$ model without TRS	$n\mathcal{PT}$ model with TRS but no PHS ($\Delta = -\tilde{\Delta}$)	$n\mathcal{PT}$ model with both TRS & PHS ($\Delta = \tilde{\Delta}$)	$s\mathcal{PT}$ model
Cause of non-Hermiticity	onsite staggered imaginary potential	non-reciprocity in t ($A \leftrightarrow A$ or $B \leftrightarrow B$)	non-reciprocity in t ($A \leftrightarrow A$ or $B \leftrightarrow B$)	non-reciprocity in t_{AB} ($A \leftrightarrow B$)
NHSE	no NHSE	normal NHSE	NHSE at both edges	no NHSE

TABLE 4.1: Presence or absence of NHSE in different NH quasi-1D models. Δ and $\tilde{\Delta}$ are the parameters, responsible for preserving (or breaking of) PHS within the $n\mathcal{PT}$ (with TRS) system, defined in Eq. (4.26).

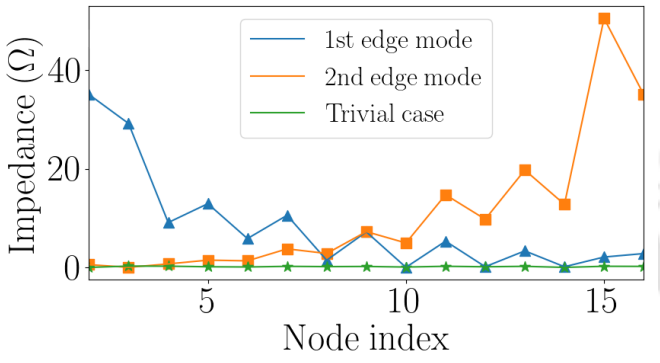

FIGURE 4.18: The IP for the $s\mathcal{PT}$ NH circuit. The plot is obtained with the same values of circuit elements used for the Hermitian case (Fig. 4.6) and fixing the value of $|C'|$ at 15 μF.

mimicking the edge modes, is shown in Fig. 4.18, as long as $C_2 + C_3 < 3C_1$, which is similar to the condition, $\epsilon < 2t$ in the TB model.

4.4 Summary

In this chapter, we have explored NH extensions of a quasi-1D ladder model, comparing them with their Hermitian counterparts to understand the effects of non-hermiticity. The extension into the NH realm bifurcates the model into two distinct versions: an $s\mathcal{PT}$ model and an $n\mathcal{PT}$ model (with or without TRS). Notably, we have found that in the $s\mathcal{PT}$ system, spontaneous $\mathcal{PT}$ symmetry breaking occurs, segregating the system into $\mathcal{PT}$-unbroken and $\mathcal{PT}$-broken phases. For the $s\mathcal{PT}$ system, depending on the choice of non-reciprocity, three different phenomena emerge, namely, a) no NHSE ($s\mathcal{PT}$ model), b) normal NHSE ($n\mathcal{PT}$ model with TRS), and c) NHSE at both edges ($n\mathcal{PT}$ model with TRS and PHS). Thus, by simply tuning the model's parameters, it is possible to realize the buildup of bulk states at either edge (normal NHSE), at both edges, or even their delocalization (no NHSE). We have constructed TECs for all three models, in which the IP of each circuit faithfully mimics the topological edge modes (or skin modes) within the corresponding TB model.

Chapter 5

Anderson Localization and NHSE in an Aubry-André (AA) Model

The previous chapters examined the NH properties of the SSH model and a quasi-1D system, uncovering a range of intriguing phenomena, from the GBZ theory to the absence of the NHSE in another variant of a non-reciprocal model (Section 4.3 of Chapter 4). These remarkable consequences of the interplay between non-hermiticity and topology naturally motivate a deeper investigation of NH systems. In this chapter, we focus on a 1D NH system in the presence of disorder. Since disorder, impurities, and defects are unavoidable in realistic material fabrication, incorporating them provides a more comprehensive and physically relevant understanding of NH systems. Since the pioneering work of Anderson in 1958 [205], it has been understood that disorder can localize a quantum particle despite the presence of quantum tunneling, widely known as Anderson localization (AL). It was shown that an infinitesimal random disorder in a system induces a transition from an extended to a localized phase in any dimension less than three. Thus, in three dimensions, for a fixed energy and beyond a critical disorder strength, quantum states transition from being delocalized to a completely localized phase. Substantial progress in elucidating the underlying physics (e.g., the role of dimensionality, mobility edge, etc) was made during the 1970s and 1980s through the development of scaling theory and field-theoretical approaches to localization.

Interestingly, the localization phenomenon is neither a prerogative of random disorders nor limited to three-dimensional systems. Quasiperiodic (QP) disorders with incommensurate periods can also result in localization effects, which we describe as AL. Among the various QP models, the Aubry-André model [206] has garnered significant attention for its theoretical elegance [207–209] and experimental realizations in platforms like photonic crystals [210–212], ultra-cold atoms [213, 214], and superconducting circuits [215]. A hallmark of the AA model is the absence of mobility edges, an energy-dependent localization transition in the system. This robustness makes the AA model an excellent platform for exploring localization phenomena. Furthermore, the interplay between disorder and non-hermiticity has also gained significant attention, particularly with the proposal of the Hatano-Nelson model in 1996 [129] (also discussed in Section 1.5 of Chapter 1 in detail). Within the TB framework, this 1D model, characterized by asymmetric hopping and random disorder, exhibits a delocalization-localization (DL) transition. Thus, disordered NH systems, particularly the NH QP models [216–221], have attracted significant research interest. Interestingly, AL and NHSE are two distinct confinement phenomena of the eigenstates, induced by disorder and non-reciprocity, respectively. Thus, understanding their interplay within a unified framework offers valuable insights into the localization properties of low-dimensional systems. In this chapter, we investigate an NH AA model, which serves as an ideal platform due to its unique self-dual properties and its ability to exhibit a DL transition in one dimension. While a substantial body of literature exists on the realization of the NHSE using TECs [4, 104, 108, 109, 175] and on AL in QP systems [222–225], the intricate interplay between these two phenomena has been addressed in only a few recent studies [222, 226–228]. For instance, Ref. [228] explores a Hatano–Nelson model with coexisting QP and periodic potentials and proposes a TEC realization. However, it does not demonstrate the competition between AL and NHSE in a realizable setup. Other theoretical works, such as Refs. [226, 227], analyze this competition, but do not address any experimental implementation. In contrast, Refs. [104, 109] present experimental demonstrations of phenomena like higher-order skin effect and scale-tailored localization in TECs, albeit in the absence of any QP disorder. Similarly, while Ref. [222] investigates the AL–NHSE transition in a non-reciprocal AA model and proposes a TEC framework; it does not provide a means to control the interplay between these two localization mechanisms, either in the TB model or its circuit realization. In this work, we bridge these gaps by offering a comprehensive analysis of the competition between AL and NHSE, demonstrating its realization in TEC as usual. However, to provide readers with a more realistic perspective on circuit construction and the corresponding outputs of TECs, we perform simulations using the LTspice software developed by 'Analog Devices' [229]. This approach yields results that closely reproduce experimental conditions and therefore offer a faithful representation of experimentally observable behavior.

The chapter is organized as follows: Section 5.1 introduces the theoretical TB framework,

outlining the fundamental physics. In section 5.2, we investigate the time evolution of the AA model when excited at an arbitrary site. Section 5.3 explores the construction of the electrical analog of the NH AA model, and the theoretical time evolution of the TEC. Sections 5.4 and 5.5 focus on the visualization of NHSE and AL, respectively, in the TEC setting through voltage measurements performed using LTspice. Section 5.6 examines the interplay between AL and NHSE within the TEC. Finally, section 5.7 summarizes our findings and discusses potential experimental realizations or device implementations inspired by our theoretical framework.

5.1 The Hamiltonian

We adopt the non-reciprocal version of the NH AA model introduced by S. Longhi [216], incorporating an interface at a particular lattice site of the chain. The Hamiltonian (in 1D) is given by,

$$H = \sum_{k=1}^{L_0} \Big[(t+\gamma)\hat{c}_{k+1}^{\dagger}\hat{c}_k + (t-\gamma)\hat{c}_k^{\dagger}\hat{c}_{k+1}\Big] + \sum_{k=L_0+1}^{2L} \Big[(t-\gamma)\hat{c}_{k+1}^{\dagger}\hat{c}_k + (t+\gamma)\hat{c}_k^{\dagger}\hat{c}_{k+1}\Big] + \sum_{k=1}^{2L+1} \lambda_k \hat{c}_k^{\dagger}\hat{c}_k, \tag{5.1}$$

where $\lambda_k = 2\lambda\cos(2\pi\beta k + i\alpha)$, and t, γ, and λ denote the strengths of the nearest-neighbor hopping, non-reciprocity, and QP disorder, respectively. All of these parameters are assumed to be real and positive. Note that all parameters in this TB model are in the unit of t. Our system comprises $(2L+1)$ lattice sites, and $(L_0+1)^{\text{th}}$ site marks the position of the interface, starting from the first node. The existence of an interface is convenient, though not indispensable, for the demonstration of a competitive behavior of AL and NHSE, which is the main focus of this chapter. For concreteness, we set $L_0 = L$ in Eq. (5.1) for further discussions and the corresponding circuit design. The parameter α introduces a complex component to the QP potential and plays a pivotal role in the delocalization-localization transition of our model. Its prominence will become evident in the subsequent discussions. β is an irrational number given by $\beta = (\sqrt{5}-1)/2$ with β^{-1} being the golden ratio. It is obtained via $\beta = \lim_{n\to\infty}\left(\frac{F_{n-1}}{F_n}\right)$, where the Fibonacci numbers F_ns are defined recursively by $F_{n+1} = F_n + F_{n-1}$ and $F_0 = 0, F_1 = 1$. The operators $\hat{c}_k$ and $\hat{c}_k^{\dagger}$ denote the annihilation and creation operators for spinless fermions at the site k.

The behavior of the system depends on two distinct scenarios: (a) $\lambda = 0$: in the absence of the QP potential, the system reduces to the clean Hatano-Nelson model (without any disorder). Here, NHSE arises due to the non-reciprocal hopping parameter γ. (b) $\lambda \neq 0$, $\alpha \neq 0$ and $\gamma \neq 0$: the model reduces to a non-reciprocal NH AA model that includes a complex QP potential with the introduction of α. In the clean Hatano-Nelson model without an interface, all the bulk states accumulate at one of the edges (termed

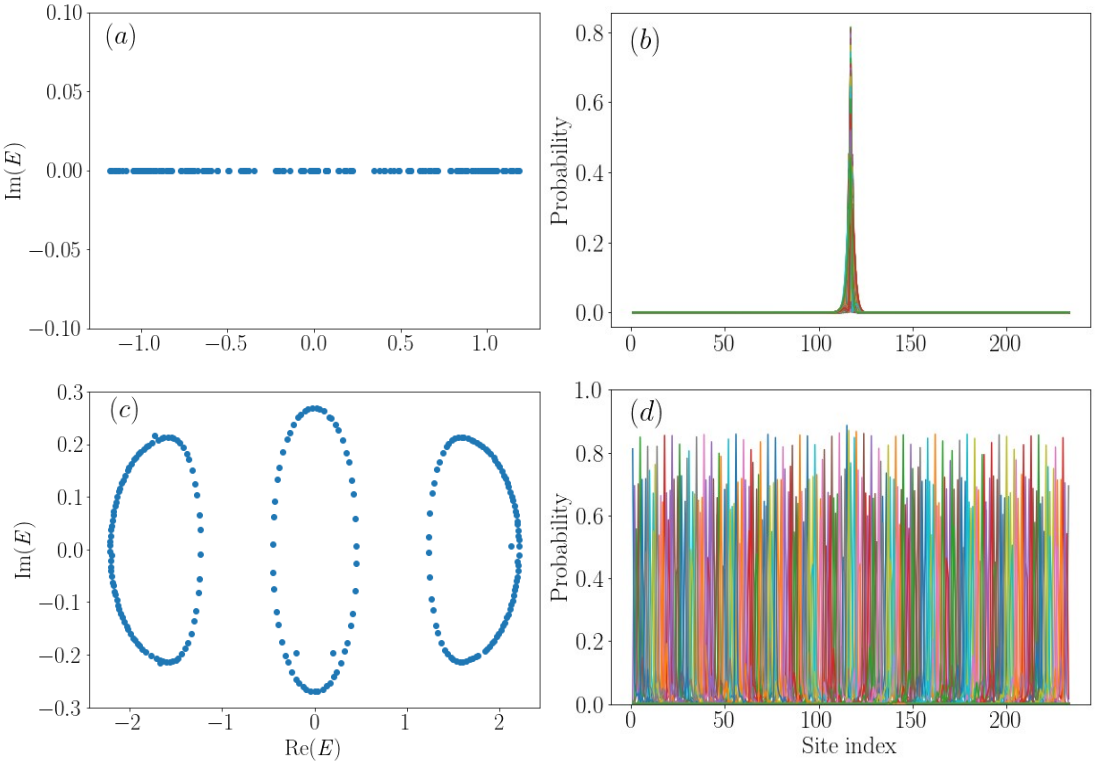

FIGURE 5.1: Numerical analyses for a total number of lattice sites, $(2L+1) = 233$, being a Fibonacci number, with $t = 0.65$ and $\gamma = 0.35$, are presented. (a) Real vs Imaginary parts of the energy spectra for $\lambda = \alpha = 0$; (b) Probability distribution of the corresponding eigenstates, which localize at site index $(L+1) = 117$. (c) Same as (a) but with $\lambda = 0.9$, $\alpha = 0.2$. (d) The skin states in (b) have now become AL states as α exceeds α_c ($\alpha_c \simeq 0.105$).

as NHSE), which is determined by the sign of the non-reciprocity parameter, γ. The energy spectra for PBC and OBC are markedly different, with the former creating closed loops in the complex plane that enclose the energy spectra corresponding to the open chain, which lies along the real axis [101]. The real valuedness of the OBC spectrum in the Hatano–Nelson model follows from the fact that its NH Hamiltonian can be mapped to a Hermitian Hamiltonian via a similarity transformation (see discussion on Fig. 1.1 in Section 1.5 of Chapter 1 for a detailed description). Fig. 5.1(a) shows the energy spectrum of H for $\lambda = 0$, which effectively represents a combination of a clean Hatano–Nelson model and its mirror image, joined back-to-back at the interface located at $k = L$. As a result of this structure, the energy spectrum becomes entirely real in the absence of the QP potential. The probability distribution of the corresponding eigenstates is shown in Fig. 5.1(b). These eigenstates localize at exactly the interface $(k = L)$.

In the presence of the QP potential ($\lambda \neq 0$, $\alpha \neq 0$) along with $\gamma \neq 0$, the spectrum displays a hierarchical structure of three bands, as illustrated in Fig. 5.1(c). In the case of $\gamma = \alpha = 0$, the system undergoes an AL transition at $\lambda = t$ [230], governed by the

NH parameters	$\alpha = 0$	$\alpha \neq 0$
$\gamma = 0$	$\lambda_c = t$	$\alpha_c = \ln \lvert t/\lambda \rvert$
$\gamma \neq 0$	$\lambda_c = \max(t+\gamma, t-\gamma)$	$\alpha_c = \ln \lvert \max(t+\gamma, t-\gamma)/\lambda \rvert$

TABLE 5.1: The table presents analytically determined delocalization-localization transition points as functions of the two NH parameters, namely, α (the imaginary phase of the QP potential) and γ (the non-reciprocity parameter in the hopping amplitude).

self-duality of the model. This property ensures the system is either fully extended or localized, dictated solely by the QP potential strength, λ. The introduction of α modifies this behavior, shifting the AL transition to a critical value of α, which is $\ln|t/\lambda|$. This occurs because all the localized eigenstates in the self-dual space share a uniform inverse localization length of $\ln|\lambda/t|$ [216]. With $\alpha = 0$ and $\gamma \neq 0$, the localization transition instead occurs at $\lambda = \max(t+\gamma, t-\gamma)$ [222]. Using Avila's global theory [231], Li *et al.* [221] demonstrated that for a generalized scenario ($\alpha \neq 0, \gamma \neq 0$), the AL transition occurs at

$$\alpha_c = \ln|\max(t+\gamma, t-\gamma)/\lambda| \tag{5.2}$$

Thus, Fig. 5.1(d) highlights this scenario through the probability distribution of eigenstates for a high value of α ($\alpha > \alpha_c$), where the AL dominates the NHSE. The above results are summarized in Table 5.1.

Let us briefly recapitulate the origin and the role of the imaginary component ($i\alpha$) in the QP potential, namely, $\lambda_k = 2\lambda\cos(2\pi\beta k + i\alpha)$. Hatano and Nelson [129] demonstrated that an imaginary vector potential induces a DL transition in a 1D randomly disordered system. Following this, extensive theoretical and experimental efforts have explored the role of an imaginary vector potential, particularly in QP-disordered 1D systems. Among those, the work of S. Longhi [216] is discernible, where he showed that an imaginary gauge field, introduced via complex QP potential having $\mathcal{PT}$ symmetry, the entire spectrum undergoes a DL transition along with $\mathcal{PT}$-symmetry-breaking when the imaginary gauge field exceeds a critical threshold value. In our system, the transition between AL and NHSE can be understood as follows. The non-reciprocity comes into play in the form of γ, which effectively swaps its role with α under a discrete Fourier transformation. Thus, when α exceeds a critical value α_c, which corresponds to the decay length of skin modes arising from γ, a DL transition occurs, converting skin modes into Anderson-localized states. In this way, α functions as a tunable imaginary gauge field that mediates the competition between boundary-localized NHSE states and disorder-induced Anderson localization.

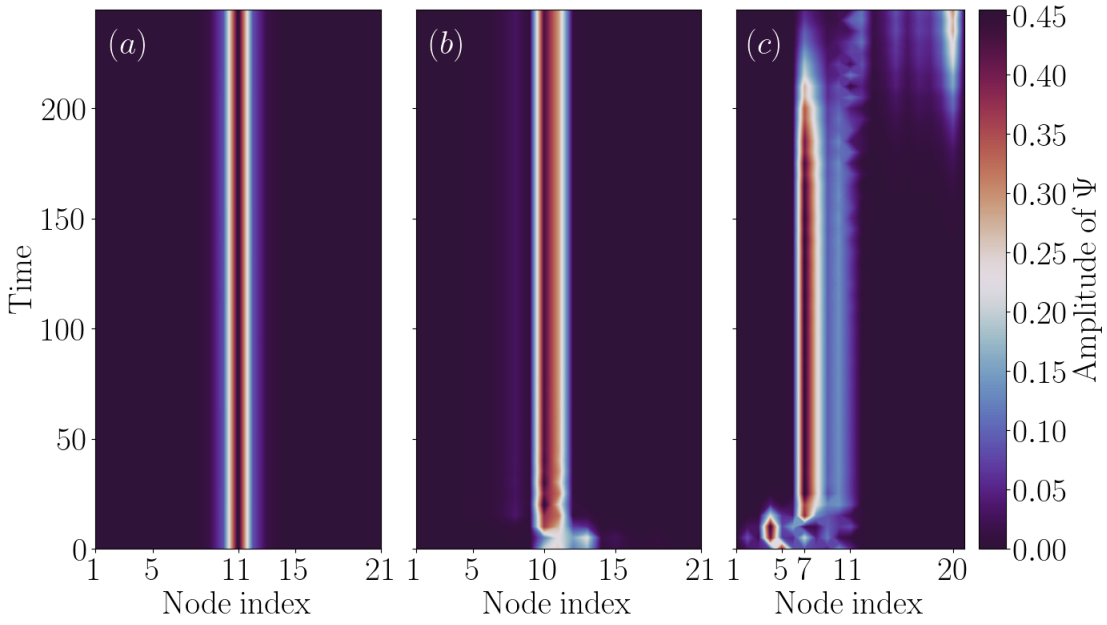

FIGURE 5.2: The temporal evolution of the excitation spectrum in our model is illustrated for three scenarios: (a) $\lambda = 0$, (b) $\lambda = 1$, $\alpha = 0.425$, and (c) $\lambda = 1$, $\alpha = 0.9$. In the first case, the wavefunction localization at the interface is attributed to the NHSE. In the second case, at $\alpha = \alpha_c$, a slight shift in the localization is observed. Finally, for a much larger value of α, the wavefunction localizes from the 5^{th} site to the 4^{th} site, then to the 7^{th} site for an extended period, and eventually localizes at the 20^{th} site.

5.2 Time Evolution of the NH AA model

We have explored the localization properties of the eigenstates of the Hamiltonian for the NH AA model given by Eq. (5.1). An intriguing question arises: does the interplay between the NHSE and the AL persist over long time scales, or does the time-evolved system unveil any interesting physics? To address this, we investigate the time evolution of an excited wavefunction in the NH AA model. Let the initial wavefunction at $t = 0$ be $|\Psi(x,0)\rangle$, which can be expanded as a linear combination of the eigenstates of H in Eq. (5.1), be given as

$$|\Psi(x,0)\rangle = \sum_{q=1}^{2L+1} a_q(0)\psi_q(x), \tag{5.3}$$

where $a_q(0)$ is the coefficient corresponding to the q^{th} eigenstate (ψ_q) at $t = 0$ and is responsible for the time evolution of the initial wavefunction, $|\Psi(x,0)\rangle$. Note that x is a discrete variable and lies in the range $x \in [1, 2L+1]$. As, the eigenstates, $\psi_q(x)$ of H form a complete orthonormal basis, we can express $a_q(0)$ and $a_q(t)$ as,

$$\begin{aligned} a_q(0) &= \langle\psi_q(x)|\Psi(x,0)|\psi_q(x)|\Psi(x,0)\rangle\,. \\ \text{At } t \neq 0, \quad a_q(t) &= \langle\psi_q(x)|\Psi(x,0)|\psi_q(x)|\Psi(x,0)\rangle\, e^{-\frac{iE_q t}{\hbar}}, \end{aligned} \tag{5.4}$$

for any q, where E_q is the eigenvalue corresponding to the eigenvector, $\psi_q(x)$.

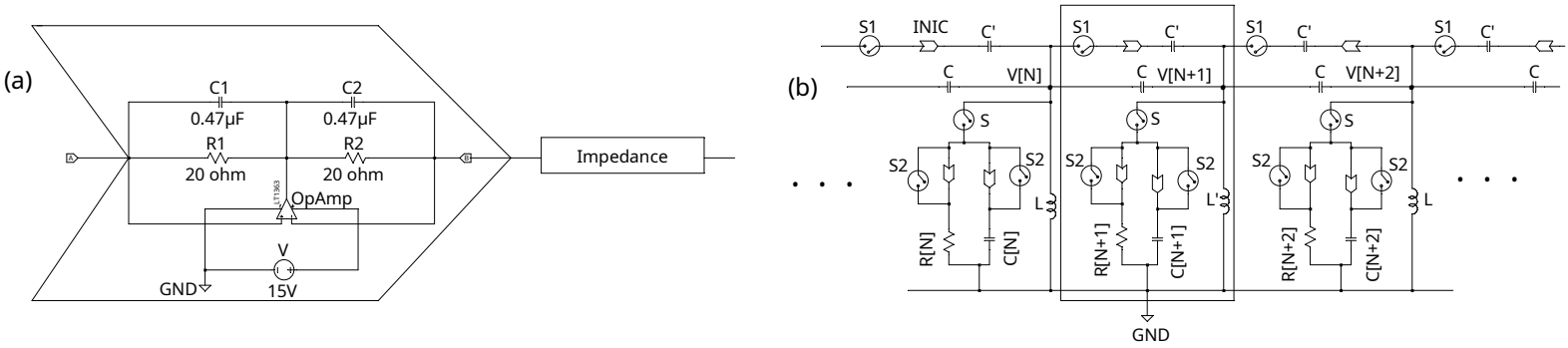

FIGURE 5.3: (a) Circuit diagram of an INIC is shown. The current entering the INIC from the left (right) side experiences a negative (positive) impedance in the rectangular box. (b) The TEC diagram corresponds to the non-reciprocal NH AA model. The rectangular box denotes the $(N+1)^{\text{th}}$ node of the TEC. $V[N]$ denotes the output voltage at N^{th} node.

Now, as an initial condition, we choose a delta-type excitation, created at $x = m$ (m : denoting the site index) of the form,

$$|\Psi(x,0)\rangle = \delta(x-m), \tag{5.5}$$

which is localized entirely at the m^{th} site and is zero elsewhere. The time evolution of $|\Psi(x,0)\rangle$ from Eqs. (5.3) and (5.4), can be expressed as,

$$|\Psi(x,t)\rangle = \sum_{q=1}^{2L+1} \langle\psi_q(x)|\Psi(x,0)|\psi_q(x)|\Psi(x,0)\rangle\, e^{-\frac{iE_q t}{\hbar}} \psi_q(x). \tag{5.6}$$

However, this equation applies explicitly to systems without boundaries, where x ranges from $-\infty$ to $+\infty$. Hence, assuming that the wavefunction yields vanishing probability density at the edges of the chain, any reflection of the state during its evolution is thereby precluded. Subsequently, we can reliably use Eq. (5.6) to determine $|\Psi(x,t)\rangle$ for any finite range of x at all subsequent times.

NH systems are known for their non-conservation of energy, leading to non-unitary time evolution. As a result, these systems violate probability conservation, resulting in the norm of the wavefunction either growing or diminishing as a function of time. Thus, we have to normalize the amplitude of the evolved wavefunction with its norm at each small interval dt, which occurs through a two-step process [232]. First, the wavefunction evolves according to,

$$|\Psi(x,t+dt)\rangle = e^{-\frac{iHdt}{\hbar}} |\Psi(x,t)\rangle\,. \tag{5.7}$$

This is hence followed by a normalization step,

$$|\Psi(x,t+dt)\rangle = \frac{|\Psi(x,t+dt)\rangle}{||\,|\Psi(x,t+dt)\rangle\,||}, \tag{5.8}$$

where ||.|| denotes the norm.

Let us now employ Eqs. (5.7) and (5.8) to numerically analyze $|\Psi(x,t)\rangle$. As an example, we excite the delta-type wavefunction at a specific site, namely the 5^{th} site, that is, $m = 5$ in Eq. (5.5). Fig. 5.2(a) illustrates the NHSE observed at the interface in the absence of any QP potential ($\lambda = 0$). Fig. 5.2(b) represents the system at a critical value of α, given by $\alpha_c = \ln|\max(t+\gamma, t-\gamma)/\lambda| \simeq 0.425$ for $\lambda = 1$. At this point, the eigenstates of H undergo a transition from exhibiting NHSE to AL, and the localization of the time-evolved wavefunction starts to shift away from the interface. For $\alpha > \alpha_c$, $|\Psi(x,t)\rangle$ no longer remains localized at the interface, as shown in Fig. 5.2(c). Instead, the wave propagates via quantized jumps between the AL states, randomly distributed across distinct sites of the chain, a phenomenon termed NH jumps [233–235]. These jumps are distinctive artefacts of the NH disorder, incorporated via the parameter α in our case. Thus, the time evolution of the wavefunction involves several NH jumps over a specific time frame, as depicted in Fig. 5.2(c). The jumps can be predicted with the help of both the initial wavefunction $|\Psi(x,0)\rangle$ and $a_q(t)$. Note that $a_q(t)$ depends on the corresponding eigenvalues, given by Eq. (5.4).

5.3 TEC of an NH AA Model

Now, we focus on forming an analog circuit corresponding to the TB model given by Eq. (5.1). To achieve the goal, the Laplacian of the circuit must accurately replicate the Hamiltonian at the resonant frequency, f_R, of the circuit. The inter-site hoppings can be modeled by capacitors (C), while the non-reciprocity in the hoppings (γ) is introduced via INIC (see Fig. 2.1(b) and the discussion therein of Chapter 2) in the circuit. As shown in Fig. 5.3(a), for the realization of the INIC, an Op-Amp is employed. The Op-Amp is operated in negative feedback configuration, meaning its output is coupled to its inverting (negative) input via the impedance formed by $C1$ and $C2$ (in our case). To ensure the stability of the circuit, two resistors ($R1 = R2 = 20\,\Omega$) are placed in parallel to the capacitors, $C1$ and $C2$, as shown in Fig. 5.3(a). The resonant frequency of the circuit is given by,

$$f_R = \frac{1}{2\pi\sqrt{2LC}} \simeq 5191\,Hz; \quad \omega_R = \frac{1}{\sqrt{2LC}}, \tag{5.9}$$

with $L = 10\,\mu$H and $C = 47\,\mu$F. All these values are standard for commercial uses and are kept fixed throughout this work. The real and the imaginary parts of the QP potential, λ_k in Eq. (5.1), are represented by node-dependent capacitors ($C[k]$) and resistors ($R[k]$), respectively, with $|\text{Re}(\lambda_k)| \equiv \omega_R\, C[k]$, and $|\text{Im}(\lambda_k)| \equiv [R[k]]^{-1}$. Here, k denotes the node index and is analogous to the site index of Eq. (5.1). Building on the formalism and methods used to simulate TEC in the previous chapters, we write KVL

and KCL for each node of the TEC corresponding to the NH AA model. The detailed mathematical rigor behind the formation of the Laplacian of this TEC is provided in Appendix C. The switches for the circuit elements are denoted by S and $S1$. The circuit also includes master switches for S and $S1$ (not shown in Fig. 5.3(b)), which control all the S and $S1$ switches across the circuit. For instance, the master switch for S ($S1$) can simultaneously open or close all S ($S1$) switches. However, this functionality does not extend to $S2$, as $S2$ is specifically designed to alter the signs of $C[k]$ or $R[k]$ based on the values of λ_k, which, in turn, depend on the node index, k. The total number of nodes is $(2N + 1) = 21$, which is kept fixed throughout the analysis. It is worth noting that 21 nodes for a TEC are sufficient to obtain reliable results with the TEC framework using LTspice [229]. Let us briefly summarize the measurement process and the data acquisition thereafter using LTspice. Users can select from LTspice's built-in device models or define their own. To construct a circuit in the software, elements from its library (or customized models) are placed on the schematic to obtain a desired circuit diagram, followed by appropriate connections. Once assembled, the circuit is simulated to observe its response under various conditions, including the presence or absence of external sources. It is important to note that LTspice presents the node voltages and currents through circuit elements as functions of time using a graphical interface. To get results in support of the theoretical results in Fig. 5.1, we have to obtain the eigenvectors of the Laplacian in terms of measurable quantities like the VP or the IP. However, to do that, every node must be excited via a current (or a voltage) source, making the process unnecessarily complicated. Instead, a more practical approach is to excite a single node using a current (or a voltage) source and simulate the voltage response of the TEC using LTspice. The calculations still allow us to observe the localization of the VP, which is analogous to NHSE and AL in the TB model (Figs. 5.1(b) and 5.1(d)). Interestingly, both these phenomena are tunable in our TEC.

5.3.1 Time Evolution of the Voltage Profile

In this section, we theoretically demonstrate the results of an NH AA circuit. It is difficult to visualize a specific eigenstate of the Laplacian, $\mathcal{L}$, as a measurable VP. This challenge arises because every node in the TEC network must be excited via a precisely calibrated current source. For example, to measure the k^{th} eigenstate of $\mathcal{L}$, denoted as V_k, the amplitude of the current source at each node must satisfy the equation,

$$I = \mathcal{L}V_k = \zeta_k V_k,$$

where ζ_k is the k^{th} eigenvalue of $\mathcal{L}$. To overcome this challenge, a current source, $I(t)$, can be applied at any node, and the VP ($V(t)$) can be measured at a later time. Similar to Eq. (5.3), $V(t)$ can also be expanded as a linear combination of the eigenvectors of

$\mathcal{L}$, with time-dependent coefficients $a_k(t)$,

$$V(t) = \sum_{k=1} a_k(t) V_k. \tag{5.10}$$

We assume that V_k forms a complete orthonormal basis for $\mathcal{L}$ with $V_a^\dagger V_b = \delta_{ab}$. Substituting these into KVL and KCL leads to

$$I(t) = \mathcal{L}V(t) = \sum_{k=1} a_k(t)\zeta_k V_k; \quad a_k(t) = \frac{V_k^\dagger I(t)}{\zeta_k}. \tag{5.11}$$

Thus, the coefficients $a_k(t)$ can be evaluated at any time t, provided the input current $I(t)$ is uniquely defined. The expression for $a_k(t)$ in Eq. (5.11) becomes directly comparable to the coefficients $a_q(t)$ in Eq. (5.4) only when $I(t)$ takes the form of a delta-type excitation, that is, a sharply peaked current pulse of very high amplitude at $t = 0$ with vanishingly short duration. Only under this condition does the time evolution of the VP in Eq. (5.10) accurately correspond to the evolution of the wavefunction $|\Psi(x,t)\rangle$ described in Eq. (5.6). However, to study the dynamical behavior of the TEC, we resort to a specific case and excite the 18^{th} node with a current source, $I(t) = \sin\omega_R t$, having an amplitude of 1 mA and ω_R representing the resonant frequency of the circuit. By employing Eqs. (5.10) and (5.11), we obtain $V(t)$, which is then represented as a colormap in Fig. 5.4. Figs. 5.4(a) and (b) illustrate the scenario for $\alpha \leq \alpha_c$, where the NHSE still dominates over AL in the TEC. This behavior mirrors that of the NH AA

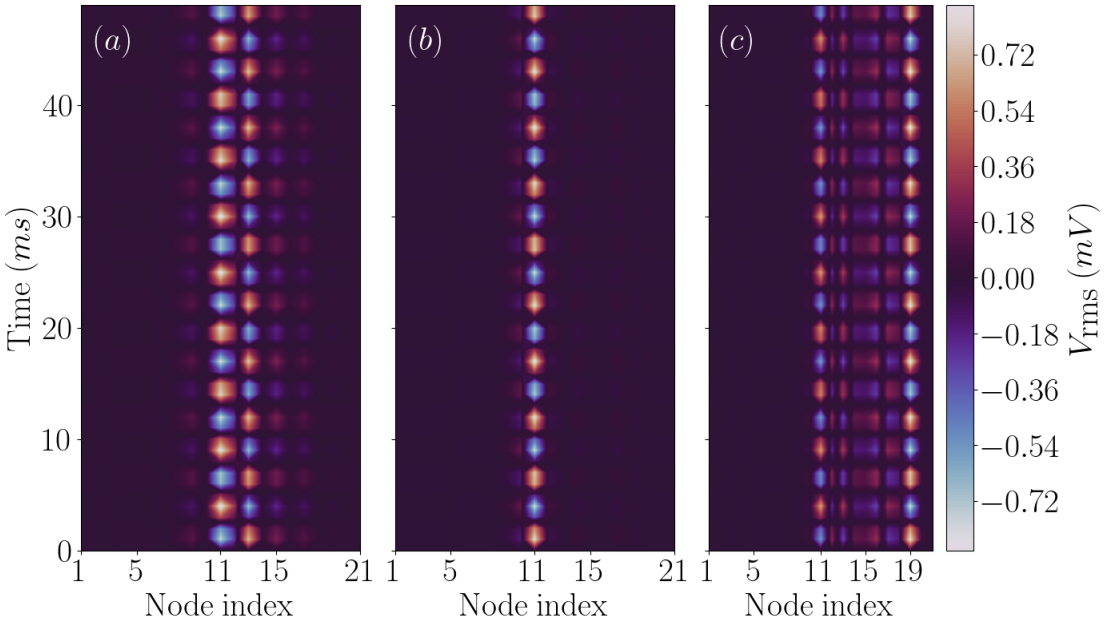

FIGURE 5.4: (a) The occurrence of NHSE is evident as the $V(t)$ localizes at the interface, specifically at 11^{th} node. (b) When $\alpha = \alpha_c$, all the eigenstates of the Laplacian $\mathcal{L}$ transition from being the skin states to the AL states, yet the VP remains localized at the interface. (c) Finally, for a larger value of α, the localization shifts towards the excitation node, which is the 18^{th} node.

model in Figs. 5.2(a) and (b), as the excitation remains localized at the interface (the 11^{th} node). However, compared to Fig. 5.2(c) for the case of the TB model, no NH jumps are observed in the TEC, as seen in Fig. 5.4(c). This difference arises because the input current $I(t)$ in the circuit is a sinusoidal function of time rather than a delta-type excitation. Instead, the VP settles at the 19^{th} node, located in the vicinity of the excitation (18^{th}) node.

5.4 NHSE in NH AA Circuit

To realize and explore the NHSE in the non-reciprocal circuit, we open (disconnect) the master switch for all the S switches and close (connect) the master switch for all the $S1$ switches in Fig. 5.3(b), thereby configuring the TEC to replicate the clean Hatano-Nelson model with an interface. To demonstrate a voltage build-up, we excite the 3^{rd} node with a voltage pulse of amplitude 1 mV for a duration of $10\,\mu$s and record the output signal at each node for $3000\,\mu$s. To effectively analyze the output, we calculate the root-mean-square (RMS) values of the voltage signal at suitable time intervals for each node. It is important to note that we have verified that all the relevant phenomena are captured with this time range ($3000\,\mu$s). Thus, for this particular setup, observations are made for a time duration of $t = 3000\,\mu$s, corresponding to the maximum value along the y-axis (representing time). Using LTspice, these data are visualized in a color map of VP as a function of time in Fig. 5.5. The results show that the VP localizes at the interface, specifically at 11^{th} node, as illustrated in Fig. 5.5. This behavior closely reflects the NHSE observed in our TB model (Fig. 5.1(b)). Moreover, this interface localization of the VP serves as a direct representation of the time-evolved wavefunction in the TB model (see Fig. 5.2(a)) and the TEC (Fig. 5.4(a)), where the delta excitation at the 5^{th} site ultimately localizes at the 11^{th} site. The grounded inductors at the edges have a distinct value of $L_{\text{edge}} \simeq 62\,\mu$H, while the inductor at the 11^{th} node, representing the interface, is chosen as $L' \simeq 6\,\mu$H. These values differ from the other grounded inductors, $L\,(= 10\,\mu\text{H})$. To ensure that the resonance conditions required by the Laplacian of the TEC (see Eq. (C.2) of Appendix C) are satisfied for faithfully reproducing the TB model, we choose specific values for L_{edge} and L'. The role of the non-reciprocity parameter, γ is implemented using $C'\,(= 32\,\mu\text{F})$ along with an INIC (see Fig. 5.3(b)). The mapping between the TB model and the circuit is thus established via the relations $(t \pm \gamma) \equiv \omega_R\,(C \pm C') \simeq (1.53 \pm 1.04)$. Recently, Liu *et al.* [104] demonstrated NHSE at the interface in TECs for both 1D and 2D systems by employing a voltage follower, where the current flows unidirectionally, instead of using an INIC. Both approaches are well-accepted and provide reliable results for constructing non-reciprocal circuits.

Let us now illustrate the measurement procedure to generate Fig. 5.5 and its production from the raw data obtained from LTspice. Since the excitation (voltage pulse) at the

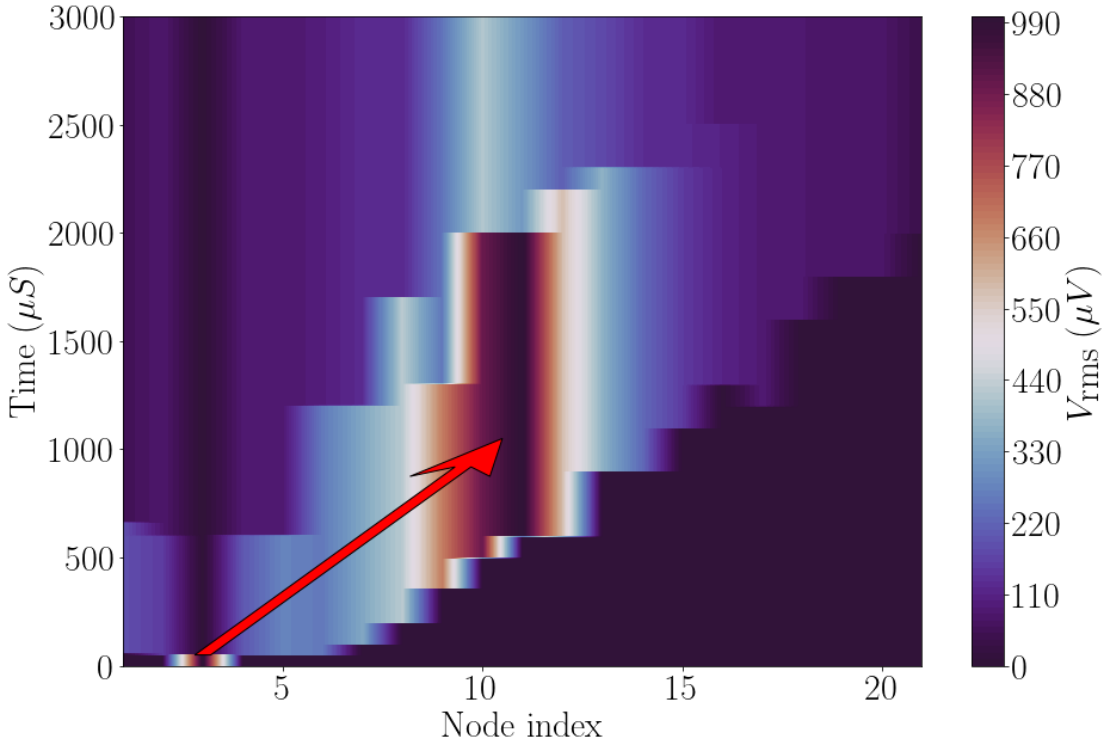

FIGURE 5.5: Colormap of the RMS values of the output VP as functions of both time and node index is shown. Commencing around 500 μs and continuing until approximately 2000 μs, the VP shows localization at the interface, located at the 11$^{\text{th}}$ node. The red arrow illustrates the progression of the excitation from the 3$^{\text{rd}}$ node to the interface at large times.

3$^{\text{rd}}$ node is short-lived and vanishes after 10 μs, localization for a short duration appears at the 3$^{\text{rd}}$ node in Fig. 5.5 when the voltage is measured. Consequently, the circuit's response is temporally constrained, implying that the output voltage at any node decays with time due to the presence of dissipative elements, such as the resistors (embedded within the INIC). This makes smooth voltage measurement as a function of time (at very short intervals) challenging. Therefore, the most effective approach is to measure the RMS values of the output over non-equivalent discrete time intervals. For instance, the output voltage at the 11$^{\text{th}}$ node (interface) is measured at the following time intervals: (i) $0-600\,\mu$s, (ii) $600-2000\,\mu$s, and (iii) $2000-3000\,\mu$s. These chosen time intervals vary from node to node, depending on where the output signal reaches its maximum amplitude and how long it is sustained before decaying. This measurement process is responsible for the appearance and disappearance of the voltage localization occurring in a stepwise manner, observed in Fig. 5.5. Furthermore, the data along the z-axis, representing the RMS values of output voltages at different nodes and time intervals, are linearly interpolated in Python to ensure smooth transitions while preserving the integrity of the raw data obtained from LTspice. Interestingly, no signal is detected at the 11$^{\text{th}}$ node up to $t = 600\,\mu$s, as the RMS value of the output voltage in this interval is nearly zero. However, during the $600 - 2000\,\mu$s interval, the RMS value

increases significantly, leading to the 'dark' region (approximately 990 μV) in Fig. 5.5. Alternatively, this can be understood by noting that, initially excited at the 3$^{\text{rd}}$ node, the signal requires 600 μs to reach the interface at the 11$^{\text{th}}$ node, represented by the red arrow, and hence, no output signal is observed at the 11$^{\text{th}}$ node before $t = 600\,\mu$s. Similarly, in the $2000 - 3000\,\mu$s interval, the RMS output voltage diminishes due to dissipation in the circuit. This localization occurs regardless of the excitation node and the pulse amplitude (or pulse form, such as square, triangular, etc.), demonstrating the robustness of the phenomenon. Interestingly, it parallels the phenomenon of topological funneling of light, where a light field within a photonic mesh lattice with an interface is directed toward the interface, irrespective of its shape or the input location [236].

5.5 AL in an NH AA Circuit

As depicted in Fig. 5.3(b), to isolate and observe the AL, we close the master switch for S while keeping $S1$ open. The only practical technique to incorporate the onsite QP potential in the circuit is to place the capacitors and resistors obeying the following equations, namely,

$$C[k] = -\text{Re}(\lambda_k)/\omega_R = -2\lambda\cos(2\pi\beta k)\ \cosh\alpha/\omega_R, \tag{5.12}$$

$$R[k] = [\text{Im}(\lambda_k)]^{-1} = [-2\lambda\sin(2\pi\beta k)\ \sinh\alpha]^{-1}, \tag{5.13}$$

derived from the expression for λ_k in Eq. (5.1) with β^{-1} being the golden ratio. It is crucial to note that both $\text{Re}(\lambda_k)$ and $\text{Im}(\lambda_k)$ being oscillatory functions, can assume negative values, and consequently, $C[k]$ and $R[k]$ may be negative. To avoid negative capacitance values, a capacitor of constant value can be grounded [225], ensuring no impact on the central results. However, this strategy is not feasible for resistors, as additional grounded resistors would unnecessarily increase dissipation in the circuit. As a remedy, we implement negative resistors using INICs. The reason behind the employment of the INIC in this case is very similar to that of $\mathcal{PT}$-symmetric SSH circuit, discussed in Section 3.3.1 of Chapter 3. To get $-R[k]$ or $-C[k]$, the absolute values of them are placed at each node based on the values of $|\text{Re}(\lambda_k)|$ and $|\text{Im}(\lambda_k)|$, respectively, and $S2$ switches are carefully toggled (closed or opened) at each node to fix the signs of $\text{Re}(\lambda_k)$ and $\text{Im}(\lambda_k)$. Moreover, the grounded inductors at the edges have a value of $L_{\text{edge}} = 20\,\mu$H, while L' is identical to L as there exists no interface in this case.

Fig. 5.6 illustrates the VP of this TEC setup, analogous to the reciprocal NH AA model, as a function of α, with $\lambda = 1$ in Eq. (5.1). A constant current source of amplitude 1 mA and frequency f_R, as defined in Eq. (5.9), is applied at the 4$^{\text{th}}$ node. This leads to a smooth variation of VP, in contrast to the stepwise pattern observed

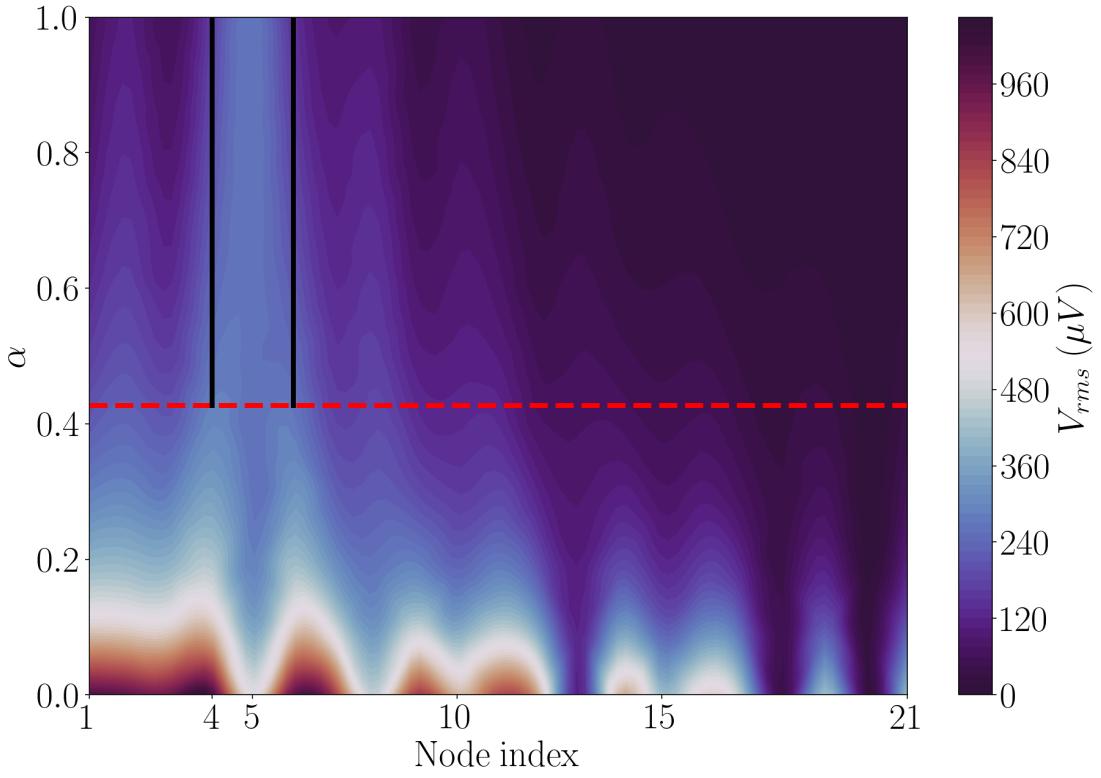

FIGURE 5.6: The RMS values of the output signal, measured over a time duration between 600 μs and 2000 μs, are presented as functions of the node indices and α. The red dashed line denotes the critical value of α, namely, α_c, obtained from Eq. (5.2). The two black vertical lines indicate the localization of the VP at the 5^{th} node for $\alpha > \alpha_c$.

in Fig. 5.5. Consequently, there is no need to compute the RMS value of the output voltage over different time segments for different nodes. For the reciprocal NH AA model, the AL transition should occur at the critical value $\alpha_c = \ln|t/\lambda|$, calculated using Eq. (5.2), with $\gamma = 0$. The red dashed line in the figure marks this critical value, $\alpha_c \simeq 0.425$. However, a sharp transition is not observed due to practical factors such as the finite system size (only 21 nodes being considered) and the simulational limitations of LTspice. Nevertheless, the results demonstrate that for $\alpha > \alpha_c$, the VP becomes predominantly localized at the 5^{th} node. When our simulation is repeated by considering excitation at different nodes (not shown here), the localization consistently occurs in the vicinity of the respective excitation node, thus highlighting a predictable and robust localization center. The predictability sharply contrasts with the NH jumps observed in our TB model (Fig. 5.2(c)), where wave packet evolution transpires not through gradual diffusion but sudden transitions between the distinct states. This discrepancy arises from the nature of the input excitation. In experimental setups, the time evolution of the VP is highly sensitive to the form of the initial stimulus. While the NH jumps in theoretical simulations result from the spontaneous evolution of an initially localized delta-type wavefunction, the VP localization for the TEC in Fig. 5.6 emerges under a steady sinusoidal current source, which we have thoroughly discussed in Section 5.3.1.

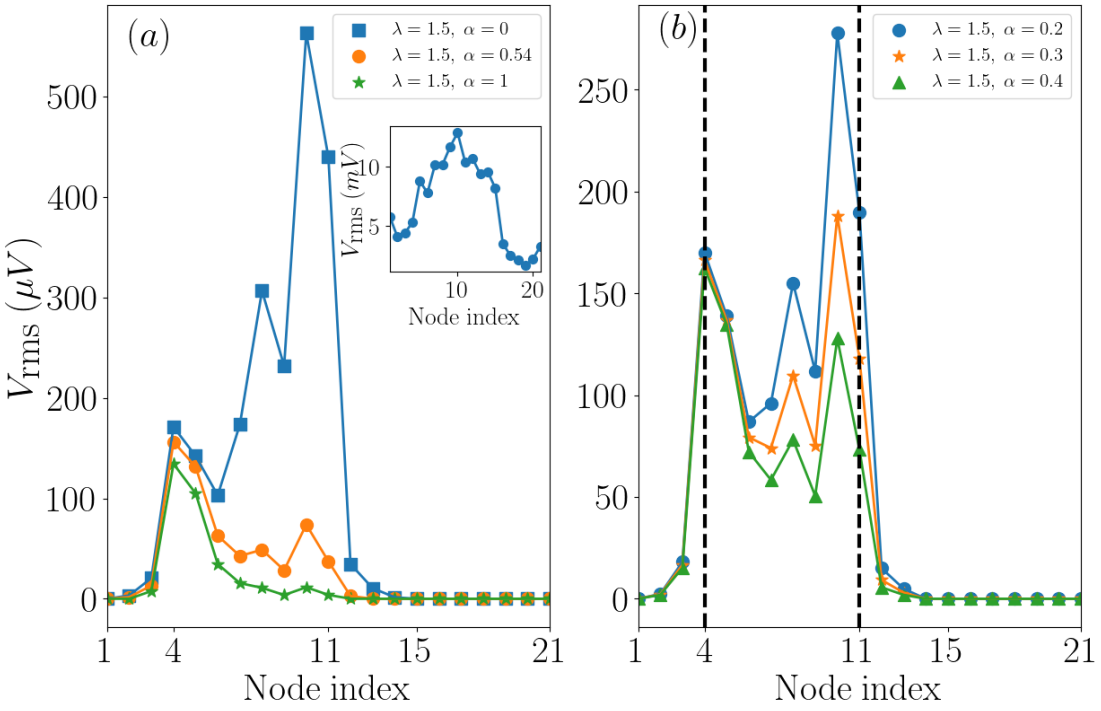

FIGURE 5.7: (a) The RMS values of the VP are plotted for different values of α at $\lambda = 1.5$. The time interval $1000\,\mu s - 3000\,\mu s$ is used as a prototype over which the integration is carried out to calculate the RMS voltage for improved accuracy. The VP moves towards the $4^{\rm th}$ node at $\alpha = \alpha_c$ with a much smaller amplitude. The inset depicts the VP without any QP potential $\lambda = 0$, measured over the duration $2000\,\mu s$ to $5000\,\mu s$. Note that all the values are in mV, suggesting voltage amplification relative to the constant external signal over a sufficiently long time. (b) The same profile, but for values of α between zero and the critical value (α_c). The two black-dashed vertical lines enclose the key nodes (exciting and interface nodes) that contain the partial delocalization of the VP.

5.6 Competition between AL and NHSE in TEC

The interplay between NHSE and AL in the NH AA model exhibits fascinating behavior in the localization transition. AL directs a single-site excitation toward a focal point, determined by the weight factors based on the overlap between the initial excitation and exponentially localized eigenstates [233], while NHSE drives it to an interface (or the edges). To probe deeper into this interplay in the TEC, we close both S and $S1$ to incorporate both the non-reciprocity and the QP potential and again excite the $4^{\rm th}$ node with a current source, as described earlier. Fig. 5.7(a) shows that when the QP disorder is real ($\alpha = 0$), the disorder potential is weak compared to the non-reciprocity parameter (γ) and is unable to drive the signal towards the excitation node. However, once α surpasses the critical value $\alpha_c \simeq 0.54$ (determined using Eq. (5.2)), the localization of the output voltage shifts to the excitation ($4^{\rm th}$) node. The VP for $\alpha = 1$ represents the analogous scenario in the TEC corresponding to the non-reciprocal NH AA model depicted in Fig. 5.1(d). An intriguing aspect of this behavior is that the output amplitude

diminishes with increasing α. This behavior is attributed to the significant rise in $|R[k]|$, which scales as $[\sinh \alpha]^{-1}$ (Eq. (5.13)). Consequently, by tuning α, one can effectively manipulate both the spatial localization and the amplitude of the output signal. This dual ability to modulate the NHSE and the AL dynamics is a distinctive feature of our TEC with potential applications similar to information transfer communication devices or developing highly sensitive sensors. Upon closer inspection, a gradual increase in α, from zero to α_c while keeping λ fixed ($\lambda = 1.5$ in this case) unveils a peculiar phenomenon.

As previously discussed, AL is spatially confined over a short range near the excitation node in the TEC. On the other hand, NHSE drives the excitation towards the interface. This interplay generates a fascinating *tug-of-war* scenario between the NHSE and the AL-induced localization, resulting in a partial delocalization of the output signal within a particular spatial range. Fig. 5.7(b) illustrates this phenomenon, where the VP shows non-zero oscillations between the two controllable key nodes, namely, the interface (11^{th}) and the excitation (4^{th}) node, beyond which VP decays to zero. During the transition, the output signal's amplitude becomes relatively uniform across the intermediate nodes, effectively creating a spatial channel for the signal. Furthermore, the position and width of this channel can be tuned by altering the excitation node or the interface of the circuit, offering versatile control over the behavior of the input signal to propagate. Thus, as said earlier, α serves as a critical parameter, acting as a switch that toggles between the phenomenon of NHSE and AL on the spreading dynamics of a single-site excitation.

5.7 Summary

In this work, we have investigated the interplay between the NHSE and AL in a 1D chain, where non-reciprocal hopping amplitudes drive the former, while quasiperiodic disorder induces the latter. Using an NH AA model, we have explored the localization properties and analyzed its time evolution under single-site excitation. Additionally, we have analyzed the time evolution to reveal quantum jumps between skin states and Anderson-localized states within the system. To bridge the gap between theory and experiment, we have proposed a TEC to realize the model. Specifically, we observe a distinct behavior in circuits: the excitation voltage remains localized near the excitation node, in contrast to the NH jumps predicted by the model. Our designed circuit can regulate the VP across the circuit network, specifically between the excitation node and the interface, leading to partial delocalization of the output voltage. The competition between Anderson localization and NHSE manifests in a tangible, experimentally accessible manner, enabling precise control over the output and establishing electrical circuits as a powerful platform for studying these effects. The data that support the findings of this chapter are openly available in Ref. [237].

Chapter 6

Competing Topological Phases in an NH TRS-broken Bernevig-Hughes-Zhang (BHZ) model

So far we have focused on 1D or quasi-1D spinless NH systems, with and without disorder, and analyzed their behavior in terms of NH topology and localization phenomena. In this chapter, we move beyond this setting and investigate a higher-dimensional spinful system in order to understand the impact of non-hermiticity in a more complex setting. To this end, we adopt the BHZ model as a representative platform. The BHZ model, which underlies QSH insulators [23], supports robust spin-filtered helical edge states in a nanoribbon geometry. These edge modes are protected by an intrinsic TRS of the model. We first introduce non-hermiticity through an on-site, spin-dependent gain–loss potential. While this NH term does not qualitatively alter the underlying topological nature of the system, it drives the energy spectrum into a complex plane. Next, we incorporate a TRS-breaking in-plane magnetic field (IPMF). Beyond a critical field strength, the helical edge states for OBC acquire a gap, and topological corner modes emerge. Strikingly, when the strength of the NH potential surpasses that of the magnetic field, the previously gapped helical edge states are restored. Through an analysis of the projected spin spectra and the spin Chern number, we clearly establish

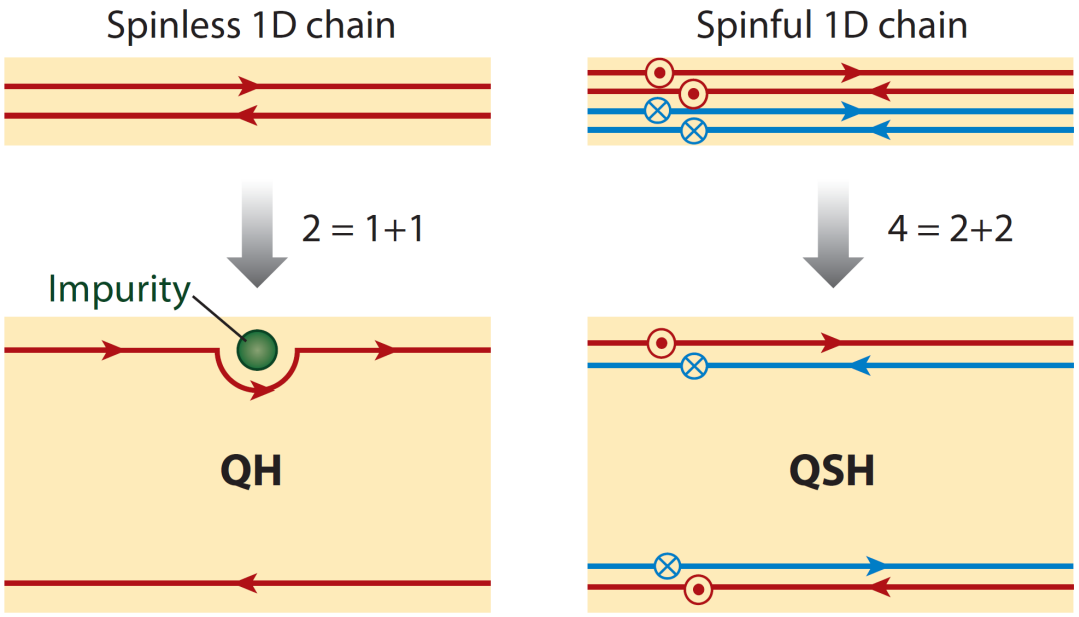

FIGURE 6.1: A spinless 1D system contains two fundamental modes: a right-moving and a left-moving channel (top left). In a quantum Hall system, these two modes are spatially separated, as schematically expressed by the relation $2 = 1+1$: the upper edge hosts only a right-moving mode, while the lower edge supports only a left-moving mode. Such chiral edge states are intrinsically robust against disorder, since they can bypass impurities without undergoing back-scattering (bottom left). In contrast, a spinful 1D system possesses twice as many degrees of freedom due to the spin degeneracy, yielding four modes in total (top right). In a time-reversal invariant QSH system, these modes are separated in a TR-symmetric manner, summarized by the relation $4 = 2+2$. On a given edge, a right-moving spin-up mode coexists with a left-moving spin-down mode, while the opposite spin configuration appears on the other edge. These helical edge states are protected against nonmagnetic disorder, i.e., impurities that preserve the TRS of the QSH phase (bottom right). The figure is adopted for illustration from Ref. [5].

the re-emergence of first-order topological features in the TRS-broken BHZ model induced by non-hermiticity. Finally, we construct a corresponding TEC that realizes both first-order topological edge modes and corner modes, in close analogy with the circuit implementations developed for the earlier models.

6.1 Introduction to the BHZ Model

The BHZ model realizes a QSH insulator, hosting helical edge modes that are protected by TRS and classified by a $\mathbb{Z}_2$ topological invariant. To set the stage, let us briefly explain the QSH effect via a pictorial representation. As noted above, the defining feature of the quantum Hall state is that electrons propagate only in a single direction along a given edge. Relative to a 1D system of spinless electrons (top left Fig. 6.1), the top edge of a quantum Hall system therefore hosts only half of the available degrees of freedom

(bottom left Fig. 6.1). This spatial separation gives rise to chiral edge channels and can be symbolically expressed as $2 = 1 + 1$, where each '1' denotes a distinct chirality. Such a chiral transport rule is highly efficient in suppressing scattering: since electrons move unidirectionally, they can circumvent impurities (green dot in bottom left Fig. 6.1) and cannot undergo backscattering. The QSH state, by contrast, can be viewed heuristically as two copies of the quantum Hall state, one for each spin species. Accordingly, the edge structure of the QSH phase (bottom right Fig. 6.1) can be visualized as a superposition of two quantum Hall edge configurations (bottom left Fig. 6.1) with opposite chiralities assigned to opposite spins. Compared to a spinful 1D system (top right Fig. 6.1), the top edge of a QSH insulator again contains only half of the degrees of freedom. The resulting boundary modes are termed helical, reflecting the locking between spin orientation and direction of motion. This form of spatial separation is captured by the symbolic relation $4 = 2 + 2$, where each '2' corresponds to a distinct helicity. Although electrons in a QSH system may propagate both forward and backward along the same edge, reversing direction necessarily requires a spin flip, which in turn demands the breaking of TRS. As long as TRS is preserved, as is the case for nonmagnetic impurities, backscattering is forbidden. In the QHE, TRS is broken by an external magnetic field, whereas in a QSH insulator, TRS is broken by an internal magnetic field. This internal field can be interpreted as a mass term for emergent Dirac fermions in $2 + 1$ dimensions, with the sign of the mass determining the chirality of the edge states. In the QSH effect, by contrast, helical edge modes arise from time-reversal invariant spin–orbit coupling. Because the QSH phase combines a bulk insulating gap with gapless helical boundary states that are robust against disorder in the presence of TRS, it constitutes a genuinely new topological state of matter and is distinct from quantum Hall phases that harvest chiral edge modes.

We are now set to study a variant of the BHZ model under different boundary conditions: (a) *Toroidal configuration*: When the lattice is periodic in both the x- and y-directions, it is referred to as the 'toroid'. (b) *Nanoribbon configuration*: When the lattice is periodic in one direction while being aperiodic in the other, it is referred to as the 'nanoribbon', with the specific periodic direction mentioned. (c) *Open boundary condition*: When the system is fully aperiodic, it has boundaries in both directions. We then construct a rhombic structure that is composed of multiple square BHZ unit cells. We refer to this as the 'rhombic supercell'. Having elaborated upon the different geometric configurations that have been used to study the topology of varying orders in the system, we now embark upon the Hamiltonian for the original (Hermitian) BHZ model [23, 238], which in the momentum space is given by:

$$H(k_x, k_y) = [\Delta - 2t(\cos k_x + \cos k_y)]\, \sigma_0 \otimes \tau_z + 2t_{sp} \left[\sin k_x (\sigma_z \otimes \tau_x) + \sin k_y (\sigma_0 \otimes \tau_y)\right]. \tag{6.1}$$

Here Δ, t, and t_{sp} are real-valued parameters with σ and τ being Pauli matrices corresponding to the spin and orbital degrees of freedom, respectively.

We now include a spin-dependent imaginary potential of the form,

$$H_{\mathrm{NH}} = \mathrm{i}\gamma\sigma_z \otimes \tau_0, \tag{6.2}$$

where γ, being a positive real quantity, describes the strength of the non-hermiticity. This balanced gain/loss induces an energy disparity between the spin-up ($\uparrow$) and the spin-down ($\downarrow$) states. Upon including an IPMF, $\boldsymbol{B} = (B_x, B_y, 0)$ such that the additional part of the Hamiltonian acquires the form,

$$H_{\mathrm{B}} = (B_x\sigma_x + B_y\sigma_y) \otimes \tau_0. \tag{6.3}$$

The total Hamiltonian H_T is now given by,

$$H_{\mathrm{T}} = H + H_{\mathrm{B}}. \tag{6.4}$$

It is worth mentioning that, without loss of generality, the magnetic field vector $\boldsymbol{B}$ is aligned along the y-direction ($B_x = 0$) unless specified otherwise. Due to the presence of the mirror symmetry M_y in the system, the spectrum of this Hamiltonian is studied on a rhombic supercell, consisting of two M_y invariant corners [239]. With no loss of generality, B_y can be made to vanish, which will simply swap the symmetry coordinates.

In this section, we discuss a nanoribbon configuration of the BHZ model that is periodic in the x-direction but has finite unit cells along the y-direction. Before delving into the specifics of the nanoribbon, it is essential to elucidate the pillar symmetry inherent in the system, which corresponds to TRS. Bernevig, Hughes, and Zhang considered a four-band model on a square lattice in which each unit cell contains two $s_{1/2}$ states, $|s,\uparrow\rangle$ and $|s,\downarrow\rangle$, and two $p_{3/2}$ states, $|p_x + ip_y,\uparrow\rangle$ and $|p_x - ip_y,\downarrow\rangle$. In simplifying the notation of $p_{3/2}$ states corresponding to the p orbital, we denote them as $|p,\uparrow\rangle$ for states with spin up, and $|p,\downarrow\rangle$ for states with spin down. The Hamiltonian of the BHZ model in the momentum space takes the form,

$$H_0(\boldsymbol{k}) = \sum_k \begin{pmatrix} c^\dagger_{\boldsymbol{k}s\uparrow} & c^\dagger_{\boldsymbol{k}p\uparrow} & c^\dagger_{\boldsymbol{k}s\downarrow} & c^\dagger_{\boldsymbol{k}p\downarrow} \end{pmatrix} H(\boldsymbol{k}) \begin{pmatrix} c_{\boldsymbol{k}s\uparrow} \\ c_{\boldsymbol{k}p\uparrow} \\ c_{\boldsymbol{k}s\downarrow} \\ c_{\boldsymbol{k}p\downarrow} \end{pmatrix}; \qquad H(\boldsymbol{k}) = \begin{pmatrix} h(\boldsymbol{k}) & 0_{2\times2} \\ 0_{2\times2} & h^*(-\boldsymbol{k}) \end{pmatrix}, \tag{6.5}$$

where $0_{2\times2}$ denotes null blocks and

$$h(\boldsymbol{k}) = \begin{pmatrix} \Delta - 2t(\cos k_x + \cos k_y) & 2t_{sp}(\sin k_x - i\sin k_y) \\ 2t_{sp}(\sin k_x + i\sin k_y) & -\Delta + 2t(\cos k_x + \cos k_y) \end{pmatrix}. \tag{6.6}$$

$c_{\boldsymbol{k}s\uparrow}$ ($c^\dagger_{\boldsymbol{k}s\uparrow}$) denotes the annihilation (creation) operator for a spin-up ($\uparrow$) electron with a momentum $\boldsymbol{k}$ in the s orbital. A similar notation has been adopted for the creation and annihilation operators corresponding to the p orbitals. t and t_{sp} denote (real-valued) hopping parameters for transitions between s (or p) orbitals and s to p orbitals (or vice-versa) respectively, located in adjacent sites. Δ ($-\Delta$) represents the onsite potential for the s (p) orbital. The TRS operator is given by $\mathcal{T} = i\sigma_y\mathcal{K}\otimes\tau_0$, where σ_y and τ_0 act on the spin and the orbital bases, respectively. $\mathcal{K}$ is simply the complex conjugation operator. The TRS in the BHZ model is verified through the relation, $\mathcal{T}H^*(-\boldsymbol{k})\mathcal{T}^{-1} = H(\boldsymbol{k})$, where $H(\boldsymbol{k})$ is the Bloch Hamiltonian in Eq. (6.5). Now, we shall discuss the x-periodic BHZ nanoribbon. The total number of unit cells in the y-direction is L_y, and the Hamiltonian of the nanoribbon is given by

$$H(n_y,k_x) = \sum_{n_y,k_x,\sigma,\alpha}(-1)^\alpha\Delta c^\dagger_{n_y,k_x\alpha\sigma}c_{n_y,k_x\alpha\sigma} - \sum_{n_y,k_x,\sigma}\Big[2t\cos k_x\left(c^\dagger_{n_y,k_xs\sigma}c_{n_y,k_xs\sigma} - c^\dagger_{n_y,k_xp\sigma}c_{n_y,k_xp\sigma}\right) + t\left(c^\dagger_{n_y+1,k_xs\sigma}c_{n_y,k_xs\sigma} - c^\dagger_{n_y+1,k_xp\sigma}c_{n_y,k_xp\sigma}\right) + t_{sp}\left(c^\dagger_{n_y+1,k_xs\sigma}c_{n_y,k_xp\sigma} - c^\dagger_{n_y-1,k_xs\sigma}c_{n_y,k_xp\sigma}\right) + 2it_{sp}\sin k_x e^{\frac{i\sigma\pi}{2}}c^\dagger_{n_y,k_xs\sigma}c_{n_y,k_xp\sigma}\Big] + \text{H.c.}, \tag{6.7}$$

where σ denotes the spin orientation, taking a numerical value of $+1$ (-1) corresponding to the up (down) spin and α represents the orbital type within a unit cell, that is, $\alpha \equiv (s,p)$, and takes the values, $0,1$, corresponding to the s, p orbitals respectively. Furthermore, $c_{n_y,k_x\alpha\sigma}$ ($c^\dagger_{n_y,k_x\alpha\sigma}$) is the annihilation (creation) operator for an electron with spin, σ (up or down), in orbital α of the n_y^{th} unit cell in the y-direction, possessing a momentum k_x. n_y runs from 1 to L_y. Similarly, the y-periodic BHZ nanoribbon, with a total number of unit cells in the x-direction being L_x, is given by,

$$H(n_x,k_y) = \sum_{n_x,k_y,\sigma,\alpha}(-1)^\alpha\Delta c^\dagger_{n_x,k_y\alpha\sigma}c_{n_x,k_y\alpha\sigma} - \sum_{n_x,k_y,\sigma}\Big[2t\cos k_y\left(c^\dagger_{n_x,k_ys\sigma}c_{n_x,k_ys\sigma} - c^\dagger_{n_x,k_yp\sigma}c_{n_x,k_yp\sigma}\right) + t\left(c^\dagger_{n_x+1,k_ys\sigma}c_{n_x,k_ys\sigma} - c^\dagger_{n_x+1,k_yp\sigma}c_{n_x,k_yp\sigma}\right) + t_{sp}e^{\frac{i\sigma\pi}{2}}\left(c^\dagger_{n_x+1,k_ys\sigma}c_{n_x,k_yp\sigma} - c^\dagger_{n_x-1,k_ys\sigma}c_{n_x,k_yp\sigma}\right) + 2it_{sp}\sin k_y c^\dagger_{n_x,k_ys\sigma}c_{n_x,k_yp\sigma}\Big] + \text{H.c.}, \tag{6.8}$$

where the mathematical symbols bear usual meaning as those for the x-periodic BHZ nanoribbon.

6.2 NH BHZ Model

When the non-hermiticity H_{NH}, described by Eq. (6.2), is introduced in the BHZ Hamiltonian (Eq. (6.1)), the helical edge states along both the x-and y-directions persist, since H_{NH} *does not* break the TRS of the system. However, the energy spectra exhibit pairs of

the form $E_R \pm i\gamma$, where E_R is the real part of the eigenspectrum. Notably, a significant amount of experimental work has been conducted concerning spin-dependent potentials within 2D ultracold atomic gases [240–243]. Now, let us include the spin-dependent imaginary potential, $H_{\rm NH}$, to the Hamiltonian $H(n_y, k_x)$, given via Eq. (6.7), and study the eigenspectra for the nanoribbon in the absence of the IPMF. As established earlier, the inclusion of $H_{\rm NH}$ does not disrupt the TRS of the system, thus ensuring the stability of QSH states. However, $H_{\rm NH}$ introduces an imaginary component to the energy spectrum, leading to all eigenenergies appearing as pairs of E and E^* $(= E \pm i\gamma)$, as illustrated in Fig. 6.2(a), as a manifestation of the TRS in the system. The absence of an energy gap along the real axis, coupled with a 2γ gap along the imaginary axis, indicates that the erstwhile robust helical edge states are now dynamically unstable. The introduction of the IPMF into the NH system brings about a nuanced interplay between the TRS-breaking effects due to the IPMF and the TRS-preserving influence of $H_{\rm NH}$. The underlying mechanism hinges on the ability of $H_{\rm NH}$ to modify the energy landscape of the system in such a way that it mimics the conditions necessary for QSH states to emerge, effectively mitigating the disruptive influence of the IPMF. As depicted in Fig. 6.2(b), when $|B_y| > \gamma$, an energy gap emerges along the real axis, indicating the absence of zero-energy helical edge states. Conversely, in the regime where $|B_y| < \gamma$, as illustrated in Fig. 6.2(c), the dominance of $H_{\rm NH}$ over the IPMF leads to the reassurance of QSH states. In this case, an energy gap appears along the imaginary axis, suggesting a transition from a real line gap to an imaginary line gap transition at $|B_y| = \gamma$. This transition underscores the critical role of the interplay between the competing influences of $H_{\rm NH}$ and B_y in shaping the system's topological characteristics. When $H_{\rm NH}$ is incorporated into the y-periodic nanoribbon $(H(n_x, k_y))$, given via Eq. (6.8) in the

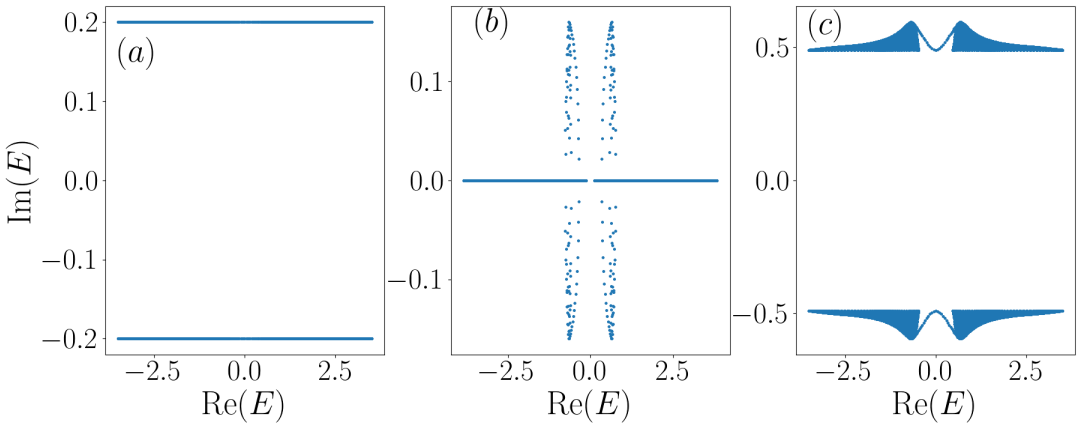

FIGURE 6.2: Real vs imaginary parts of the eigenspectra of an x-periodic ribbon are plotted for (a) $|B_y| = 0, \gamma = 0.2$, (b) $|B_y| = 0.4, \gamma = 0.2$, and (c) $|B_y| = 0.5, \gamma = 0.7$.

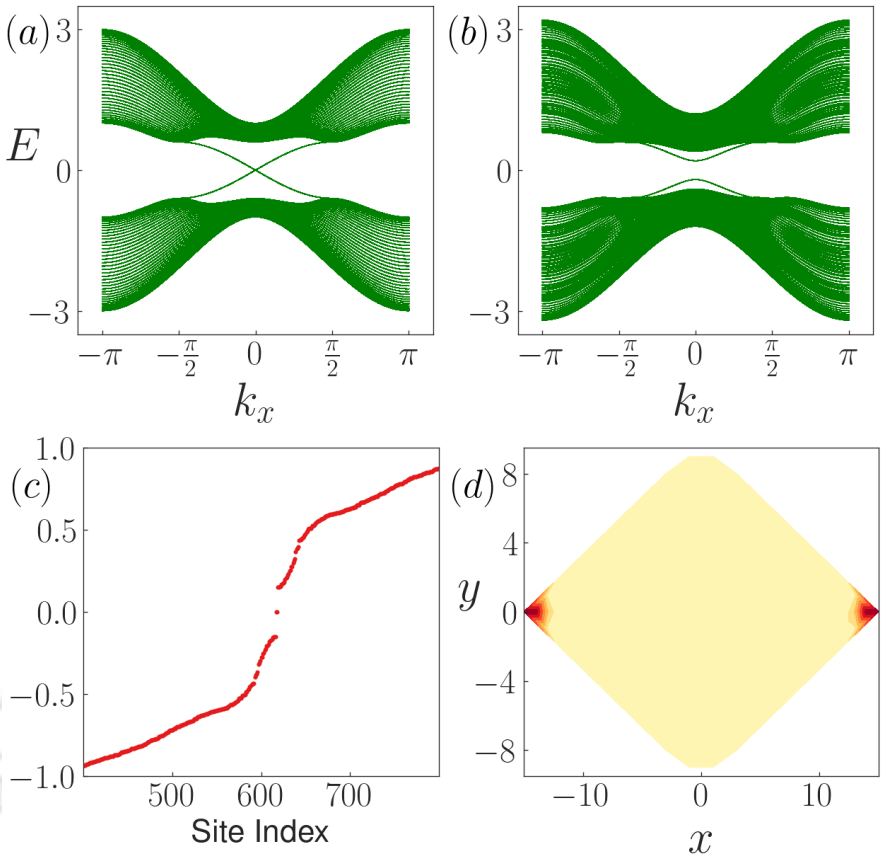

FIGURE 6.3: The spectra of the Hermitian x-periodic nanoribbon, $H(n_y, k_x)$, is depicted in (a) the absence ($|B_y| = 0$), and (b) the presence ($|B_y| = 0.2$) of the IPMF. Without the IPMF, the system resembles the original BHZ model with helical edge states. However, on applying the IPMF, these helical edge states get gapped out. (c) The energy spectra of the Hermitian BHZ model under the influence of the IPMF ($|B_y| = 0.2$) show the presence of distinct zero-energy states separated from the bulk when projected on a rhombic supercell. (d) The probability density of the zero-energy states shows confinement at two specific corners of the rhombic supercell $|B_y| = 0.2$.

absence of the IPMF, the Hamiltonian exhibits results analogous to those observed in the x-periodic NH BHZ nanoribbon, as particularly noted in Fig. 6.2(a).

6.3 Influence of in-Plane Magnetic Field on the BHZ Model

The introduction of the IPMF, described by $H_Z = B_y\sigma_y \otimes \tau_0$ (Eq. (6.3)), to the x-periodic nanoribbon, $H(n_y, k_x)$ (Eq. (6.7)), fundamentally alters the symmetry properties of the system. When $\Delta/2t < 2$, a pair of edge states appears along the boundary of the system, as shown in Fig. 6.3(a). These edge states remain robust even when subjected to TR invariant perturbations and are protected by the presence of TRS, which gives rise to a Z_2 topological invariant. Consequently, this system is equivalent to two independent quantum Hall systems with equal and opposite Hall conductivities, which guarantees a pair of spin-filtered counter-propagating edge states on each boundary of the system.

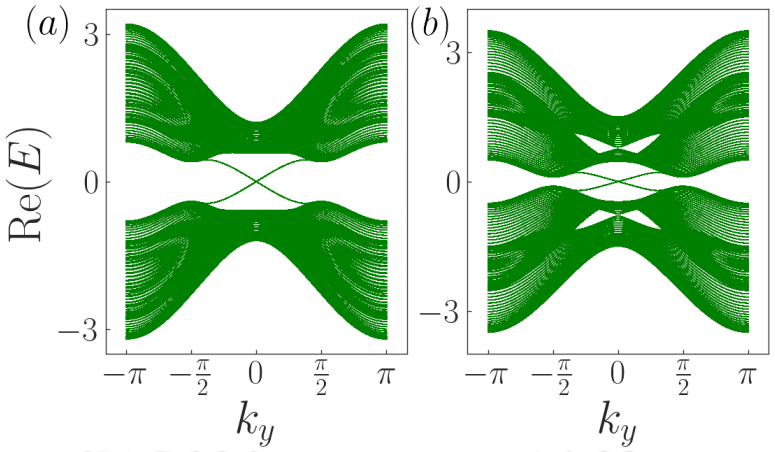

FIGURE 6.4: Band structure of $H(n_x, k_y)$ in the presence of IPMF is plotted for (a) $|B_y| = 0.2$, (b) $|B_y| = 0.5$ in the absence of any non-hermiticity. Interestingly, the introduction of the IPMF generates duplicate energy bands and narrows the gap between them, bringing the system closer to a (semi-)metallic state. The total number of unit cells in the x-direction is fixed at 32. The other parameters are $t = 0.5$, $t_{sp} = 0.3$, and $\Delta = 1.0$.

In essence, the system represents a topologically nontrivial insulator that cannot be smoothly transformed into a trivial insulator through adiabatic processes. The direct consequence of breaking TRS with an IPMF is the destabilization and eventual vanishing of the QSH states (Fig. 6.3(b)) and the emergence of two pairs of zero energy in gap corner states, which is vividly captured in the associated energy spectra for a rhombic supercell with fully OBC, shown in Fig. 6.3(c). These states are localized at the two opposite corners of the rhombic supercell, as shown in Fig. 6.3(d), and provide a clear illustration of the first-order topology getting gapped out, and the system transcends into into a higher-order topological phase (HOTP). This transformation from edge states to corner states under the influence of an IPMF is a clear demonstration of how external fields can be utilized to manipulate the transition between different topological phases.

Let us now discuss the fate of the QSH states in the presence of the IPMF in the y-periodic BHZ nanoribbon. Despite the disruption of TRS by B_y, the unique helical edge states show resilience at lower magnetic field strengths, as demonstrated in Fig. 6.4(a). The magnetic field influences the system by splitting the spin and narrowing the band gap. As the strength of B_y increases, we observe the bands drawing closer, leading to an eventual overlap shown in Fig. 6.4(b). This signals a shift towards a more (semi-)metallic state with the formation of sub-bands. However, it can be safely said that the effect of IPMF on the edge states of a y-periodic nanoribbon is much weaker than that of an x-periodic one. Upon integrating the IPMF with the NH BHZ nanoribbon, intriguing properties emerge in the system. As illustrated in Fig. 6.4(c), non-hermiticity effectively resists the impending band overlap initially caused by the IPMF (as depicted in Fig. 6.4(b)), leading to the re-strengthening of the QSH states.

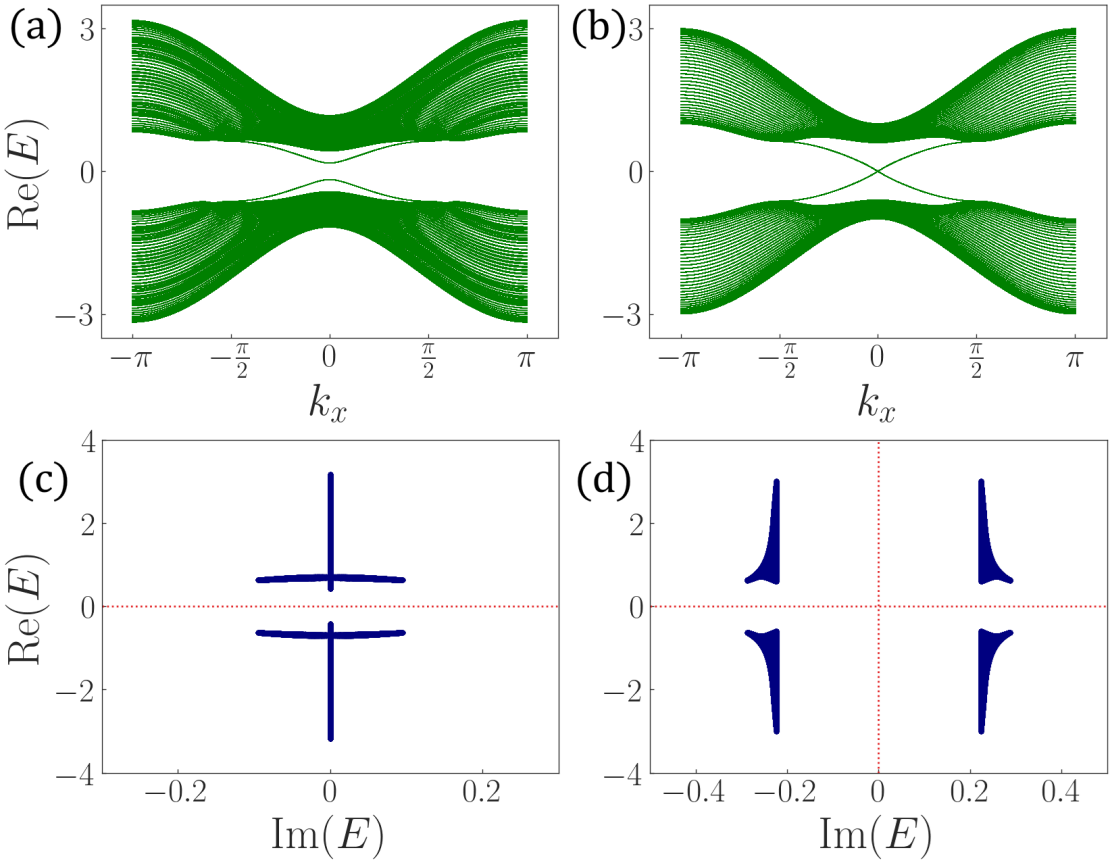

FIGURE 6.5: (a) The real part of the energy spectra of the x-periodic nanoribbon for the Hamiltonian H_{R} is plotted. For $\gamma < |B_y|$ ($|B_y| = 0.2$), the real energy spectrum is gapped. (b) The helical states are restored when γ exceeds B_y. (c) The bulk Re(E) vs. Im(E) spectra show a transition from a real line gap to (d) a mixed line gap as a function of the non-hermiticity parameter. Here, the strength of the non-hermiticity, that is γ, takes a value of 0.1 for (a) and (c), and 0.3 for (b) and (d), respectively.

6.4 Competition between Non-Hermiticity and Magnetic Field

Our primary objective is to investigate the impact of non-hermiticity on the x-periodic nanoribbon in the presence of the IPMF, observing how the edge states, which are gapped out by the IPMF, respond to non-hermiticity. Henceforth, unless otherwise specified, we will refer to the nanoribbon as the x-periodic only. We find that as the strength of the non-hermiticity γ approaches the strength of the IPMF, $|B_y|$, the band gap in the real part of the energy spectra slowly diminishes, as presented in Fig. 6.5(a). At the critical point, $\gamma = |B_y|$, this real energy band gap closes, and thus, the dispersive helical states connecting the conduction and valence bands are revived in the region $\gamma \geq |B_y|$ (Fig. 6.5(b)). Let us denote the resulting Hamiltonian by H_{R}, which under a toroidal configuration, is obtained via adding H_{NH} (Eq. (6.2)) to H_{T} (Eq. (6.3)),

$$H_{\mathrm{R}} = H_{\mathrm{T}} + H_{\mathrm{NH}}. \tag{6.9}$$

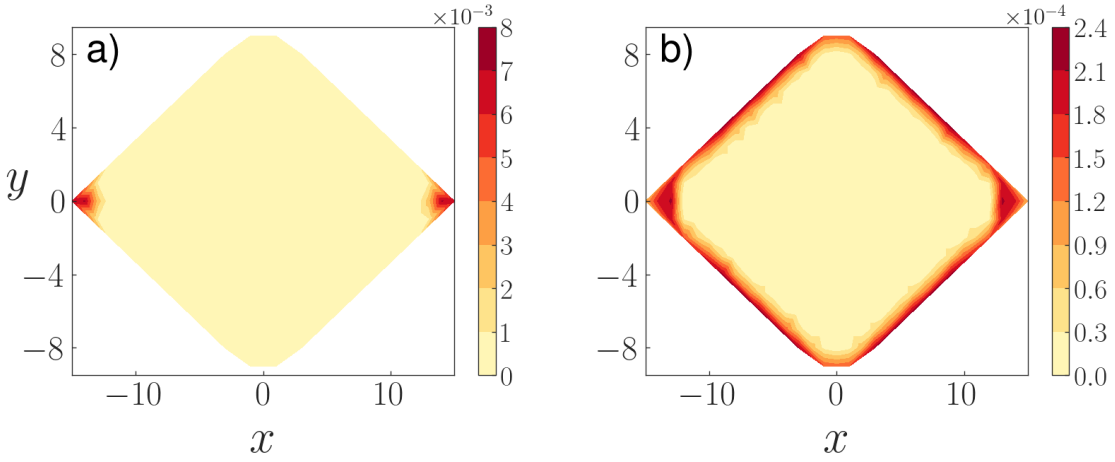

FIGURE 6.6: (a) The probability distribution of the zero energy states in the NH HOTP, that is, $\gamma < |B_y|$, is shown. (b) The probability distribution of the same state in the regime $\gamma > |B_y|$ shows a spread along the edges of the supercell, signaling the retrieval of the helical edge modes. The value of $|B_y|$ is kept fixed at 0.2.

The spectrum of H_{R} illustrates a noteworthy transition: from a real line gap [35] for $\gamma \leq |B_y|$ (Fig. 6.5(c)), to a mixed line gap in the region where γ exceeds $|B_y|$ (Fig. 6.5(d)). The spectral gap transition, occurring at $\gamma = |B_y|$, signals the presence of exceptional points in the system, marking the onset of a criticality where the properties undergo significant transformations. We now focus on analyzing the Hamiltonian under full OBC. In the region where $\gamma < |B_y|$, diagonalization of H_{R} on the previously mentioned rhombic supercell shows that the zero energy states similar to the Hermitian case (Eq. (6.4)) still persist. The biorthogonal probability densities of these zero energy states ($\mathrm{Re}(E) = \mathrm{Im}(E) = 0$) show confinement at the M_y invariant corners of the rhombus, which confirms the existence of the NH HOTP as long as the effect of the IPMF dominates over the NH parameter (Fig. 6.6(a)). Beyond the critical point ($\gamma = |B_y|$), the probability distribution of the states that were earlier confined at the corners of the rhombus now gets delocalized along the edges of the supercell (Fig. 6.6(b)). This situation highlights the re-emergence of the first-order topological phase, characterized by the presence of helical edge states. Hence, we affirm that a very clear tussle exists between a first-order and higher-order topology, which is directly influenced by the strength of the non-hermiticity.

6.4.1 Revival of the Helical Edge Modes

We now focus on analyzing the physical mechanism behind the suppression of the HOTP and resurgence of the helical edge states in the NH BHZ model in the presence of the IPMF. Due to the absence of TRS in the system, the conventional strategy of calculating the $\mathbb{Z}_2$ invariant ceases to be useful. Hence, we switch to calculating SCN, $C_{\uparrow/\downarrow}$, a valid topological invariant for QSH systems having no TRS [244, 245]. Our initial emphasis

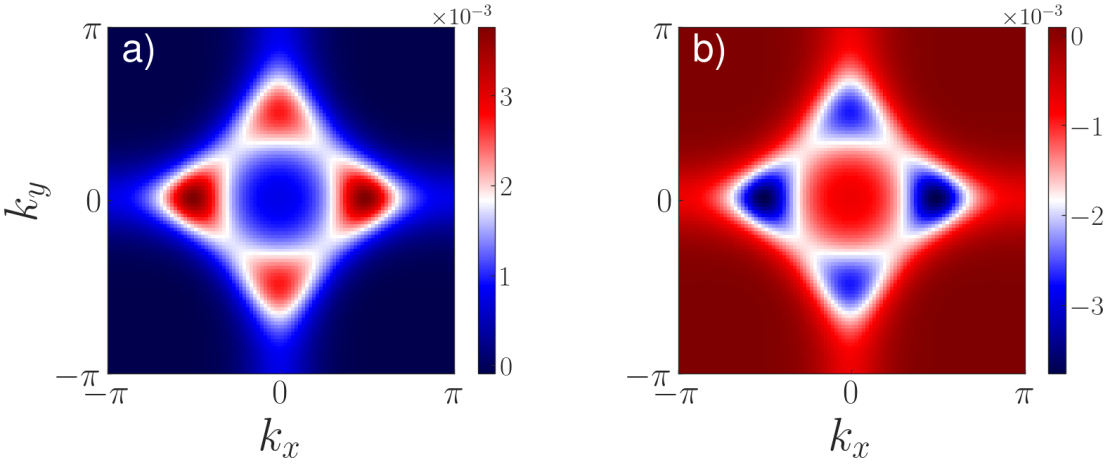

FIGURE 6.7: The spin Berry curvature for the (a) ↑-spin and the (b) ↓-spin states is calculated using the eigenvectors ζ_1 and ζ_4 of the Hermitian-projected spin operator $S(\mathbf{k})$ (Eq. (6.11)), respectively. t, Δ, t_{sp} and B_y are kept fixed at 0.5, 1, 0.3 and 0.2 respectively.

would be on analyzing how the indicator of a first-order topological phase (in our case, the SCN) for the hermitian BHZ Hamiltonian gets affected by the IPMF. To evaluate $C_{\uparrow/\downarrow}$, we construct a projector, $P(\mathbf{k})$, on the occupied subspace of the Hamiltonian, H_{T}, presented by the Eq. (6.4),

$$P(\mathbf{k}) = |u_1(\mathbf{k})\rangle\langle u_1(\mathbf{k})| + |u_2(\mathbf{k})\rangle\langle u_2(\mathbf{k})|, \tag{6.10}$$

where $|u_1(\mathbf{k})\rangle$ and $|u_2(\mathbf{k})\rangle$ correspond to the valence eigenstates. In this case, the projector is a 4×4 matrix. The projected spin operator S is constructed via,

$$S(\mathbf{k}) = P(\mathbf{k})\hat{O}P(\mathbf{k}), \tag{6.11}$$

where $\hat{O} = \sigma_z \otimes \tau_0$. Diagonalization of S gives four distinct eigenvalues, $(E_1^s, E_2^s, E_3^s, E_4^s)$, of which $|E_1^s| = |E_4^s|$ and $E_2^s = E_3^s = 0$. Employing the Fukui's method [246], the SCNs $C_\uparrow$ and $C_\downarrow$ are now respectively calculated using the eigenvectors $|\zeta_1\rangle$ and $|\zeta_4\rangle$ of $S(\mathbf{k})$, corresponding to the eigenenergies E_1^s and E_4^s. Further the spin Berry curvature, $\Omega^s_{\uparrow/\downarrow}(k_x, k_y)$ is plotted in Fig. 6.7 where [246, 247],

$$\Omega^s_{\uparrow/\downarrow}(\vec{k}) = i\left[\left\langle \frac{\partial\zeta(\vec{k})}{\partial k_x}\middle|\frac{\partial\zeta(\vec{k})}{\partial k_y}\right\rangle - \left\langle \frac{\partial\zeta(\vec{k})}{\partial k_y}\middle|\frac{\partial\zeta(\vec{k})}{\partial k_x}\right\rangle\right]. \tag{6.12}$$

Here $\zeta \in \{\zeta_1, \zeta_4\}$ corresponding to the ↑-spin and ↓-spin states respectively. An alternative to Fukui's method, integrating the spin Berry curvature over the entire BZ also yields the SCN ($C_{\uparrow/\downarrow}$). We observe that the SCN for the Hamiltonian H_{T} is non-trivial, namely, $C_\uparrow = -C_\downarrow = 1$, even in the presence of the IPMF. This indicates that the IPMF *does not* destroy the first-order bulk topology. It only provides a channel through which the ↑-spin state can scatter into a ↓-spin state. This scattering leads to the gapping

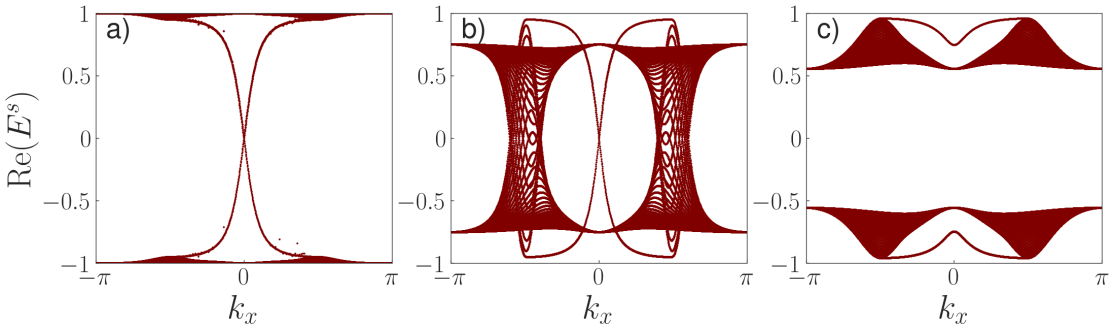

FIGURE 6.8: The real energy spectra for the NH projected spin operator on the nanoribbon configuration are plotted (Eq. (6.13)) corresponding to (a) $\gamma = 0.0$, (b) $\gamma = 0.1$, and (c) $\gamma = 0.3$. The bands correspond to the real parts of the energy eigenvalues, namely, $\mathrm{Re}(E_1^s)$ and $\mathrm{Re}(E_4^s)$, similar to the Hermitian scenario as mentioned in Eq. (6.11). The value of B_y is kept fixed at 0.2.

out of helical edge states, consequently giving rise to the HOTP, as observed in the form of corner states on the rhombic supercell. Nevertheless, the introduction of H_{NH} gradually mitigates this scattering effect. We show this by plotting the spectra of the projected spin operator S_{NH} constructed for H_{R} over the nanoribbon configuration for different strengths of the non-hermiticity γ in Fig. 6.8. The projected spin operator, $S(k)$ presented in Eq. (6.11), is redefined for the NH systems as,

$$S_{\mathrm{NH}}(k_x) = P_L(k_x)\hat{O}P_R(k_x), \tag{6.13}$$

where

$$P_L(k_x) = \sum_{n\in N_{\mathrm{occ}}} |u_n^L(k_x)\rangle\langle u_n^L(k_x)|; \tag{6.14a}$$

$$P_R(k_x) = \sum_{n\in N_{\mathrm{occ}}} |u_n^R(k_x)\rangle\langle u_n^R(k_x)|. \tag{6.14b}$$

Here, $|u_n^L(k_x)\rangle$ (eigenvector of $H_R^\dagger$) and $|u_n^R(k_x)\rangle$ (eigenvector of H_R) refer to the left and right occupied eigenstates for the nanoribbon configuration. The orthonormality condition in this case is given by, $\left\langle u_m^L | u_n^R \right\rangle = \delta_{mn}$, where m and n correspond to the band indices [199].

Let us now discuss Fig. 6.8 in detail. We observe that when $\gamma = 0$ and $B_y \neq 0$ (no non-hermiticity, only IPMF), the band gap of the projected spin spectra is absent, as illustrated in Fig. 6.8(a), and it remains so as long as $\gamma \leq |B_y|$, depicted in Fig. 6.8(b). This observation, in conjunction with the non-trivial spin Berry curvature (Fig. 6.7), indicates that the inclusion of the IPMF only establishes an $\uparrow\leftrightarrow\downarrow$ spin scattering at the edges of the nanoribbon, without harming the topology of the bulk. This, in turn, causes the spin-filtered states at the edges of the BHZ model, in the presence of IPMF, to be gapped, as shown in Fig. 6.5(a). Note that the gap in the spin spectra is non-existent both in bulk and at the edges in Fig. 6.8(b). However, as the value of γ exceeds

$|B_y|$ in Fig. 6.8(c), the spectrum becomes fully gapped. We thus establish that the $\uparrow \leftrightarrow \downarrow$ scattering caused by the IPMF is suppressed as the non-hermiticity becomes the dominating factor in the system. This opens the gap in the spin spectra, as shown in Fig. 6.8(c), and retrieves the spin-filtered edge states (Fig. 6.5(b)).

6.5 TEC Realization

Using the TEC construction formalism developed in the previous chapters, we now realize a circuit implementation of the NH BHZ model defined in Eq. (6.9). The hopping amplitude t_{sp}, corresponding to the coupling $s_x^{i-1} \leftrightarrow p_x^i$ (with i labeling the lattice site along the x-direction), is implemented by a capacitor C_{sp}. Likewise, the hopping t_s,

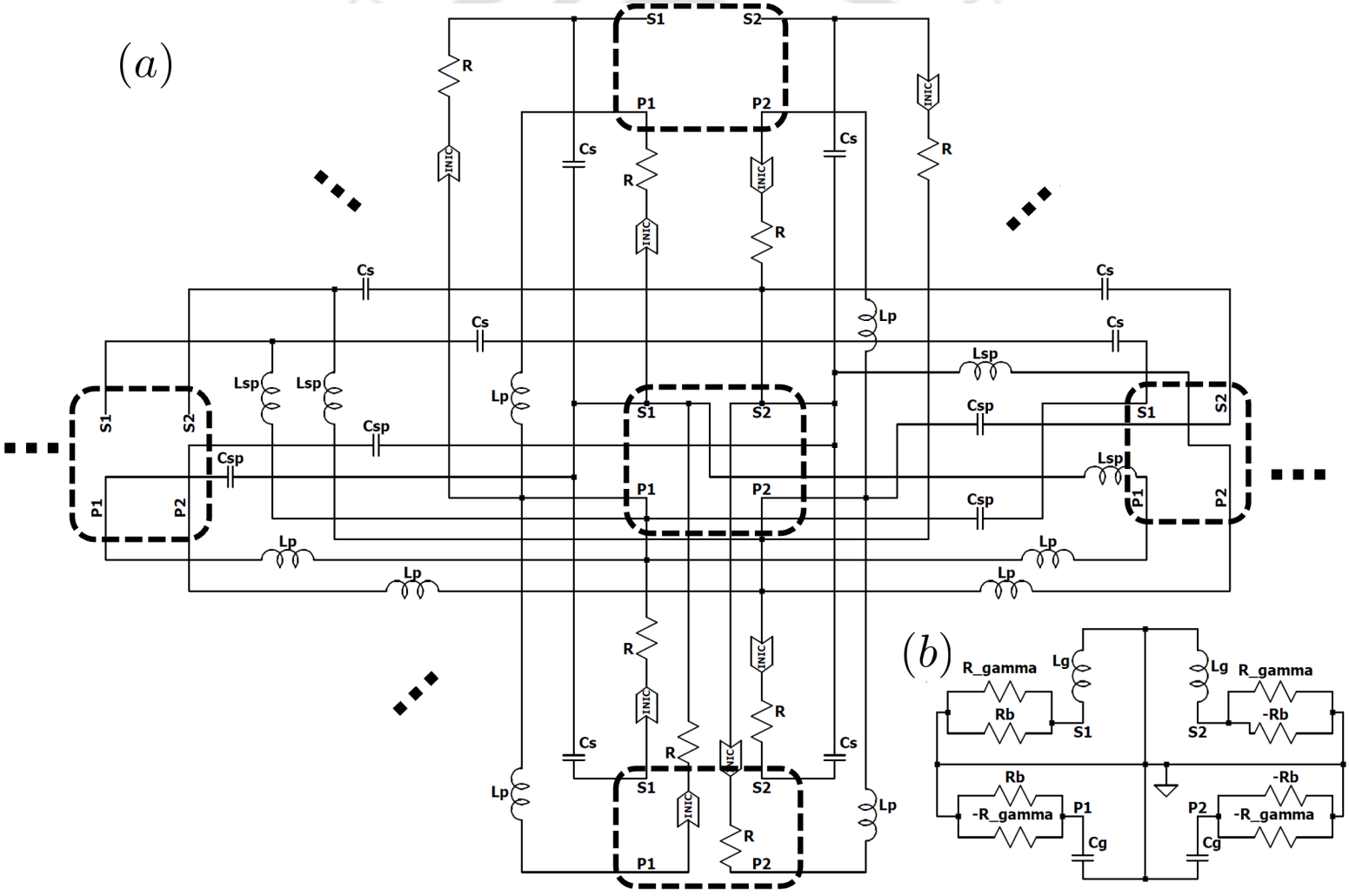

FIGURE 6.9: (a) Circuit realization of the NH BHZ model. Each dotted square represents a unit cell corresponding to the TB model. Each unit cell consists of four subnodes, $s1$, $s2$, $p1$, and $p2$, to emulate the four sites of the BHZ model: $s\uparrow$, $s\downarrow$, $p\uparrow$, and $p\downarrow$. (b) TEC configuration for a particular unit cell incorporating both the IPMF and non-hermiticity.

which represents $s^{i-1} \leftrightarrow s^i$ coupling, is replaced by a capacitor C_s, and throughout the TEC construction we set $t_s = t$. In contrast, hoppings with a negative sign are implemented using inductive elements. Specifically, the hopping $-t_{sp}$, corresponding to $s_k^{i+1} \leftrightarrow p_k^i$, is realized by an inductor L_{sp}, while the hopping $t_p\,(= -t)$, describing $p^{i+1} \leftrightarrow p^i$ coupling, is implemented by using another inductor, L_p. The imaginary hoppings $\pm it_{sp}$ encode the couplings $s_y^{i-1} \leftrightarrow p_y^i$ and $s_y^{i+1} \leftrightarrow p_y^i$ with opposite signs. In the TEC, these terms are implemented through imaginary potentials $\pm i\gamma$: a resistor R is used to realize the dissipative term corresponding to $-it_{sp}$, while a resistor in series with an INIC (see Fig. 2.1(b) of Chapter 2) is employed to generate the effective gain term corresponding to $+it_{sp}$. The complete TEC schematic corresponding to the NH BHZ model is shown in Fig. 6.9(a). To incorporate the spin-dependent imaginary on-site potential given in Eq. (6.2), we follow the same strategy used for the $s\mathcal{PT}$ SSH circuit discussed in Section 3.3.1 of Chapter 3. In particular, grounded resistors R_γ are used to implement the $-i\gamma$ potential, while an INIC connected in series with R_γ generates the $+i\gamma$ term. In this configuration, the INIC does not act as a reciprocity-breaking element; instead, since the opposite end is grounded, it simply provides an effective negative impedance. A detailed discussion of this mechanism can be found in Section 3.3.1 of Chapter 3.

At first glance, one might expect that the magnetic field used in the TB model could be applied directly to the circuit. However, doing so would have no effect on the TEC, since a physical magnetic field does not modify the circuit Laplacian. Therefore, the influence of the IPMF must instead be incorporated at the level of the effective Hamiltonian. To this end, we first analyze how the IPMF modifies the TB Hamiltonian. The IPMF term, H_B (Eq. (6.3)), with the B_x component set to zero, enters into the diagonal elements of the momentum-space BHZ Hamiltonian (Eq. (6.6)). Because the remaining field component B_y is coupled to σ_y, it generates terms of the form $\pm iB_y$ in the TB description. As a result, the implementation of the IPMF in the TEC follows the same strategy as that used for the spin-dependent imaginary potential. Specifically, it is realized using resistors R_B together with INICs connected in series. The circuit configuration for a particular unit cell incorporating both the IPMF and non-hermiticity is shown schematically in Fig. 6.9(b).

In Fig. 6.10, we present the IP of the 2D NH BHZ TEC, obtained using the same measurement protocol adopted in the previous chapters. When $R_\gamma < R_B$, corner-localized modes emerge clearly in the IP (Fig. 6.10(a)), corresponding to the situation illustrated for the TB model in Fig. 6.6(a). This regime therefore implements the HOTP in the TB description. By contrast, when R_γ exceeds R_B, equivalently, when $|\gamma| > B_x$ in the TB model, the corner localization disappears and edge modes resurface in the TEC, as shown in Fig. 6.10(b).

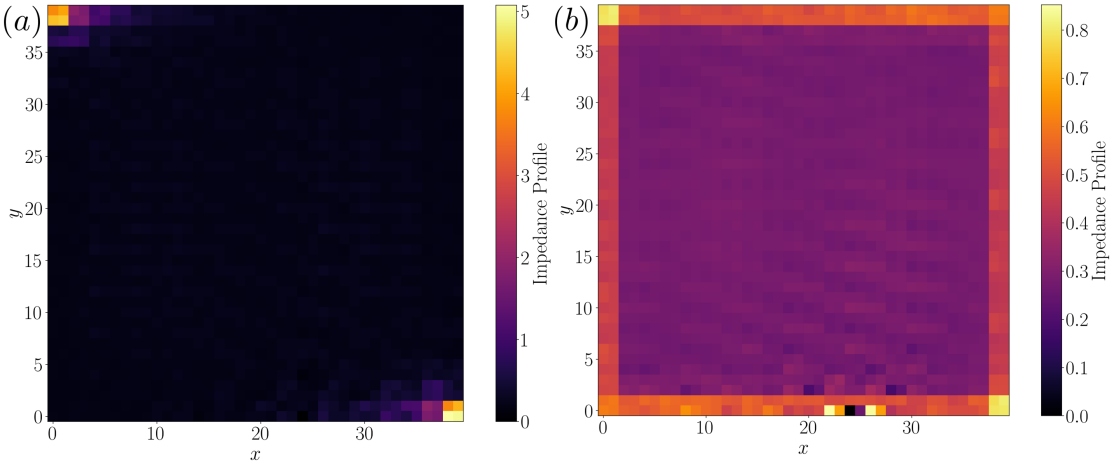

FIGURE 6.10: (a) TEC realization of HOTP for $R_\gamma < R_B$. The topological corner modes can be realized via the IP of the circuit, where impedance is higher at the opposite corners of the TEC. This is analogous to Fig. 6.6(a). (b) Revival of the first-order topological phase within the TEC when $R_\gamma > R_B$. The black spot at $20 < x < 30$, $y = 0$ marks the connection of the power supply to the TEC.

6.6 Summary

In this work, we investigate the consequences of the interplay between non-hermiticity, introduced via an onsite spin-dependent gain–loss potential, and IPMF confined to the plane of the BHZ model. While non-hermiticity alone does not qualitatively modify the topological characteristics of the system, it renders the energy eigenspectra to acquire a complex structure, as the imaginary potential preserves TRS. Upon introducing a TRS-breaking unidirectional IPMF ($\gamma \leq |B_y|$), the helical edge modes become gapped, and corner modes emerge beyond a critical field strength. Remarkably, when the strength of the NH potential exceeds that of the IPMF ($\gamma \geq |B_y|$), the previously gapped helical edge states reappear. By analyzing the projected spin spectra and the spin Chern number, we unambiguously demonstrate the revival of first-order topological properties in the TRS-broken BHZ model in the presence of non-hermiticity. The suppression of this spin channel by non-hermiticity is also exhibited by the spin spectrum of the nanoribbon in the regime $\gamma > |B_y|$, and subsequently, the corner modes in the rhombic supercell get delocalized along the edges. We have also built TECs corresponding to the TB models and realized first- and higher-order topological models via the IP of the circuit.

Chapter 7

Second-order Skin Effect in a Brick-Wall (BW) Lattice

Having discussed the competition between first- and higher-order topologies in the previous chapter, let us explore the interplay between topology and the skin effect in two dimensions. 2D lattices exhibiting Dirac-like crossings in their eigenspectra provide a versatile platform for studying topological quasiparticles and effects of Berry phase on the band topology [11, 248] as well as emergent topological order [249]. In this context, the honeycomb lattice provides a prominent platform for hosting Dirac fermions, and the effect of various kinds of symmetry breaking on the topology of the hexagon has been extensively studied [250–252]. Evidently, Dirac-like band crossings present a useful setting for studying numerous emergent topological effects. However, it is imperative to mention here that such band crossings are not limited to the hexagonal lattice structure, but can also be obtained in other lattice geometries as well, including the Lieb and Kagome lattices [253, 254]. Another model with an underlying square geometry, which is topologically equivalent to the honeycomb and consequently supports Dirac band crossings, is demonstrated by the Brick-Wall (BW) lattice [255]. Geometrically, a BW lattice can be obtained by stretching the honeycomb lattice appropriately, such that the resulting structure resembles a square lattice with alternately missing vertical bonds. The BW lattice is hence a 2D bipartite structure providing an alternative realization of the hexagonal topology, but on a much simpler lattice geometry. This formulation has been employed to explore the topology of the hexagon and hence study non-trivial insulating phases in cold atoms and optical lattices [256]. Recent literature has also

extensively explored the effect of hopping anisotropy, flux patterns, as well as NH and time-periodic perturbations that shift, merge, or gap out Dirac-like band crossings in square and variants of the square lattices, thereby generating novel emergent topological phases in a geometry much simpler than the hexagonal [135, 257, 258]. Interestingly, our engineered BW structure exhibits two Dirac cones that merge under certain conditions.

On the other hand, investigations of higher-order skin effects in higher-dimensional systems have recently become a central theme in the study of NH physics due to their distinctive localization properties [142–145]. In particular, in the first-order NHSE, an extensive number of eigenstates accumulate at the system boundaries. More precisely, in a d-dimensional lattice of linear size L, the number of skin modes scales as $\mathcal{O}(L^d)$. In contrast, for the higher-order NHSE discussed in Section 1.5.3 of Chapter 1, the majority of eigenstates remain delocalized and form bulk bands, while only a subset of states exhibits skin localization. In particular, for the second-order skin effect (SOSE) in two dimensions, a system of size $L \times L$ hosts $\mathcal{O}(L^2)$ bulk modes together with $\mathcal{O}(L)$ corner skin modes (see Fig. 1.2 for details). Another interesting phenomenon, which originates from the unique interplay between NHSE and topology, and leads to eigenstate localization at lower-dimensional boundaries, such as corners in 2D lattices, is the HST effect [144]. Motivated by the above, in this chapter, we study the BW lattice or its engineered variant, which may exhibit features not discussed in the thesis so far. Specifically, we consider an NH variant of our modified BW model, in which non-reciprocal hopping in the vertical direction is the source of non-hermiticity. We further compare the results obtained for the NH BW lattice with the previously reported findings for the NH square lattice [142, 259]. This chapter is organized as follows. In Section 7.1, we first analyze the Hermitian BW lattice and discuss its band structure in momentum space. Section 7.2 analyzes the study of the SOSE in the NH square lattice. In Section 7.3, we demonstrate how dynamically stable HST modes emerge when the NH square lattice is continuously transformed into the NH BW lattice. This transformation is achieved by tuning the inter-chain couplings of the initial square lattice along the vertical direction. For each case, we also propose corresponding TEC implementations for both the NH square lattice and the NH BW lattice, enabling direct visualization of the predicted HST modes.

7.1 Model Hamiltonian for a BW Lattice

The ordinary Hermitian BW lattice provides a convenient representation of a bipartite structure that is topologically similar to a honeycomb lattice, yet realized on a square lattice. The essential low-energy characteristics of the honeycomb lattice (and by extension, graphene) are thus captured accurately in a BW structure. In fact, the BW lattice can be visualized as a stretched honeycomb, with the hexagonal unit cell stretched to

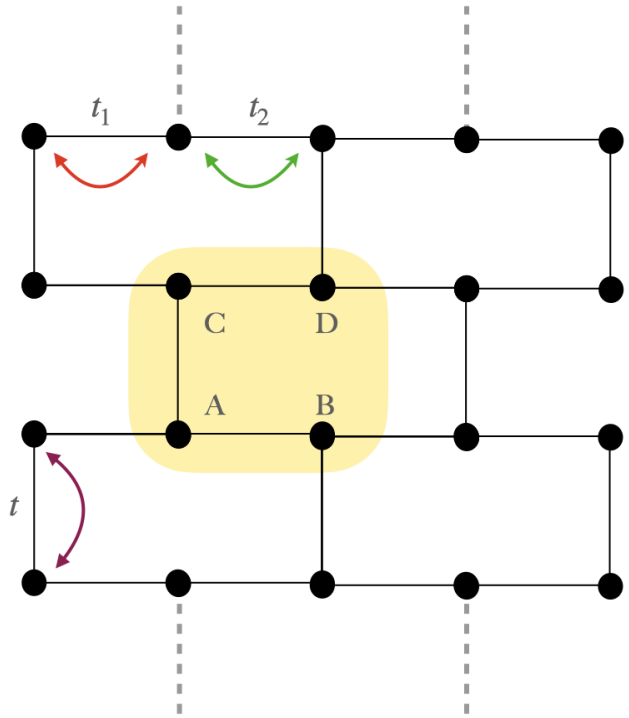

FIGURE 7.1: A schematic representation of the modified BW lattice is shown. The vertical hopping, which is allowed only between the intracell A and C sub-lattices and intercell B and D sub-lattices, is denoted by t. The horizontal direction resembles a stacked SSH model with a bipartite hopping structure characterized by hopping strengths t_1 and t_2. This model is Hermitian, with the hopping terms identical for both in the forward (upward) and reverse (downward) directions.

flatten the upper and lower vertices while keeping the hopping and sub-lattice structure the same. This modification retains the Dirac cones while changing the crystal symmetry from C_6 to C_4. We study a slightly modified version of the original BW lattice that retains the alternating vertical-hopping structure while discarding the direct correspondence with the stretched honeycomb geometry. To begin with, our version of the Hermitian BW lattice consists of four sub-lattices, namely A, B, C, and D (as shown in Fig. 7.1). The real space Hamiltonian is given via,

$$H = \sum_{\vec{r}}^{L_x, L_y} \left[t_1 \left(c^\dagger_{\vec{r},A}\, c_{\vec{r},B} + c^\dagger_{\vec{r},C}\, c_{\vec{r},D} \right) + t_2 \left(c^\dagger_{\vec{r}+\hat{x},A}\, c_{\vec{r},B} + c^\dagger_{\vec{r}+\hat{x},D}\, c_{\vec{r},C} \right) + t \left(c^\dagger_{\vec{r},A}\, c_{\vec{r},D} + c^\dagger_{\vec{r}+\hat{y},B}\, c_{\vec{r},C} \right) + H.c \right], \tag{7.1}$$

where L_x and L_y are the number of sites in x- and y-directions, respectively. The hopping in the vertical direction is denoted by t and assumes an alternating structure similar to the original BW lattice. To elaborate, while the intra-cell hopping between the A and C sub-lattices is allowed and has a hopping amplitude t, inter-cell hopping between the sub-lattices is restricted, giving rise to the required BW structure. In the horizontal direction, the hopping within the unit cell is denoted by t_1, whereas it is t_2 for the

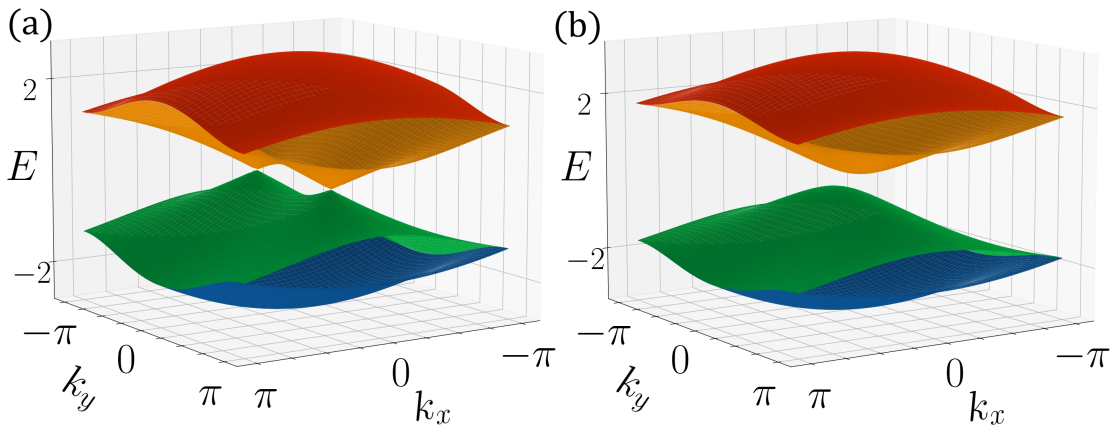

FIGURE 7.2: The bulk bandstructure showing (a) the presence of four-fold Dirac cones for $t < t_1 + t_2$ and (b) the gapped spectra for $t > t_1 + t_2$.

intra-unit cell hoppings. The horizontal direction, therefore, resembles a stack of SSH chains with dimerized hopping structures, denoted by t_1 and t_2. The bulk Hamiltonian for this 4-band Hermitian model is given by,

$$H(\vec{k}) = \left(t_1 + t_2 e^{-ik_x}\right) c^{\dagger}_{\vec{k},A}\, c_{\vec{k},B} + \left(t_1 + t_2 e^{ik_x}\right) c^{\dagger}_{\vec{k},C}\, c_{\vec{k},D} + t\, c^{\dagger}_{\vec{k},A}\, c_{\vec{k},D} + t e^{-ik_y} c^{\dagger}_{\vec{k},B}\, c_{\vec{k},C} + H.c. \tag{7.2}$$

This modified version of the BW lattice amalgamates the topology of the SSH model with the honeycomb to give rise to two four-fold degenerate Dirac cones in the regime $t < t_1 + t_2$. At $t = t_1 + t_2$, the Dirac cones merge at the Γ point of the BZ to finally gap out beyond this point. The band structure is, however, completely invariant with respect to the relative magnitude of t_1 and t_2.

As mentioned earlier, the modified Hermitian BW lattice exhibits the presence of two Dirac cones in the bulk Hamiltonian when the strength of the vertical hopping t is less than the strength of the horizontal hopping t_1 and t_2 combined, as shown in Fig. 7.2(a). The Dirac cones move towards each other and merge at the Γ point when $t = t_1 + t_2$, finally gapping out for t exceeding $(t_1 + t_2)$ (Fig. 7.2(b)). A nanoribbon geometry shows the Dirac points being connected by a flat band (Fig. 7.3(a)). For $t > t_1 + t_2$, the valence and the conduction bands in the nanoribbon are completely disconnected. However, in-gap states are found to traverse the energy gap in this parameter region (Fig. 7.3(b)). There are no significant topological properties of the Hermitian model; hence, we have only demonstrated the spectral properties. Having discussed the Hermitian BW model, we now move to the NH BW lattice, where we introduce non-reciprocal hopping in the vertical direction, which drastically changes the nature of the energy eigen spectra. For the NH counterpart of the modified BW lattice, we introduce non-reciprocal hopping such that two successive vertical rungs permit upward hopping with amplitude t, while the next two vertical rungs allow downward hopping with the same strength. We will return to the detailed consequences of this construction shortly. Before

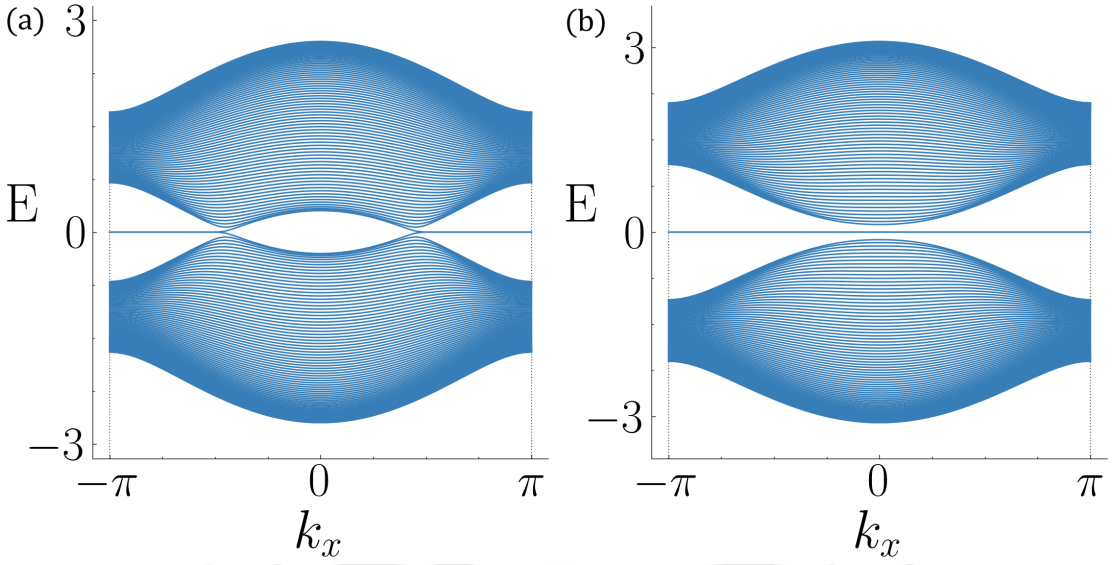

FIGURE 7.3: The ribbon (x-periodic) spectra for (a) $t < t_1 + t_2$ and (b $t > t_1 + t_2$. For $t > t_1 + t_2$, the spectrum is completely gapped. However, the existence of an in-gap flat band is observed.

doing so, however, it is instructive to first consider a reference system that exhibits a SOSE. To this end, we discuss NHSE in an NH square lattice.

7.2 SOSE in an NH Square Lattice

We begin with a simple Hermitian square lattice in which the chains along the x-direction emulate the traditional SSH model, featuring staggered hopping amplitudes t_1 and t_2, while those along the y-direction are uniform with amplitude t. In this particular variant of the model, non-reciprocity is introduced by rendering the y-direction chains non-reciprocal, allowing hopping only in one direction. The directions of the hopping are reversed along the alternate chains; that is, the hopping amplitudes along the neighboring chains are oriented in mutually opposite directions. The bulk Hamiltonian for this model is given via,

$$H_s(\vec{k}) = \sum_{k_x,k_y} \left[\left(t_1 + t_2 e^{-ik_x}\right) c^\dagger_{\vec{k},A}\, c_{\vec{k},B} + \left(t_1 + t_2 e^{ik_x}\right) c^\dagger_{\vec{k},C}\, c_{\vec{k},D} + t e^{-ik_y}\, c^\dagger_{\vec{k},A}\, c_{\vec{k},D} + t e^{ik_y}\, c^\dagger_{\vec{k},C}\, c_{\vec{k},B} \right]. \tag{7.3}$$

$H_s(k)$ has both the mirror symmetries, $\mathcal{M}_x$ and $\mathcal{M}_y$, which are defined via,

$$\mathcal{M}_x \equiv \tau_0 \otimes \sigma_x; \quad \text{and} \quad \mathcal{M}_y \equiv \tau_x \otimes \sigma_0, \tag{7.4}$$

where τs and σs are the Pauli matrices that describe additional degrees of freedom. Consequently, $H_s(k)$ has the inversion symmetry, which is defined via the product of $\mathcal{M}_x$ and $\mathcal{M}_y$. A closely related model to $H_s(k)$, that exhibits SOSE, was discussed by

Kawabata *et al.* in Ref. [142]. It was further argued that such an NH square lattice can be systematically extended to a Hermitian Benalcazar–Bernevig–Hughes model, which serves as a paradigmatic example of a second-order topological insulator, originally proposed by Benalcazar, Bernevig, and Hughes [135, 260]. Specifically, if $H(k)$ exhibits SOSE, then the corresponding Hermitian Benalcazar–Bernevig–Hughes Hamiltonian in k space can be constructed as,

$$\tilde{H}_{\mathrm{BBH}}(k) = \begin{pmatrix} 0 & H_s(k) \\ H_s^{\dagger}(k) & 0 \end{pmatrix}. \tag{7.5}$$

In this model, no edge modes appear when open boundary conditions are imposed along only one spatial direction. However, when the system is open along both directions, zero-energy modes emerge at the corners once the intra-cell hopping becomes weaker than the inter-cell hopping. This model respects both the inversion and the chiral symmetries, which together play a crucial role in stabilizing higher-order topology. In particular, when a 2D Hermitian system possesses chiral and inversion symmetries, which are denoted by mutually anti-commuting operators, intrinsic second-order topology emerges [261]. As a consequence, the Hamiltonian $H(k)$ supports an intrinsic SOSE, as proposed in Ref. [259], where topological zero-energy corner modes are protected by the bulk topology. By extending the notion of second-order topology to point gaps, the authors of Ref. [259] further demonstrated that NH systems can host skin modes localized at the corners. This scenario is referred to as an intrinsic SOSE, as the corner localization is directly rooted in the bulk topological properties. In contrast, an extrinsic HOTP arises when the bulk is topologically trivial, while the edges are topologically nontrivial. In such cases, the edge bands carry an imprint of 1D first-order topology protected by the chiral symmetry, and the edge–corner correspondence yields corner modes through closing of the edge gap at zero energy. The nontrivial topology of the 1D edges can then support skin modes localized at the corners. However, unlike $H(k)$ in Eq. (7.5), the NH square-lattice Hamiltonian $H_s(k)$ cannot be extended to a Hermitian Hamiltonian (with inversion symmetry) that exhibits intrinsic second-order topology. As a result, $H_s(k)$ does not exhibit intrinsic SOSE. Instead, it realizes an extrinsic SOSE, according to Ref. [259], where the corner skin modes originate from the interplay between non-hermiticity and first-order topology of the SSH chains along the x-direction (see Fig. 7.1). This mechanism underlies what is commonly referred to as the *hybrid skin–topological effect* [144].

We now turn to the spectral and localization properties of the NH square lattice with open boundaries imposed along both directions, focusing on the regime $t < t_1 + t_2$. The real parts of the eigenenergies, shown in Fig. 7.4(a), indicate the absence of an energy gap. The corresponding complex-energy spectra, plotted in Fig. 7.4(b), reveal that the spectral trajectories associated with the HST modes exhibit a nontrivial winding

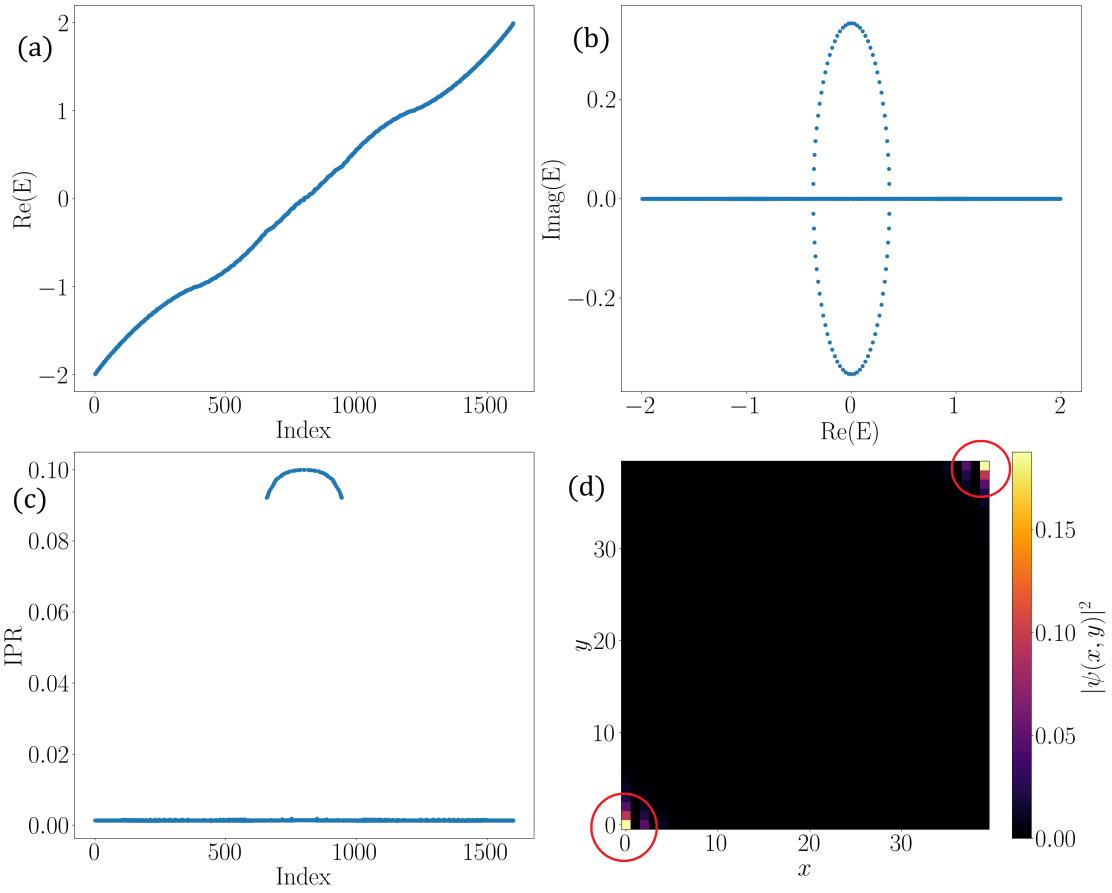

FIGURE 7.4: (a) The real part of the energy spectra of a finite NH square lattice (OBC in both directions) for $t < t_1 + t_2$. (b) The spectral distribution in the complex plane. The corner skin modes are arranged as an ellipse. (c) IPR of the corner skin modes is non-zero. (d) The probability distribution of a random second-order skin mode, shown via yellow dots inside the red circles.

in the complex plane. Such winding is forbidden in the case of the first-order NHSE, highlighting the distinct properties of these modes. Fig. 7.4(c) displays the IPR, which is finite for the corner skin modes, demonstrating their localized character. These modes are not part of the bulk spectrum and are instead confined to the system boundaries, with localization occurring specifically at the corners, while the remaining bulk modes remain delocalized. Out of the total number of eigenstates ($L_x \times L_y$ of them), the number of corner skin modes is $2L_y$, whereas the number of delocalized bulk modes is $L_y \times (L_x - 2)$. This counting follows from the fact that each SSH chain along the x-direction contributes two zero-energy topological modes, and there are L_y such chains in total. For the numerical results presented here, we set $L_x = L_y = 40$, yielding 80 HST modes. A representative probability distribution for one such corner skin mode is shown in Fig. 7.4(d). Importantly, when the SSH chains along the x-direction are tuned into the topologically trivial regime, that is, $t_1 > t_2$, these corner skin modes disappear. This confirms that their existence originates from the interplay between first-order topology and non-hermiticity.

7.2.1 TEC of an NH Square Lattice

We now construct the TEC corresponding to the NH square lattice model. This construction is relatively straightforward, since the system consists of SSH chains along the x-direction, and the Hermitian SSH circuit has already been demonstrated in Section 2.4 of Chapter 2. The only additional step is to couple these SSH circuits along the y-direction using unidirectional hoppings with amplitude t, in accordance with the tight-binding model. To realize the unidirectional couplings along the y-direction, we employ diodes, which restrict the flow of the current along a single direction. Notably, INICs are not required here, even though the model is non-reciprocal. This is because the non-reciprocity arises purely from direction-selective hoppings along the y-axis, rather than from asymmetric bidirectional couplings. The complete TEC layout is shown in Fig. 7.5(a), while the configuration of the grounded inductors is depicted in Fig. 7.5(b). In general, skin modes are visualized through the VP of the TEC, as demonstrated in Section 3.2.2 of Chapter 3 and in Chapter 5. However, for the SOSE, only $\mathcal{O}(L)$ skin modes exist out of a total of $\mathcal{O}(L^2)$ bulk modes. In this situation, the HST modes are more effectively designated through the IP of the circuit. This is because the corner skin modes exhibit a much stronger localization at the corners compared to bulk states, giving them a disproportionately large contribution to the impedance between two nodes, as described by Eq. (2.11) of Chapter 2, even though their energies are not exactly zero. To measure the IP, the TEC is excited by injecting a current at a randomly chosen node, and the impedance at each node is recorded, following the same procedure as described in the earlier chapters. The angular frequency of the AC driving source is fixed at $\omega = 10^6\,\mathrm{MHz}$. The circuit parameters are chosen as $C_1 = 0.5\,\mu\mathrm{F}$, $C_2 = 1\,\mu\mathrm{F}$, and $C = 0.5\,\mu\mathrm{F}$. The grounded inductors are set to,

$$L_1 = L_2 = \left[\omega^2\,(C + C_1 + C_2)\right]^{-1} \approx 0.67\,\mu\mathrm{H}. \tag{7.6}$$

The resulting IP is shown in Fig. 7.5(c). A pronounced enhancement of the impedance is observed at the two opposite corners, reaching values of order $\sim 3 \times 10^7\,\Omega$. This behavior faithfully reproduces the HST modes observed in the tight-binding results shown in Fig. 7.4(d).

7.3 SOSE in an NH BW Lattice

We now turn to the NH BW lattice and examine the distinctive properties of the associated skin modes. To introduce non-reciprocity into the otherwise Hermitian BW model, we render the hopping along the y-direction asymmetric in a patterned manner: two consecutive y-direction chains are made unidirectional with the same orientation, while the two subsequent chains are assigned unidirectional hopping in the opposite direction.

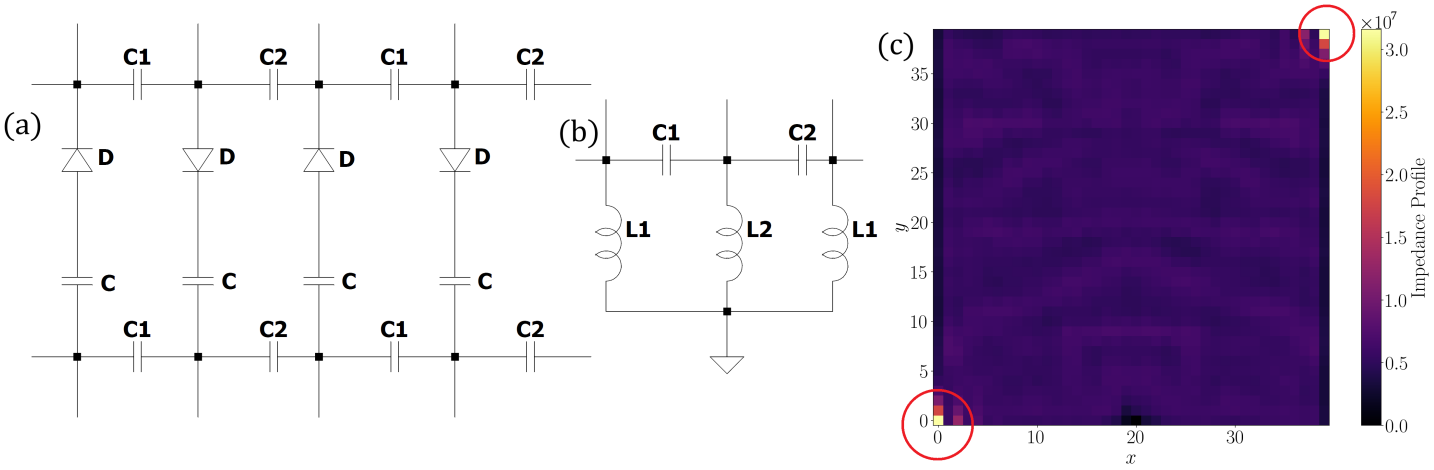

FIGURE 7.5: (a) TEC design of NH square lattice. (b) Grounded inductors, associated with each node. (c) IP of the TEC, imitating the corner skin modes (yellow dots inside the red circles) in Fig. 7.4(d).

As we shall see, his staggered arrangement of non-reciprocity plays a crucial role in distinguishing the second-order skin modes obtained from the NH square lattice. The bulk Hamiltonian for this model is given via,

$$H_{BW}(\vec{k}) = \sum_{k_x,k_y} \left[\left(t_1 + t_2 e^{-ik_x}\right) c^{\dagger}_{\vec{k},A}\, c_{\vec{k},B} + \left(t_1 + t_2 e^{ik_x}\right) c^{\dagger}_{\vec{k},C}\, c_{\vec{k},D} + t\, c^{\dagger}_{\vec{k},A}\, c_{\vec{k},D} + t e^{ik_y}\, c^{\dagger}_{\vec{k},C}\, c_{\vec{k},B} \right]. \tag{7.7}$$

Since the BW lattice is obtained by selectively removing hoppings from the square lattice, it does not possess mirror symmetry about the x-axis, that is, it lacks $\mathcal{M}_x$. It does, however, retain mirror symmetry about the y axis, with the corresponding operator given by $\mathcal{M}_y \equiv \tau_x \sigma_x$. Since inversion can be viewed as the product of the two mirror operations, $\mathcal{M}_x$ and $\mathcal{M}_y$, the Hermitian BW lattice does not exhibit inversion symmetry. As in the previous case, the Hamiltonian $H_{BW}(k)$ cannot be promoted to a Hermitian Hamiltonian that preserves inversion symmetry and supports intrinsic second-order topology. Therefore, the second-order skin modes realized in the NH BW lattice are also extrinsic in nature. In other words, they correspond to HST modes, arising from the interplay between non-hermiticity and lower-dimensional topological features rather than from an intrinsic bulk second-order topology.

Now we turn to the most interesting part of this chapter. The NH BW lattice exhibits substantially richer physics than the NH square lattice. As shown in Fig. 7.6(a), the real part of the spectrum develops a clear energy gap. The small step-like structures visible inside this gap correspond to the extrinsic second-order skin modes (or HST modes). In addition, the spectrum contains two zero-energy edge modes that originate from the parent Hermitian BW lattice. To be precise, in a Hermitian BW lattice of size $L_x \times L_y$, there are $2L_y$ first-order topological edge modes for $t \leq t_1$. These originate from the L_y

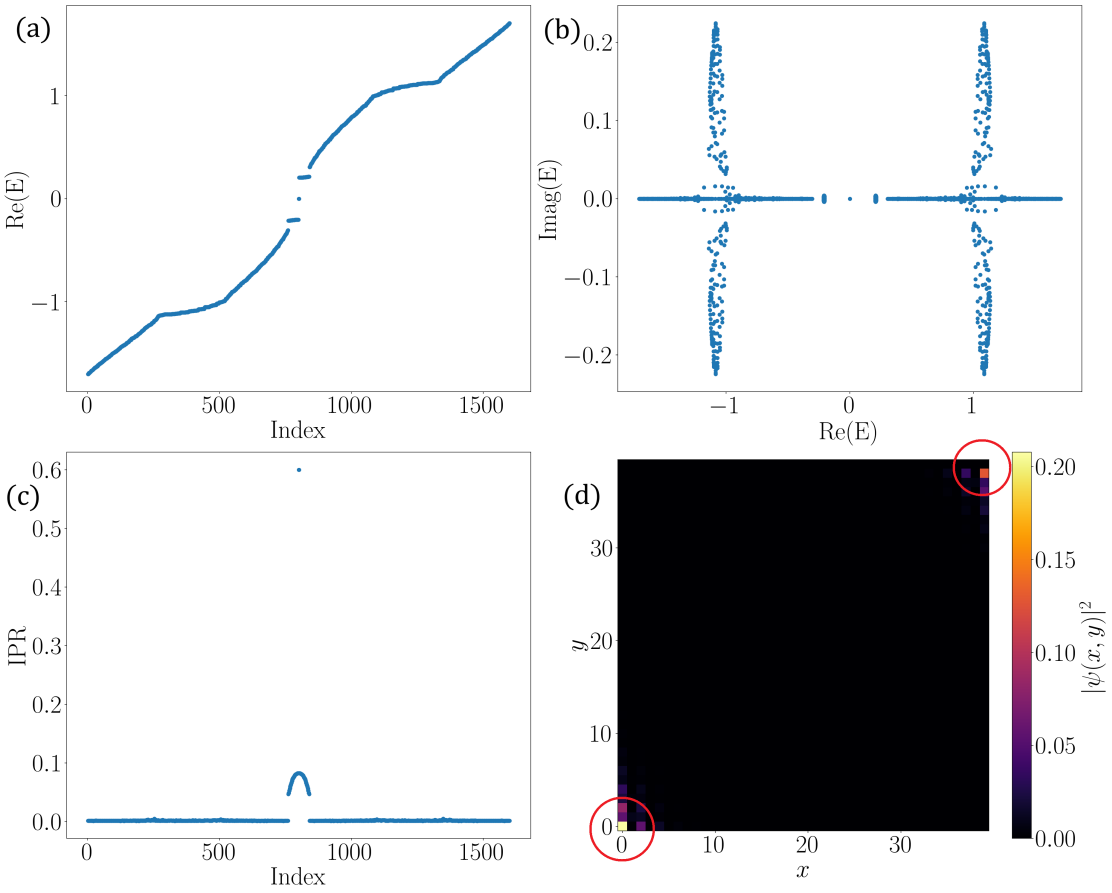

FIGURE 7.6: (a) The real part of the energy spectra of an NH BW lattice with OBC in both directions for $t < t_1 + t_2$. (b) The spectral distribution in the complex plane. The corner skin modes now form EP-like structures. (c) IPR of the corner skin modes is non-zero. However, there are two zero-energy modes that have much higher IPR than the corner skin modes. (d) The probability distribution of a random second-order skin mode is shown via yellow dots inside the red circles.

independent SSH chains along the x-direction, with each chain contributing two topological edge modes. Among these $2L_y$ modes, however, only two lie exactly at zero energy ($E = 0$). The remaining $(2L_y - 2)$ modes have finite energies $E = \pm t$. Importantly, the two zero-energy modes are localized at two corners of the lattice, whereas the other $(2L_y - 2)$ first-order modes are localized along the y edges. These $(2L_y - 2)$ modes are degenerate at energies $E = \pm t$ in the Hermitian limit, but this degeneracy is not associated with the EPs. Upon introducing non-hermiticity, these $(2L_y - 2)$ degenerate edge modes evolve into extrinsic second-order skin modes localized at the other two corners of the lattice. Their energies become almost degenerate, acquiring only a very small imaginary part, which gives rise to the step-like features observed in Fig. 7.6(a). These modes are neither zero-energy modes nor part of the bulk spectrum; instead, they remain spectrally isolated from the bulk bands. In Fig. 7.6(b), these modes appear as two point-like clusters in the complex-energy plane. These skin modes are remarkable for two key reasons, namely,

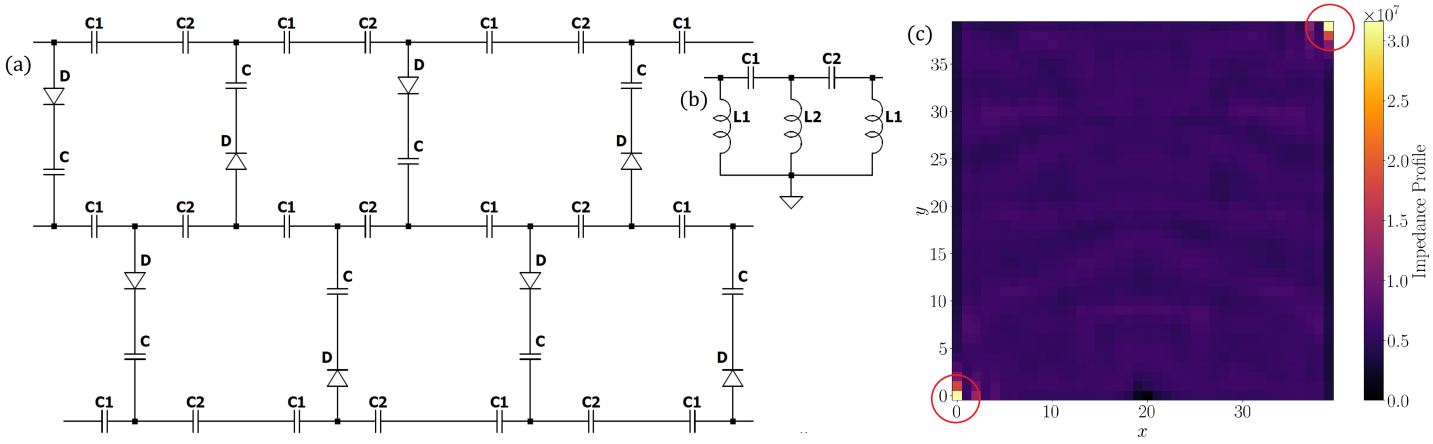

FIGURE 7.7: (a) TEC design of NH BW model. (b) Grounded inductors, associated with each node, are shown. (c) IP of the TEC, imitating the corner skin modes, shown via yellow dots inside the red circles, in Fig. 7.6(d).

1. they originate from degeneracies of the parent Hermitian Hamiltonian (the Hermitian BW lattice in this case). Consequently, despite their appearance, they are not exceptional points.

2. They are almost dynamically stable, possessing only negligible imaginary parts in their energies. This behavior is highly unusual compared to previously studied HST systems [142, 144, 259], where the skin modes typically exhibit appreciable amplification or decay.

Fig. 7.6(c) shows the IPR of the corner skin modes. $(2L_y - 2)$ modes have a lower IPR, while the remaining two zero-energy modes inherited from the Hermitian BW lattice become localized at a single corner of the lattice. Fig. 7.6(d) shows the probability distribution of a random second-order skin mode, localized at two opposite corners of the lattice.

7.3.1 TEC of an NH BW Lattice

We conclude this chapter by constructing the TEC corresponding to the NH BW model. The procedure closely follows that used for the NH square lattice in Section 7.2.1. The only modifications required are the removal of selected capacitors along the y-direction and an appropriate reorientation of the diodes along the y-axis, which together implement the NH BW lattice geometry and its non-reciprocal couplings. The resulting NH BW circuit diagrams are shown in Figs. 7.7(a) and 7.7(b). All the circuit element values are kept identical to those used in Section 7.2.1. The corresponding IP is presented in Fig. 7.7(c). This IP closely resembles that of the NH square lattice shown in Fig. 7.5(c) and successfully reproduces the HST behavior observed in the TB results of Fig. 7.6(d). It should be noted, however, that the two special corner skin modes identified in the NH

BW TB model cannot be individually resolved in the TEC realization. This limitation arises since, in terms of the probability density, these modes are indistinguishable from the other corner skin modes when computing the impedance via Eq. (2.11) of Chapter 2. As a result, while the TEC faithfully captures the overall HST localization, it does not allow separate identification of these particular corner modes.

7.4 Summary

In this chapter, we have investigated the NH variant of the BW model, which realizes an HST effect (or extrinsic SOSE), and systematically compared its behavior with that of the NH square lattice. To set the stage, we first introduced the Hermitian BW model and analyzed its spectral properties. In the Hermitian variant, the BW lattice does not host intrinsic higher-order topology; any topological features arise solely from the dimerized hopping emulating the SSH chains along the x-direction. Upon introducing non-hermiticity, the BW model displays several unusual features in the spectral properties of the HST modes. In contrast to previously studied SOSE systems, these modes do not generate non-trivial spectral windings in the complex plane. Instead, they appear similar to the EPs in the complex-energy spectrum, although they are not genuine EPs. Among all the corner skin modes, only two, which descend from the topological corner modes of the Hermitian BW lattice, are localized at individual corners. The remaining corner skin modes accumulate at the opposite pair of corners. This behavior is markedly different from that observed in the NH square lattice, where the corner skin modes are distributed more uniformly. For both the NH square lattice and the NH BW lattice, we have constructed corresponding TEC realizations. These circuit implementations enable direct visualization of the HST modes and faithfully simulate an experimental platform to corroborate the theoretical predictions.

Chapter 8

Conclusion

This thesis investigates a broad range of compelling physical phenomena arising from the interplay among non-Hermitian physics, localization phenomena, and topological quantum systems, with particular emphasis on the nature of non-Hermitian topology and its associated localization properties. Truly closed quantum systems are seldom realized experimentally, as unavoidable exchanges of energy or particles with the surrounding environment effectively render the system Hamiltonian, or the corresponding governing equations, non-Hermitian. As a result, interest in non-Hermitian quantum physics has grown rapidly over the past few decades. In parallel, topological systems have assumed a central role in condensed matter physics owing to the incorporation of topological concepts within energy band structures. The convergence of these two major developments has uncovered a wealth of novel phenomena, including the non-Hermitian skin effect, in which systems exhibit extreme sensitivity to boundary conditions; the formulation of non-Bloch band theory; and the emergence of exceptional points, together with generalized Brillouin zone theory. These distinctive features, unique to non-Hermitian topology, have proven highly valuable in experimental contexts. For instance, exceptional points, where both eigenvalues and eigenvectors coalesce, enhance system sensitivity and have been exploited in optical and photonic sensing applications. Likewise, the global localization of eigenstates associated with the skin effect offers a mechanism to confine quantum particles at specific spatial and temporal locations. Motivated by these promising theoretical insights and practical applications, this thesis explores non-Hermitian topology in several tight-binding models and realizes them experimentally using electrical circuits

engineered to emulate the underlying theoretical frameworks. Such circuit implementations provide a versatile platform for probing quantum-to-classical correspondence and for extracting practical insights relevant to a wide range of applications. Moreover, owing to the accessibility, low cost, and high flexibility of circuit components, topolectrical circuits offer an excellent opportunity for use in undergraduate laboratories as tangible demonstrations of quantum-mechanical phenomena.

Chapter 1 introduces the foundational concepts required to understand this thesis and outlines the motivation for the work presented.

Chapter 2 then develops the formalism and methodologies for implementing quantum systems in topolectrical circuits, accompanied by representative examples. Specifically, we demonstrate the working principles of the basic circuit components required to construct a complete electrical circuit that realizes tight-binding models. We also mention a few examples of topolectrical circuits, including (non-Hermitian) Su-Schrieffer-Heeger models, along with a driven Creutz ladder, and present the topological edge modes and skin modes within the circuit.

Chapter 3 focuses on the NH SSH model, exploring how its topological characteristics differ between $\mathcal{PT}$-symmetric and non-$\mathcal{PT}$-symmetric regimes. In the non-$\mathcal{PT}$-symmetric case, non-reciprocity is introduced in both the inter- and intra-cell hopping amplitudes. This leads to a non-trivial winding of the complex energy spectrum under periodic boundary conditions, signaling a complete breakdown of bulk-boundary correspondence and the emergence of the skin effect. We have explained this phenomenon via the non-Bloch theory. Conversely, in the $\mathcal{PT}$-symmetric scenario, reciprocity of all hopping amplitudes is maintained by a complex on-site staggered potential. As a result, the system preserves the usual bulk-boundary correspondence and exhibits no skin effect. The topological behavior of this $\mathcal{PT}$-symmetric case closely mirrors that of its Hermitian counterpart, but with an additional feature, a spontaneous $\mathcal{PT}$-symmetry breaking that occurs upon tuning the strength of the imaginary staggered potential, where we find that the broken and unbroken regions can be characterized by eigenvalues being real and complex, respectively.

After developing a foundational understanding of NH topological phenomena, we turn our attention to exploring the exceptional features of the NHSE in the **Chapter 4**. Our investigation centers around a quasi-1D, two-orbital model with intra- and inter-orbital hoppings. It is commonly expected that systems with non-reciprocal hopping amplitudes naturally exhibit NHSE. However, our results reveal notable exceptions, underscoring the need for a more comprehensive analysis to accurately identify the presence or absence of NHSE and its variants. Interestingly, we find that introducing non-reciprocity in the inter-orbital hopping terms can give rise to three distinct behaviors: conventional NHSE, NHSE at both edges, or a complete absence of NHSE. Extending the Hermitian model

into the NH regime effectively divides it into two distinct cases: a $\mathcal{PT}$-symmetric model and a non-$\mathcal{PT}$-symmetric model (which may or may not respect time-reversal symmetry). In the $\mathcal{PT}$-symmetric scenario, we observe spontaneous $\mathcal{PT}$-symmetry breaking, separating the system into regions characterized by real or complex eigenvalues in the $\mathcal{PT}$-unbroken and $\mathcal{PT}$-broken phases, respectively, with no sign of NHSE. It appears that the nonreciprocal, yet $\mathcal{PT}$-symmetric, model possesses an inherent pseudo-skew-Hermitian property, leading to the suppression of the NHSE and the preservation of the bulk-boundary correspondence. To probe the topological properties of these NH systems, we employ the complex Berry phase as a topological invariant. Altogether, our study constructs a versatile model where tuning the degree and type of non-reciprocity leads to three distinct regimes: (a) No NHSE — for the $\mathcal{PT}$-symmetric model, (b) Normal NHSE — for the non-$\mathcal{PT}$-symmetric model with time-reversal symmetry, and (c) Dual-edge NHSE — for the non-$\mathcal{PT}$-symmetric model possessing both time-reversal and particle-hole symmetries. Thus, by simply adjusting the model parameters, one can control the localization behavior of bulk states, inducing their accumulation at a single edge (normal NHSE), both edges (dual-edge NHSE), or eliminating localization entirely (no NHSE).

Chapter 5 deals with the disordered NH model. In this work, we have investigated the interplay between the NHSE and AL in a one-dimensional chain, where non-reciprocal hopping amplitudes drive the former, while quasiperiodic disorder induces the latter. Starting with a 1D NH AA model featuring an interface separating two non-equivalent AA chains, we explored the localization properties and analyzed the time evolution under single-site excitation. Additionally, we have analyzed the time evolution to reveal quantum jumps between skin states and Anderson-localized states within the system. Within the topolectrical circuits, we observe a distinct behavior: the excitation voltage remains localized near the excitation node, in contrast to NH jumps, as predicted by the model. As previously discussed, AL is spatially confined over a short range near the excitation node in the topolectrical circuit. On the other hand, NHSE drives the excitation towards the interface. This interplay generates a fascinating *tug-of-war* scenario between the NHSE and the AL-induced localization, resulting in a *partial* delocalization of the output signal within a particular spatial range in the topolectrical circuit.

After exploring disordered systems, we next incorporated spin degrees of freedom to examine how a spinful system responds to an external field, specifically, an in-plane magnetic field. This investigation forms the focus of **Chapter 6**. The Bernevig-Hughes-Zhang (BHZ) model serves as a paradigmatic platform for quantum spin Hall insulators, supporting robust spin-filtered helical edge states in a nanoribbon geometry. In this work, we investigate the consequences of the interplay between non-Hermiticity, introduced via an onsite spin-dependent gain–loss potential, and a planar magnetic field confined to the plane of the BHZ model. While non-Hermiticity alone does not qualitatively

modify the topological characteristics of the system, it renders the energy eigenspectra complex, as the imaginary potential preserves time-reversal symmetry. Upon introducing a time-reversal symmetry-breaking planar magnetic field, the helical edge modes become gapped, and corner modes emerge beyond a critical field strength. Remarkably, when the strength of the non-Hermitian potential exceeds that of the magnetic field, the previously gapped helical edge states reappear. By analyzing the projected spin spectra and the spin Chern number, we unambiguously demonstrate the revival of first-order topological properties in the time-reversal symmetry-broken BHZ model in the presence of non-Hermiticity.

In **Chapter 7**, we investigate the emergence of a hybrid skin–topological effect, which manifests as the action of the skin effect exclusively on topological edge modes in higher-dimensional systems. This behavior is realized by selectively suppressing specific hopping processes along the vertical direction, thereby generating a brick-wall lattice that can be interpreted as a stretched two-dimensional honeycomb geometry. By continuously tuning the inter-chain couplings of an initially square lattice along the vertical axis, we identify dynamically stable hybrid skin–topological modes. In this process, the second-order skin modes of the square lattice collapse into well-defined energy eigenvalues. This condensation arises from the Hermitian topology brick-wall model itself. Thus, the interplay of the first-order topology of the Hermitian brick-wall model and the skin effect from the selective non-reciprocity introduced in the y-direction induces hybrid skin–topological effect within the system.

We have constructed topolectrical circuits for all of these systems to bridge the gap between theory and experiment. The impedance profile or voltage profile, obtained by anchoring one port at the edge of the circuit and systematically connecting the other to each node in the circuit network, faithfully mimics the edge or skin modes of the corresponding TB models for the topological phase.

Appendix A

Circuit Laplacian of an NH Creutz Ladder

In this section, we are going to construct and analyze the Laplacian of the TEC corresponding to the Hamiltonian H_{tot}. The real space Hamiltonian is given by,

$$H = -\sum_n t_H(e^{i\phi}a_n^\dagger a_{n+1} + e^{-i\phi}b_n^\dagger b_{n+1}) + t_D(a_n^\dagger b_{n+1} + a_{n+1}^\dagger b_n) + t_V a_n^\dagger b_n + h.c., \quad \text{(A.1)}$$

which comprises three main components, expressed as $H = H_H + H_D + H_V$, where H_H, H_D, and H_V represent the Hamiltonians associated with the horizontal, diagonal, and vertical hopping terms, respectively, as depicted in Fig. 1. For an electrical network consisting of N_0 nodes, let $\mathcal{L}$ denote the Laplacian matrix of the circuit, and let $V_{i,A/B}$ and $I_{i,A/B}$ represent the voltage and net external current at the subnode A/B of the i^{th} node, respectively. We now derive the Laplacian $\mathcal{L}$ of the TEC that emulates the Hamiltonian of the Creutz ladder in Eq. (2.23), as shown in Fig. 6(a) of the main text, driven at an arbitrary angular frequency ω_a. By applying Kirchhoff's current law at each

node in the absence of any external source, we obtain the following set of $2N_0$ equations,

$$\begin{aligned}
&\frac{V_{1,A}}{R_G(A)}+\frac{V_{1,A}}{+R_H}+\frac{V_{1,A}}{i\omega_a L}+i\omega_a C_D\,V_{1,A}+i\omega_a C_V\,(V_{1,A}-V_{1,B})+\frac{(V_{1,A}-V_{2,A})}{-R_H}+\\
&\qquad\qquad i\omega_a C_D\,(V_{1,A}-V_{2,B})=0,\\
&\frac{V_{1,B}}{R_G(B)}+\frac{V_{1,B}}{+R_H}+\frac{V_{1,B}}{i\omega_a L}+i\omega_a C_D\,V_{1,B}+i\omega_a C_V\,(V_{1,B}-V_{1,A})+\frac{(V_{1,B}-V_{2,B})}{-R_H}+\\
&\qquad\qquad i\omega_a C_D\,(V_{1,B}-V_{2,A})=0,\\
&\qquad\qquad\vdots\\
&\frac{V_{i,A}}{R_G(A)}+\frac{V_{i,A}}{i\omega_a L}+\frac{(V_{i,A}-V_{i-1,A})}{+R_H}+i\omega_a C_D\,(V_{i,A}-V_{i-1,B})+i\omega_a C_V\,(V_{i,A}-V_{i,B})+\\
&\qquad\qquad\frac{(V_{i,A}-V_{i+1,A})}{-R_H}+i\omega_a C_D\,(V_{i,A}-V_{i+1,B})=0,\\
&\frac{V_{i,B}}{R_G(B)}+\frac{V_{i,B}}{i\omega_a L}+\frac{(V_{i,B}-V_{i-1,B})}{+R_H}+i\omega_a C_D\,(V_{i,B}-V_{i-1,A})+i\omega_a C_V\,(V_{i,B}-V_{i,A})+\\
&\qquad\qquad i\omega_a C_D\,(V_{i,B}-V_{i+1,A})+\frac{(V_{i,B}-V_{i+1,B})}{-R_H}=0,\\
&\qquad\qquad\vdots\\
&\frac{V_{N,A}}{R_G(A)}+\frac{V_{N,A}}{-R_H}+\frac{V_{N,A}}{i\omega_a L}+i\omega_a C_D\,V_{N,A}+i\omega_a C_V\,(V_{N,A}-V_{N,B})+\frac{(V_{N,A}-V_{N-1,A})}{+R_H}+\\
&\qquad\qquad i\omega_a C_D\,(V_{N,A}-V_{N-1,B})=0,\\
&\frac{V_{N,B}}{R_G(B)}+\frac{V_{N,B}}{-R_H}+\frac{V_{N,B}}{i\omega_a L}+i\omega_a C_D\,V_{N,B}+i\omega_a C_V\,(V_{N,B}-V_{N,A})+\frac{(V_{N,B}-V_{N-1,B})}{+R_H}+\\
&\qquad\qquad i\omega_a C_D\,(V_{N,B}-V_{N-1,A})=0,
\end{aligned}$$

By expressing the set of $2N_0$ equations in matrix form as $I=\mathcal{L}V$, where I and V denote the column vectors of currents and voltages at each node, respectively, the resulting Laplacian matrix $\mathcal{L}$ accurately reproduces the Hamiltonian H_{tot} (Eq. (A.1)) at the resonant angular frequency ω_R. Thus, the matrix form of $\mathcal{L}$ is obtained as,

$$\mathcal{L}(\omega_R)=\begin{pmatrix}
\frac{1}{R_G(A)} & -i\omega_R C_V & \frac{1}{R_H} & -i\omega_R C_D & 0 & \cdots\cdots\\
-i\omega_R C_V & \frac{1}{R_G(B)} & -i\omega_R C_D & \frac{1}{R_H} & 0 & \cdots\cdots\\
\vdots & \vdots & \vdots & \vdots & \vdots & \\
\cdots-\frac{1}{R_H} & -i\omega_R C_D & \frac{1}{R_G(A)} & -i\omega_R C_V & \frac{1}{R_H} & -i\omega_R C_D\cdots\\
\cdots-i\omega_R C_D & -\frac{1}{R_H} & -i\omega_R C_V & \frac{1}{R_G(B)} & -i\omega_R C_D & \frac{1}{R_H}\cdots\\
\vdots & \vdots & \vdots & \vdots & \vdots & \\
\cdots & 0 & -\frac{1}{R_H} & -i\omega_R C_D & \frac{1}{R_G(A)} & -i\omega_R C_V\\
\cdots & 0 & -i\omega_R C_D & -\frac{1}{R_H} & -i\omega_R C_V & \frac{1}{R_G(B)}
\end{pmatrix} \tag{A.2}$$

Appendix B

Absence of Skin Effect in the Non-Reciprocal Model

Until now, a substantial body of literature suggests the NHSE is directly connected to the system being non-reciprocal. Through the reciprocal skin effect found in Ref. [107], it is known that non-reciprocity is not a necessary condition for NHSE. What we really demonstrate in our work is that non-reciprocity is neither *a necessary nor a sufficient condition* for NHSE. In our particular case, the absence of NHSE in a non-reciprocal, yet $\mathcal{PT}$-symmetric, system can be explained through mathematical reasoning. Let us elaborate on these below.

B.1 Pseudo-Hermiticity of the Hamiltonian

NH Hamiltonians with real eigenvalues necessarily belong to a particular class, namely the pseudo-Hermitian (PH) Hamiltonians, which are discussed in detail in Ref. [43]. The condition for pseudo-Hermicity for an arbitrary NH Hamiltonian, H_{NH}, can be stated as,

$$H_{NH}^{\dagger} = \eta\, H_{NH}\, \eta^{-1}, \tag{B.1}$$

where η is the PH operator and H_{NH} is called η-PH Hamiltonian. In our case, the Bloch Hamiltonian for the non-reciprocal model can be written as (Eq. (4.29) of Chapter 4),

$$h_4(k) = \begin{pmatrix} \epsilon - 2t\cos k & 2i(t_{AB}+\delta)\sin k \\ -2i(t_{AB}-\delta)\sin k & -\epsilon + 2t\cos k \end{pmatrix}. \tag{B.2}$$

Specifically, consider an operator, $\tilde{\eta}$, for which $h_4(k)$ also satisfies the following relation,

$$h_4^{\dagger}(k) = -\tilde{\eta}\, h_4(k) \tilde{\eta}^{-1}, \tag{B.3}$$

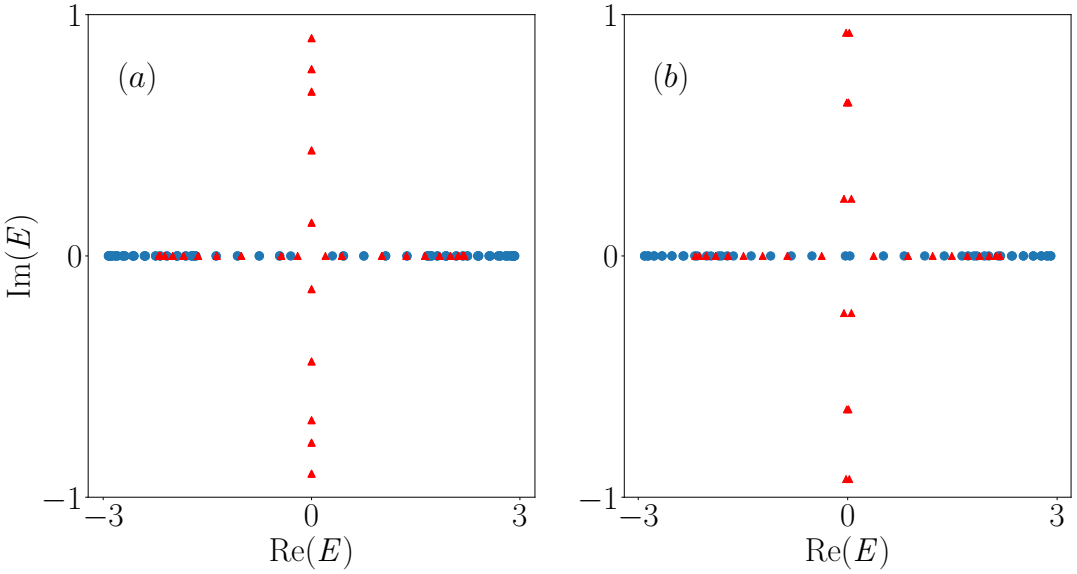

FIGURE B.1: Real and imaginary parts of the energy, corresponding to the Hamiltonian H_4, given via Eq.(4.28) in Chapter 4, for PBC (left panel) and OBC (right panel). The blue circles and the red triangles correspond to the cases, $\epsilon < 2t$ and $\epsilon > 2t$, respectively.

where $\tilde{\eta} = U^\dagger \sigma_z U$ with $U = \frac{1}{\sqrt{2}} \begin{pmatrix} 1 & -1 \\ 1 & 1 \end{pmatrix}$ and σ_z is z-component of the Pauli matrix. Hence, $h_4(k)$ qualifies as a $\tilde{\eta}$-pseudo-skew-Hermitian ($\tilde{\eta}$-PSH) Hamiltonian, since it anticommutes with $\tilde{\eta}$. By this argument, the system (obeying Eq. (B.3)) exhibits the behavior of a skew-Hermitian system owing to its pseudo-skew-Hermiticity. This characteristic effectively suppresses the occurrence of the NHSE in our system. It is worth mentioning that, we have shown that $h_4(k)$ is $\mathcal{PT}$-symmetric through a unitary transformation via the same operator U, that is $h_4'(k) = U^\dagger h_4(k) U$. Since $h_4'(k)$ respects $\mathcal{PT}$ symmetry, expressed via $\mathcal{PT} \equiv \sigma_x \mathcal{K}$, where $\mathcal{K}$ denotes the complex conjugation operator, the following relation holds,

$$h_4'(k) = (\mathcal{PT}) h_4'(k) (\mathcal{PT})^{-1}. \tag{B.4}$$

Hence, Eq. (B.3) illustrates a more general aspect of the $\mathcal{PT}$ symmetry inherent in $h_4'(k)$. Adhering to the properties of PH Hamiltonians outlined in Ref. [43], it can be demonstrated that, for PSH Hamiltonians, one of the following conditions must hold,

1. The eigenvalues of the Hamiltonian are real and come in positive and negative pairs, that is, $(\pm E)$.

2. The complex eigenvalues come in negative complex conjugate pairs with opposite signs, that is, $(E, -E^*)$.

Fig. B.1 provides a clear visualization of the above conditions. The blue circles represent the eigenspectra of the Hamiltonian H_4 (see Eq.(4.28) of Chapter 4) in the topological

region ($\epsilon < 2t$), where the eigenvalues are real and occur in positive and negative pairs. In contrast, the red triangles are in the trivial region ($\epsilon > 2t$), where some eigenvalues are real, occurring in positive and negative pairs, and others are purely imaginary. The essential hallmark of NHSE lies in the sensitivity of the eigenspectra to changes in the boundary conditions of the system [102]. The illustration in Fig. B.1 clearly depicts that the eigenvalue spectra exhibit insensitivity to boundary conditions (open and periodic), except for the presence of zero energy modes in the topological phase. This insensitivity is a crucial observation, providing robust evidence that the non-reciprocal Hamiltonian does not manifest any NHSE.

B.2 Non-Bloch Band Theory

The non-Bloch band theory dictates that the reformulation of the Bloch Hamiltonian $h_4(k)$, in Eq. (B.2), must be rewritten in terms of $h_4(\beta)$, where $\beta \equiv e^{ik}$ [134]. The ensuing characteristic equation, denoted as $|h_4(\beta) - E\mathbb{1}| = 0$ subsequently leads to an equation for a function of β, namely $f(\beta)$, where

$$f(\beta) = \left(\delta^2 + t^2 - t_{AB}^2\right)\left(\beta + \frac{1}{\beta}\right)^2 - 2\epsilon t\left(\beta + \frac{1}{\beta}\right) + \epsilon^2 + 4(t_{AB}^2 - \delta^2) = E^2, \tag{B.5}$$

where E is the energy. Since this equation is quartic, it admits four solutions for β, which may be denoted by β_1, β_2, β_3, and β_4. To ensure the existence of continuum bands, the following condition must be satisfied,

$$|\beta_1| \leq |\beta_2| = |\beta_3| \leq |\beta_4|. \tag{B.6}$$

In the framework of Hermitian systems, the GBZ, represented as C_β, takes the form of a unit circle in the complex plane. It is hence crucial to establish that the solutions of Eq. (B.5) fulfill the condition $|\beta_2| = |\beta_3| = 1$ to show that it still mimics the behavior of a Hermitian system and hence respects BBC, despite the non-reciprocity of the system. This assertion implies that the solutions β_2 and β_3 lie on a unit circle in the complex plane, akin to the characteristic behavior observed in Hermitian systems.

It will aid if we can decompose $f(\beta)$ in Eq. (B.5) to two quadratic equations. To this end, let us assume that β and β' are two distinct solutions (any two out of four in Eq. (B.6)), that satisfy Eq. (B.5) and $|\beta| \geq |\beta'|$. We then assume $\beta = \alpha\beta' e^{i\theta}$, with θ being real and $\theta \in (0, 2\pi)$ and $\alpha \geq 1$. From Eq. (B.5), we get $f(\beta) - f(\beta') = 0$, which can be written as,

$$\left(\delta^2 + t^2 - t_{AB}^2\right)\left(\beta + \frac{1}{\beta}\right)^2 - 2\epsilon t\left(\beta + \frac{1}{\beta}\right) - \left(\delta^2 + t^2 - t_{AB}^2\right)\left(\beta' + \frac{1}{\beta'}\right)^2 + 2\epsilon t\left(\beta' + \frac{1}{\beta'}\right) = 0.$$

Putting the value of β' in terms of β in the above equation, we get,

$$\left[\frac{\beta e^{-i\theta}}{\alpha}+\frac{\alpha e^{i\theta}}{\beta}-\beta-\frac{1}{\beta}\right]\left[\left(\delta^2+t^2-t_{AB}^2\right)\left(\frac{\beta e^{-i\theta}}{\alpha}+\frac{\alpha e^{i\theta}}{\beta}+\beta+\frac{1}{\beta}\right)-2\epsilon t\right]=0. \quad \text{(B.7)}$$

Vanishing of the first square bracket yields,

$$\frac{\beta e^{-i\theta}}{\alpha}+\frac{\alpha e^{i\theta}}{\beta}-\beta-\frac{1}{\beta}=0. \quad \text{(B.8)}$$

The above equation demands that $\alpha = 1$, which confirms the desired conditions namely, $|\beta| = |\beta'| = 1$. Thus, β from Eq. (B.8) and $\beta' = \frac{\beta e^{-i\theta}}{\alpha}$ yields β_2 and β_3 and confirms that $|\beta_2| = |\beta_3| = 1$. The other solutions namely, β_1 and β_4 are obtained for vanishing of the second square bracket in Eq. (B.7). The mathematical explanation presented above provides a rigorous proof of the Hermiticity of our Hamiltonian, despite its non-reciprocity, clarifying why the NHSE is not observed in our work.

Appendix C

Circuit Laplacian of an NH AA Model

The TEC corresponding to the Hamiltonian, H (Eq. (5.1) of Chapter 5), is constructed and analyzed in section 5.3. For an electrical network with $2N+1$ nodes, which is 21 for this case ($N = 10$), let $\mathcal{L}$ represent the Laplacian, and V_i and I_i, respectively, denote the voltage and the total current from an external source at i^{th} node. Let us now derive the Laplacian of the circuit (refer to Fig. 5.3(b)) under the condition where the master switch for S is open and S_1 is closed, representing the non-reciprocal circuit without the QP potential. Following the general equation (take Eq. (3.35) of Chapter 3 as an example) to construct TEC corresponding to a TB model, we write down the KVL and KCL at each node of the TEC. Without any external source and the following $2N+1$ equations,

$$\begin{aligned}
\frac{1}{j\omega L_{\text{edge}}}V_1 + j\omega(C-C')(V_1-V_2) &= 0,\\
\frac{1}{j\omega L}V_2 + j\omega(C+C')(V_2-V_1) + j\omega(C-C')(V_2-V_3) &= 0,\\
&\vdots\\
\frac{1}{j\omega L'}V_{N+1} + j\omega(C+C')(V_{N+1}-V_N) + j\omega(C-C')(V_{N+1}-V_{N+2}) &= 0,\\
&\vdots\\
\frac{1}{j\omega L}V_{2N} + j\omega(C-C')(V_{2N}-V_{2N-1}) + j\omega(C+C')(V_{2N}-V_{2N+1}) &= 0,\\
\frac{1}{j\omega L_{\text{edge}}}V_L + j\omega(C-C')(V_{2N+1}-V_{2N}) &= 0,
\end{aligned}$$

where V_i is the voltage at i^{th} node, and the values of the circuit elements, C, C', L, L' and L_{edge} are defined in the sections 5.4 and 5.5 of Chapter 5. Note that j represents the imaginary number ($= \sqrt{-1}$) and $(N+1)^{\text{th}}$ node denotes the interface. When we formulate these $2N+1$ ($= 21$) equations corresponding to Kirchhoff's law in the form

$I = \mathcal{L}V$, the resulting Laplacian matrix, $\mathcal{L}$ is given as,

$$\mathcal{L}(\omega) = \begin{pmatrix} \frac{1}{j\omega L_{\text{edge}}} + j\omega(C-C') & -j\omega(C-C') & 0 & \cdots & \\ -j\omega(C+C') & \frac{1}{j\omega L} + 2j\omega C & -j\omega(C-C') & 0 & \cdots \\ \vdots & \vdots & \vdots & \vdots & \vdots \\ \cdots 0 & -j\omega(C+C') & \frac{1}{j\omega L'} + 2j\omega(C+C') & -j\omega(C+C') & 0\cdots \\ \vdots & \vdots & \vdots & \vdots & \vdots \\ \cdots & 0 & -j\omega(C-C') & \frac{1}{j\omega L} + 2j\omega C & -j\omega(C+C') \\ & \cdots & 0 & -j\omega(C-C') & \frac{1}{j\omega L_{\text{edge}}} + j\omega(C-C') \end{pmatrix}. \tag{C.1}$$

Note that the diagonal terms vanish at the resonant frequency,

$$\omega_R = \frac{1}{\sqrt{2LC}} = \frac{1}{\sqrt{L_{\text{edge}}(C-C')}} = \frac{1}{\sqrt{2L'(C+C')}}. \tag{C.2}$$

Subsequently, at $\omega = \omega_R$, $\mathcal{L}$ becomes,

$$\mathcal{L}(\omega_R) = -j \begin{pmatrix} 0 & \omega_R(C-C') & 0 & \cdots & \\ \omega_R(C+C') & 0 & \omega_R(C-C') & 0 & \cdots \\ \vdots & \vdots & \vdots & \vdots & \vdots \\ \cdots 0 & \omega_R(C+C') & 0 & \omega_R(C+C') & 0\cdots \\ \vdots & \vdots & \vdots & \vdots & \vdots \\ \cdots & 0 & \omega_R(C-C') & 0 & \omega_R(C+C') \\ & \cdots & 0 & \omega_R(C-C') & 0 \end{pmatrix}. \tag{C.3}$$

Thus, the Laplacian, $\mathcal{L}$, effectively replicates the matrix form of H with $\lambda = 0$, including a scaling factor of $-j$. Consequently, the eigenvalues and the eigenvectors of $\mathcal{L}$ directly correspond to those of H with $\lambda = 0$. This equivalence ensures that the localization properties of the eigenvectors of the TB model are reflected in the VP derived from the Laplacian. Note that the capacitors are analogous to the hopping terms in the TB model, where $(t \pm \gamma) \equiv \omega_R(C \pm C')$.

Let us incorporate the QP potential, as described in Eq. (5.1), into the TEC. This addition introduces extra diagonal terms in $\mathcal{L}$, stemming from the node-specific values of the capacitors, $C[k]$, and the resistors, $R[k]$ at the k^{th} node. According to Eq. (5.1), the QP potential is expressed as,

$$\lambda_k = 2\lambda\left[\cos(2\pi\beta k)\cosh\alpha - i\sin(2\pi\beta k)\sinh\alpha\right].$$

Thus, at the resonant frequency, ω_R, $C[k]$ and $R[k]$ assume following forms,

$$C[k] = -\text{Re}(\lambda_k)/\omega_R = -2\lambda\cos(2\pi\beta k)\ \cosh\alpha/\omega_R, \quad R[k] = [\text{Im}(\lambda_k)]^{-1} = [-2\lambda\sin(2\pi\beta k)\ \sinh\alpha]^{-1}.$$

After including these grounded capacitors and the resistors in Eq. (C.3), $\mathcal{L}$ assumes,

$$\mathcal{L}(\omega_R) = -j \begin{pmatrix} -\omega_R C[1] + \frac{j}{R[1]} & \omega_R(C - C') & 0 & \cdots & \\ \omega_R(C + C') & -\omega_R C[2] + \frac{j}{R[2]} & \omega_R(C - C') & 0 & \cdots \\ \vdots & \vdots & \vdots & \vdots & \vdots \\ \cdots 0 & \omega_R(C + C') & -\omega_R C[N+1] + \frac{j}{R[N+1]} & \omega_R(C + C') & 0 \cdots \\ \vdots & \vdots & \vdots & \vdots & \vdots \\ \cdots & 0 & \omega_R(C - C') & -\omega_R C[2N] + \frac{j}{R[2N]} & \omega_R(C + C') \\ & \cdots & 0 & \omega_R(C - C') & -\omega_R C[2N+1] + \frac{j}{R[2N+1]} \end{pmatrix}. \tag{C.4}$$

Thus, Eqs. (C.3) and (C.4) represent the Laplacians for non-reciprocal TECs in the absence and presence of the complex QP disorder, respectively.

Bibliography

[1] N. Okuma and M. Sato, Annual Review of Condensed Matter Physics **14**, 83 (2023).

[2] H. Yang, L. Song, Y. Cao, and P. Yan, Physics Reports **1093**, 1 (2024), circuit realization of topological physics.

[3] C. H. Lee, S. Imhof, C. Berger, F. Bayer, J. Brehm, L. W. Molenkamp, T. Kiessling, and R. Thomale, Communications Physics **1**, 39 (2018).

[4] T. Helbig, T. Hofmann, S. Imhof, M. Abdelghany, T. Kiessling, L. W. Molenkamp, C. H. Lee, A. Szameit, M. Greiter, and R. Thomale, Nature Physics **16**, 747 (2020).

[5] J. Maciejko, T. L. Hughes, and S.-C. Zhang, Annual Review of Condensed Matter Physics **2**, 31 (2011).

[6] L. D. Landau and E. M. Lifshitz, *Statistical Physics* (Pergamon Press, Oxford, 1980).

[7] K. v. Klitzing, G. Dorda, and M. Pepper, Phys. Rev. Lett. **45**, 494 (1980).

[8] D. J. Thouless, M. Kohmoto, M. P. Nightingale, and M. den Nijs, Phys. Rev. Lett. **49**, 405 (1982).

[9] M. Nakahara, *Geometry, Topology, and Physics* (A. Hilger, London, 1990).

[10] M. Z. Hasan and C. L. Kane, Rev. Mod. Phys. **82**, 3045 (2010).

[11] X.-L. Qi and S.-C. Zhang, Rev. Mod. Phys. **83**, 1057 (2011).

[12] N. P. Armitage, E. J. Mele, and A. Vishwanath, Rev. Mod. Phys. **90**, 015001 (2018).

[13] B. Q. Lv, T. Qian, and H. Ding, Rev. Mod. Phys. **93**, 025002 (2021).

[14] A. W. W. Ludwig, Physica Scripta **2016**, 014001 (2015).

[15] A. Altland and M. R. Zirnbauer, Phys. Rev. B **55**, 1142 (1997).

[16] W. P. Su, J. R. Schrieffer, and A. J. Heeger, Phys. Rev. Lett. **42**, 1698 (1979).

[17] S. Ryu, A. P. Schnyder, A. Furusaki, and A. W. W. Ludwig, New Journal of Physics **12**, 065010 (2010).

[18] E. H. Hall, London, Edinburgh, and Dublin Philosophical Magazine and Journal of Science **12**, 157 (1881).

[19] F. D. M. Haldane, Phys. Rev. Lett. **61**, 2015 (1988).

[20] J. Sinova, D. Culcer, Q. Niu, N. A. Sinitsyn, T. Jungwirth, and A. H. MacDonald, Phys. Rev. Lett. **92**, 126603 (2004).

[21] S. Murakami, N. Nagaosa, and S.-C. Zhang, Science **301**, 1348 (2003).

[22] C. L. Kane and E. J. Mele, Phys. Rev. Lett. **95**, 226801 (2005).

[23] B. A. Bernevig, T. L. Hughes, and S.-C. Zhang, Science **314**, 1757 (2006).

[24] M. König, S. Wiedmann, C. Brüne, A. Roth, H. Buhmann, L. W. Molenkamp, X.-L. Qi, and S.-C. Zhang, Science **318**, 766 (2007).

[25] N. Moiseyev, *Non-Hermitian quantum mechanics* (Cambridge University Press, 2011).

[26] P. A. M. Dirac, *The principles of quantum mechanics*, 27 (Oxford university press, 1981).

[27] Y. Ashida, Z. Gong, and M. Ueda, Advances in Physics **69**, 249 (2020).

[28] E. J. Bergholtz, J. C. Budich, and F. K. Kunst, Rev. Mod. Phys. **93**, 015005 (2021).

[29] K. Ding, C. Fang, and G. Ma, Nature Reviews Physics **4**, 745 (2022).

[30] I. Rotter, Journal of Physics A: Mathematical and Theoretical **42**, 153001 (2009).

[31] C. M. Bender and D. W. Hook, Rev. Mod. Phys. **96**, 045002 (2024).

[32] C. M. Bender, *PT Symmetry: In Quantum and Classical Physics* (World Scientific, 2018).

[33] A. Ghatak and T. Das, Journal of Physics: Condensed Matter **31**, 263001 (2019).

[34] Z. Gong, Y. Ashida, K. Kawabata, K. Takasan, S. Higashikawa, and M. Ueda, Phys. Rev. X **8**, 031079 (2018).

[35] K. Kawabata, K. Shiozaki, M. Ueda, and M. Sato, Phys. Rev. X **9**, 041015 (2019).

[36] A. Banerjee, R. Sarkar, S. Dey, and A. Narayan, Journal of Physics: Condensed Matter **35**, 333001 (2023).

[37] V. Meden, L. Grunwald, and D. M. Kennes, Reports on Progress in Physics **86**, 124501 (2023).

[38] R. Lin, T. Tai, L. Li, *et al.*, Frontiers of Physics **18**, 53605 (2023).

[39] K. Yang, Z. Li, J. L. K. König, L. Rødland, M. Stålhammar, and E. J. Bergholtz, Reports on Progress in Physics **87**, 078002 (2024).

[40] L. Zhou and D.-J. Zhang, Entropy **25**, 10.3390/e25101401 (2023).

[41] C. M. Bender and S. Boettcher, Phys. Rev. Lett. **80**, 5243 (1998).

[42] C. M. Bender, Reports on Progress in Physics **70**, 947 (2007).

[43] A. Mostafazadeh, Journal of Mathematical Physics **43**, 205 (2002).

[44] W. D. Heiss, Journal of Physics A: Mathematical and Theoretical **45**, 444016 (2012).

[45] S. Yao and Z. Wang, Phys. Rev. Lett. **121**, 086803 (2018).

[46] R. El-Ganainy, K. G. Makris, D. N. Christodoulides, and Z. H. Musslimani, Opt. Lett. **32**, 2632 (2007).

[47] C. E. Rüter, K. G. Makris, R. El-Ganainy, D. N. Christodoulides, M. Segev, and D. Kip, Nature Physics **6**, 192 (2010).

[48] A. Guo, G. J. Salamo, D. Duchesne, R. Morandotti, M. Volatier-Ravat, V. Aimez, G. A. Siviloglou, and D. N. Christodoulides, Phys. Rev. Lett. **103**, 093902 (2009).

[49] K. G. Makris, R. El-Ganainy, D. N. Christodoulides, and Z. H. Musslimani, Phys. Rev. Lett. **100**, 103904 (2008).

[50] K. G. Makris, R. El-Ganainy, D. N. Christodoulides, and Z. H. Musslimani, Phys. Rev. A **81**, 063807 (2010).

[51] Z. H. Musslimani, K. G. Makris, R. El-Ganainy, and D. N. Christodoulides, Phys. Rev. Lett. **100**, 030402 (2008).

[52] H. Alaeian, B. Baum, V. Jankovic, M. Lawrence, and J. A. Dionne, Phys. Rev. B **93**, 205439 (2016).

[53] P. Ambichl, K. G. Makris, L. Ge, Y. Chong, A. D. Stone, and S. Rotter, Phys. Rev. X **3**, 041030 (2013).

[54] Y. D. Chong, L. Ge, H. Cao, and A. D. Stone, Phys. Rev. Lett. **105**, 053901 (2010).

[55] Y. D. Chong, L. Ge, and A. D. Stone, Phys. Rev. Lett. **106**, 093902 (2011).

[56] S. Longhi, Phys. Rev. A **82**, 031801 (2010).

[57] J. Li, A. K. Harter, J. Liu, L. de Melo, Y. N. Joglekar, and L. Luo, Nature Communications **10**, 855 (2019).

[58] S. Park, Y. Hwang, H. C. Choi, and B.-J. Yang, Nature communications **12**, 6781 (2021).

[59] J. Del Pino, J. J. Slim, and E. Verhagen, Nature **606**, 82 (2022).

[60] Y. Aurégan and V. Pagneux, Phys. Rev. Lett. **118**, 174301 (2017).

[61] S. A. Cummer, J. Christensen, and A. Alù, Nature Reviews Materials **1**, 1 (2016).

[62] R. Fleury, A. B. Khanikaev, and A. Alu, Nature communications **7**, 11744 (2016).

[63] H. Alaeian and J. A. Dionne, Phys. Rev. A **89**, 033829 (2014).

[64] D. Schurig, J. J. Mock, B. J. Justice, S. A. Cummer, J. B. Pendry, A. F. Starr, and D. R. Smith, Science **314**, 977 (2006).

[65] O. Vázquez-Candanedo, J. C. Hernández-Herrejón, F. M. Izrailev, and D. N. Christodoulides, Phys. Rev. A **89**, 013832 (2014).

[66] I. V. Barashenkov, G. S. Jackson, and S. Flach, Phys. Rev. A **88**, 053817 (2013).

[67] C. M. Bender, B. K. Berntson, D. Parker, and E. Samuel, American Journal of Physics **81**, 173 (2013).

[68] K. Li and P. G. Kevrekidis, Phys. Rev. E **83**, 066608 (2011).

[69] R. Shankar, *Principles of Quantum Mechanics*, 2nd ed. (Springer, 2012).

[70] C. Shi, M. Dubois, Y. Chen, L. Cheng, H. Ramezani, Y. Wang, and X. Zhang, Nature Communications **7**, 11110 (2016).

[71] K. Ding, G. Ma, M. Xiao, Z. Q. Zhang, and C. T. Chan, Phys. Rev. X **6**, 021007 (2016).

[72] M.-A. Miri and A. Alù, Science **363**, eaar7709 (2019).

[73] T. Ozawa, H. M. Price, A. Amo, N. Goldman, M. Hafezi, L. Lu, M. C. Rechtsman, D. Schuster, J. Simon, O. Zilberberg, and I. Carusotto, Rev. Mod. Phys. **91**, 015006 (2019).

[74] X. Yin and X. Zhang, Nature Materials **12**, 175 (2013).

[75] Z. Zhang, Y. Zhang, J. Sheng, L. Yang, M.-A. Miri, D. N. Christodoulides, B. He, Y. Zhang, and M. Xiao, Phys. Rev. Lett. **117**, 123601 (2016).

[76] L. Feng, Z. J. Wong, R.-M. Ma, Y. Wang, and X. Zhang, Science **346**, 972 (2014).

[77] B. Midya, H. Zhao, and L. Feng, Nature Communications **9**, 2674 (2018).

[78] D. Zhang, X.-Q. Luo, Y.-P. Wang, T.-F. Li, and J. Q. You, Nature Communications **8**, 1368 (2017).

[79] T. Yoshida and Y. Hatsugai, Phys. Rev. B **100**, 054109 (2019).

[80] J. Schindler, A. Li, M. C. Zheng, F. M. Ellis, and T. Kottos, Phys. Rev. A **84**, 040101 (2011).

[81] J. Schindler, Z. Lin, J. M. Lee, H. Ramezani, F. M. Ellis, and T. Kottos, Journal of Physics A: Mathematical and Theoretical **45**, 444029 (2012).

[82] N. Bender, S. Factor, J. D. Bodyfelt, H. Ramezani, D. N. Christodoulides, F. M. Ellis, and T. Kottos, Phys. Rev. Lett. **110**, 234101 (2013).

[83] S. Assawaworrarit, X. Yu, and S. Fan, Nature **546**, 387 (2017).

[84] P.-Y. Chen, M. Sakhdari, M. Hajizadegan, Q. Cui, M. M.-C. Cheng, R. El-Ganainy, and A. Alù, Nature Electronics **1**, 297 (2018).

[85] T. Stehmann, W. D. Heiss, and F. G. Scholtz, Journal of Physics A: Mathematical and General **37**, 7813 (2004).

[86] R. Lefebvre, O. Atabek, M. Šindelka, and N. Moiseyev, Phys. Rev. Lett. **103**, 123003 (2009).

[87] J. Rubinstein, P. Sternberg, and Q. Ma, Phys. Rev. Lett. **99**, 167003 (2007).

[88] P. San-Jose, J. Cayao, E. Prada, and R. Aguado, Scientific Reports **6**, 21427 (2016).

[89] J. Avila, F. Peñaranda, E. Prada, P. San-Jose, and R. Aguado, Communications Physics **2**, 133 (2019).

[90] P. Cejnar, S. Heinze, and M. Macek, Phys. Rev. Lett. **99**, 100601 (2007).

[91] Z. Lin, H. Ramezani, T. Eichelkraut, T. Kottos, H. Cao, and D. N. Christodoulides, Phys. Rev. Lett. **106**, 213901 (2011).

[92] B. Peng, Ş. K. Özdemir, F. Lei, F. Monifi, M. Gianfreda, G. L. Long, S. Fan, F. Nori, C. M. Bender, and L. Yang, Nature Physics **10**, 394 (2014).

[93] H. Hodaei, M.-A. Miri, M. Heinrich, D. N. Christodoulides, and M. Khajavikhan, Science **346**, 975 (2014).

[94] H. Xu, D. Mason, L. Jiang, and J. G. E. Harris, Nature **537**, 80 (2016).

[95] T. Gao, E. Estrecho, K. Y. Bliokh, T. C. H. Liew, M. D. Fraser, S. Brodbeck, M. Kamp, C. Schneider, S. Höfling, Y. Yamamoto, F. Nori, Y. S. Kivshar, A. G. Truscott, R. G. Dall, and E. A. Ostrovskaya, Nature **526**, 554 (2015).

[96] T. Gao, G. Li, E. Estrecho, T. C. H. Liew, D. Comber-Todd, A. Nalitov, M. Steger, K. West, L. Pfeiffer, D. W. Snoke, A. V. Kavokin, A. G. Truscott, and E. A. Ostrovskaya, Phys. Rev. Lett. **120**, 065301 (2018).

[97] W. D. Heiss, Journal of Physics A: Mathematical and Theoretical **41**, 244010 (2008).

[98] A. Cerjan, M. Xiao, L. Yuan, and S. Fan, Phys. Rev. B **97**, 075128 (2018).

[99] A. Cerjan, A. Raman, and S. Fan, Phys. Rev. Lett. **116**, 203902 (2016).

[100] Y. Xiong, Journal of Physics Communications **2**, 035043 (2018).

[101] X. Zhang, T. Zhang, M.-H. Lu, and Y.-F. Chen, Advances in Physics: X **7**, 2109431 (2022).

[102] C. H. Lee and R. Thomale, Phys. Rev. B **99**, 201103 (2019).

[103] D. Zou, T. Chen, W. He, *et al.*, Nature Communications **12**, 7201 (2021).

[104] B. Liu, Y. Li, B. Yang, X. Shen, Y. Yang, Z. H. Hang, and M. Ezawa, Phys. Rev. Res. **5**, 043034 (2023).

[105] Z. Lu, X. Chen, Y. Hu, J. Wu, J. Lu, X. Huang, W. Deng, and Z. Liu, Phys. Rev. Appl. **21**, 034043 (2024).

[106] C. Liu, B. Ruan, W. Hu, W. Lin, X. Dai, J. Wu, L. Jiang, and Y. Xiang, Phys. Rev. Appl. **21**, 054013 (2024).

[107] T. Hofmann, T. Helbig, F. Schindler, N. Salgo, M. Brzezińska, M. Greiter, T. Kiessling, D. Wolf, A. Vollhardt, A. Kabaši, C. H. Lee, A. Bilušić, R. Thomale, and T. Neupert, Phys. Rev. Res. **2**, 023265 (2020).

[108] W. Lin, B. Ruan, C. Liu, X. Dai, and Y. Xiang, Applied Physics Letters **125**, 173104 (2024).

[109] C. X. Guo, L. Su, Y. Wang, *et al.*, Nature Communications **15**, 9120 (2024).

[110] S. Weidemann, M. Kremer, T. Helbig, T. Hofmann, A. Stegmaier, M. Greiter, R. Thomale, and A. Szameit, Science **368**, 311 (2020).

[111] W. Zhu and J. Gong, Phys. Rev. B **108**, 035406 (2023).

[112] Z. Fang, M. Hu, L. Zhou, and K. Ding, Nanophotonics **11**, 3447 (2022).

[113] X. Zhu, H. Wang, S. K. Gupta, H. Zhang, B. Xie, M. Lu, and Y. Chen, Phys. Rev. Res. **2**, 013280 (2020).

[114] Y. Song, W. Liu, L. Zheng, Y. Zhang, B. Wang, and P. Lu, Phys. Rev. Appl. **14**, 064076 (2020).

[115] J. Zhong, K. Wang, Y. Park, V. Asadchy, C. C. Wojcik, A. Dutt, and S. Fan, Phys. Rev. B **104**, 125416 (2021).

[116] K. Wang, A. Dutt, K. Y. Yang, C. C. Wojcik, J. Vučković, and S. Fan, Science **371**, 1240 (2021).

[117] H. Xin, W. Song, S. Wu, Z. Lin, S. Zhu, and T. Li, Phys. Rev. B **107**, 165401 (2023).

[118] L. Zhang, Y. Yang, Y. Ge, *et al.*, Nature Communications **12**, 6297 (2021).

[119] Q. Zhou, J. Wu, Z. Pu, *et al.*, Nature Communications **14**, 4569 (2023).

[120] Z. Gu, H. Gao, H. Xue, *et al.*, Nature Communications **13**, 7668 (2022).

[121] H. Gao, H. Xue, Z. Gu, L. Li, W. Zhu, Z. Su, J. Zhu, B. Zhang, and Y. D. Chong, Phys. Rev. B **106**, 134112 (2022).

[122] T. Wan, K. Zhang, J. Li, Z. Yang, and Z. Yang, Science Bulletin **68**, 2330 (2023).

[123] J. Wu, R. Zheng, J. Liang, M. Ke, J. Lu, W. Deng, X. Huang, and Z. Liu, Phys. Rev. Lett. **133**, 126601 (2024).

[124] Q. Zhang, Y. Leng, L. Xiong, Y. Li, K. Zhang, L. Qi, and C. Qiu, Advanced Materials **36**, 2403108 (2024).

[125] W. Wang, X. Wang, and G. Ma, Nature **608**, 50 (2022).

[126] M. Brandenbourger, X. Locsin, E. Lerner, *et al.*, Nature Communications **10**, 4608 (2019).

[127] A. Ghatak, M. Brandenbourger, J. van Wezel, and C. Coulais, Proceedings of the National Academy of Sciences **117**, 29561 (2020).

[128] W. Wang, M. Hu, X. Wang, G. Ma, and K. Ding, Phys. Rev. Lett. **131**, 207201 (2023).

[129] N. Hatano and D. R. Nelson, Phys. Rev. Lett. **77**, 570 (1996).

[130] N. Hatano and D. R. Nelson, Phys. Rev. B **56**, 8651 (1997).

[131] N. Okuma, K. Kawabata, K. Shiozaki, and M. Sato, Phys. Rev. Lett. **124**, 086801 (2020).

[132] Z. Yang, K. Zhang, C. Fang, and J. Hu, Phys. Rev. Lett. **125**, 226402 (2020).

[133] K. Zhang, Z. Yang, and C. Fang, Phys. Rev. Lett. **125**, 126402 (2020).

[134] K. Yokomizo and S. Murakami, Phys. Rev. Lett. **123**, 066404 (2019).

[135] W. A. Benalcazar, B. A. Bernevig, and T. L. Hughes, Science **357**, 61 (2017).

[136] J. Langbehn, Y. Peng, L. Trifunovic, F. von Oppen, and P. W. Brouwer, Phys. Rev. Lett. **119**, 246401 (2017).

[137] Z. Song, Z. Fang, and C. Fang, Phys. Rev. Lett. **119**, 246402 (2017).

[138] A. Matsugatani and H. Watanabe, Phys. Rev. B **98**, 205129 (2018).

[139] E. Khalaf, H. C. Po, A. Vishwanath, and H. Watanabe, Phys. Rev. X **8**, 031070 (2018).

[140] F. K. Kunst, G. van Miert, and E. J. Bergholtz, Phys. Rev. B **97**, 241405 (2018).

[141] S. Liu, A. Vishwanath, and E. Khalaf, Phys. Rev. X **9**, 031003 (2019).

[142] K. Kawabata, M. Sato, and K. Shiozaki, Phys. Rev. B **102**, 205118 (2020).

[143] K. Zhang, Z. Yang, and C. Fang, Nature Communications **13**, 2496 (2022).

[144] C. H. Lee, L. Li, and J. Gong, Phys. Rev. Lett. **123**, 016805 (2019).

[145] E. Edvardsson, F. K. Kunst, and E. J. Bergholtz, Phys. Rev. B **99**, 081302 (2019).

[146] V. V. Albert, L. I. Glazman, and L. Jiang, Phys. Rev. Lett. **114**, 173902 (2015).

[147] S. Imhof, C. Berger, F. Bayer, *et al.*, Nature Physics **14**, 925 (2018).

[148] T. Hofmann, T. Helbig, C. H. Lee, M. Greiter, and R. Thomale, Phys. Rev. Lett. **122**, 247702 (2019).

[149] T. Helbig, T. Hofmann, C. H. Lee, R. Thomale, S. Imhof, L. W. Molenkamp, and T. Kiessling, Phys. Rev. B **99**, 161114 (2019).

[150] J. Wu, Z. Wang, Y. Biao, *et al.*, Nature Electronics **5**, 635 (2022).

[151] S. M. Rafi-Ul-Islam, Z. B. Siu, C. Sun, and M. B. A. Jalil, New Journal of Physics **22**, 023025 (2020).

[152] J. Ningyuan, C. Owens, A. Sommer, D. Schuster, and J. Simon, Phys. Rev. X **5**, 021031 (2015).

[153] Z. Wang, Y. Biao, X.-T. Zeng, X. Chen, X.-L. Sheng, S. A. Yang, and R. Yu, Phys. Rev. B **107**, L201101 (2023).

[154] R. Li, B. Lv, H. Tao, J. Shi, Y. Chong, B. Zhang, and H. Chen, National Science Review **8**, nwaa192 (2020).

[155] Z. Wang, X.-T. Zeng, Y. Biao, Z. Yan, and R. Yu, Phys. Rev. Lett. **130**, 057201 (2023).

[156] Y. Biao and R. Yu, Phys. Rev. B **108**, 165128 (2023).

[157] C. H. Lee, A. Sutrisno, T. Hofmann, *et al.*, Nature Communications **11**, 4385 (2020).

[158] Y. Lu, N. Jia, L. Su, C. Owens, G. Juzeliūnas, D. I. Schuster, and J. Simon, Phys. Rev. B **99**, 020302 (2019).

[159] S. Liu, S. Ma, C. Yang, L. Zhang, W. Gao, Y. J. Xiang, T. J. Cui, and S. Zhang, Phys. Rev. Appl. **13**, 014047 (2020).

[160] X.-X. Zhang and M. Franz, Phys. Rev. Lett. **124**, 046401 (2020).

[161] S. Liu, R. Shao, S. Ma, L. Zhang, O. You, H. Wu, Y. J. Xiang, T. J. Cui, and S. Zhang, Research **2021** (2021).

[162] A. Stegmaier, S. Imhof, T. Helbig, T. Hofmann, C. H. Lee, M. Kremer, A. Fritzsche, T. Feichtner, S. Klembt, S. Höfling, I. Boettcher, I. C. Fulga, L. Ma, O. G. Schmidt, M. Greiter, T. Kiessling, A. Szameit, and R. Thomale, Phys. Rev. Lett. **126**, 215302 (2021).

[163] M. Ezawa, Phys. Rev. B **98**, 201402 (2018).

[164] P. Zhu, X. Q. Sun, T. L. Hughes, *et al.*, Nature Communications **14**, 720 (2023).

[165] S. Guo, G. Pan, J. Huang, R. Huang, F. Zhuang, S. Su, Z. Lin, W. Qiu, and Q. Kan, Applied Physics Letters **123**, 043102 (2023).

[166] F. Zangeneh-Nejad and R. Fleury, Phys. Rev. Lett. **123**, 053902 (2019).

[167] R. Chen, C.-Z. Chen, J.-H. Gao, B. Zhou, and D.-H. Xu, Phys. Rev. Lett. **124**, 036803 (2020).

[168] S. S. Yamada, T. Li, M. Lin, *et al.*, Nature Communications **13**, 2035 (2022).

[169] L. Song, H. Yang, Y. Cao, *et al.*, Nature Communications **13**, 5601 (2022).

[170] P. M. Lenggenhager, A. Stegmaier, L. K. Upreti, *et al.*, Nature Communications **13**, 4373 (2022).

[171] A. Chen, H. Brand, T. Helbig, *et al.*, Nature Communications **14**, 622 (2023).

[172] W. Zhang, F. Di, X. Zheng, *et al.*, Nature Communications **14**, 1083 (2023).

[173] D. Halder, S. Ganguly, and S. Basu, Journal of Physics: Condensed Matter **35**, 105901 (2022).

[174] D. Halder and S. Basu, Journal of Physics: Condensed Matter **36**, 335301 (2024).

[175] D. Halder, R. Thomale, and S. Basu, Phys. Rev. B **109**, 115407 (2024).

[176] D. Halder and S. Basu, Phys. Rev. B **111**, 235447 (2025).

[177] D. Halder, S. Lahiri, and S. Basu, Phys. Rev. B **110**, 115132 (2024).

[178] J. W. Nilsson, *Electric circuits* (Pearson Education India, 2008).

[179] F. Y. Wu, Journal of Physics A: Mathematical and General **37**, 6653 (2004).

[180] M. Grifoni and P. Hänggi, Phys. Rep. **304**, 229 (1998).

[181] J. Cayssol, B. Dóra, F. Simon, and R. Moessner, Phys. Status Solidi RRL **7**, 101 (2013).

[182] A. Gómez-León and G. Platero, Phys. Rev. Lett. **110**, 200403 (2013).

[183] N. Goldman and J. Dalibard, Phys. Rev. X **4**, 031027 (2014).

[184] K. Roy and S. Basu, Phys. Rev. B **108**, 045415 (2023).

[185] M. Rechtsman, J. M. Zeuner, Y. Plotnik, Y. Lumer, D. Podolsky, F. Dreisow, S. Nolte, M. Segev, and A. Szameit, Nature **496**, 196 (2013).

[186] K. Wintersperger, C. Braun, F. N. Ünal, A. Eckardt, M. Di Liberto, M. Aidelsburger, I. Bloch, and N. Goldman, Nat. Phys. **16**, 1058 (2020).

[187] L. J. Maczewsky, J. M. Zeuner, S. Nolte, and A. Szameit, Nat. Commun. **8**, 13756 (2017).

[188] S. Mukherjee, A. Spracklen, M. Valiente, E. Andersson, P. Öhberg, N. Goldman, and R. R. Thomson, Nat. Commun. **8**, 13918 (2017).

[189] K. Roy, D. Halder, K. Gogoi, B. Tanatar, and S. Basu, Phys. Rev. Res. **7**, 043331 (2025).

[190] M. Creutz, Phys. Rev. Lett. **83**, 2636 (1999).

[191] R. Roy and F. Harper, Phys. Rev. B **96**, 155118 (2017).

[192] A. P. Schnyder, S. Ryu, A. Furusaki, and A. W. W. Ludwig, Phys. Rev. B **78**, 195125 (2008).

[193] S. S. Dabiri and H. Cheraghchi, Journal of Applied Physics **134**, 084303 (2023).

[194] M. Chitsazi, H. Li, F. M. Ellis, and T. Kottos, Phys. Rev. Lett. **119**, 093901 (2017).

[195] M. A. Quiroz-Juárez, K. S. Agarwal, Z. A. Cochran, J. L. Aragón, Y. N. Joglekar, and R. d. J. León-Montiel, Phys. Rev. Appl. **18**, 054034 (2022).

[196] J. K. Asbóth, L. Oroszlány, and A. Pályi, *A short course on topological insulators*, Vol. 919 (Springer, 2016).

[197] S. Lieu, Phys. Rev. B **97**, 045106 (2018).

[198] C. Yin, H. Jiang, L. Li, R. Lü, and S. Chen, Phys. Rev. A **97**, 052115 (2018).

[199] F. K. Kunst, E. Edvardsson, J. C. Budich, and E. J. Bergholtz, Phys. Rev. Lett. **121**, 026808 (2018).

[200] A. Mostafazadeh, Physics Letters A **264**, 11 (1999).

[201] B. Kramer and A. MacKinnon, Reports on Progress in Physics **56**, 1469 (1993).

[202] M. V. Berry, Journal of Physics A: Mathematical and General **18**, 15 (1985).

[203] Z.-Y. Wang, J.-S. Hong, and X.-J. Liu, Phys. Rev. B **108**, L060204 (2023).

[204] S.-X. Wang, Phys. Rev. B **109**, L081108 (2024).

[205] P. W. Anderson, Phys. Rev. **109**, 1492 (1958).

[206] S. Aubry and G. André, Ann. Isr. Phys. Soc. **3**, 133 (1980).

[207] S. Ganeshan, K. Sun, and S. Das Sarma, Phys. Rev. Lett. **110**, 180403 (2013).

[208] S. Ganeshan, J. H. Pixley, and S. Das Sarma, Phys. Rev. Lett. **114**, 146601 (2015).

[209] G. De Tomasi, S. Bera, J. H. Bardarson, and F. Pollmann, Phys. Rev. Lett. **118**, 016804 (2017).

[210] Y. Lahini, R. Pugatch, F. Pozzi, M. Sorel, R. Morandotti, N. Davidson, and Y. Silberberg, Phys. Rev. Lett. **103**, 013901 (2009).

[211] Y. E. Kraus, Y. Lahini, Z. Ringel, M. Verbin, and O. Zilberberg, Phys. Rev. Lett. **109**, 106402 (2012).

[212] S. Dey, N. R. Das, and S. Ghosh, Optics Communications **506**, 127593 (2022).

[213] G. Roati, C. D'Errico, L. Fallani, M. Fattori, C. Fort, M. Zaccanti, G. Modugno, M. Modugno, and M. Inguscio, Nature **453**, 895 (2008).

[214] F. A. An, K. Padavić, E. J. Meier, S. Hegde, S. Ganeshan, J. H. Pixley, S. Vishveshwara, and B. Gadway, Phys. Rev. Lett. **126**, 040603 (2021).

[215] H. Li, Y.-Y. Wang, Y.-H. Shi, K. Huang, X. Song, G.-H. Liang, Z.-Y. Mei, B. Zhou, H. Zhang, J.-C. Zhang, S. Chen, S. P. Zhao, Y. Tian, Z.-Y. Yang, Z. Xiang, K. Xu, D. Zheng, and H. Fan, npj Quantum Information **9**, 40 (2023).

[216] S. Longhi, Phys. Rev. Lett. **122**, 237601 (2019).

[217] S. Schiffer, X.-J. Liu, H. Hu, and J. Wang, Phys. Rev. A **103**, L011302 (2021).

[218] S. Longhi, Phys. Rev. B **103**, 054203 (2021).

[219] Y. Liu, Q. Zhou, and S. Chen, Phys. Rev. B **104**, 024201 (2021).

[220] Y.-M. Sun, X.-Y. Wang, and L.-J. Zhai, Phys. Rev. B **110**, 054202 (2024).

[221] S.-Z. Li, E. Cheng, S.-L. Zhu, and Z. Li, Phys. Rev. B **110**, 134203 (2024).

[222] H. Jiang, L.-J. Lang, C. Yang, S.-L. Zhu, and S. Chen, Phys. Rev. B **100**, 054301 (2019).

[223] Q.-B. Zeng and Y. Xu, Phys. Rev. Res. **2**, 033052 (2020).

[224] X. Xia, K. Huang, S. Wang, and X. Li, Phys. Rev. B **105**, 014207 (2022).

[225] H. Wang, W. Zhang, H. Sun, and X. Zhang, Phys. Rev. B **108**, 144203 (2023).

[226] X. Sun and C. Liu, Physics Letters A **482**, 129043 (2023).

[227] Y. Zhang, L. Su, and S. Chen, Phys. Rev. B **111**, L140201 (2025).

[228] S. R. Padhi, A. Padhan, S. Banerjee, and T. Mishra, Phys. Rev. B **110**, 174203 (2024).

[229] To know more, please visit the following link: https://www.analog.com/en/resources/design-tools-and-calculators/ltspice-simulator.html.

[230] In usual notation, the localization-delocalization transition occurs at $\lambda = 2t$. However, we have absorbed a factor of 2 in the QP potential in Eq. (1).

[231] A. Avila, Acta Mathematica **215**, 1 (2015).

[232] A. Chakrabarty and S. Datta, Phys. Rev. B **107**, 064305 (2023).

[233] S. Weidemann, M. Kremer, S. Longhi, *et al.*, Nature Photonics **15**, 576 (2021).

[234] A. F. Tzortzakakis, K. G. Makris, A. Szameit, and E. N. Economou, Phys. Rev. Res. **3**, 013208 (2021).

[235] A. Leventis, K. G. Makris, and E. N. Economou, Phys. Rev. B **106**, 064205 (2022).

[236] S. Weidemann, M. Kremer, T. Helbig, T. Hofmann, A. Stegmaier, M. Greiter, R. Thomale, and A. Szameit, Science **368**, 311 (2020).

[237] The Python codes along with the dataset are available at the following link: https://github.com/DIPENDU-PHY/BD14939.git.

[238] M. König, S. Wiedmann, C. Brüne, A. Roth, H. Buhmann, L. W. Molenkamp, X.-L. Qi, and S.-C. Zhang, Science **318**, 766 (2007).

[239] Y. Ren, Z. Qiao, and Q. Niu, Phys. Rev. Lett. **124**, 166804 (2020).

[240] Y.-J. Lin, K. Jiménez-García, and I. B. Spielman, Nature **471**, 83 (2011).

[241] V. Galitski and I. B. Spielman, Nature **494**, 49 (2013).

[242] P. Wang, Z.-Q. Yu, Z. Fu, J. Miao, L. Huang, S. Chai, H. Zhai, and J. Zhang, Phys. Rev. Lett. **109**, 095301 (2012).

[243] X.-J. Liu, K. T. Law, and T. K. Ng, Phys. Rev. Lett. **112**, 086401 (2014).

[244] E. Prodan, Phys. Rev. B **80**, 125327 (2009).

[245] Y. Yang, Z. Xu, L. Sheng, B. Wang, D. Y. Xing, and D. N. Sheng, Phys. Rev. Lett. **107**, 066602 (2011).

[246] T. Fukui, Y. Hatsugai, and H. Suzuki, Journal of the Physical Society of Japan **74**, 1674 (2005).

[247] J. E. Avron, L. Sadun, J. Segert, and B. Simon, Phys. Rev. Lett. **61**, 1329 (1988).

[248] L. Fu and C. L. Kane, Phys. Rev. Lett. **100**, 096407 (2008).

[249] R. Wang, Z. Y. Xie, B. Wang, and T. Sedrakyan, Phys. Rev. B **106**, L121117 (2022).

[250] N. Nagaosa, J. Sinova, S. Onoda, A. H. MacDonald, and N. P. Ong, Rev. Mod. Phys. **82**, 1539 (2010).

[251] C. L. Kane and E. J. Mele, Phys. Rev. Lett. **95**, 146802 (2005).

[252] N. H. Lindner, G. Refael, and V. Galitski, Nature Physics **7**, 490 (2011).

[253] K. Asano and C. Hotta, Phys. Rev. B **83**, 245125 (2011).

[254] M. Niţă, B. Ostahie, and A. Aldea, Phys. Rev. B **87**, 125428 (2013).

[255] J. Priestley, G. Valentí-Rojas, and P. Öhberg, Phys. Rev. A **109**, 023322 (2024).

[256] A. R. Kolovsky, Phys. Rev. A **98**, 013603 (2018).

[257] F. Schindler, A. M. Cook, M. G. Vergniory, Z. Wang, S. S. P. Parkin, B. A. Bernevig, and T. Neupert, Science Advances **4**, eaat0346 (2018).

[258] S. Lahiri, K. Bhattacharyya, and S. Basu, Phys. Rev. B **112**, 115406 (2025).

[259] R. Okugawa, R. Takahashi, and K. Yokomizo, Phys. Rev. B **102**, 241202 (2020).

[260] W. A. Benalcazar, B. A. Bernevig, and T. L. Hughes, Phys. Rev. B **96**, 245115 (2017).

[261] E. Khalaf, Phys. Rev. B **97**, 205136 (2018).

Awards & Honors

- Awarded with **APS Global Physics Summit DCMP Graduate Student Travel Awards** in the APS March Meeting 2025 in Anaheim, California.
- Qualified CSIR National Eligibility Test (NET) with AIR **40** in 2021.
- Qualified Joint Entrance Screening Test (JEST) with AIR **166** in 2020.
- Qualified Graduate Aptitude Test in Engineering (GATE) with all India Rank (AIR) **107** in 2020.
- Awarded with prestigious INSPIRE scholarship (2015), which is given to the top one percent of students based on higher secondary marks.

Vita

Dipendu Halder was born on 21st October 1997 in West Bengal, India. He completed his B.Sc. with Physics Honours in 2018 from Presidency University, Kolkata, and his M.Sc. in Physics from University of Hyderabad in 2020. Dipendu had enrolled in the Ph.D program at the Indian Institute of Technology Guwahati in January 2021. He had qualified for the CSIR-UGC NET in December 2019 and 2020, the Joint Entrance Screening Test (JEST) in 2020, and the Graduate Aptitude Test in Engineering (GATE) in 2020. He is a researcher in Theoretical Condensed Matter Physics, focusing on the interplay between non-Hermitian Physics, topological phases of matter, and their realization through electrical circuits. His work thoroughly investigates topics such as parity-time symmetry, non-Hermitian skin effect, non-Bloch band theory, exceptional points, Anderson localization in NH systems, higher-order topology, and topolectrical circuits.